Multiple Coulomb Scattering in the MICE Experiment

John Columba Nugent

Department of Physics and Astronomy
College of Science and Engineering
University of Glasgow
2016

A thesis submitted for the degree of Doctor of Philosophy
at the College of Science & Engineering,
University of Glasgow

Multiple Coulomb Scattering in the MICE Experiment

Abstract

The International Muon Ionisation Cooling Experiment (MICE) aims to give the first demonstration of ionisation cooling. MICE will use a low Z absorber to first reduce the momentum of a muon beam; then use a series of radio-frequency (RF) cavities to restore its longitudinal momentum. This action will reduce the overall phase-space volume of the muon beam. The goal of MICE is to reduce the emittance of a muon beam by 5% and to measure the change in emittance to a precision of 1%.

In 2011 MICE took data in its Step I configuration with the goal of understanding the muon beam that will serve the MICE experiment. In order to evaluate the expected performance of the beam using extensive simulation data the MICE user software had to be installed on the Grid. A G4beamline model of the MICE muon beam was updated and validated with Step I data and used for production jobs on the Grid. The results presented in this thesis demonstrate that the simulation is in good agreement with data.

These data were also used to determine the pion contamination in the MICE muon beam using the Time-Of-Flight (TOF) and Kloe-light (KL) detectors. The measurement of ionisation cooling in MICE relies on the selection of a pure sample of muons that traverse the experiment. To make this selection, the MICE Muon Beam is designed to deliver a beam of muons with less than $\sim$1% contamination. The upper limit for the pion contamination measured in this thesis is $f_\pi < 1.4\%$ at 90% C.L., including systematic uncertainties. A similar procedure applied to the G4Beamline and MAUS Monte Carlo simulation yields a pion contamination of $f_\pi < 1.7\%$ at 90% C.L., including statistical and systematic errors. The expectation from the simulated MICE Muon Beam is for a contamination of (0.22 $\pm$ 0.01)%. Therefore, the MICE Muon Beam is able to meet the stringent pion-contamination requirements for the study of ionisation cooling.

In 2015 and 2016, MICE took data in its Step IV configuration giving the first measurement of multiple scattering with the MICE apparatus. In this thesis the results of the measurement of the scattering of muons in gaseous xenon and lithium hydride are reported. The motivation

for the gaseous xenon measurement is to benchmark Multiple Coulomb Scattering (MCS) in a high-Z material, in order to perform further measurements of MCS in the MICE experiment. From this baseline the same analysis was applied to the lithium hydride data, a material for which it is essential to accurately model the MCS for the demonstration of ionisation cooling for muon acceleration. Results from this analysis are compared to GEANT4 simulations and to predictions from an analytical formula advocated by the Particle Data Group (PDG).

Acknowledgements

I would like to thank my supervisor, Paul Soler, for his generous support throughout this endeavour. Without his depth of knowledge and keen insight this thesis would not have been possible.

I would also like to thank Ryan Bayes for his guidance and being so freely giving of his time. I would also like to thank all of my fellow MICE collaborators for our various interactions over the course of this thesis. Whether it was sharing midnight shifts together or discussions at meetings I would like to thank everyone for their input.

Finally I would like to thank my friends and family without whose love, laughter and company this thesis could never have been completed.

Declaration

The results presented in this thesis are my own work unless otherwise stated. Chapters 1 and 2 are reviews of the physics of neutrinos, a description of the baseline neutrino factory and of the Muon Ionisation Cooling Experiment (MICE) respectively. The reviews were carried out by the author, referencing from the established literature.

The simulation and service work described in chapter 3 updated and developed code common to the MAUS software group. The specific functionality that I added and maintained is described, although numerous suggestions came about through discussions with the MAUS software group. The tools to model the beam line in G4beamline were entirely my own work. The code to measure the beam parameters and evaluate the simulations was provided by Victoria Blackmore (Imperial College). The data that is used to validate the new simulations was collected in 2010.

When I joined the MICE collaboration the pion contamination measurement was underway, with the fundamental principles of the method understood. I created the MC simulations to complement the data and updated and revised all aspects of the analysis with the final result presented in this thesis. The data used in this analysis were collected in December of 2011.

The multiple scattering analysis was entirely my own work. I created the G4beamline simulations and Ryan Bayes (Glasgow) used these to seed the various MAUS simulations. These simulations are compared to data in the analysis. Appropriate references are provided when the results of others are mentioned. The research presented here was not submitted for another degree in any other department or university. The data used in this analysis were collected in December of 2015 and March of 2016.

Wir müssen wissen, wir werden wissen!

David Hilbert

Contents

List of Figures

List of Tables

Chapter 1

Neutrino Physics

1.1 Neutrino Discovery

In 1930 Wolfgang Pauli proposed the existence of an electrically neutral particle to resolve the problem of the apparent non-conservation of energy, momentum and angular momentum in beta decay [1]. The anomaly arose in the shape of the end point spectrum of beta decay, as can be seen in figure 1.1. In a two body decay, a sharp peak at the end point was expected. However what was observed was a continuous spectrum. Several radical proposals were put forward to resolve this, including the statistical violation of nature's fundamental conservation laws. However, Pauli's hypothesis of a new particle proved to be accurate.

For confirmation of his claim, Pauli had to wait 26 years until in 1956 Cowan and Reines detected Pauli's particle via beta capture [3]. Cowan and Reines placed two tanks of water surrounded by liquid scintillator in close proximity to a nuclear reactor at the Savannah River Plant in South Carolina. The reactor provided a neutrino flux of 5×10^{13} neutrinos per second per square centimetre with the inverse beta decay process proceeding according to:

$$\bar{\nu}_e + p \rightarrow n + e^+. \tag{1.1}$$

The positron annihilates with an electron and the neutron is captured by a nucleus. A gamma ray pair is created from the positron annihilation and the neutron capture also produces a number of gamma rays a few milliseconds later, with the detection of both sets of gammas giving the prompt and delayed signal that a neutron decay has occurred. This coincident signal can be detected cleanly above the background noise of individual gamma rays. With this setup, Cowan and Reines demonstrated the first observation of a new fundamental particle—the neutrino.

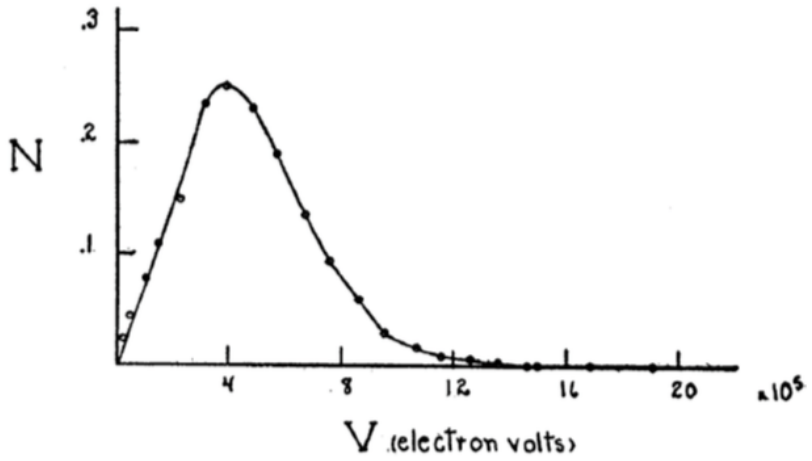

Figure 1.1: The experimentally observed energy spectrum for beta decay from a Radium-E source, figure taken from Ref. [2].

1.2 Neutrino Oscillation

Neutrino oscillation is the phenomenon whereby neutrinos created with a specific lepton flavour can be measured at a later point to have a different flavour. In the formalism of local quantum field theory, used to construct the Standard Model (SM), this means that the left-handed (LH) flavour neutrino fields $\nu_{lL}(x)$, which enter into the expression for the lepton current in the charged current (CC) weak interaction Lagrangian, are linear combinations of the fields of three (or more) neutrinos $\nu_{jL}(x)$ where $j = 1, 2, 3$, having masses $m_j \neq 0$ for at least one j:

$$\nu_{lL}(x) = \sum_j U_{lj}\nu_{jL}(x), \qquad l = e, \mu, \tau. \tag{1.2}$$

where ν_{jL}(x) is the LH component of the field of ν_j possessing a mass m_j and U is a unitary matrix. This unitary matrix is often referred to as the Pontecorvo-Maki-Nakagawa-Sakata (PMNS) matrix and describes lepton mixing. Currently all compelling neutrino oscillation data can be described assuming 3-flavour neutrino mixing in vacuum.

In the case of n neutrino flavours and n massive neutrinos, the $n \times n$ unitary neutrino mixing matrix U can be parametrised by $n(n-1)/2$ Euler angles and $n(n+1)/2$ phases. If the massive neutrinos ν_j are Dirac particles, only $(n-1)(n-2)/2$ phases are physical and can be responsible for CP violation in the lepton sector. Viewed in this way, neutrino mixing with a Dirac massive neutrino is similar to quark mixing. If $n = 3$ there is just one CP violating phase in U. The test for CP invariance is to determine if $U^* = U$. Given the abundance of matter over anti-matter in nature, identifying a mechanism responsible for this asymmetry is of considerable interest. The Sakharov conditions [4] stipulate that any explanation for this asymmetry must include a CP-violating process. Thus, observation of such a process in the

lepton sector would be a landmark discovery. Therefore, the measurement of CP invariance in the lepton sector is of fundamental importance.

A simplified version of the derivation of the expressions for neutrino and antineutrino oscillation probabilities will be outlined following [5]. In this discussion, relativistic neutrinos are considered; all current and planned neutrino experiments operate in this regime. It is also assumed that the spectrum of neutrino masses is not degenerate, therefore the states $|\nu_j; \widetilde{p_j}\rangle$ will in general have different energies and momenta.

In this scenario, neutrinos travel a distance L in vacuum and are detected at time T in the detector's rest frame via a CC weak interaction process. Then, the amplitude of the probability that neutrino $\nu_{l'}$ will be observed if neutrino ν_l was produced at the neutrino source can be expressed as:

$$A(\nu_l \to \nu_{l'}) = \sum_j U_{l'j} D_j U^{\dagger}_{jl}, \qquad\qquad l, l' = e, \mu, \tau, \tag{1.3}$$

where $D_j = D_j(\tilde{p_j}; L, T)$ describes the propagation of ν_j between the source and the detector, $U^{\dagger}_{jl}$ and $U_{l'j}$ are the amplitudes to find ν_j in the initial and in the final flavour neutrino state, respectively. Considering relativistic Quantum Mechanics, it can be shown that [6; 7]

$$D_j \equiv D_j(\tilde{p_j}; L, T) = e^{-i\tilde{p_j}(x_j - x_0)} = e^{-i(E_j T - p_j L)}, \qquad p_j \equiv |\boldsymbol{p}_j| \tag{1.4}$$

where x_0 and x_j are the space-time coordinates of the points of neutrino production and detection, $T = (t_f - t_0)$ and $\tilde{L} = \tilde{k}(x_j - x_0)$, $\boldsymbol{k}$ being the unit vector in the direction of neutrino momentum, $\boldsymbol{p}_j = \boldsymbol{k} p_j$. When calculating the probability $P(\nu_l \to \nu_{l'}) = |A(\nu_l \to \nu_{l'})|^2$ the relevant factor is $D_j D^*_k$, which has a dependence on the phase

$$\delta\psi_{jk} = (E_j - E_k)T - (p_j - p_k)L = (E_j - E_k)\left[T - \frac{E_j + E_k}{p_j + p_k}L\right] + \frac{m_j^2 - m_k^2}{p_j + p_k}L. \tag{1.5}$$

By assuming that $E_j = E_k = E_0$ the first term on the r.h.s of equation 1.5 disappears thus

$$\delta\psi_{jk} \cong \frac{m_j^2 - m_k^2}{2p}L = 2\pi\frac{L}{L^{\nu}_{jk}}\text{sgn}(m_j^2 - m_k^2), \tag{1.6}$$

where $p = (p_j + p_k)/2$ and

$$L^{\nu}_{jk} = 4\pi\frac{p}{|\Delta m^2_{jk}|} \cong 2.48\text{m}\frac{p[\text{MeV}]}{|\Delta m^2_{jk}|[\text{eV}^2]} \tag{1.7}$$

is the neutrino oscillation length associated with Δm^2_{jk}. It is assumed that p is the zero

neutrino mass momentum, $p = E$. The phase difference $\delta\psi_{jk}$ from equation 1.6 is Lorentz-invariant.

Therefore if we combine equations 1.3, 1.4 and 1.5 the oscillation probabilities for $\nu_l \to \nu_{l'}$ and $\bar{\nu}_l \to \bar{\nu}_{l'}$ are:

$$P(\nu_l \to \nu_{l'}) = \sum_j |U_{l'j}|^2 |U_{lj}|^2 + 2\sum_{j>k} |U_{l'j}U^*_{lj}U_{lk}U^*_{l'k}| \cos\left(\frac{\Delta m^2_{jk}}{2p}L - \psi_{l'l;jk}\right), \tag{1.8}$$

$$P(\bar{\nu}_l \to \bar{\nu}_{l'}) = \sum_j |U_{l'j}|^2 |U_{lj}|^2 + 2\sum_{j>k} |U_{l'j}U^*_{lj}U_{lk}U^*_{l'k}| \cos\left(\frac{\Delta m^2_{jk}}{2p}L + \psi_{l'l;jk}\right), \tag{1.9}$$

where $l, l' = e, \mu, \tau$ and $\psi_{l'l;jk} = \arg(U_{l'j}U^*_{lj}U_{lk}U^*_{l'k})$. It is clear from equation 1.6 that at least two non-degenerate neutrino masses and lepton mixing, $U \neq 1$, are required if neutrino oscillations are to occur. The oscillation effect can be large in the case where

$$\frac{|\Delta m^2_{jk}|}{2p}L = 2\pi\frac{L}{L^\nu_{jk}} \gtrsim 1, j \neq k. \tag{1.10}$$

or any higher multiple of this value for at least one Δm^2_{jk} with figure 1.2 showing the the development of the osciallion probability in the two neutrino case. This condition has a simple physical interpretation: the neutrino oscillation length L^ν_{jk} should be of the order of, or smaller than, the source-detector distance L, otherwise the oscillations will not have time to develop before neutrinos reach the detector.

Inspection of equation 1.8 and 1.9 tells us that there are CP violation effects in neutrino oscillation only if $\psi_{l'l;jk} \neq \pi q, q = 0, 1, 2$, i.e., if $U_{l'j}U^*_{lj}U_{lk}U^*_{l'k}$ and therefore U itself, is not real. To measure the CP asymmetry the amplitude:

$$A^{(l'l)}_{CP} \equiv P(\nu_l \to \nu_{l'}) - P(\bar{\nu}_l \to \bar{\nu}_{l'}), \tag{1.11}$$

must be measured. Applying equations 1.8 and 1.9, it follows directly that

$$A^{(l'l)}_{CP} = 4\sum_{j>k} \mathrm{Im}(U_{l'j}U^*_{lj}U_{lk}U^*_{l'k}) \sin\frac{\Delta m^2_{jk}}{2p}L, \qquad l, l' = e, \mu, \tau. \tag{1.12}$$

To date the three-neutrino mixing data is best described by one of the two independent mass square differences, with one difference, Δm^2_{21}, being much smaller in absolute value than the

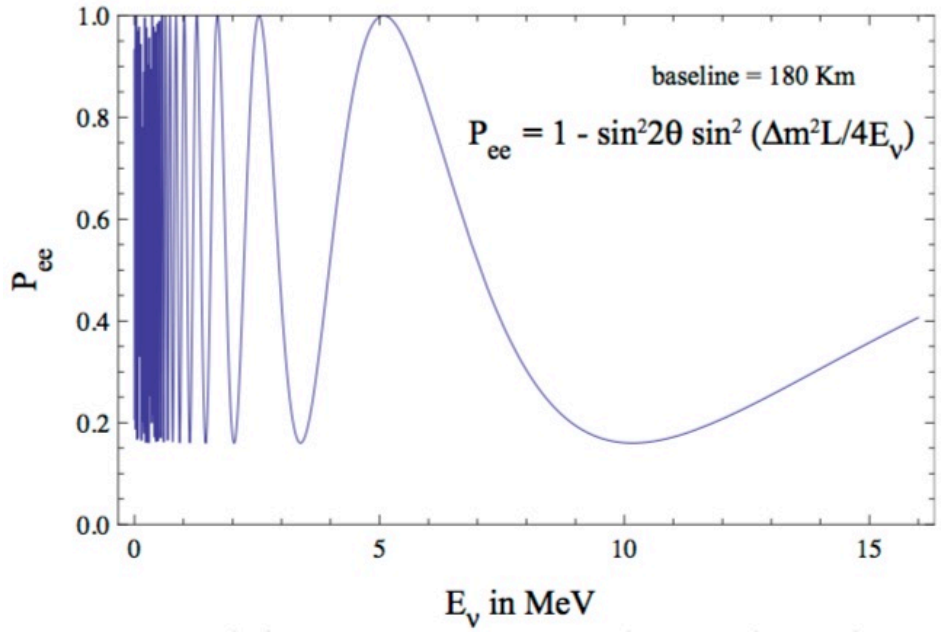

Figure 1.2: The $\nu_e(\bar{\nu}_e)$ survival probability $P(\nu_e \to \nu_e) = P(\bar{\nu}_e \to \bar{\nu}_e)$, assuming 2-neutrino mixing, as a function of the neutrino energy for $L = 180$ km, $\Delta m^2 = 7.0 \times 10^5 \text{eV}^2$ and $\sin^2 2\theta = 0.84$, figure taken from Ref. [8].

second one, Δm^2_{31}. In summary:

$$\begin{aligned} |\Delta m^2_{21}| &\cong 7.5 \times 10^{-5}\text{eV}^2, \\ |\Delta m^2_{31}| &\cong 2.5 \times 10^{-3}\text{eV}^2, \\ |\Delta m^2_{21}|/|\Delta m^2_{31}| &\cong 0.03, \end{aligned} \tag{1.13}$$

In this case, by keeping only the oscillating terms involving Δm^2_{n1}, we obtain from equation 1.8 and 1.9:

$$P(\nu_{l(l')} \to \nu_{l'(l)}) \cong P(\bar{\nu}_{l(l')} \to \bar{\nu}_{l'(l)}) \cong \delta_{ll'} - 2|U_{ln}|^2\left[\delta_{ll'} - |U_{l'n}|^2\right](1 - \cos\frac{\Delta m^2_{n1}}{2p}L). \tag{1.14}$$

Choosing $l = e(\mu)$ and $l' = \mu(e)$ and setting $n = 3$ we get:

$$P(\nu_{\mu(e)} \to \nu_{e(\mu)}) \cong 2|U_{\mu 3}|^2|U_{e3}|^2(1 - \cos\frac{\Delta m^2_{31}}{2p}L) \tag{1.15}$$

where

$$\sin^2\theta_{13} = |U_{e3}|^2, \qquad \sin^2\theta_{23}\cos^2\theta_{13} = |U_{\mu 3}|. \tag{1.16}$$

The probability equation 1.15 describes with good precision the $\nu_\mu \to \nu_e$ and $\bar{\nu}_\mu \to \bar{\nu}_e$

oscillations in conditions similar to those expected in long-baseline neutrino oscillation experiments.

θ_{12} is commonly referred to as the "solar" and θ_{23} as the "atmospheric" neutrino mixing angle. In a similar manner Δm^2_{12} is referred to as the "solar" and Δm^2_{31} as the "atmospheric" neutrino mass squared difference. This is under the assumption that $0 < \Delta m^2_{21} < |\Delta m^2_{31(32)}|$ and $|U_{e3}|^2 = |\sin\theta_{13}|^2 \ll 1$. These labels are due to the experiments that characterised these parameters i.e. solar or atmospheric experiments.

The probability in equation 1.15 depends on $(1 - \cos 2\pi L/L^\nu)$ and it is this dependence that gives rise to the label "neutrino oscillation". There is also a dependence on the neutrino energy $p = E$, hence neutrino experiments are characterised by these two parameters, the average energy of the neutrinos and the source-detector distance L. Therefore the statement

$$P_{\mu e} \sim \sin^2\theta_{13}\sin^2 2\theta_{13}\sin^2\left(\frac{\Delta m^2_{13}L}{4E}\right), \tag{1.17}$$

gives the probability that a neutrino created with one flavour is detected some distance away as a neutrino of another flavour. In this case it is a muon neutrino changing to an electron neutrino. The observation of neutrino oscillation [9] between different neutrino flavours conclusively demonstrated the non-zero value of the neutrino masses. The SM predicts that neutrinos are massless and neutrino oscillations can only be incorporated into the SM in an *ad hoc* manner. As such, neutrino masses are considered to be a signature of beyond the SM physics.

1.2.1 Neutrino Oscillation in Matter

Neutrino oscillation depends on the Hamiltonian of the neutrino system. This can be substantially changed for neutrinos propagating through matter compared with neutrinos propagating through vacuum [5]. This difference stems from neutrinos interacting with matter as they traverse it. For instance, the neutrinos may elastically or quasi-elastically scatter off the electrons, protons or neutrons present in matter. The mean free path of neutrinos for incoherent scattering processes is $\sim 10^{10}$ km in the centre of the sun (matter density ~ 150 g/cm^3) for neutrinos with energy 1 MeV. This scattering process is of negligible importance, which is useful as such a scattering process would destroy the coherence between the neutrino states.

When the coherent elastic scattering of the neutrinos is considered, different indices of refraction are generated for ν_e and ν_μ. The scattering processes of importance are $\nu_e - e^-$ and $\nu_\mu - e^-$. The real part of the amplitudes in the forward direction ($\theta = 0$) $F_{\nu_e - e^-}(0)$ and

$F_{\nu_\mu - e^-}(0)$ can be calculated in the Standard Model. Only the diagram with exchange of a virtual $W^\pm$-boson contributes to the real part of the scattering amplitude at leading order. It can be shown [10]

$$\begin{aligned}\kappa(\nu_e) - \kappa(\nu_\mu) &= \frac{2\pi}{p^2}\big(\text{Re}[F_{\nu_e - e^-}(0)] - \text{Re}[F_{\nu_\mu - e^-}(0)]\big) \\ &= -\frac{1}{p}\sqrt{2}G_F N_e,\end{aligned} \tag{1.18}$$

where N_e is the electron number density in matter. Taking this $\kappa(\nu_e) - \kappa(\nu_\mu)$, the system of evolution equations describing the $\nu_e \leftrightarrow \nu_\mu$ oscillation in matter reads [10]

$$i\frac{d}{dt}\begin{pmatrix} A_e(t,t_0) \\ A_\mu(t,t_0)\end{pmatrix} = \begin{pmatrix} -\epsilon(t) & \epsilon' \\ \epsilon' & \epsilon(t)\end{pmatrix}\begin{pmatrix} A_e(t,t_0) \\ A_\mu(t,t_0)\end{pmatrix} \tag{1.19}$$

where $A_e(t,t_0)(A_\mu(t,t_0))$ is the amplitude of the probability to find $\nu_e(\nu_\mu)$ at time t of the evolution of the system if at time $t_0 \leq t$ the neutrino ν_e or ν_μ was produced and

$$\epsilon(t) = \frac{1}{2}\left[\frac{\Delta m^2}{2E}\cos 2\theta - \sqrt{2}G_F N_e(t)\right], \quad \epsilon' = \frac{\Delta m^2}{4E}\sin 2\theta, \tag{1.20}$$

with θ the mixing angle and Δm^2 the mass-squared difference of the neutrino mass eigenstates. It is the factor $\sqrt{2}G_F N_e(t)$ in $\epsilon(t)$, with G_F the Fermi coupling constant, that accounts for the difference in neutrino oscillations for neutrinos in matter and in vacuum. The behaviour is commonly referred to as the Mikheyev, Smirnov, Wolfenstein (or MSW) effect [11; 10].

In the case of $\nu_e \leftrightarrow \nu_\mu$ oscillations in matter the eigenstates of the Hamiltonian of the neutrino system in vacuum, $|\nu_{1,2}\rangle$ are not eigenstates of H_m. When diagonalising the evolution matrix on the r.h.s of the system in equation 1.19 the eigenstates $|\nu^2_{1,2}\rangle$ of H_m are:

$$|\nu_e\rangle = |\nu_1^m\rangle\cos\theta_m + |\nu_2^m\rangle\sin\theta_m, \quad |\nu_\mu\rangle = -|\nu_1^m\rangle\sin\theta_m + |\nu_2^m\rangle\cos\theta_m, \tag{1.21}$$

where θ_m is the neutrino mixing angle in matter [10],

$$\sin 2\theta_m = \frac{\tan 2\theta}{\sqrt{(1-\frac{N_e}{N_e^{res}})^2 + \tan^2 2\theta}}, \cos 2\theta_m = \frac{1 - N_e/N_e^{res}}{\sqrt{(1-\frac{N_e}{N_e^{res}})^2 + \tan^2 2\theta}} \tag{1.22}$$

with

$$N_e^{res} = \frac{\Delta m^2 \cos 2\theta}{2E\sqrt{2}G_F} \cong 6.56 \times 10^6 \frac{\Delta m^2[\text{eV}^2]}{E[M\text{eV}]} \cos 2\theta \, \text{cm}^{-3}\text{N}_A. \tag{1.23}$$

This is referred to as the "resonance density" (when $\Delta m^2 \cos 2\theta > 0$ and N_A is Avogadro's number). The difference in energy between "adiabatic" [1] states $|\nu_{1,2}^M\rangle$ is:

$$E_2^m = E_1^m = \frac{\Delta m^2}{2E}\left((1 - \frac{N_e}{N_e^{res}})^2 \cos^2 2\theta + \sin^2 2\theta\right)^{\frac{1}{2}} \equiv \frac{\Delta M^2}{2E}. \tag{1.24}$$

We arrive at the statement that the probability of $\nu_e \to \nu_\mu$ transition in matter with N_e constant or slowly varying, is of the form [10]

$$\begin{aligned} P_m^{2\nu}(\nu_e \to \nu_\mu) = |A_\mu(t)|^2 = \frac{1}{2}\sin^2 2\theta_m \left[1 - \cos 2\pi \frac{L}{L_m}\right] \\ L_m = 2\pi/(E_2^m - E_1^m), \end{aligned} \tag{1.25}$$

where L_m is the oscillation length in matter. Therefore the presence of matter can lead to a strong enhancement of the oscillation probability $P_m^{2\nu}(\nu_e \to \nu_\mu)$ even if oscillations in vacuum would otherwise be strongly suppressed by a small value of $\sin^2 2\theta$. A particular example is the case of solar neutrino oscillations that are observed and will be discussed in Section 1.3.3. This behaviour is due to the MSW effect for the neutrinos travelling through the dense matter in the sun.

1.2.2 Neutrino Mass Hierarchy

The difference between neutrino mass eigenstates is known from atmospheric and reactor neutrino experiments [12], however the hierarchy of these states is yet to be confirmed, as can be seen in figure 1.3. One way of determining the nature of the neutrino mass hierarchy is by measuring neutrino oscillations for neutrinos travelling through matter. The MSW effect changes the $\nu_\mu \to \nu_e$ probability of oscillation from [13] :

$$P_{\mu e} = \sin^2\theta_{23} \sin^2 2\theta_{13} \sin^2\left[\frac{\Delta m_{13}^2 L}{4E}\right] + \text{"subleading"} \tag{1.26}$$

to,

$$P_{\mu e} \sim \sin^2\theta_{23} \sin^2 2\theta_{13}^{\text{eff}} \sin^2\left(\frac{\Delta_{13}^{\text{eff}} L}{2}\right), \tag{1.27}$$

[1] Where "adiabatic" is the case in which the density varies slowly compared to the oscillation length of the neutrino.

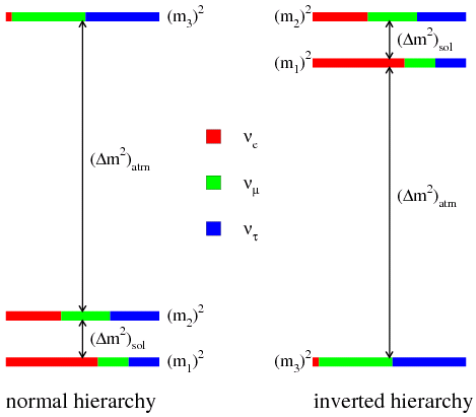

Figure 1.3: The difference between neutrino mass states is known, however the nature of the hierarchy, normal or inverted, has yet to be determined. Figure taken from Ref. [13].

where,

$$\begin{aligned} \sin^2 2\theta_{13}^{\text{eff}} &= \frac{\Delta_{13}^2 \sin^2 2\theta_{13}}{(\Delta_{13}^{\text{eff}})^2} \\ \Delta_{13}^{\text{eff}} &= \sqrt{(\Delta_{13}\cos 2\theta_{13} - A)^2 + \Delta_{13}^2 \sin^2 2\theta_{13}} \\ \Delta_{13} &= \frac{\Delta m_{13}^2}{2E} \\ A &= \pm\sqrt{2} G_F N_e \end{aligned} \tag{1.28}$$

The probability of oscillation now depends on the relative sign of Δ_{13} and A. $P_{\mu e}$ is now different for the two different mass hierarchies allowing the cases to be distinguished.

1.2.3 Helicity

Helicity is defined as the projection of a particle's spin onto the direction of its momentum,

$$h = \frac{\overrightarrow{S} \cdot \overrightarrow{p}}{|\overrightarrow{p}|} \tag{1.29}$$

where $\overrightarrow{S}$ is the spin and $\overrightarrow{p}$ is the momentum. In the case where the neutrino's spin and direction of motion are parallel (anti-parallel) the neutrino is said to be right-handed (left-handed). There is currently no compelling evidence for the existence of predominantly right-handed relativistic neutrinos. However the LSND [14] and MiniBooNE [15] experiments have both reported interesting hints at the possibility of right-handed neutrinos.

Given the unconfirmed and sometimes conflicting reports, the existence of further generations of neutrinos beyond the three active generations currently known is a topic of continued

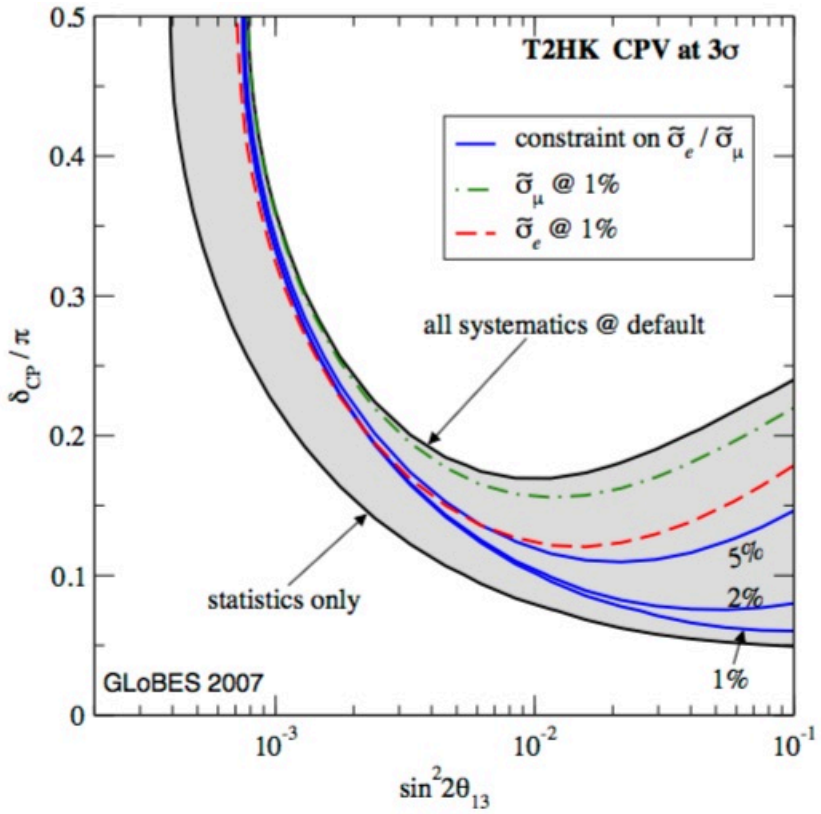

Figure 1.4: T2HK sensitivity to CP-invariance violation at 3σ. The sensitivity that would be obtained in the absence of systematic uncertainties is shown by the lower solid black line. Taking systematic errors into account, as described in [16] yields the sensitivity shown by the upper solid black line. The sensitivity that would pertain if the product of the efficiency and the (anti)neutrino scattering cross sections (denoted $\sigma^{-}_{\mu,e}$) are known with a precision of 1% are shown by the dashed red, and dot dashed green lines. The solid blue lines show the effect of an uncertainty of 1%, 2% and 5% on the ratio of the electron to muon neutrino times the relevant efficiency. Figure taken from Ref. [16].

interest. In the SM only the left-handed neutrinos couple to the weak force. As a consequence any right-handed neutrinos would only interact via gravity and hence are known as "sterile". Detection of these particles would involve deviations from the predicted rates of oscillation between the known active generations. As such, searches for right-handed neutrinos require the neutrino cross-sections to be known to an unprecedented level of accuracy.

1.2.4 Neutrino Cross-Sections

The cross section is an effective area that quantifies the intrinsic likelihood of a scattering event when an incident beam strikes a target made of discrete particles. In order to accurately study neutrino oscillations the neutrino cross sections must be known. Such considerations are now particularly acute with the discovery of a large θ_{13} angle. Recent studies [17] have illustrated this point for the T2HK experiment. The sensitivity of T2HK to CP-invariance

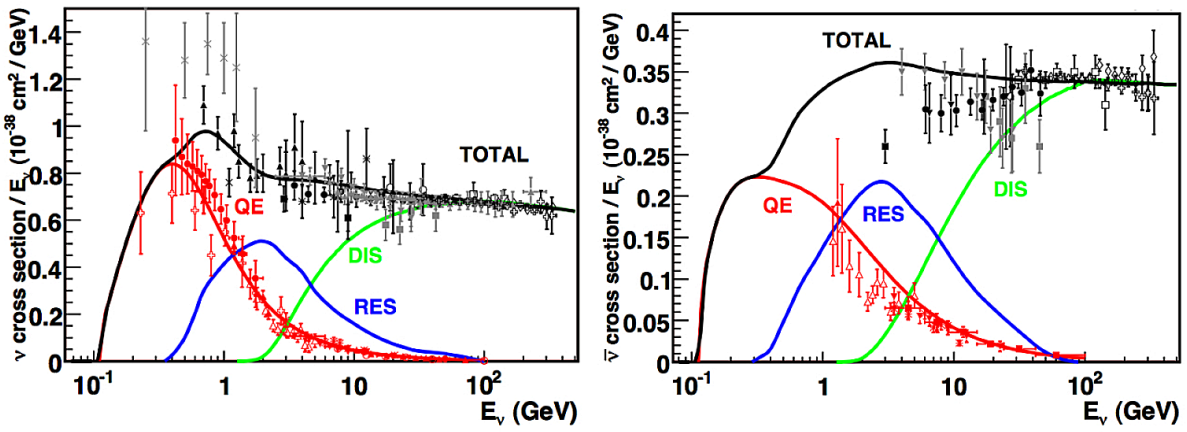

Figure 1.5: The neutrino-nucleon (left panel) and antineutrino-nucleon (right panel) cross sections plotted as a function of (anti)neutrino energy [18]. The data are compared to the expectations of the models described in [19]. The processes that contribute to the total cross section (shown by the black lines) are: quasi-elastic (QE, red lines) scattering; resonance production (RES, blue lines); and deep inelastic scattering (DIS, green lines). The uncertainties in the energy range of interest are typically 10-40%. Figure taken from Ref. [20].

violation is shown as function of $\sin^2 2\theta_{13}$ in figure 1.4. The experiment considered in this analysis assumes a proton beam power of 4 MW generating a conventional super-beam, where neutrinos are created from the decay of pions, illuminating a 500 kT water Cherenkov detector at a distance of 295 km from the source. The analysis assumes a 0.1 kT water Cherenkov near detector at a distance of 2 km.

From figure 1.4, taking the accepted value of $\sin^2 2\theta_{13} \approx 0.1$ in order to make full use of the statistics on offer the neutrino scattering cross sections times efficiencies must be known to a precision of $\sim 1\%$. In addition, the ratio of the electron-neutrino cross section times efficiency to the muon-neutrino cross section times efficiency must also be known to a precision of $\sim 1\%$. If a near/far detector combination is employed by a wide-band neutrino beam experiment it is possible to resolve the first and second oscillation maxima. Such experiments are less curtailed by the lack of detailed knowledge of the neutrino cross sections. However even in these cases significant sensitivity to CP-invariance violation is gained if it is assumed that the cross sections are known to a precision of $\sim 1\%$ or better.

A number of experiments currently taking data [21] are studying these neutrino interactions. Fig. 1.5 shows the present data on the charged-current neutrino-scattering cross sections in the relevant energy range excluding the most recent measurements by T2K [22] and Minerva [23]. At present, there is little data on the electron-neutrino cross sections and they are inferred [24] by extrapolation of the muon neutrino cross sections. Such extrapolations suffer from substantial uncertainties arising from non-perturbative hadronic corrections and it is therefore

essential that detailed measurements of the $\nu_e N$ and $\nu_\mu N$ scattering cross sections and hadron-production rates are performed.

Facilities such as the Neutrino Factory (Section 1.4), therefore, have a unique opportunity. The flavour composition of the beam and the neutrino energy spectrum are both known precisely. In addition, the storage ring instrumentation combined with measurements at the near detector will allow the neutrino flux to be measured with a precision of 1%. Thus the $\nu_e N$ and $\nu_\mu N$ scattering cross sections for neutrino energies in the range $1 - -3$ GeV can be determined with a precision approaching 1%. This will be of fundamental importance to the present and next generation of long-baseline neutrino oscillation experiments.

1.3 Neutrino Experiments

Since Cowan and Reines' discovery of the neutrino more than half a century ago, a multitude of neutrino experiments have taken data. A detailed discussion of these experiments is beyond the scope of this thesis, however this section will give a brief overview of important milestones in this field.

1.3.1 Reactor Experiments

Neutrinos are a byproduct of the nuclear reactions that take place within reactors from which the resultant flux of neutrinos can be very high. An example of such an experiment is Daya Bay which took first data in 2012. The Daya Bay nuclear power complex is located on the southern coast of China, 55 km to the northeast of Hong Kong. The complex consists of six 2.9 GW_{th} reactors with an estimated flux of 1×10^{21} antineutrinos per second. A large and reliable antineutrino flux makes reactor experiments attractive with the additional feature that both the energy spectrum and flux of the neutrinos are well known [25].

Reactor experiments typically offer a large value of L/E due to the low neutrino energy and so can be used to probe mass differences over short base lines. This has the added advantage that the neutrino flux will clearly be higher at the detector at these shorter baselines. As an example, the base line of the Daya Bay experiment to the two near detectors was 470 m and 576 m and the baseline to the far detector was 1648 m. The $\bar{\nu}_e$ is detected via the inverse β-decay (IBD) reaction, $\bar{\nu}_e + p \rightarrow e^+ + n$, in a gadolinium-doped liquid scintillator (Gd-LS) [26]. The coincidence of the prompt scintillation from the e^+ and the delayed neutron capture on Gd provides a distinctive $\bar{\nu}_e$ signature. Figure 1.6 shows a schematic of a Daya Bay antineutrino detector.

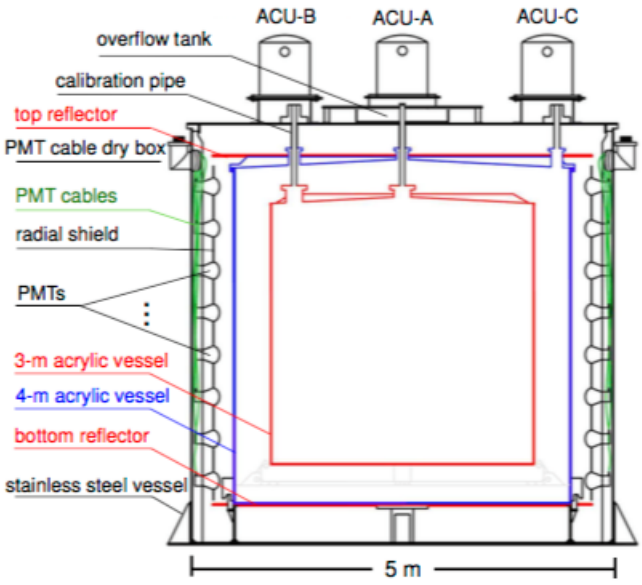

Figure 1.6: Schematic for a Daya Bay antineutrino detector, figure taken from Ref. [25].

The $\bar{\nu}_e$ rate in the far hall was predicted with a weighted combination of the two near-hall measurements assuming no oscillation. The weights were determined by the thermal power of each reactor and its baseline to each antineutrino detector. A deficit was observed in the far hall, expressed as a ratio of observed to expected events [27],

$$R = 0.940 \pm 0.011\,(\text{stat.}) \pm 0.004\,(\text{syst.}) \tag{1.30}$$

The value of $\sin^2 2\theta_{13}$ was determined with a χ^2 constructed with residual terms accounting for the correlation of the systematic errors,

$$\chi^2 = \sum_{d=1}^{6} \frac{[M_d - T_d(1 + \epsilon + \sum_r \omega_r^d \alpha_r + \epsilon_d) + \eta_d]^2}{M_d + B_d} + \sum_r \frac{\alpha_r^2}{\sigma_r^2} + \sum_{d=1}^{6} \left(\frac{\epsilon_d^2}{\sigma_d^2} + \frac{\eta_d^2}{\sigma_B^2} \right), \tag{1.31}$$

where M_d is the measured IBD events of the dth antineutrino detector with backgrounds subtracted, B_d is the corresponding background, T_d is the prediction based on the neutrino flux, MC and neutrino oscillations, ω_r^d is the fraction of IBD contribution of the rth reactor to the dth antineutrino detector determined by baselines and reactor fluxes. ϵ is the absolute normalisation, σ_d, σ_r and σ_B are the residual parameters corresponding the uncorrelated reactor uncertainties and ϵ_d, α_r and η_d are the corresponding residual parameters. Figure 1.7 shows that the χ^2 distribution and the best-fit value is [27]

$$\sin^2 2\theta_{13} = 0.092 \pm 0.016(\text{stat.}) \pm 0.005(\text{syst.}) \tag{1.32}$$

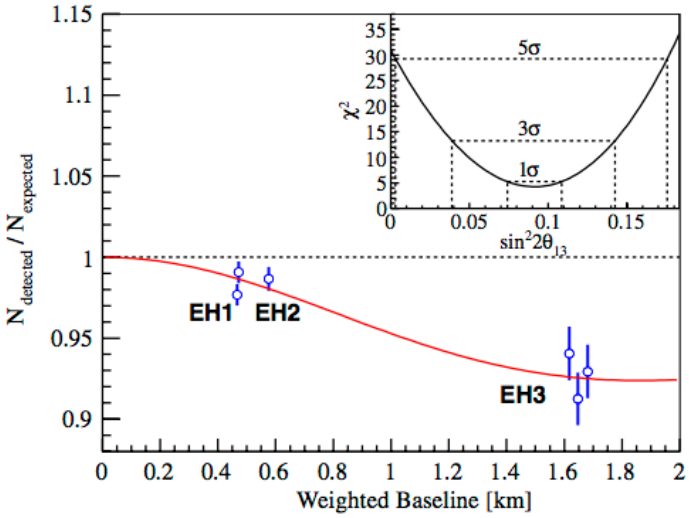

Figure 1.7: Ratio of measured versus expected signal in each detector, assuming no oscillation. The error bar is the uncorrelated uncertainty of each antineutrino detector, including statistical, detector-related, and background-related uncertainties. The expected signal is corrected with the best-fit normalisation parameter. Reactor and survey data were used to compute the flux weighted average baselines. The oscillation survival probability at the best-fit value is given by the smooth curve. The AD4 and AD6 data points are displaced by -30 and $+30$ m for visual clarity. The χ^2 versus $\sin^2 2\theta_{13}$ is shown in the inset. Figure taken from Ref. [27].

with a χ^2/NDF of 4.26/4. A rate-only analysis was also performed with the observed $\bar{\nu}_e$ spectrum in the far hall compared to the prediction extrapolated from the near hall measurements (figure 1.8). The disagreement in this spectrum gives further weight to the claim to the observation of neutrino oscillation.

This was the first measurement with a significance of greater than 5 standard deviations of a non-zero θ_{13}. It was also a significant discovery as against expectation the measured value of θ_{13} was large. Future plans for this project involve an upgrade of the detector. Project JUNO [28] will replace the far detector with a 20 kTon liquid scintillator detector at a distance of 50 km giving a 3% energy resolution (at 1 MeV). It is anticipated that the neutrino mass hierarchy may be resolved with this precision experiment.

1.3.1.1 KamLAND

The KamLAND (KAMioka Liquid scintillator ANti-neutrino Detector) experiment first took data in 2002. Rather than resolving one particular mixing angle as was the case for Daya Bay KamLAND was looking for confirmation of neutrino oscillation previously hinted at by SuperKamiokande and SNO. The experiment was serviced by nuclear reactors across Japan (53 in total) with more than 80% of the neutrino flux having a baseline of 140–210 km. The detector itself comprises a 13 m diameter spherical steel inner volume holding 1 kiloton of

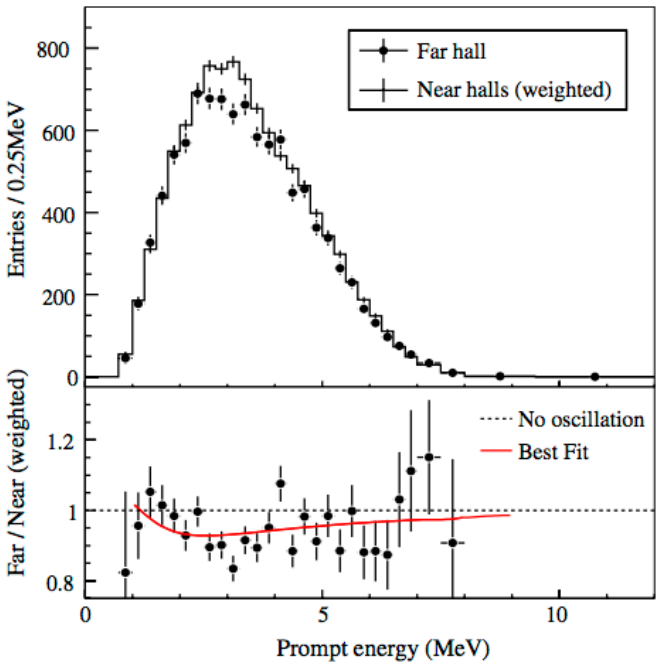

Figure 1.8: Top: Measured prompt-energy spectrum of the far hall (sum of three antineutrino detectors) compared with the no oscillation prediction from the measurements of the two near halls. Spectra were background subtracted. Uncertainties are statistical only. Bottom: The ratio of measured and predicted no oscillation spectra. The solid curve is the best-fit solution with $\sin^2 2\theta_{13} = 0.092$ obtained from the rate-only analysis. The dashed line is the no-oscillation prediction. Figure taken from Ref. [27].

ultra-pure liquid scintillator, with 1,879 PMTs lining the inner volume. This is surrounded by a 3.2 kiloton water–Cherenkov detector with 225 PMTs which provides shielding from natural sources of radiation. The most precise result for the two neutrino oscillation scenario was determined by combining KamLAND data with the solar neutrino data giving best fit values of $\tan^2\theta = 0.47 \pm 0.06$ and $\Delta m^2 = 7.59 \pm 0.21 \times 10^5 \text{eV}^2$ [29]. This result was of great significance as this was the first confirmation of neutrino oscillation independent of a purely lepton flavour changing process.

1.3.2 Atmospheric Experiments

Cosmic rays from a variety of sources are continually bombarding the earth's upper atmosphere. These rays particle (mainly protons, but also helium nuclei and other heavier nuclei) produce atmospheric pions from nuclear collisions with the upper atmosphere, which decay to muons via

$$\pi^{\pm} \rightarrow \mu^{\pm} + \nu_{\mu}(\bar{\nu}_{\mu}) \tag{1.33}$$

These muons subsequently decay to neutrinos

$$\mu^{\pm} \rightarrow e^{\pm} + (\bar{\nu}_{\mu})\nu_{\mu} + (\nu_e)\bar{\nu}_e \tag{1.34}$$

where the neutrino energy ranges from ~ 100 MeV to several hundred GeV and above.

Super-Kamiokande is the world's largest water Cherenkov detector located 1000 m underground in the Kamioka mine in Japan. The cylindrical tank, which has a diameter of 39.3 m and is 41.4m high, is filled with 50,000 tons of pure water and the detector consists of two layers, comprising inner and outer detectors optically separated from each other. In the inner detector 11,146 50 cm diameter photomultiplier tubes are instrumented on all surfaces and 40% of the surface of the inner detector wall is covered by photocathodes. The inner detector is surrounded by an outer veto detector layer of water with thickness 2.6–2.75 m.

The Super-Kamiokande experiment looked at two cases for atmospheric neutrinos; downward travelling neutrinos and upward-travelling neutrinos. The downward-travelling neutrinos have a path length of ~ 15 km whereas the upward-travelling neutrinos' path length is $\sim 13,000$ km. The zenith angle of the incoming neutrino is a direct measure of flight length L, and hence neutrino oscillation manifests itself as a possible distortion of the zenith angle distribution (figure 1.9), which does not depend on uncertainties in the absolute flux or cross sections. The observations clearly show the deficit of muons in the sub-GeV and multi-GeV energy range, an up-down asymmetry of zenith angle distribution for those muons, and the

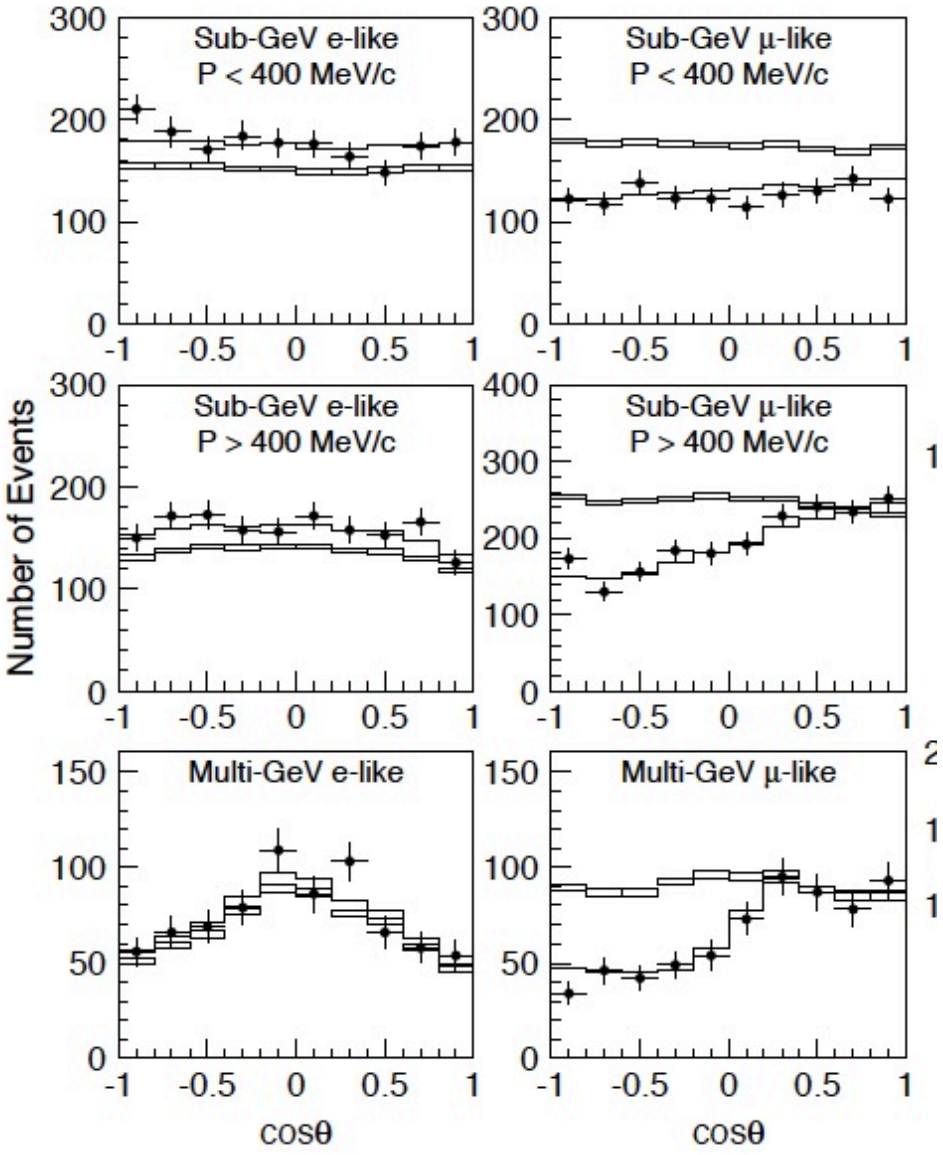

Figure 1.9: The zenith angle distribution for fully-contained 1-ring events in the Super-K detector. The points show the data, box histograms show the non-oscillated Monte Carlo events and the lines show the best-fit expectations for $\nu_\mu \leftrightarrow \nu_\tau$ oscillations with $\sin^2 2\theta = 1.00$ and $\Delta m^2_{32} = 2.110^3$ eV ^{2}, figure taken from Ref. [30].

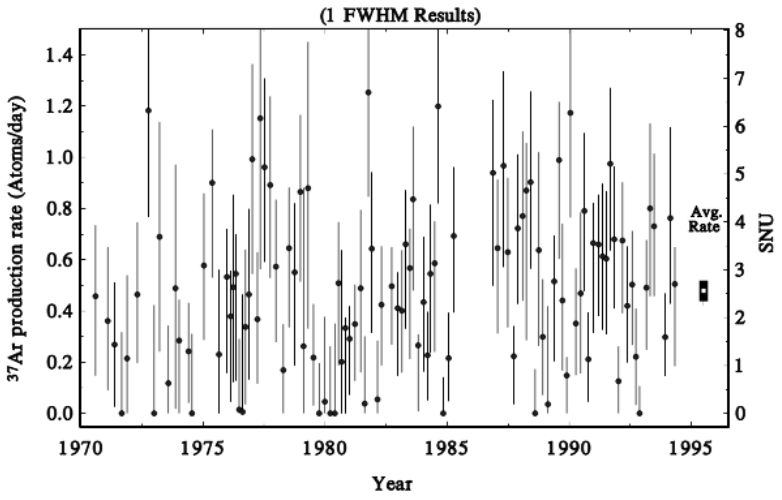

Figure 1.10: Homestake Experiment FWHM results. Results for 108 individual solar neutrino observations made with the Homestake chlorine detector. The average rate is $\sim 1/3$ of the expected rate. Figure taken from Ref. [31].

deficit of upward stopping muons. Detailed analyses show the no-oscillation hypothesis to be completely ruled out and $\nu_\mu \rightarrow \nu_\tau$ oscillations to be consistent with the observed atmospheric neutrino data. While this observation is unambiguous confirmation of neutrino oscillation, it did not resolve the solar neutrino problem which will be discussed in Section 1.3.3.

1.3.3 Solar Experiments

The first hints of neutrino oscillation were found by the Homestake experiment [31], where the flux of neutrinos at earth was approximately one third the expected rate based on nuclear models of the sun's fusion processes (figure 1.10). The Homestake Mine experiment was a 30 year effort led by Raymond Davis to measure the solar electron neutrino flux using a Chlorine detector. As with the Cowan and Reines experiment, the reaction of interest proceeds via inverse beta-decay

$$\nu_e + {}^{37}\text{Cl} \rightarrow {}^{37}\text{Ar} + e^-, \tag{1.35}$$

which has a threshold of 0.814 MeV for ^{37}Cl. Located at a depth of 2500 m the detector consists of a tank of 615 metric tons of tetrachloroethylene, C_2Cl_4. Argon produced due to the flux of solar neutrinos was filtered out and counted, the rate of argon production being proportional to the neutrino flux. After decades of data taking and exhaustive reviews of the experiment and procedures it became clear that either models for solar nuclear processes were incorrect or that something was happening to the neutrinos in transit from the sun to earth changing the expected flux. The mechanism proposed to account for this deficit had been put forward almost 40 years before by Pontecorvo [7] - neutrino oscillation.

As neutrinos are left-handed neutral leptons they can only interact via the weak force in the SM. Neutrinos in the energy range typical at the Savannah reactor have a cross-section of $\sim 5 \times 10^{-44}$cm^2. As a consequence, neutrino sources of extreme intensity are required for the determination of parameters related to these particles. The sun's nuclear fusion processes create an abundant source of neutrinos which has been exploited at experiments from the Homestake mine [31] to ICECUBE [32]. While Homestake was the first to observe the solar neutrino problem, substantial weight was given to the issue by the gallium experiments SAGE [33] and GALLEX [34] and the liquid scintillator experiment Borexino [35]. The gallium experiments operated on the same principle, however the inverse beta decay reaction on gallium has a lower threshold (0.233 MeV) than that of chlorine, thus a greater fraction of the solar neutrino spectrum can be sampled. The threshold for Borexino is 0.862 MeV and also samples different parts of the solar spectrum.

After three decades of data taking the solar neutrino problem thrown up by Homestake could no longer be ignored. In order to resolve this issue the SNO [36] experiment measured the flux of not only electron neutrinos but also that of muon and tau neutrinos from the sun. The Sudbury Neutrino Observatory (SNO) was a neutrino observatory located 2100 m underground in Creighton Mine in Sudbury, Canada. The SNO detector is an imaging water Cherenkov detector. 1000 metric tons of ultra-pure D_2O were contained within a spherical acrylic vessel 12 m in diameter. SNO measured the ^8B solar neutrinos through the reactions:

$$\begin{aligned} \nu_e + d &\rightarrow p + p + e^- \quad (CC) \\ \nu_x + d &\rightarrow p + n + \nu_x \quad (NC) \\ \nu_x + e^- &\rightarrow \nu_x + e^- \quad (ES) \end{aligned} \tag{1.36}$$

The different interaction processes are sensitive to different neutrino flavours. The charged current reaction (CC) is sensitive exclusively to electron-type neutrinos and has a 2.225 keV threshold, whereas the neutral current (NC), with a threshold of 1.442 keV, and elastic scattering (ES) reactions are sensitive to all active neutrino flavours. Comparison between the ^{8}B flux measured via the ES reaction assuming no neutrino oscillations, $(\phi^{ES}(\nu_x))$, and that measured via the CC reaction $(\phi^{CC}(\nu_e))$ can provide clear evidence of flavour transformation without reference to solar model flux calculations.

The SNO detector support structure is shown in figure 1.11, this support structure consists of ten rope loops made of synthetic fibre. Surrounding the acrylic vessel is a geodesic structure of stainless-steel struts carrying the 9438 inward-looking photomultiplier tubes employed by SNO.

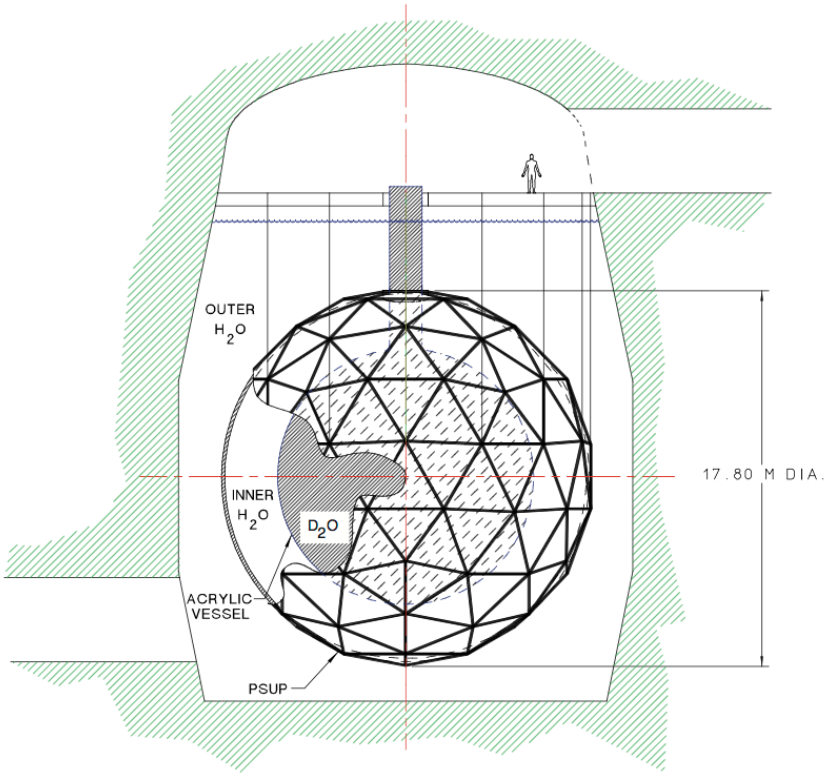

Figure 1.11: The PMT support structure (PSUP) shown inside the SNO cavity, surrounding the acrylic vessel, with light water and heavy water volumes located as indicated. Figure taken from Ref. [37].

After 240.95 live time days of data taking, mostly in the year 2000, SNO published their measurements of the solar neutrino flux at earth. Normalising to the integrated rates above the kinetic energy threshold, the measured ^{8}B neutrino fluxes were [36]:

$$\begin{aligned}\phi^{CC}_{SNO}(\nu_e) &= 1.75 \pm 0.07(\text{stat.})^{+0.12}_{-0.11}(\text{sys.}) \pm 0.05(\text{theor.}) \times 10^6 \text{cm}^{-2} s^{-1}, \\ \phi^{ES}_{SNO}(\nu_x) &= 2.39 \pm 0.34(\text{stat.})^{+0.16}_{-0.14}(\text{sys.}) \times 10^6 \text{cm}^{-2} s^{-1},\end{aligned} \tag{1.37}$$

where the theoretical uncertainty is the CC cross section uncertainty. Using this information, SNO predicted the flux of non-electron flavour active neutrinos $(\phi(\nu_{\mu\tau}))$ against the flux of electron neutrinos (figure 1.12). The best fit of the data to $\phi(\nu_{\mu\tau})$ was:

$$\phi(\nu_{\mu\tau}) = 3.69 \pm 1.13 \times 10^6 \text{cm}^{-2}\text{s}^{-1}. \tag{1.38}$$

This observation was the first direct indication of a non-electron flavour component in the solar neutrino flux and hence confirmation of neutrino flavour change. This result by SNO resolved the solar neutrino problem more than 30 years after it was first measured by Homestake.

1.3.4 Accelerator Experiments

Neutrinos from reactor or solar sources are produced across a wide spectrum of energies and, in the solar case, the neutrinos are produced in a variety of flavours. Accelerator experiments have the advantage that the source is man-made hence the energy of the neutrino beam can be controlled. Current experiments operate up to a few GeV in neutrino energy. Conventional neutrino beams exploit π decay:

$$\begin{aligned}\pi^+ &\rightarrow \mu^+ + \nu_\mu \\ \pi^- &\rightarrow \mu^- + \bar{\nu}_\mu\end{aligned} \tag{1.39}$$

and look for the appearance of ν_e or ν_τ in the beam or the disappearance of ν_μ.

The Main Injector Neutrino Oscillation Search (MINOS) experiment operated off the FermiLab main injector at two sites. The near detector is situated a few hundred metres away from the target and the far detector is located in the Soudan mine in northern Minnesota, at a distance of 735 km. Both detectors are steel-scintillator sampling calorimeters made from alternate planes of magnetised steel and plastic scintillator, with the far detector having a larger fiducial volume, see figure 1.13. Both detectors have the same design so any potential sources of systematic error in the final analysis are cancelled. The magnetic field generated in the de-

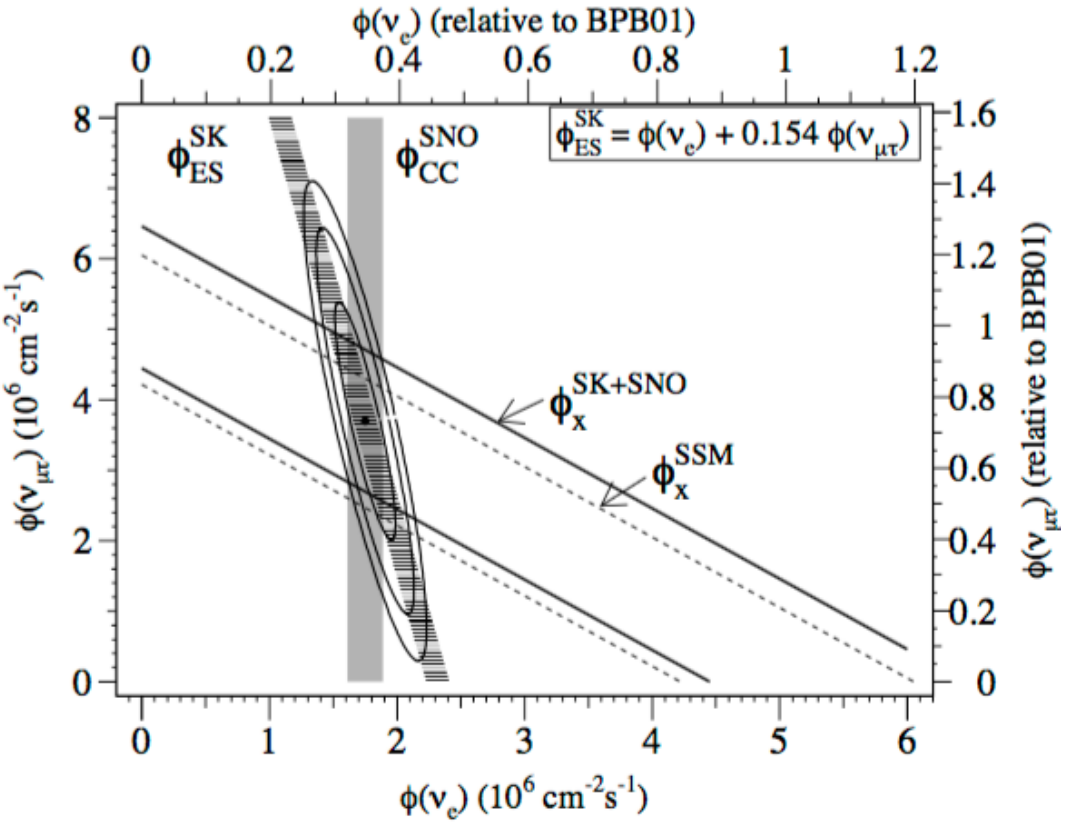

Figure 1.12: Flux of ^{8}B solar neutrinos which are μ or τ flavour vs. the flux of electron neutrinos as deduced from the SNO and Super-Kamiokande data. The diagonal bands show the total ^{8}B flux $\phi(\nu_x)$ as predicted by BPB01 (dashed lines) and that derived from the SNO and Super-Kamiokande measurements (solid lines). The intercepts of these bands with the axes represent the $\pm 1\sigma$ errors. Figure taken from Ref. [36].

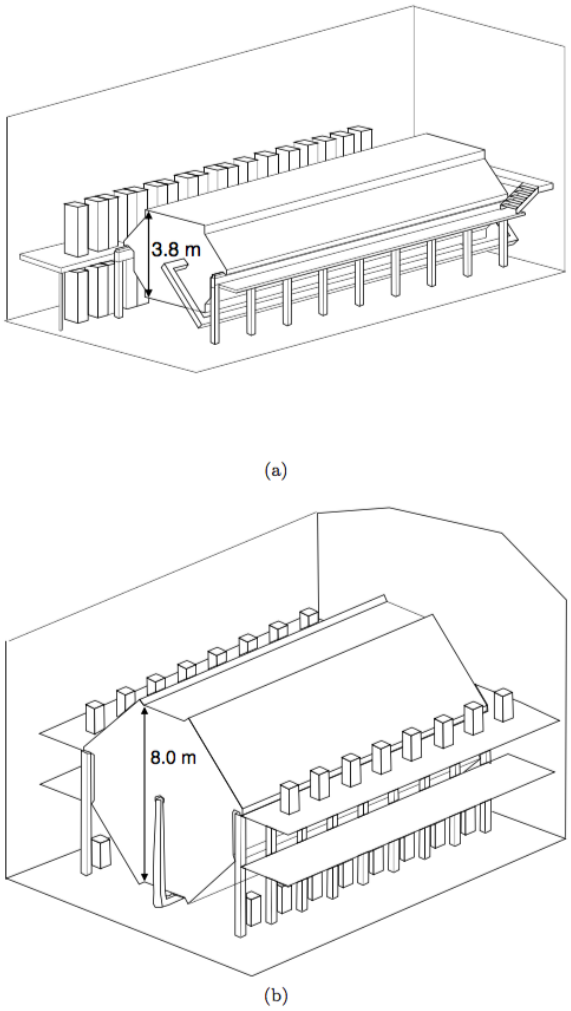

Figure 1.13: The MINOS Near (a) and Far (b) Detectors. The Far Detector consists of two functionally identical modules, only one of which is shown in the figure. Figure taken from Ref. [38].

tector causes charged particles trajectories to bend, which can be used for particle identification and momentum measurement.

In total, MINOS analysed more than 2.95×10^{20} protons on target. With these data it was able to constrain both the Δm^2_{32} and θ_{23} oscillation parameters. Neutrino interactions in the MINOS detector proceed via [39];

1. CC ν_μ and $\bar{\nu}_\mu$: interaction with a nucleus X mediated by exchange of a W boson. Such events produce a muon which can be identified by its curvature in the magnetic field and the characteristic hadronic shower at the interaction vertex.

2. NC ν: interaction with a nucleus X mediated by exchange of a Z boson. The scattering neutrino leaves the detector without being detected, therefore only a hadronic shower will be observed. With no charged outgoing particle the original neutrino flavour cannot

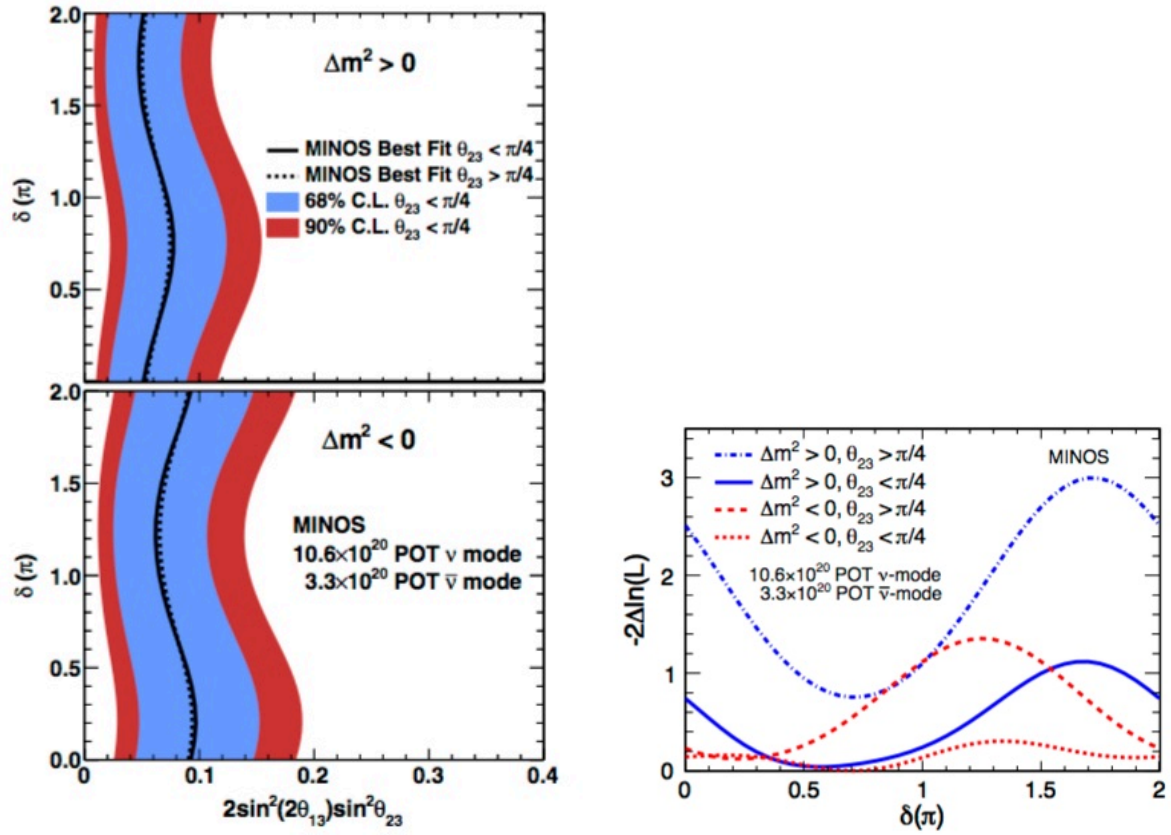

Figure 1.14: Left: the $\nu_\mu \to \nu_e$ appearance contour shown as a function of $2\sin^2 2\theta_{13}\sin^2\theta_{23}$ and δ_{CP} for the MINOS experiment. The normal hierarchy is shown in the top panel, and the inverted hierarchy below, with the 68% and 90% contours shown for the lower octant of θ_{23}. The best fit curve is also shown for the upper octant, showing little sensitivity to the octant of θ_{23}. Right: the likelihood shown as a function of δ_{CP} for the four combinations of mass hierarchy and θ_{23} octant. Figure from Ref. [40].

be determined.

3. CC ν_e and $\bar{\nu}_e$: interaction with a nucleus X mediated by exchange of a W boson. These events create a small electromagnetic shower in the detector, however given the lack of track topology no distinction can be made between CC ν_e and $\bar{\nu}_e$ events

The results of the $\nu_\mu \to \nu_e$ appearance analysis are shown in figure 1.14 with the null hypothesis of no appearance excluded at approximately the 96% confidence level. A full three flavour oscillation analysis was developed giving the most precise measurement of the atmospheric mass splitting Δm^2_{32} to date. The results are, assuming $\delta = 0$ and $\theta_{23} < \pi/4$, the data allow for values of $0.01 < 2\sin^2(2\theta_{13})\sin^2(\theta_{23}) < 0.12$ at 90% C.L. with the best-fit value of $2\sin^2(2\theta)\sin^2(\theta) = 0.051^{+0.038}_{-0.030}$. Assuming an inverted mass hierarchy, $\delta = 0$, and $\theta_{23} < \pi/4$, they find that the data allow for values of $0.03 < 2\sin^2(2\theta_{13})\sin^2(\theta_{23}) < 0.18$ at 90% C.L. with the best-fit value of $2\sin^2(2\theta)\sin 2(\theta) = 0.093^{+0.054}_{-0.049}$. The best-fit values show very weak

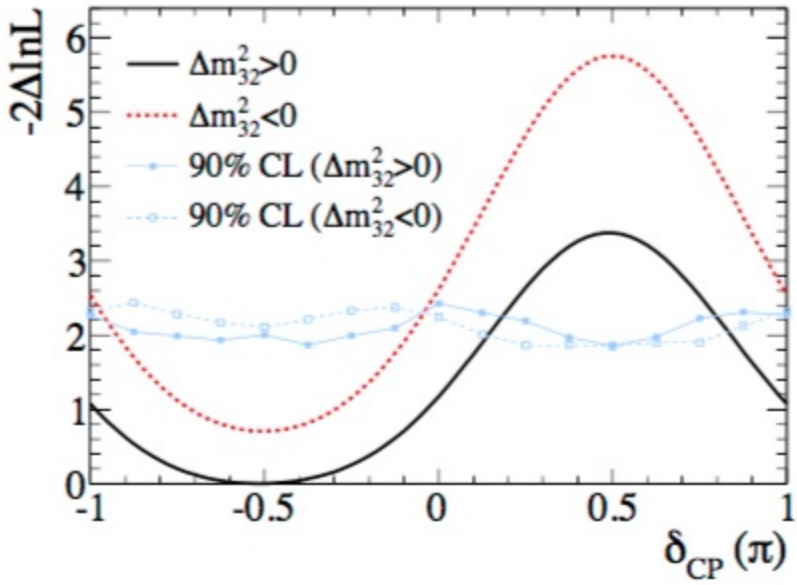

Figure 1.15: The $2\Delta \ln \mathrm{L}$ value as a function of δ_{CP} for normal hierarchy (solid line) and inverted hierarchy (dotted line) obtained by the T2K experiment. The likelihood is marginalised over $\sin^2 2\theta_{13}$, $\sin^2 \theta_{23}$ and Δm^2_{32}. The solid (dotted) line with markers corresponds to the 90% CL limits for normal (inverted) hierarchy, evaluated by using the Feldman-Cousins method. The δ_{CP} regions with values above the lines are excluded at 90% CL. [42].

dependence on the choice of octant for θ_{23}.

The results of the $\bar{\nu}_\mu \rightarrow \bar{\nu}_\mu$ disappearance analysis reported by MINOS [41] are $\Delta\bar{m} = [2.62^{+0.31}_{-0.28}(\text{stat.}) \pm 0.09(\text{syst.})] \times 10^{-3}$ eV ^{2} and $\sin^2(2\bar{\theta}) = 0.95^{+0.10}_{-0.11}(\text{stat.}) \pm 0.01(\text{syst.})$ for antineutrinos where θ is the $\bar{\nu}_\mu$ mixing angle. This is the most precise measurement of these parameters and this result is in agreement with the values reported for ν_μ neutrinos.

1.3.4.1 T2K

The T2K experiment employs the Super-Kamiokande water Cherenkov detector that was used in the atmospheric experiments that first discovered neutrino oscillation. However rather than atmospheric neutrinos, an off-axis beam of neutrinos produced at J–PARC is directed toward the detector 295 km away and the subsequent neutrino oscillation behaviour studied. T2K started taking data in 2010, with first electron neutrino appearance results in 2011.

In early 2013 T2K took data with its muon neutrino beam and observed 28 electron neutrino events [42]. This corresponded to a 7.2 σ significance for the detection of electron neutrino appearance given the expected 4.92 ± 0.55 background events. In addition by combining these data with the reactor result $\delta_{\mathrm{CP}} < 0$ is preferred, see figure 1.15.

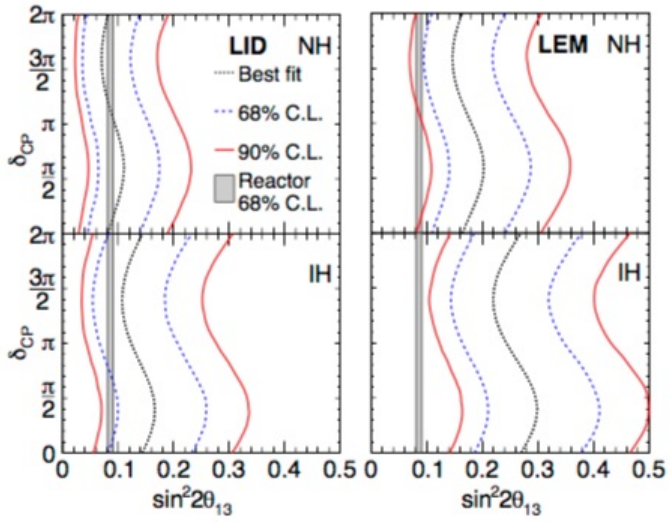

Figure 1.16: Allowed values of δ_{CP} vs $\sin^2 2\theta_{13}$. for the NOνA experiment. Top (bottom) plots show the NH (IH). Left (right) plots show results for the primary (secondary) selector. Both have $\sin^2 \theta_{23}$ fixed at 0.5. [43].

1.3.4.2 NOνA

MINOS is not the only neutrino experiment to use the Fermilab Main Injector beam. Located at a site 810 km from Fermilab NOνA is a tracking calorimeter composed of cells of liquid scintillator encased in polyvinyl chloride extrusions with the far detector having a mass of $\sim$14 kton. NOνA has also observed electron neutrino appearance and they have so far observed 33 events in the far detector for background expectations of 10.3 ± 1.0 (syst.) giving a $> 8\sigma$ significance [44]. This analysis also excludes lower octant around $\delta_{\text{CP}} = \pi/2$, see figure 1.16.

1.3.4.3 DUNE and Hyper-K

While the current generation of accelerator experiments have several years of data taking remaining, plans have already been put forward for the next generation of neutrino accelerator experiments. These involve upgrading the existing accelerator sources at JPARC and Fermilab and developing new and more sensitive detectors at these sites. The two principle proposals are DUNE [45] and Hyper-K [46]. The DUNE proposal involves building a 40 kt liquid argon TPC detector with the neutrino source at Fermilab. This novel detector technology has never been demonstrated at this scale and would provide significant insight into δ_{CP} in the lepton sector, see figure 1.17. Hyper-K will replace the current Super-Kamiokande 50 kt water Cherenkov detector with two 260 kton water Cherenkov detectors. The design and operation of such a system is well understood through many years of operating Super-Kamiokande, however the increased fiducial volume of the detector will give significantly greater sensitivity to δ_{CP}. Both experiments are to take data from 2025. These planned facilities offer an order of magnitude more statistics in the appearance and disappearance channels of interest with the corresponding

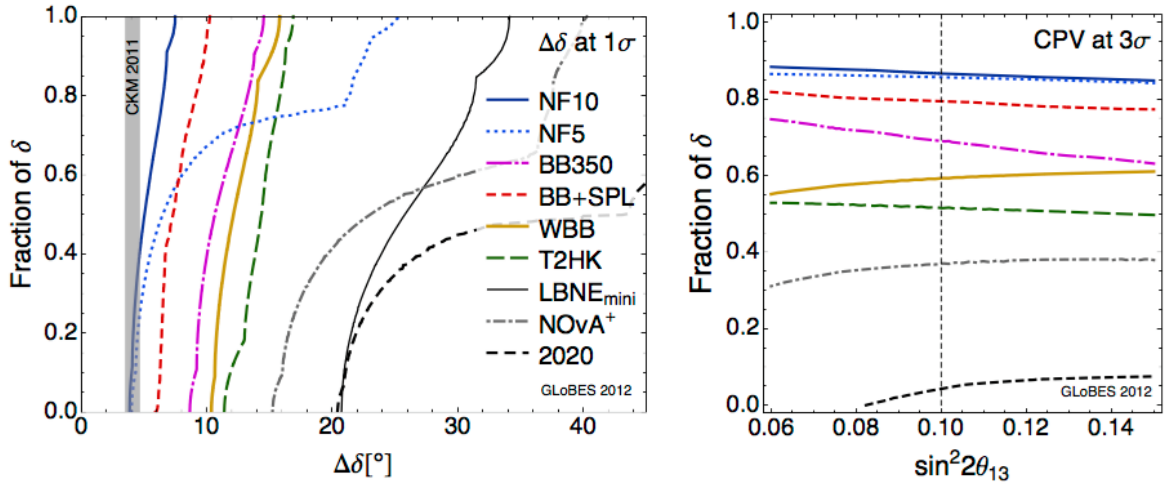

Figure 1.17: Comparison between different future neutrino experiments taken from Ref. [47]. Also included in the comparison the results that would be obtained by 2020 through the combination of T2K, NOνA and reactors. Left panel: Fraction of δ as a function of the precision at 1σ for $\sin^2 2\theta_{13} = 0.1$. Right panel: Fraction of δ for which CPV can be established at 3σ as a function of $\sin^2 2\theta_{13}$ in the currently allowed range. A true normal hierarchy has been assumed, and no sign degeneracies have been accounted for. The vertical dotted line in the right panel corresponds to $\sin^2 2\theta_{13} = 0.1$, which is the true value chosen for θ_{13} in the left panel. In the left panel, the vertical grey band depicts the current precision for the CPV phase in the quark sector. NF10 refers to the 10 GeV low energy neutrino factory [48], NF5 the 5 GeV low energy neutrino factory [47], BB350 the beta-beam facility with $\gamma = 350$ [49], BB+SPL the beta-beam facility with $\gamma = 100$ [50], WBB the LAGUNA facility [51], T2HK the Hyper-Kamiokande facility [46], LBNE$_{\text{mini}}$ is proposed LBNE configuration [52], NOνA is the NOνA experiment [43] and 2020 is the combination of currently running facilities including T2K, NOνA and reactors [53].

increase in sensitivity to the related oscillation parameters.

1.4 Neutrino Factory

A proposed future facility which can measure δ_{CP} with 5° accuracy, figure 1.17, and the neutrino mixing angles with a precision to match the quark sector is the neutrino factory [48]. A schematic of the neutrino factory is shown in figure 1.18. In the neutrino factory a high power (2-5 MW) proton driver and target create charged pions, which are captured in a 20 T superconducting solenoidal field. These pions decay to muons and are then treated by the neutrino factory front-end which bunches, phase-rotates and cools (figure 1.19) the beam prior to acceleration. A chicane with an absorber at the end is inserted to remove particles other than pions and muons, reducing energy deposition in the downstream systems. As illustrated in the schematic figure 1.18 the muons are then passed to a series of linacs, recirculating linacs (RLAs) and fixed field alternating gradient accelerators (FFAGs) which accelerate the muons

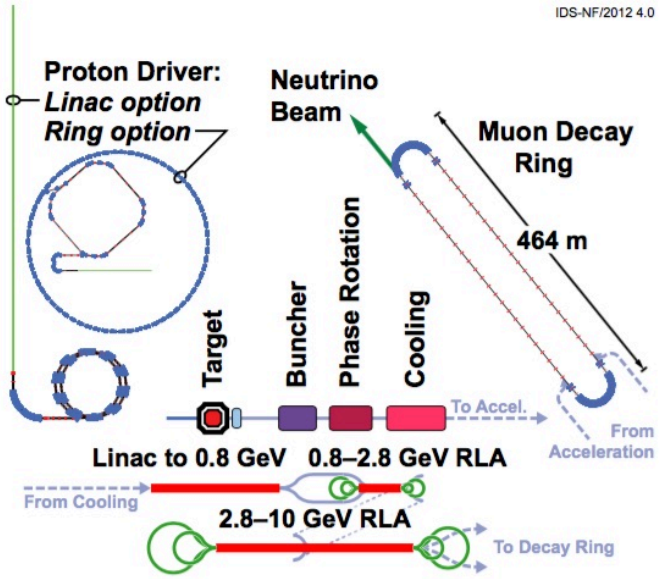

Figure 1.18: Schematic of the Neutrino Factory according to the International Design Study baseline. Figure taken from Ref. [48].

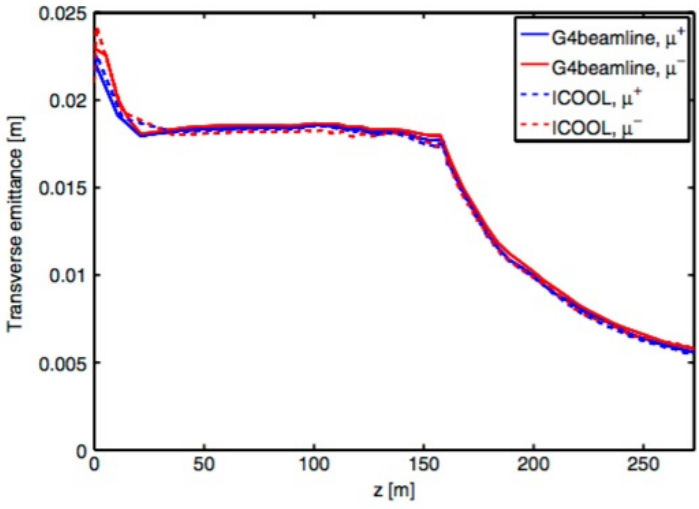

Figure 1.19: Performance of the cooling channel as a function of distance along the channel, as simulated using and G4beamline 2.06. The evolution of the rms transverse emittance (computed over all bunches). Figure taken from Ref. [54].

to ~ 10 GeV. The accelerated muons are now injected into a decay ring, where after ~ 70 turns of the circuit the muons decay predominantly via the mode

$$\mu^- \rightarrow e^- + \bar{\nu}_e + \nu_\mu, \tag{1.40}$$

which has a branching ratio approaching 100%. Decays also proceed via the modes,

$$\mu^- \rightarrow e^- + \bar{\nu}_e + \nu_\mu + \gamma \tag{1.41}$$

or

$$\mu^- \rightarrow e^- + \bar{\nu}_e + \nu_\mu + e^+ + e^-, \tag{1.42}$$

which shares the same flavour content as the dominant mode, however they have a branching ratio <1%, hence the composition and energy spectrum of the resultant neutrino beam is well known. The decay modes of the μ^+ are the charge conjugate of those for the μ^-.

The daughter neutrinos are directed to a far detector site a few thousand kilometres away with the oscillations occurring during the intervening flight studied at the far detector. Of principle interest is the so called "golden channel" of ν_μ appearance, $\nu_e(\bar{\nu}_e) \rightarrow \nu_\mu(\bar{\nu}_\mu)$. Oscillation analyses look for the "wrong" signed muon to be detected in the far detector i.e. μ^+ when the beam in the decay ring was μ^-. The proposed detector design is a 100 kTon magnetised iron-scintillator calorimeter MIND (Magnetised Iron Neutrino Detector). The fact that the detector is magnetised increases its sensitivity to wrong signed particles. To reduce systematics, the near detector would be of identical design with a smaller mass. Observation of discrepancies between the rate of $P(\nu_e \leftrightarrow \nu_\mu)$ and $P(\bar{\nu}_e \leftrightarrow \bar{\nu}_\mu)$ would be evidence of CP violation in the lepton sector.

The neutrino factory has been referred to as the "ultimate precision" machine to study the neutrino sector [47]. It offers considerable advantages in terms of higher luminosity, higher purity of the flavour content and better precision in the energy spectrum of the neutrinos generated over a conventional neutrino beam generated directly from pion decay. However as it is the first accelerator of its kind, it faces several technical challenges including operating the high power target in strong magnetic fields (20 T) and implementing the front-end (bunching, phase-rotation and cooling) [55].

In particular, beam cooling is critical if the neutrino factory is to reach its design luminosity of $\sim 10^{21}$ muon decays per year. The neutrino beam from muon acceleration is a tertiary beam, therefore the transverse size of the beam is large and divergent while the front-end linacs and

decay ring have only a small acceptance. Neutrino factory proposals therefore include a ~ 100 m cooling channel to reduce the transverse emittance of the muon beam. In addition to the value in resolving questions surrounding neutrino oscillation parameters and CP-violation, the neutrino factory also has the capability to measure neutrino cross-sections and to search for sterile neutrinos with unprecedented precision.

1.5 Muon Collider

The discovery of the Higgs boson [56] has generated significant interest in a Higgs factory. A facility capable of producing an intense source of Higgs bosons would allow their properties to be precisely determined. The Standard Model (SM) Higgs is a CP-even scalar of spin 0. The Higgs mass is dependent on the quartic coupling λ, a free parameter in the SM, hence there is no a priori prediction for the value of the Higgs' mass. The particle observed at ATLAS and CMS has a mass of approximately 125 GeV and appears consistent with the SM Higgs. However a Higgs factory remains of interest in the context of further constraining the SM and investigating New Physics (NP). A proposed concept for such an experiment is a muon collider [57]. As muons have a mass $\sim$200 times greater than that of the electron the fraction of energy lost as synchrotron radiation is dramatically reduced. Consequently far higher energies can be probed at a muon collider compared with an e^+e^- collider of comparable size. Furthermore, at a muon collider, the backgrounds would be significantly smaller than those typically encountered in a hadron collider and the precision in scanning around the Higgs resonance is much better, due to reduced beam-strahlung. Given the increased energy reach of such a machine, the muon collider would also be an excellent discovery machine probing physics up to the multi-TeV scale. A muon collider would rely on even more stringent cooling than a neutrino factory so there is considerable interest in the muon accelerator community concerning the development of the front end of the neutrino factory, which is the first step towards a muon collider.

1.6 Conclusions

An overview of neutrino physics has been reported with attention given to the discovery of neutrinos, neutrino oscillation and the experiments conducted to investigate these phenomena. Since the discovery of the neutrino some 60 years ago, a large number of experiments have been conducted of which only a few are reported here. They span a number of neutrino sources and encompass a variety of detector technologies. These experiments have measured or placed limits on the principle parameters relating to the neutrino, namely its mass, mixing angles and CP violation in the lepton sector. However, if further progress is to be made, precision in the measurement of the mixing angles, mass differences and CP violation phase comparable to

that achieved in the quark sector are required. The final section discussed a facility capable of achieving such precision, the neutrino factory, which requires muon ionsation cooling, which is the topic of this thesis.

Chapter 2

The Muon Ionisation Cooling Experiment

Both the muon collider and the neutrino factory require the phase-space volume occupied by the muon beam to be reduced before injection into the storage ring. The only cooling technique that can act within the lifetime of the muon is ionisation cooling. If these facilities are ever to be realised then it is first necessary to demonstrate ionisation cooling in practice as effective cooling technology will form a key component in their designs. The Muon Ionisation Cooling Experiment (MICE) project aims to give the first demonstration of ionisation cooling, to measure the expected cooling performance and to provide the tools and expertise to make proposed future facilities possible.

2.1 Emittance

The phase space volume occupied by a beam is typically characterised by its emittance and change in emittance is a useful metric when considering the performance of a cooling channel. The description of emittance given here follows [58]. When considering the transport of a beam of particles through an accelerator it is not practical to calculate the trajectory of each individual particle. A more useful approach is to use our knowledge of statistical mechanics and Liouville's theorem. Liouville's theorem states that under the influence of conservative forces the particle density in phase space remains constant. This is a powerful statement as it implies that knowledge of the area occupied by the particles in phase space at one point in the beam line allows us to determine the location and distribution of the beam at any other place in the beam line without reference to individual particle trajectories.

In the MICE experiment the position, momentum and energy of each muon is measured before and after cooling. For each particle x, y, t, $x' = dx/dz = p_x/p_z$, $y' = dy/dz = p_y/p_z$ and $t' = dt/dz = E/p_z$ are measured; p_i is the i^{th} component of momentum where $i = x, y, z$, E is the energy and the MICE coordinate system is defined such that the z axis is parallel to the

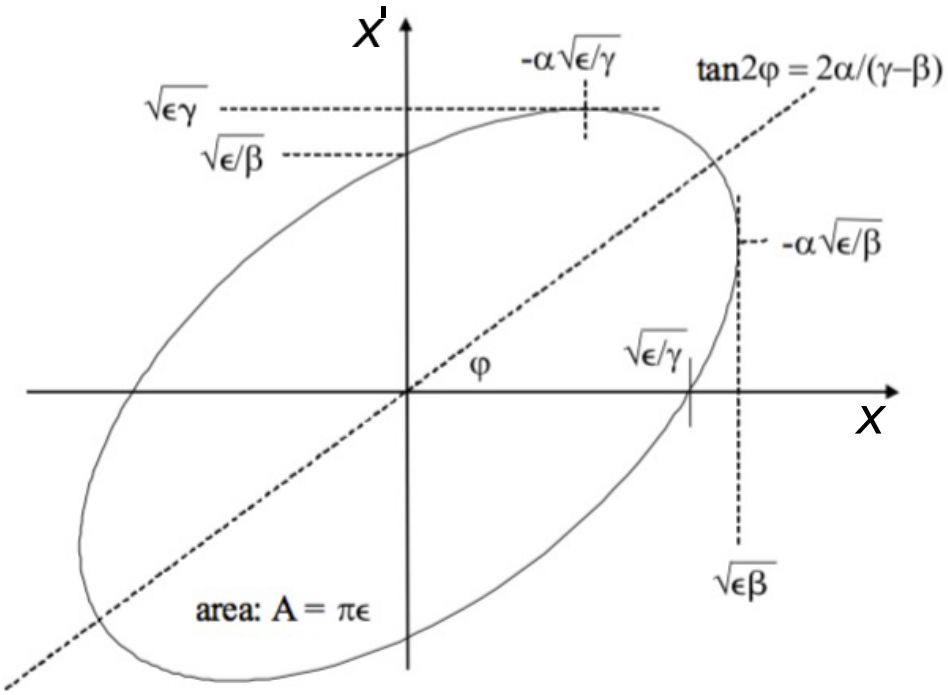

Figure 2.1: Transverse phase space ellipse, figure from [58].

nominal beam axis, the y axis points vertically upward and the x axis completes a right-handed coordinate system. The time, t, corresponds to the moment the particle crosses a reference surface within the tracking volume.

The description of the beam in phase space is typically represented via phase space plots such as that shown in figure 2.1 for two dimensions, x and x'. The ellipse surrounds all the particles in the beam and is described by the expression:

$$\gamma x^2 + 2\alpha x x' + \beta x'^2 = \varepsilon, \tag{2.1}$$

where α, β, γ and ε are commonly referred to as the Twiss parameters. The area enclosed by this ellipse is defined as the beam emittance in two dimensions:

$$\int_{ellipse} dx dx' = \pi\varepsilon. \tag{2.2}$$

As stated, the particle density remains constant. Therefore while the shape or orientation of the ellipse may change based on the Twiss parameters, the area will remain constant. All particles in a beam within a given ellipse remain within that ellipse while the conditions of Liouville's theorem remain true. Therefore with one ellipse the behaviour of all particles contained within that ellipse can be described by the dynamics of a single particle.

The transformation rules for such ellipses in two-dimensions down a beam line are:

$$u^T \sigma^{-1} u = 1, \tag{2.3}$$

where in the two-dimensional case σ is the symmetric matrix,

$$\sigma = \varepsilon^2 \begin{pmatrix} \beta & -\alpha \\ -\alpha & \gamma \end{pmatrix}, \tag{2.4}$$

u^T is the transpose of the coordinate vector u where,

$$u = \begin{pmatrix} x \\ x' \end{pmatrix}. \tag{2.5}$$

This can be generalised to four, and six dimensions, to characterise the full phase space by defining,

$$u = \begin{pmatrix} x \\ x' \\ y \\ y' \end{pmatrix} \tag{2.6}$$

in four dimensions and

$$u = \begin{pmatrix} x \\ x' \\ y \\ y' \\ \tau \\ \delta \end{pmatrix} \tag{2.7}$$

in six dimensions where τ is time and $\delta = E/p_z$. The volume of this six-dimensional ellipse is:

$$V_n = \frac{\pi^{n/2}}{\Gamma(1 + n/2)} \sqrt[n]{\det(\sigma)}, \tag{2.8}$$

where Γ is the gamma function and $n = 6$ for six dimensions. In the two dimensional case it simplifies to:

$$V_2 = \pi \sqrt{\det(\sigma)} = \pi \sqrt{\sigma_{11}\sigma_{22} - \sigma_{12}^2} = \pi\varepsilon \tag{2.9}$$

which is consistent with the previous definition.

In a typical particle accelerator, the particle beam will have a Gaussian-like shape in terms of particle distribution. The beam matrix elements describe this distribution in phase space, hence a uniform definition for these matrix elements are chosen to match the expected distribution. For a particular particle, the betatron oscillation amplitude in two dimensions in the x_i and x_i' coordinates, where i labels each muon, are given by:

$$x_i = a_i\sqrt{\beta}\cos(\phi+\phi_i), \tag{2.10}$$

$$x_i' = a_i\frac{\beta'}{2\sqrt{\beta}}\cos(\phi+\phi_i) - a_i\frac{1}{\sqrt{\beta}}\sin(\phi+\phi_i). \tag{2.11}$$

An expression for the definition of the emittance for arbitrary particle distributions can be derived from equations 2.10 and 2.11. Assuming a Gaussian particle distribution and a beam emittance defined by $\frac{1}{2}a_i^2 = \varepsilon$ it follows that:

$$\begin{aligned}
\langle x_i^2\rangle &= a_i^2\beta\langle\cos^2(\phi+\phi_i)\rangle = \frac{1}{2}a_i^2\beta = \varepsilon\beta \\
\langle {x'}_i^2\rangle &= a_i^2\frac{\alpha^2}{\beta}\frac{1}{2} + a_i^2\frac{1}{\beta}\frac{1}{2} = \frac{1}{2}a_i^2\frac{1+\alpha^2}{\beta} = \varepsilon\gamma \\
\langle x_i x_i'\rangle &= -a_i^2\alpha\frac{1}{2} = -\varepsilon\alpha.
\end{aligned} \tag{2.12}$$

This definition holds for the beam within one standard deviation of the expected distribution in multidimensional phase space. The beam matrix elements are defined as:

$$\begin{aligned}
\sigma_{11} &= \langle x_i^2\rangle = \varepsilon\beta \\
\sigma_{22} &= \langle {x'}_i^2\rangle = \varepsilon\gamma \\
\sigma_{12} &= \langle x_i x_i'\rangle = -\varepsilon\alpha.
\end{aligned} \tag{2.13}$$

Finally the beam emittance in two dimensions can be expressed as:

$$\varepsilon^2 = \sigma_{11}\sigma_{22} - \sigma_{12}^2 = \langle x_i^2\rangle\langle {x'}_i^2\rangle - \langle x_i x_i'\rangle^2. \tag{2.14}$$

The normalised emittances, ε_n, of a beam of N muons can therefore be determined from the measurements of the phase-space coordinates of each of the single muons using a tracking detectors. This statement can also be generalised to the four, and six, dimensional case, where the σ matrix becomes the covariance matrix defined between the x, y, t, x', y' and t' variables. Starting from this four, or six, dimensional object the four, or six, dimensional emittance can be derived in a similar manner. The determinant of the transverse covariance matrix $|\mathbf{V}_\perp|$ in

two dimensions is given by [59]:

$$\sqrt{|\mathbf{V}_\perp|} = p_z^2(< x^2 >< x'^2 > - < xx' >^2) \tag{2.15}$$

where

$$\begin{aligned} < x^2 > &= \frac{\Sigma_{i=1}^N x_i^2}{N} \\ < x'^2 > &= \frac{\Sigma_{i=1}^N x'^2_i}{N} \\ < xx' > &= \frac{\Sigma_{i=1}^N x_i x'_i}{N}. \end{aligned} \tag{2.16}$$

Therefore

$$\varepsilon_n = \frac{\sqrt{|\mathbf{V}_\perp|}}{m} \tag{2.17}$$

in the two dimensional transverse case. Proceeding in a similar manner and starting from the covariance matrix in either four or six dimensions the emittance in either four or six dimensions can be calculated with the expressions:

$$\varepsilon_n = \frac{\sqrt[4]{|\mathbf{V}_\perp|}}{m} \tag{2.18}$$

$$\varepsilon_n = \frac{\sqrt[6]{|\mathbf{V}_\perp|}}{m}. \tag{2.19}$$

The six dimensional emittance is of interest when longitudinal cooling is also a consideration however from here on we will only consider the transverse cooling, the six dimensional case is only included here for completeness.

2.2 Ionisation Cooling

Traditional methods of cooling beams such as stochastic cooling rely on feedback loops to incrementally cooling beams. Stochastic cooling has been effectively implemented at a number of experiments employing protons or electrons as the beam particle. Critically these particles are stable over the lifetime of the cooling process however this is not the case for muons which have a lifetime of 2.2 μs. Novel cooling techniques are required in the treatment of muons in accelerators. Ionisation cooling was first proposed by Skrinsky [61] and brought to the attension of the wider community by Neuffer [62] with the aim of resolving this issue. The

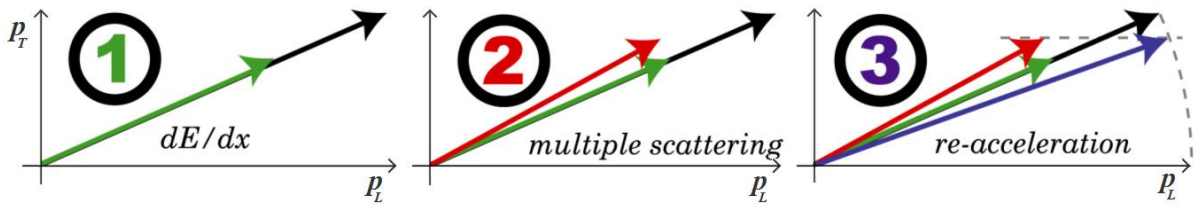

Figure 2.2: Change in emittance for an individual muon when passing through a cooling channel. The vectors represent the phase space vector for the muon in the cooling channel therefore any change is due to the average dE/dx or angular spread in the channel. Process 1 and 2 happen simultaneously as the particles pass through the cooling channel where the colour of the number represents the new phase space vector after the change. During the muon transiting the cooling channel it will also undergo reacceleration in a series of RF cavities as shown in the process labelled 3.

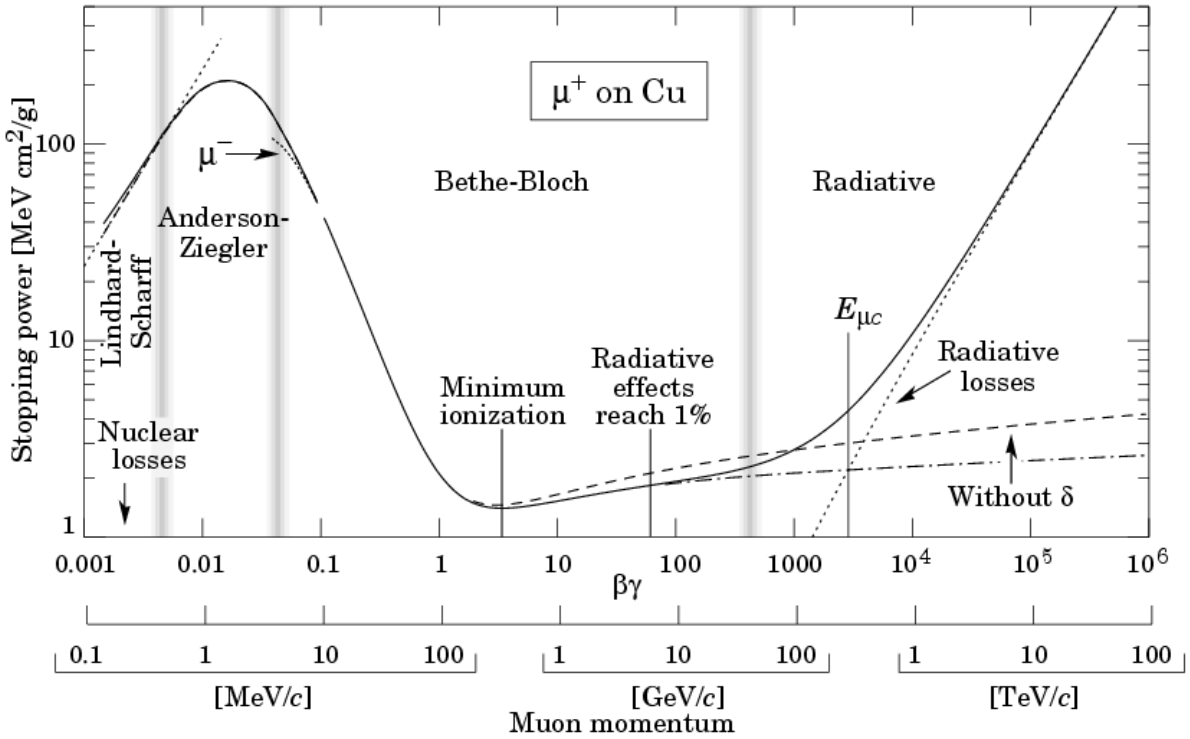

Figure 2.3: Mass stopping power ($= dE/dx$) for positive muons in copper as a function of $\beta\gamma = p/Mc$ over nine orders of magnitude in momentum (12 orders of magnitude in kinetic energy). Solid curves indicate the total stopping power. Vertical bands indicate boundaries between different approximations. dE/dx in the radiative region is not simply a function of β. Figure taken from Ref. [60].

technique is considered sound in principle but it has yet to be implemented in practice.

When muons pass through material, two processes affect the distribution of particles in the beam. Firstly, the muons lose energy as atoms are ionised and, secondly, the muons scatter off atoms in the material. The goal of cooling is to create a high intensity source of muons within a small acceptance. The reduction of the transverse emittance of the beam is achieved through energy loss. Conversely the scattering process acts to increase the transverse emittance of the beam as shown in figure 2.2.

In the following treatment [62], energy straggling is neglected. The ionisation energy loss is described by the Bethe–Bloch formula, which characterises the mean energy change of the beam per unit length of the absorber, dE/dz. The Bethe-Bloch curve is shown in figure 2.3 showing the ionisation energy loss. For the scattering process, a Gaussian fit is made to the Moliere scattering formula of the mean squared increase in angular spread per unit length with variance [60]

$$\frac{d\langle x'^2\rangle}{dz} \approx \frac{(13.6\,\text{MeV})^2 c^2}{(p\beta_{\text{rel}}^2 X_0)}. \tag{2.20}$$

where x' is the angular divergence of a particle from the beam axis in the x direction, p is the beam momentum, c is the speed of light, $\beta_{\text{rel}} = pc/E$ and X_0 is the material's radiation length. The change in emittance on passing through material of thickness dz is

$$\frac{d\varepsilon_n}{dz} = \frac{1}{2m^2\varepsilon_n}\frac{d\sqrt{|\mathbf{V}_\perp|}}{dz} \tag{2.21}$$

Inspection of 2.15 shows that terms of the form $< q_i q_j >$ and $< q_i q_j' >$ remain constant hence the terms contributing to emittance change are:

$$\frac{d\varepsilon_n}{dz} \approx \frac{1}{2m^2\varepsilon_n}\left(2\frac{dp_z}{dz}\frac{\sqrt{|\mathbf{V}_\perp|}}{p_z} + < x^2 > p_z^2\frac{d < x'^2 >}{dz}\right). \tag{2.22}$$

If the substitution $EdE/dz \approx p_z dp_z/dz$ and eqn. 2.15 are made the rate of change of normalised emittance due to ionisation cooling in a medium of thickness z may be described as 2.2:

$$\frac{d\varepsilon_n}{dz} \approx -\frac{\varepsilon_n}{{\beta_{\text{rel}}}^2 E}\left\langle\frac{dE}{dz}\right\rangle + \frac{\beta(13.6\,\text{MeV})^2}{2{\beta_{\text{rel}}}^3 E m X_0}; \tag{2.23}$$

where ε_n is the normalised transverse (two-dimensional) emittance of the beam, X_0 is the radiation length of the medium and β is the betatron function. The first term on the right hand side of equation 2.23 describes the cooling effect and the second the heating due to multiple

scattering. The emittance of the beam when these two effects are at equilibrium is:

$$\varepsilon_{eq} \approx \frac{\beta(13.6\text{MeV})^2}{2\beta_{\text{rel}} m X_0} \left\langle \frac{dE}{dz} \right\rangle^{-1}. \tag{2.24}$$

The lower the equilibrium emittance the better the cooling channel. To achieve this β should be minimised, which requires strong focusing at the absorber, and $X_0 \left\langle \frac{dE}{dz} \right\rangle$ should be maximised, suggesting liquid hydrogen or another low Z material should be used as the absorber material.

2.3 MICE Experiment at RAL

While the technique of ionisation cooling is widely accepted as sound in principle, it has never been demonstrated in practice. The goal of the Muon Ionisation Cooling Experiment (MICE), which is currently under construction at the Rutherford-Appleton Laboratory (RAL), is to make the first measurement of muon ionisation cooling.

2.3.1 MICE Configurations

As the construction of the various pieces of MICE hardware has progressed, new beam line components have been installed and commissioned in the MICE hall. This phased construction schedule has been interspersed with data taking efforts. The two principal configurations pertinent to this thesis will be outlined here, namely Step I and Step IV.

Step I (figure 2.5) was the first data taking configuration and served to characterise the muon beam using the TOF, Cherenkov and KL detectors which are described in Section 2.3.6. The layout of the beam line is described in table 2.1. The beam was characterised in terms of its intrinsic emittance [64] and pion contamination [63] (further details in chapter 4) with effort also given to the commissioning of further detectors [65]. The experiment operated in this configuration between 2010 and 2013.

The Step IV (figure 2.5) beam line incorporates the two spectrometer solenoids and one focus coil with further details given in 2.3.6. With the absorber module installed, material physics can be investigated at this Step. Multiple Coulomb scattering data in gaseous xenon and lithium hydride were taken, which will be discussed in greater depth in Section 6. For these, data analyses evaluating the energy loss in the absorber are also ongoing. Step IV was the first time data were taken with the two scintillating fibre trackers installed, necessitating a concerted effort

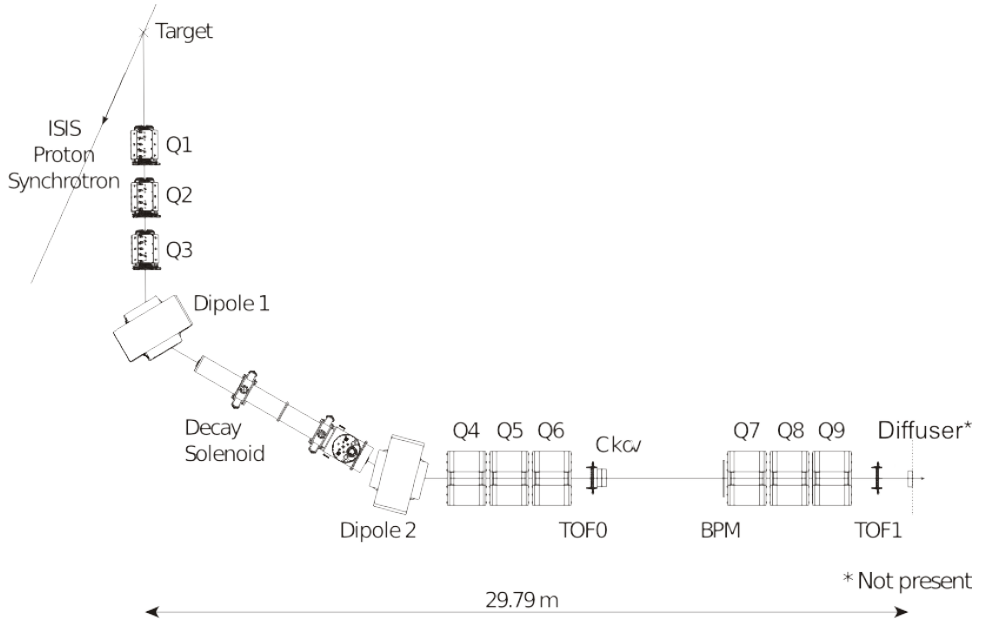

Figure 2.4: Top view of the MICE Muon Beam and its instrumentation for Step I. Figure taken from Ref. [63].

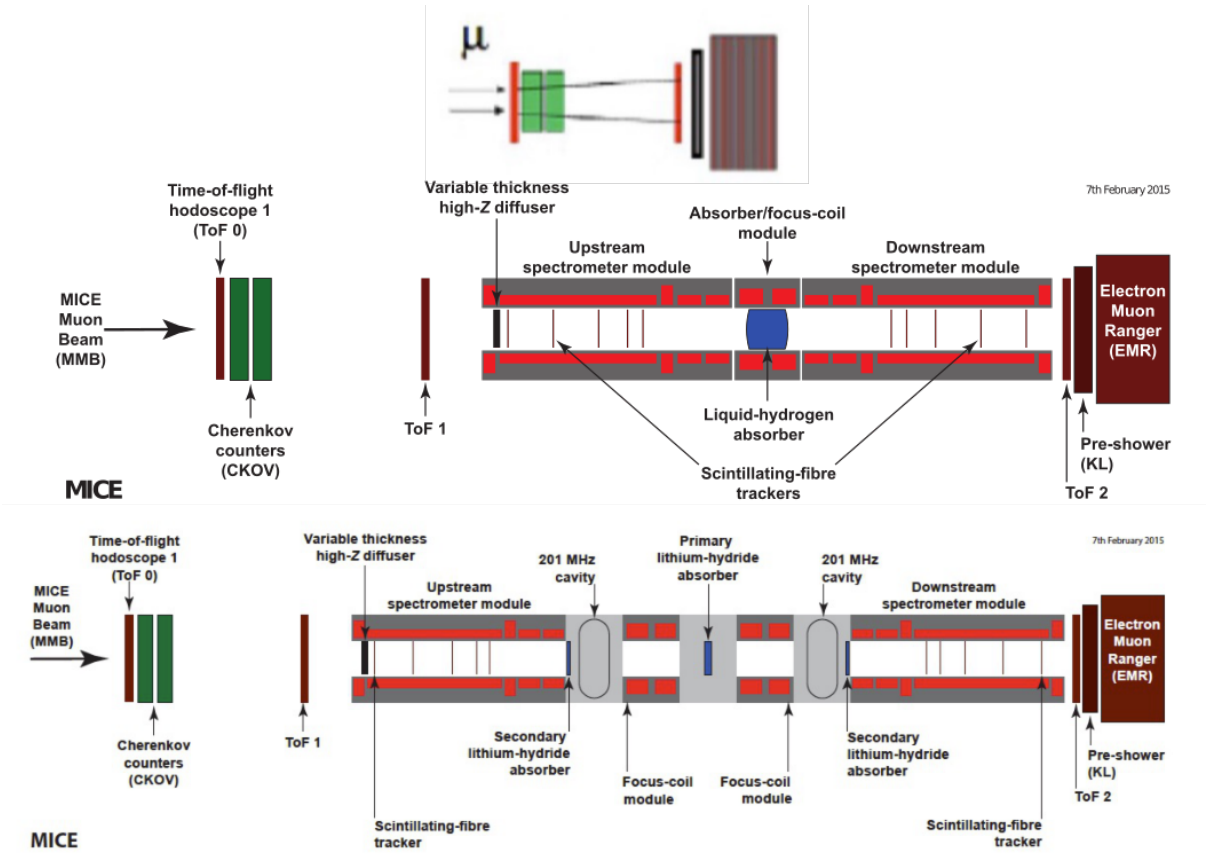

Figure 2.5: Top: MICE Step I, middle: Step IV cooling channel, bottom: Demonstration of muon ionisation cooling.

Table 2.1: The MICE beam line elements and detectors for Step I.

Element	Distance from target [along nominal beam axis]	L_{eff}	Max field/gradient		Radius (Pole tip)	1/2-aperture [H/V]	
	(mm)	(mm)	(T)	(T/m)	(mm)	mm	mm
Q1	3000.0	888	-	1.6	101.5		
Q2	4400.0	888	-	1.6	101.5		
Q3	5800.0	888	-	1.6	101.5		
D1	7979.1	1038	1.6	-	125	330.0	100.0
Decay Solenoid	12210.7	5000	5.7	-	57.5		
Proton absorber	14880	Plastic sheets 15, 29, 49, 54 mm					
GVA1	15050.0	Scintillation counter (0.02 X_0)					
D2	15808.1	1038	0.85	-	125	330.0	100.0
BPM1	16992.0	Scintillating fibres (0.005 X_0)					
Q4	17661.6	660	-	2.3	171.5		
Q5	18821.6	660	-	2.3	171.5		
Q6	19981.6	660	-	2.3	171.5		
TOF0	21088.0	Segmented scintillator (0.12 X_0)					
Ckova	21251.5	Aerogel threshold Cherenkov (0.019 X_0)					
Ckovb	21910.9	Aerogel threshold Cherenkov (0.031 X_0)					
BPM2	24293.7	scintillating fibres (0.005 X_0)					
Q7	25293.7	660	-	2.3	171.5		
Q8	26453.7	660	-	2.3	171.5		
Q9	27613.7	660	-	2.3	171.5		
TOF1	28793.1	Segmented scintillator (0.12 X_0)					
TOF2	31198.1	Segmented scintillator (0.12 X_0)					
KL	31323.1	Lead + scintillator (2.5 X_0)					
Tag counters	31423.1	Scintillation bars (0.06 X_0)					

in commissioning, debugging and aligning this new system. A paper on the first emittance measurement with the upstream spectrometer solenoid energised is in preparation. Ultimately this Step will give the first measurement of normalised transverse emittance reduction without re-acceleration when the full chain of superconducting magnets are energised, which will be the contents of future MICE publications. MICE has been in the Step IV configuration since the summer of 2015 and is currently taking data in this mode.

The final phase is the demonstration of ionisation cooling, as can be seen in figure 2.5. Radio frequency cavities will be installed in the cooling channel to re-accelerate muons after cooling and to partially restore the longitudinal component of their momentum thus achieving sustainable cooling. The simulated transmission and expected change in emittance are shown in figures 2.6 and 2.7. An expected cooling performance of 5.8% is expected from this Step for muon beams of momentum between 140 and 240 MeV/c. This would constitute the first demonstration of ionisation cooling, with first data in this configuration expected in the final

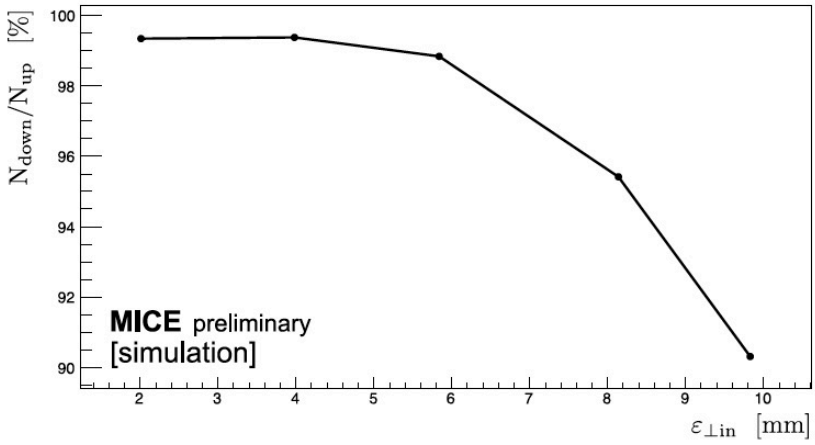

Figure 2.6: Transmission in percentage as a function of initial emittance for the cooling-demonstration lattice in the 200 MeV/c configuration. Figure taken from Ref. [66].

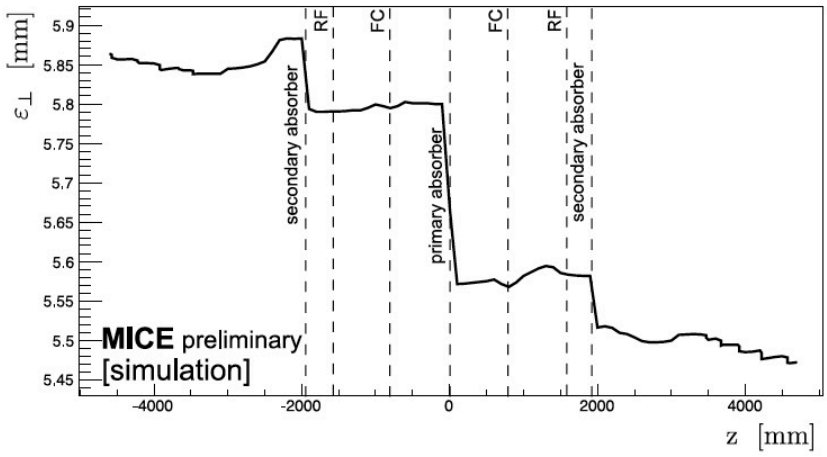

Figure 2.7: Emittance variation of an initial $\varepsilon = 6$ mm beam for the cooling-demonstration lattice design in the 200 MeV/c configuration as a function of the longitudinal coordinate z. The vertical dashed lines with labels show the centre of the positions of the absorbers, RF cavities and focus coil modules. Figure taken from Ref. [66].

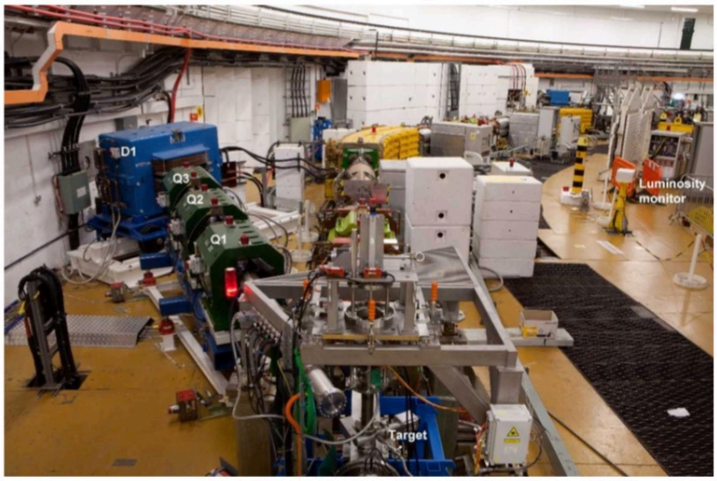

Figure 2.8: Upstream beam line. The target may be seen in the foreground of the photograph. The magnets that make up the upstream beam line (Q1-3 and D1) lie to the left of straight 7 of the ISIS proton synchrotron which can be seen in the centre of the figure. The luminosity monitor, surrounded by its white, borated-polythene shielding may be seen close to the right-hand edge of the photograph.

quarter of 2017.

2.3.2 MICE Target

The MICE experiment is fed parasitically by the ISIS proton accelerator, as can be seen in figure 2.8. ISIS accelerates protons up to 800 MeV at a repetition rate of 50 Hz. Pions are generated by the interactions of the proton beam on a target [67]. The target, made out of titanium, is dipped into the beam at a rate of $\sim$1 Hz and the pions that are generated are captured by a triplet of quadrupoles (Q1-3) see figures 2.9 and 2.10.

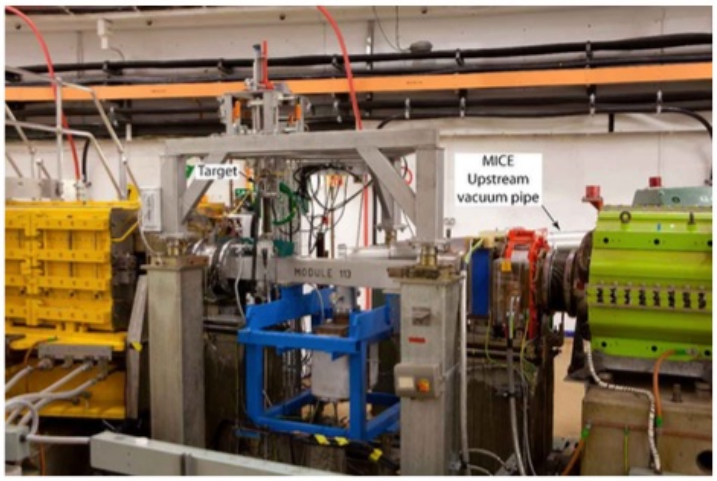

Figure 2.9: The MICE target installed in ISIS.

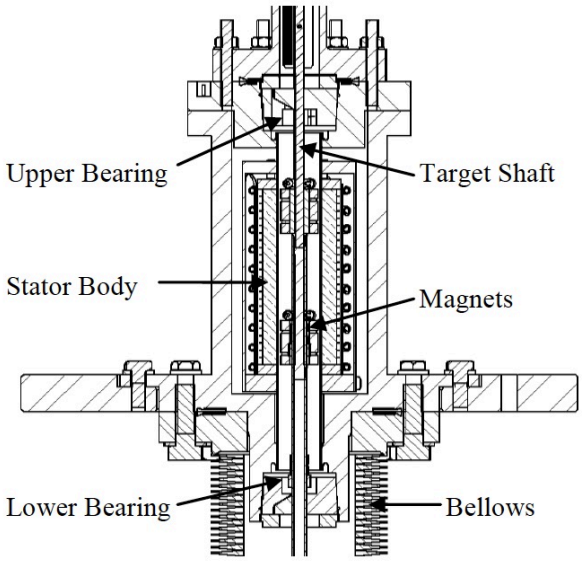

Figure 2.10: The target body showing the stator mounted within the flanges and supporting the top and bottom bearings. Figure taken from Ref. [67].

The MICE target is a hollow titanium cylinder with an outer diameter of 6 mm and an inner bore of 4.6 mm [68]. The target dips vertically into the beam, intercepting it over the last 3 ms of the acceleration cycle ($\sim$ 4 000 turns). During operation of the MICE beam line the target experiences acceleration of $\sim$80 g. A replica of the target was tested on the bench and operated for 2.15×10^6 actuations. During this operation, the replica target experienced no problems, with some dust released due to excessive wear on the VESPEL® bearings. This study shows that the MICE target can be operated without interfering with the ISIS beam line [69].

The mechanism for injecting the target into the ISIS beam (figure 2.10) is a linear electromagnetic motor in which permanent magnets mounted on the target shaft are accelerated by a series of 24 coils contained within the stator. To monitor the position of the shaft and control the drive current to the 24 coils an optical position-sensing system with laser quadrature readout is used.

2.3.3 MICE Beam Line Magnets

The first triplet of quadrupole magnets, Q1-3, are Type-IV quadrupoles [68] which originally formed part of the NIMROD accelerator at RAL, as can be seen in figure 2.8. Such magnets are open on one side. Pions are produced isotropically at the MICE target and the upstream beam line acts to capture pions at the highest possible rate. Downstream of Q1-3 the beam is passed to two dipoles (D1, D2) and a decay solenoid (DS). The two dipoles were also recovered from the NIMROD experiment and are rectangular Type-1 dipoles [68]. D1 and D2 act to select the momentum distribution of the muon beam. The first bending magnet selects pions

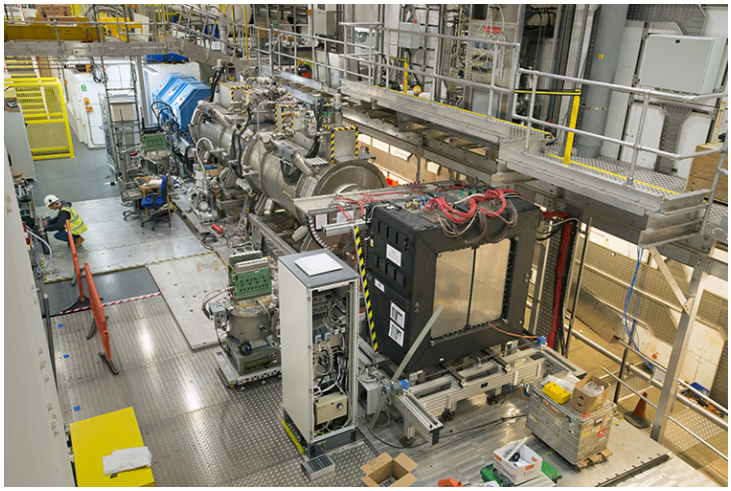

Figure 2.11: MICE beam line. The EMR detector can be seen at the end of the beam line proceeded by the two spectrometer solenoids with the beam line magnets and DSA just visible at the extreme left.

with a range of momenta proportional to the magnet current. By examining the kinematics of pion decay it can be determined that the momenta of the muons produced will be in the range $p_{\mu min} \leq p_{\mu} \leq p_{\mu max}$ illustrated in figure 2.12. When $p_{D1} \geq 200$ MeV/c, then $p_{D1} \approx p_{\mu max}$. At D2 the backward-going muons in the pion rest frame are selected. This is achieved when D2 is operating such that $p_{D2} \approx p_{\mu min}$. The aim of MICE is to demonstrate ionisation cooling for several muon beams at various momenta and the dipole magnets allow beams of different momenta to be selected.

The DS was provided by the Paul Scherrer Institute and constructed for use in the μE4 beam. The DS is included to increase the channel acceptance for π decay in transit. The pion contamination of the beam is reduced by setting $p_{D2} = p_{\mu min} \approx p_{D1}/2$. It is essential that a high purity muon beam is delivered to the MICE experiment hence the aforementioned selection. Simulations have shown (figure 2.12, right) that when the backward going muons are selected the pion contamination in the MICE beam will be lower than 1% [70], which is an acceptable level for the MICE experiment.

Beams are referred to by their transverse normalised emittance, ε_n and their longitudinal momentum, p_z. Within the MICE collaboration emittance is quoted in units of π mm·rad and momentum in units of MeV/c. The "nominal" values of ε_n and p_z are defined such that the nominal value of ε_n is evaluated in the upstream spectrometer solenoid and the nominal value of p_z is evaluated in the cooling channel. Tallying up and taking into account the two possible charges of the beams there are eighteen possible beam configurations which constitute the MICE program. Each configuration is achieved by selecting the momentum of the beam with the dipole magnets and selecting the emittance of the beam with the diffuser (Section 2.3.5).

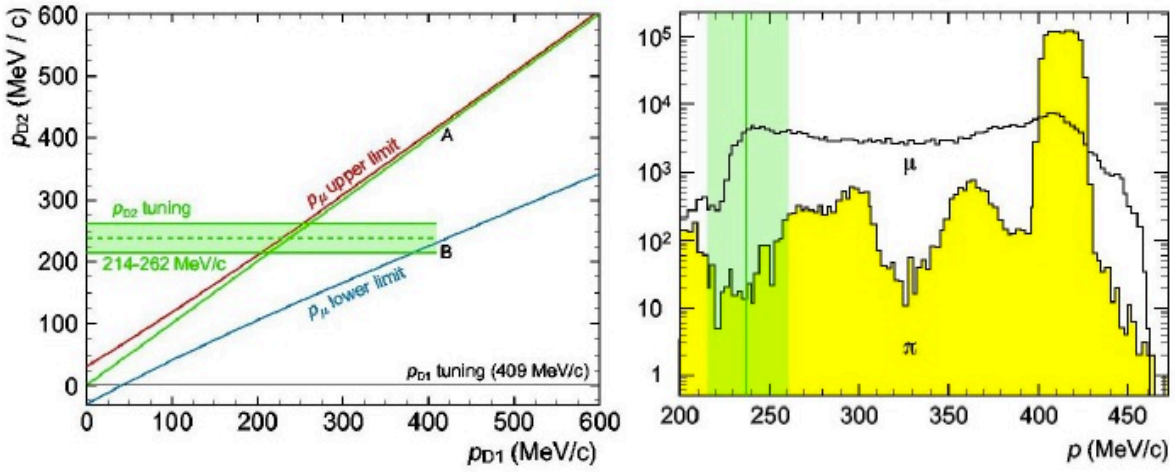

Figure 2.12: Working principle of the MICE beam line. Left–hand panel: the red and blue lines are the kinematic limits of the spectrum for muons produced in pion decays. The red line represents the maximum pion momentum that will be selected by D1 while the blue line shows the minimum momentum selected by D2. The points labelled A and B represent the mean momentum selection for each dipole and illustrate the point raised in the text that for a 200 MeV/c beam of muons $p_{D2} \approx p_{D1}/2$. By tuning D2 to the backward going muon peak an almost pion-free sample is produced. Right–hand panel: simulation showing pion and muon spectra at the end of the decay solenoid. Only high momentum pions survive. The green band shows the acceptance of D2, when tuned to the backward-going muon peak. Figure taken from Ref. [68].

The second and third quadrupole triplets downstream of D2 are Type QC dipoles provided by DESY, see figure 2.11 [68]. They have cross-shaped apertures and the circular aperture measures 352 mm at the pole tips. The magnet settings for these triplets were derived such that the muon beam delivered to the MICE experiment is matched in the upstream spectrometer solenoid. Tuning of the quadrupole current optimises the beam size and divergence at the upstream face of the cooling channel. An ideal beam would meet the following criteria [68]:

1. The Twiss parameters are: $\beta_x = \beta_y = \beta = 2p_z[\text{GeV/c}]/(0.3B[\text{T}])$ and $\alpha_x = \alpha_y = \alpha = 0$ in the upstream spectrometer solenoid, downstream of the diffuser;

2. The beam size at the entrance of the diffuser (essentially the same as the beam size at the exit of the diffuser) is such that the rms width of the beam in x and y satisfies $\sigma_x^2 = \sigma_y^2 = (\varepsilon_n\beta)/\gamma$, with $\gamma = E/m_\mu$;

3. The beam angular divergence at the upstream surface of the diffuser (${\sigma_x}^2$ and ${\sigma_y}^2$), increased by multiple Coulomb scattering in the diffuser ($\sigma^2_{\theta,MCS}$), is equal to the desired angular divergence in the spectrometer solenoid, i.e.: $\sigma_x^2 + \sigma^2_{\theta,MCS} = \sigma_y^2 + \sigma^2_{\theta,MCS} = \varepsilon_n/(\beta\gamma)$;

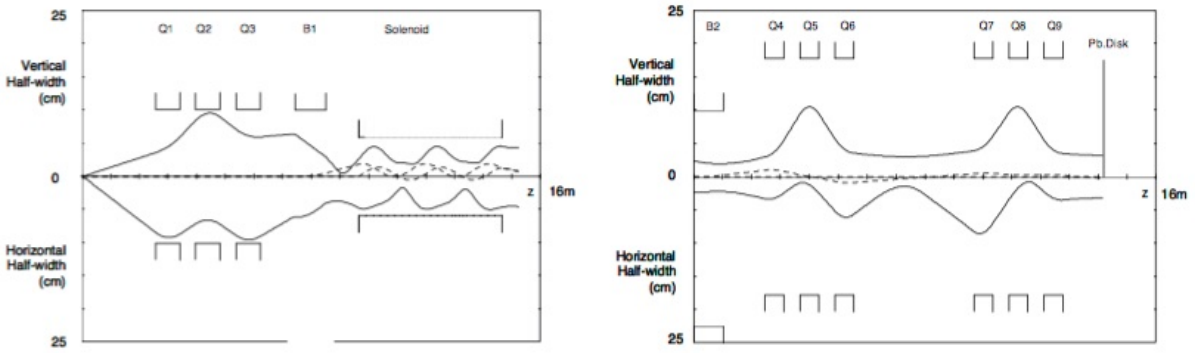

Figure 2.13: MICE beam line envelope for the baseline case with $\varepsilon_n = 6\pi$ mm $\cdot$ rad and $p_z = 200$ MeV/c. Left panel: pion optics for the upstream section. Right panel: muon optics for the downstream section. The diffuser used in this simulation has been realised using brass and tungsten. For both panels the top half of the plot shows the vertical envelope and the bottom half shows the horizontal envelope, figure taken from [68].

4. The central momentum selected by D2 matches the nominal momentum p_z, once corrected for the calculated energy loss in all material encountered by the beam as it travels from D2 to the cooling channel.

In practice the selected beam will not fulfil all criteria completely. By the very nature of the bending magnet D2 the beam will not have the same emittance and dispersion in the horizontal and vertical planes. Additionally it is not possible to include all of the characteristics of the beam in the transport models, for example the horizontal beam dispersion was neglected.

For the pion capture triplet upstream the matrix-evolution code TRANSPORT [71] was used to determine the optics. From D1 downstream the beam is no longer under vacuum and interactions in air must be taken into account. Hence the downstream optics calculation were done with the Decay-TURTLE package [72]. Both packages can be used to transport the 1 σ beam envelope down the beam line with the results of these simulation shown in figure 2.13. For the downstream optimisation an average match was determined by using the 4D covariance matrix from which the 4D emittance and the Twiss parameters of the beam can be determined. In a similar manner to the upstream optimisation these parameters were evolved through the beam line and diffuser until the match conditions, those conditions agreeing with the definition of an ideal beam, were met and the beam line settings optimised.

2.3.4 Proton Absorber

Before D2 there is a proton absorber in the beam line composed of sheets of borated-polyethylene of varying thickness. The number of sheets can be changed allowing the thickness of the absorber to be tailored to the momentum of the beam. For negative beams all of the sheets are

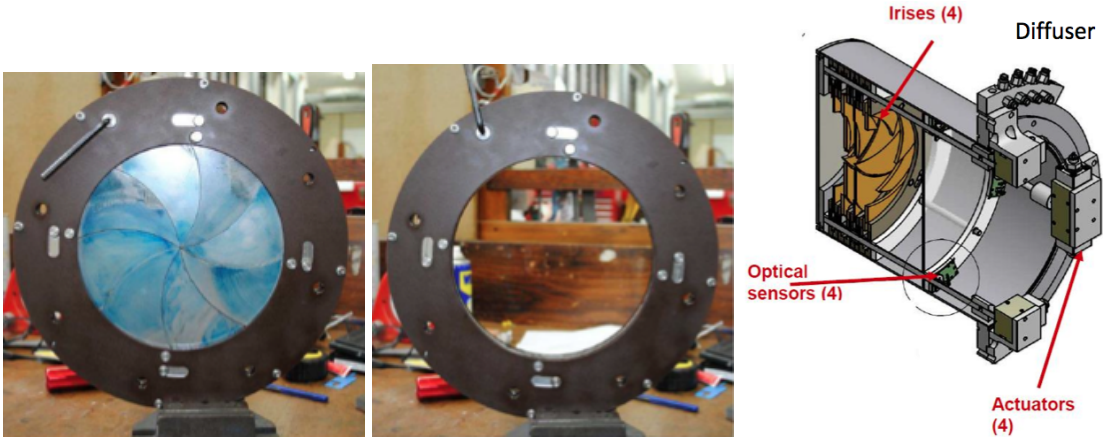

Figure 2.14: Left panel: picture of the MICE diffuser showing the irises. Centre panel: one of the brass irises being tested. Right panel: Schematic of diffuser, figure taken from Ref. [73].

removed from the beam line as the number of protons in the beam will be negligible. For 140 MeV/c positive beams the thickness of the absorber is 44 mm, for the 200 MeV/c beams it is 83 mm and for the 240 MeV/c beams it is 147 mm. If this absorber was not included then the number of protons that reached the first time of flight detector (TOF0) would lead to unacceptable levels of contamination. This mechanism works in the momentum range of interest as proton energy loss per unit length is greater than that of pions.

2.3.5 Diffuser

As discussed in Section 2.3.3, a diffuser is required to create beams with various emittance profiles. The diffuser is a stainless steel drum with four irises each with a different radiation length, as can be seen in figure 2.14. By inserting different combinations of the irises into the beam line, multiple Coulomb scattering increases the divergence of the beam which can be used to control the emittance of the beam. As the diffuser must be operated in proximity to large magnetic fields it cannot rely on electromagnetic motors or magnetic components to remove or insert it into the beam line. Consequently the diffuser uses an air compressor system to close or retract its various irises.

2.3.6 Particle Identification Detectors

2.3.6.1 Cherenkov Detectors

Downstream of D2 is the second triplet of quadrupoles (Q4-6) followed by two Cherenkov detectors (Ckova and Ckovb), as can be seen in figure 2.15. The two Cherenkov detectors have different aerogel densities with the muon thresholds at $p^{th}_{\mu,a} = 278$ MeV/c in Ckova and $p^{th}_{\mu,b} = 210$ MeV/c in Ckovb. The pion thresholds are $p^{th}_{\pi,a} = 367$ MeV/c and $p^{th}_{\pi,b} = 277$ MeV/c

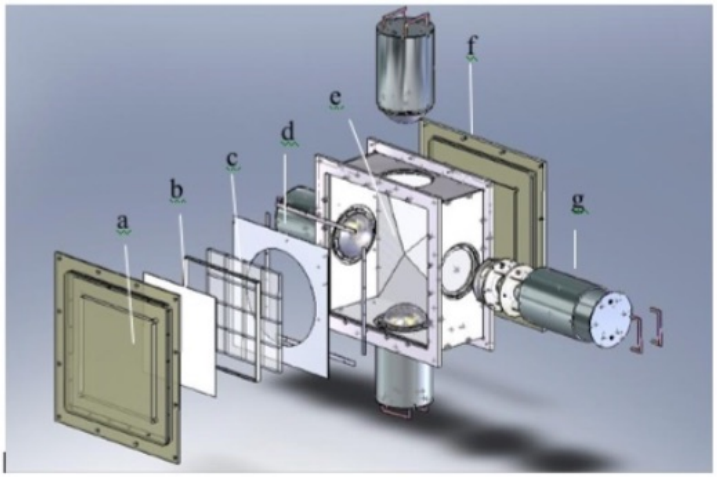

Figure 2.15: Aerogel Cherenkov counter blowup: a) entrance window, b) mirror, c) aerogel mosaic, d) acetate window, e) GORE reflector panel, f) exit window and g) 8 inch PMT in iron shield. Figure taken from Ref. [68].

and the density of the aerogels in the detectors are $\rho_a = 0.225$ gcm^{-3} and $\rho_b = 0.370$ gcm^{-3} respectively. The indices of refraction are $n_a = 1.07$ and $n_b = 1.12$ and it is this property that allows the pion contamination of the beam to be determined using the Cherenkov detectors. In the 200 MeV/c beams, pions are below the threshold which would fire the detector for both Ckova and Ckovb whereas muons are above only for Ckovb. For the 240 MeV/c beams, pions are above the threshold for Ckovb while muons are above for both Ckova and Ckovb, see figure 2.16. Using this information and information collected by the TOF detectors, algorithms can be written that produce likelihood distributions of particle type. However for Step I (see Section 2.3.1) running, only the TOF system was used to identify particles since there was not an independent measurement of momentum provided by the spectrometer solenoids in Step IV (see Section 2.3.1).

2.3.6.2 TOF Detectors

Immediately before the Cherenkov detectors is the first time-of-flight (TOF) detector and downstream of the third triplet of quadrupole magnets, Q7-9, there are two more, see figure 2.17, one immediately upstream and one immediately downstream of the cooling channel. The detectors are both composed of two planes of orthogonally oriented scintillator slabs read at both edges by fast conventional Hamamatsu R4998 photomultipliers. The slabs have a thickness of 1 inch and the active area of the TOF stations are 40×40 cm^2, 42×42 cm^2 and 60×60 cm^2 for TOF0, TOF1 and TOF2 respectively. The slabs are 4 cm wide for TOF0 and TOF1 and 6 cm wide for TOF2. The TOFs have a timing resolution of 50 ps. Such fine timing resolution can be achieved by the use of an active divider base in the PMTs and leading-edge discriminators to sample the rise time.

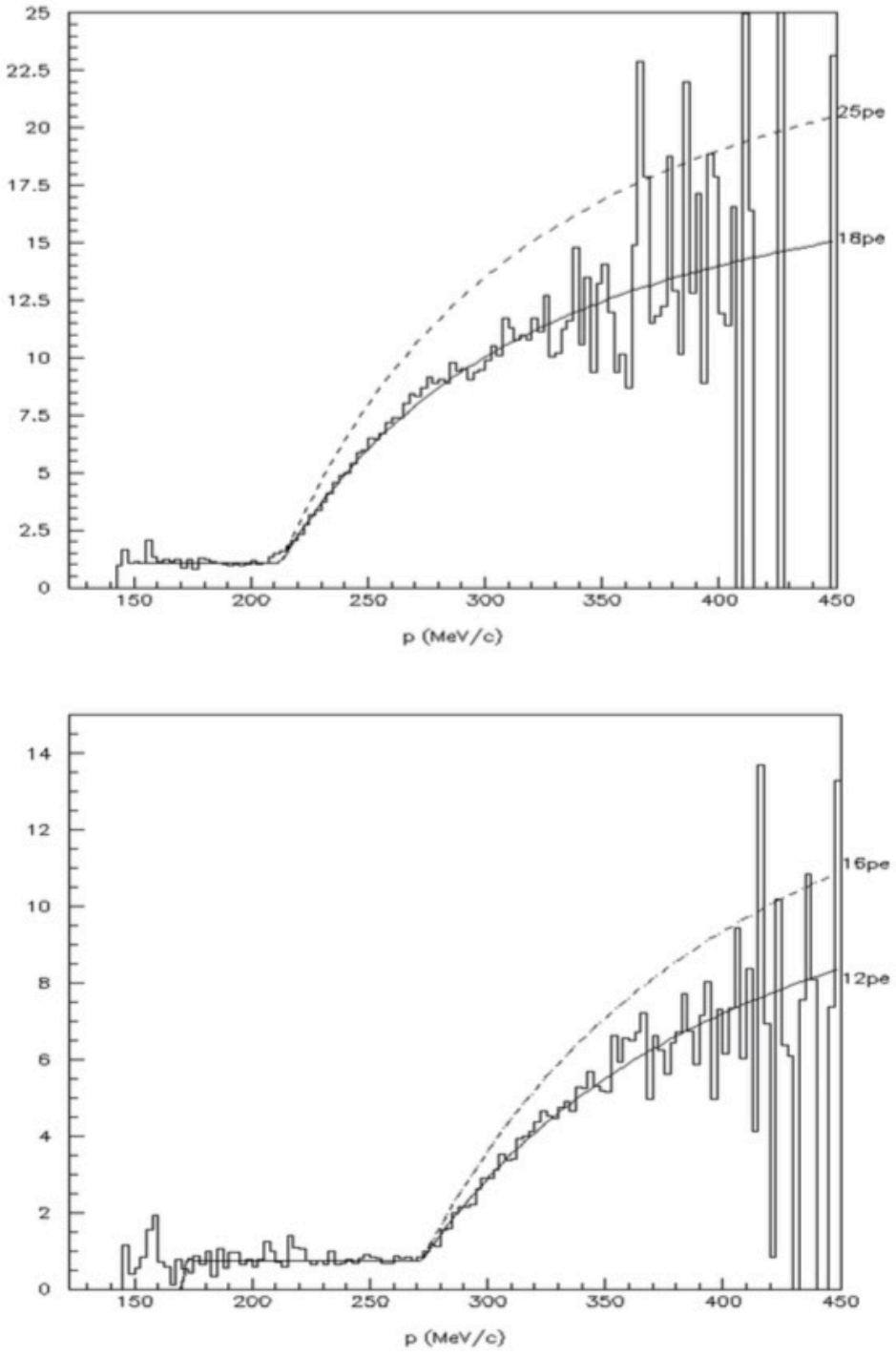

Figure 2.16: Photoelectron curves versus momentum for muons in Ckov-b (top panel) with the superimposed function $f = 1.1 + 18[1(213/p)2]$, and similarly for muons in Ckov-a (bottom), with $f = 0.75 + 12[1(272/p)2]$. Figure taken from Ref. [74].

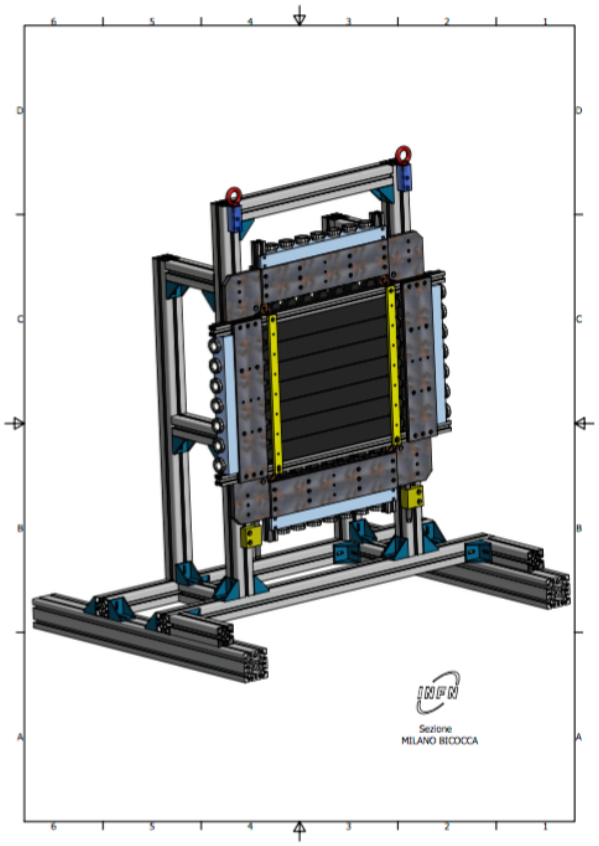

Figure 2.17: 3-D view of the full TOF1 detector with magnetic shielding in place, mounted on its support structure. Figure taken from Ref. [75].

The two planes can be used to locate the position in both x and y where a particle crossed the scintillator planes. This is done by calculating the time for a signal corresponding to a particle crossing the active region of the TOF detector to reach the PMTs located at either ends of the scintillator slabs. The signal arrival time, t_i(i=1,2), is given by [68]:

$$t_i = t_0 + \frac{L/2 \pm x}{v_{eff}} + \delta_i; \tag{2.25}$$

where t_0 is the particle arrival time, x its distance from the counter centre, L the scintillator length, v_{eff} the effective velocity of light in the scintillator slab and δ_i includes all time delays (in cables, PMT transit time, etc.). Using this, the transverse impact position, u, of a particle on a TOF station may be reconstructed from the difference between the time measurements from the two PMTs i, j at the ends of a counter as:

$$u = \frac{v_{eff}}{2} \times ((t_i - \delta_i) - (t_j - \delta_j)). \tag{2.26}$$

For the vertical position $x = u$ and for the horizontal position $y = u$. The TOFs are capable of giving spatial resolution to $\sim$1 cm. The TOF system determines the velocity of a particle independently of the Cherenkov system. This speed information is fed into the global particle identification.

TOF0 and TOF1 are designed to measure the time at which particles pass through them with a resolution of 50 ps [65]. Before the start of data taking the TOF0 and TOF1 detectors were refurbished. A resolution of $\sim$50 ps was measured in the 2010 data-taking run for TOF0 and TOF2, while for TOF1 the value was $\sim$60 ps [76]. The resolution of the TOF0 station (4 cm wide slabs) and that of the TOF2 station (6 cm wide slabs) were similar, showing that path length fluctuations were negligible. This result prompted the rebuild of TOF0 and TOF1, changing the older PMTs to refurbished PMTs from Hamamatsu (Japan). This operation involved changing the active divider of the older H6533MOD assemblies to a new one. Of the 68 assemblies 50 were changed in a refurbishing operation that involved extensive laboratory tests to assess the quality and performances of the new mounted assemblies [77]. After the refurbishing of TOF0 and TOF1 and following a detector calibration, the values of the TOF detector intrinsic time resolutions were 55 ps for TOF0, 53 ps for TOF1 and 50 ps for TOF2 [76; 77].

2.3.6.3 KLOE-Light Calorimeter

The KL, figure 2.18, is based on the calorimeter for the KLOE experiment at Frascati National Laboratories (LNF) in Italy. The KL calorimeter is composed of scintillating fibres and extruded lead foils, with an active volume of 93 $\times$ 93 $\times$ 4 cm^3. It has 21 cells, and the light from

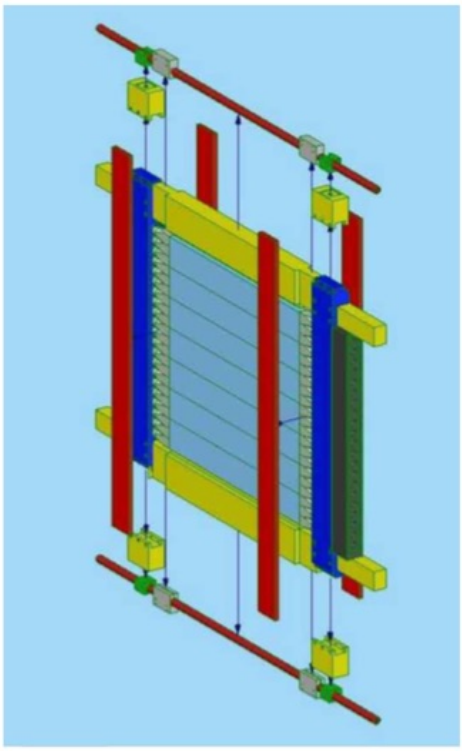

Figure 2.18: Global layout of KL assembly. The exploded view shows the various custom made components for support and magnetic shielding: in yellow and dark blue the mechanical support and the PMT soft iron magnetic shields, in green the iron bars housing the PMT voltage dividers and in red the additional iron bars covering the Winston cones light-guides. Figure taken from Ref. [68].

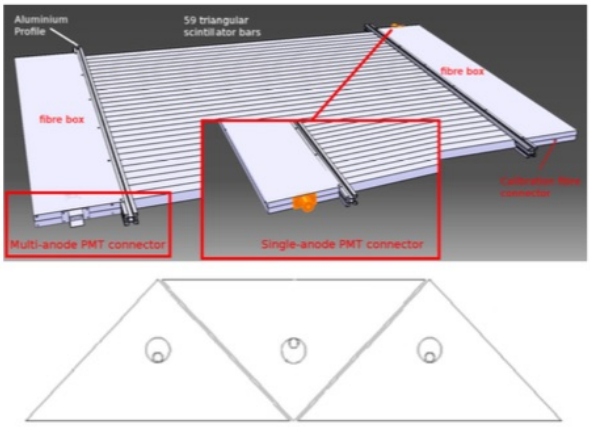

Figure 2.19: CAD drawing of one EMR plane (top) and cross section of 3 bars and their threaded WLS fibres (bottom). Figure taken from Ref. [65].

its scintillating fibres is collected by 42 Hamamatsu R1355 PMTs. The PMT signals are sent via a shaper module to 14 bit CAEN V1724 flash ADCs. The shapers stretch the signal in time in order to match the flash ADC sampling rate. A detailed description of KL is given in [68]. The KL is positioned downstream of the cooling channel. The number of pions that will be transported through the cooling channel is small, however muons decaying to electrons in the cooling channel can also lead to contamination. To avoid biasing, the emittance measurement, the KL and Electron Muon Ranger (EMR) (Section 2.3.6.4) are located downstream of the cooling channel to perform Particle Identification (PID). The KL performs pre-showering and provides energy deposition and timing information. It was also used for the pion contamination study, which will be discussed in chapter 4

The KL has an energy resolution of 7% and timing resolution of 70 ps/$\sqrt{E}$. In order to compensate for light attenuation in the scintillator, the KL response to a particle is defined in terms of the product of the digitised signals from the left and right sides of each slab divided by their sum [70]:

$$\text{ADC product } = 2\frac{\text{ADC}_{\text{left}} \times \text{ADC}_{\text{right}}}{\text{ADC}_{\text{left}} + \text{ADC}_{\text{right}}} \tag{2.27}$$

where the factor of 2 is present for normalisation. The products are summed for all slabs in KL above threshold. It can be shown that the normalised ADC product combines the PMT signals in a way that is less sensitive to the particle hit position along the fibre length. This is due to the attenuation of light in the fibres, which includes two attenuation lengths of which one is much shorter than the other [77; 78].

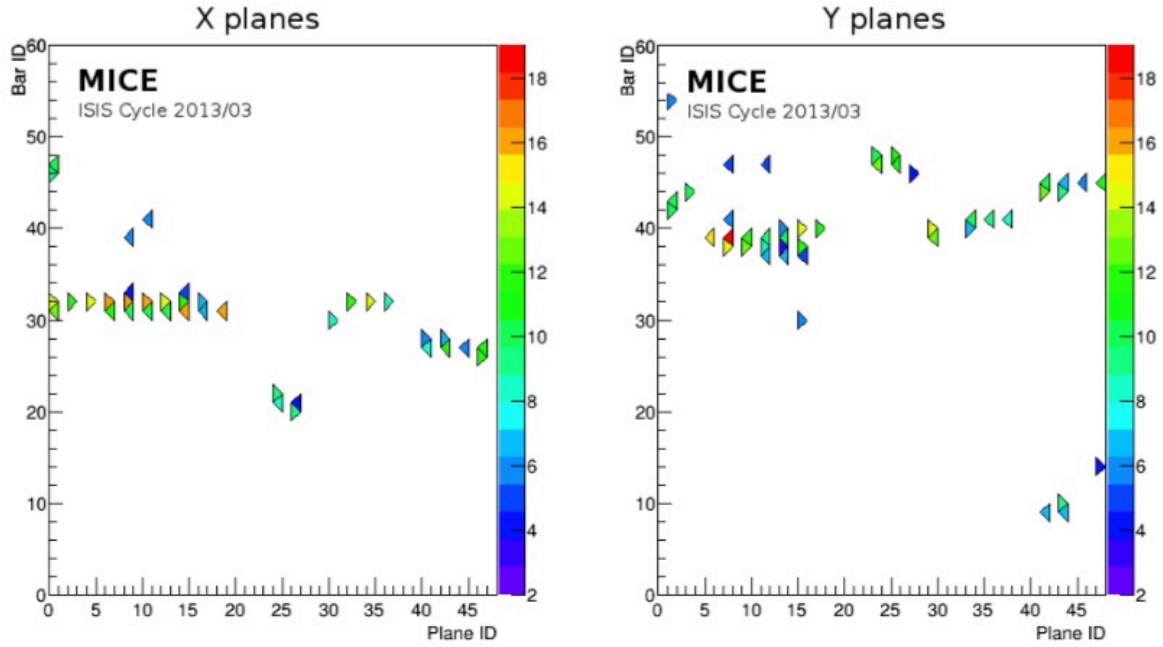

Figure 2.20: EMR event display of the energy deposited by a positron shower ($p_{D2} = 450\,\text{MeV/c}$) in the two projections. The location of a hit is defined by the plane number (Plane ID, 0-47) and bar number (Bar ID, 1-59) and the energy deposited is represented by the colour code in units of time-over-threshold. Figure taken from Ref. [65].

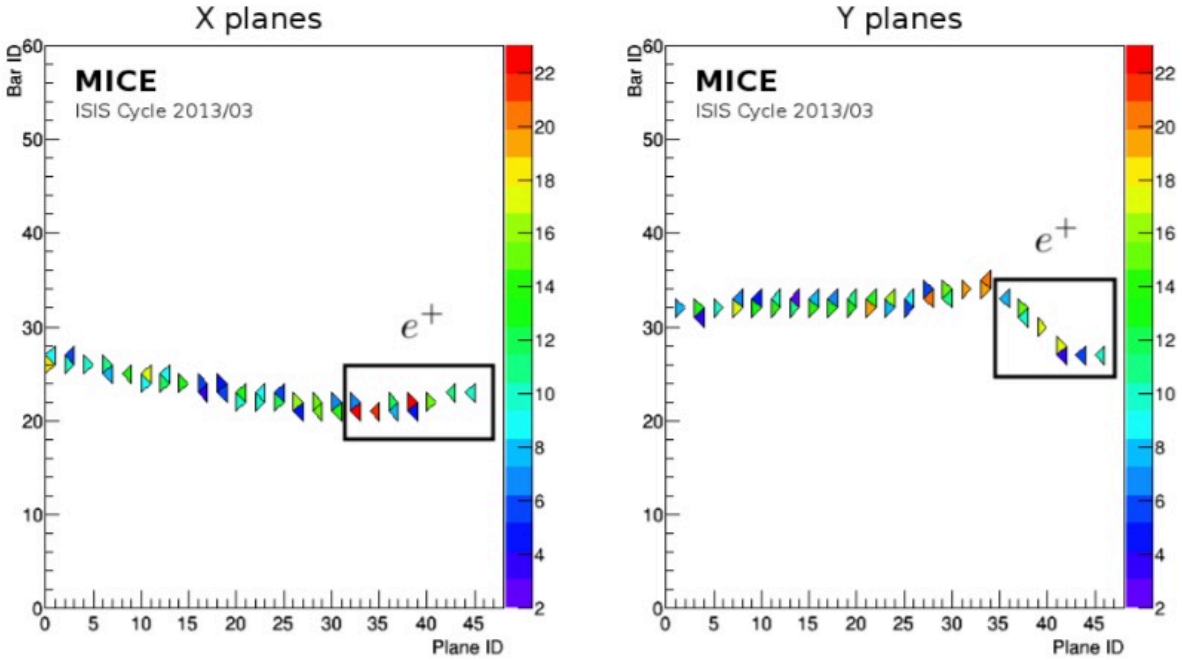

Figure 2.21: EMR event display of the energy deposited by a μ^+ which decays in the detector volume. The location of a hit is defined by the plane number (Plane ID, 0-47) and bar number (Bar ID, 1-59) and the energy deposited is represented by the colour code in units of time-over-threshold. Figure taken from Ref. [65].

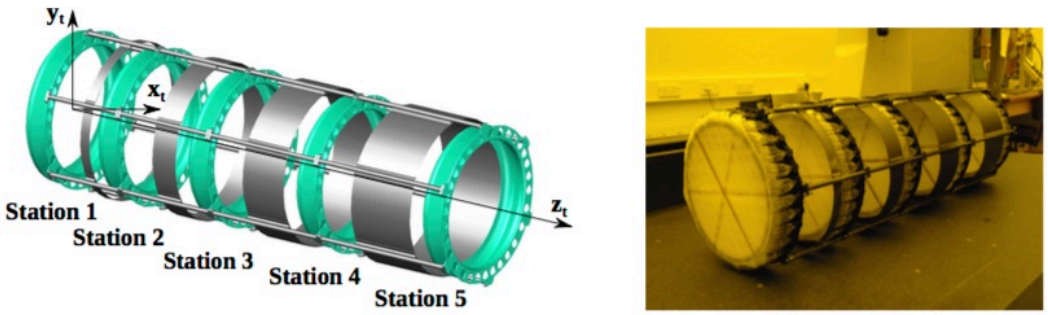

Figure 2.22: Left: A schematic of the tracker carbon fibre frame, showing the detector station positions. The fibre planes are glued on to the upstream edge (lower z_t position) of the carbon fibre station frames (shown in green). Right: A photograph of a tracker. The orange tint is due to the special lighting needed to protect the fibres. The intersecting lines visible on the station faces indicates the direction of the fibres in each plane. [80].

2.3.6.4 Electron Muon Ranger

The second part of the downstream PID suite is the EMR. The EMR is composed of triangular scintillator bars arranged in planes of 59 bars, as can be seen in figure 2.19, with the light collected and transported by wavelength shifting (WLS) fibres which are read out by Hamamatsu R7600-00-M64 EG multianode photo-multiplier tubes of dimension 1 m^3. The full detector consists of 48 of these planes with adjacent planes rotated by 90° with respect to each other, with one orientated parallel to the x-axis and the other the y-axis.

The EMR allows electrons transported through the cooling channel to be identified. Muon and electron tracks can be distinguished, as in general muons will exhibit clear straight tracks through the EMR followed by a decay if the muon comes to rest, whereas electrons will scatter in the EMR material. The difference in the event topology of an electron shower and a muon track can be clearly seen in figures 2.20 and 2.21. If electrons were not removed from the data they would bias the muon emittance calculation. The detector is capable of identifying electrons with an efficiency of 98.6% [79], providing a purity for the MICE beam that exceeds 99.8%. The EMR also proved to be a powerful tool for the reconstruction of muon momenta in the range 100-280 MeV/c.

Information from the EMR, as with all of the MICE detectors, is fed into the global particle identification, which utilises a log likelihoods scheme. PDFs of particle type are produced for each of the detectors from which the final particle identification weighting is calculated.

2.3.7 Scintillating Fibre Trackers

The goal of MICE is to measure a reduction in emittance for a muon beam. It is therefore necessary to measure position and momentum information before and after the cooling channel to reconstruct the emittance before and after cooling. This is done in Step IV by means of two scintillating fibre trackers positioned immediately up- and downstream of the absorber module [80]. Each tracker plane has a 300 mm diameter and the tracker frame measures 1.1m from the most upstream plane to the most downstream. Each tracker is housed in a 4 T superconducting solenoid to allow the momentum measurement to be performed. The trackers are labelled tracker upstream and tracker downstream which reflects their location in the MICE beam line. The upstream tracker is rotated through 180° with respect to the downstream tracker.

The trackers are composed of 5 stations labelled 1 to 5 illustrated in figure 2.22. Both trackers are of the same design with fibres of 350 μm chosen in order to minimise multiple scattering. The resulting low light yield is compensated by employing Visible Light Photon Counters (VLPC) with high quantum efficiency. Studies have been performed and the space point efficiency of the tracker was determined to be 99.7$\pm$0.1% [80].

A station is formed from three planes of scintillating fibre orientated at 120 degrees with respect to each other. The fibres are arranged in a doublet layer structure to give 100% coverage and backed by a sheet of mylar plastic. The station closest to the absorber in both trackers is defined to be the reference surface, for both trackers this is station 1. The tracker software builds higher level objects in the reconstruction from the raw detector readout. At the lowest level, digits are formed representing the digitisation of a detector channel response to an incident track. These are organised into clusters which represent groups of neighbouring digits arising from the same particle crossing multiple channels. Spacepoints are formed that group clusters from adjacent detector planes to give a real space position in terms of (x, y, z). At the highest level, tracks are formed which group together spacepoints from different tracker stations according to the particle track that generated them using a Kalman filter [81]. These can either be straight or helical depending on whether the cooling channel magnets were on or off.

Studies have been conducted looking at the performance of the tracker software. In these studies, the final Kalman fit performance is benchmarked against MC truth data for the output beam parameters x, y, z, p_x, p_y and p_z at the tracker reference plane. Residuals for the position are shown in figures 2.23 and 2.24 and for the momentum in figures 2.25 to 2.27. In both cases the reconstructed variable shows excellent agreement with the MC truth. For the position residuals the reconstruction is close to optimal, however for the momentum residuals a small systematic offset remains which requires further investigation. With the tracker working at or

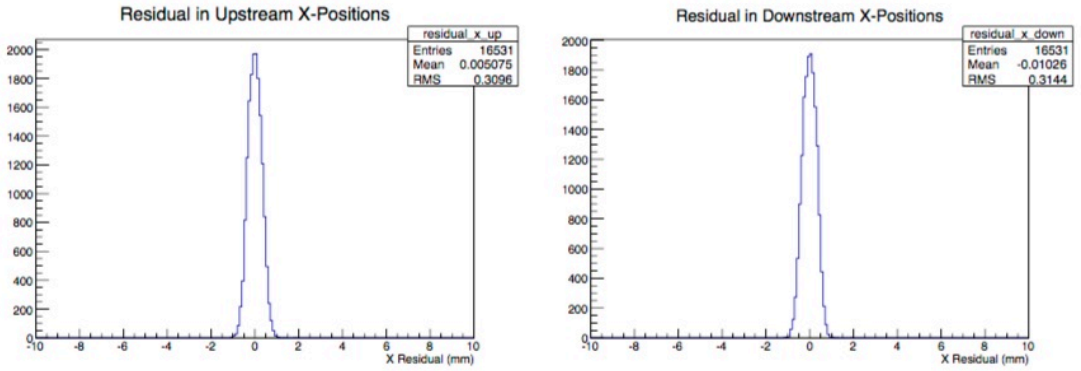

Figure 2.23: The x residuals of the upstream (left) and downstream (right) trackers for a 6π mm·rad 4D emittance, and 200 MeV/c momentum beam. Figure taken from Ref. [80].

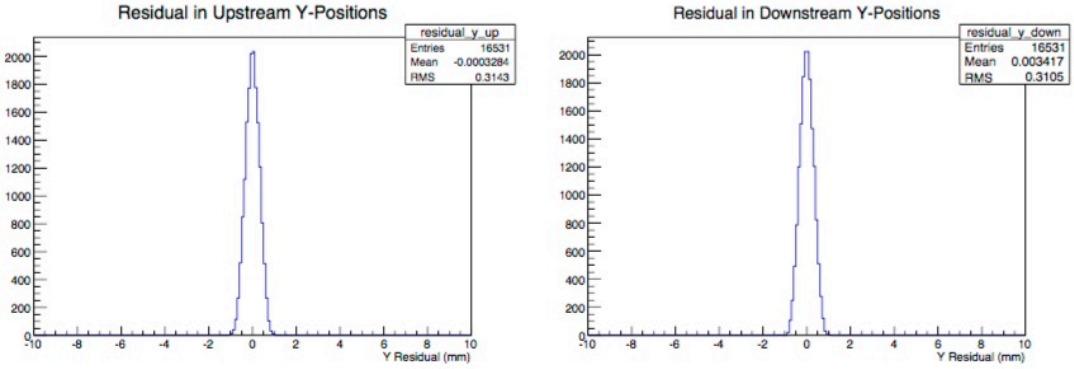

Figure 2.24: The y residuals of the upstream (left) and downstream (right) trackers for a 6π mm·rad 4D emittance, and 200 MeV/c momentum beam. Figure taken from Ref. [80].

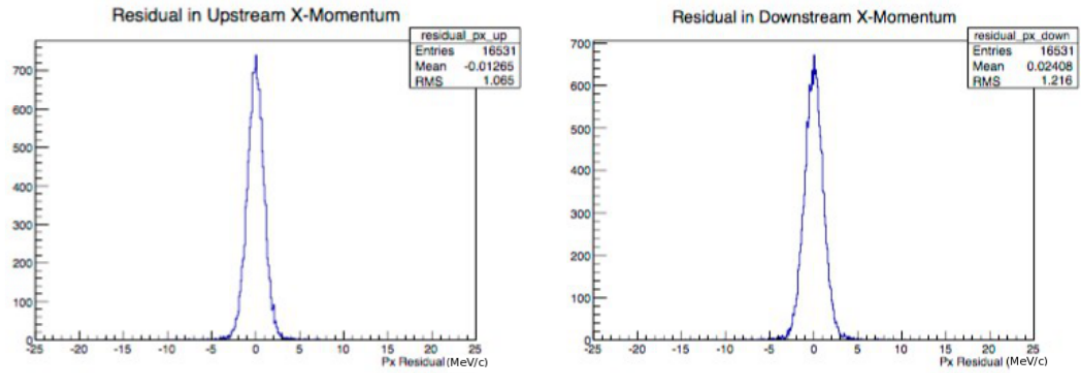

Figure 2.25: The p_x residuals of the upstream (left) and downstream (right) trackers for a 6π mm·rad 4D emittance, and 200 MeV/c momentum beam. Figure taken from Ref. [80].

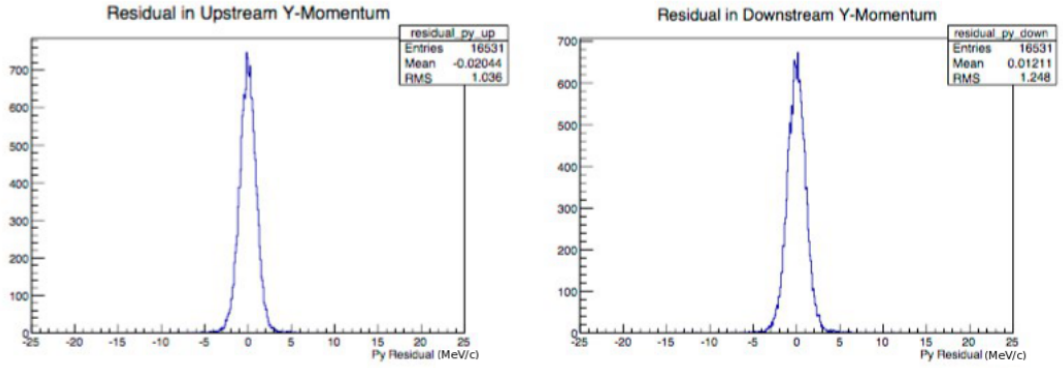

Figure 2.26: The p_y residuals of the upstream (left) and downstream (right) trackers for a 6π mm·rad 4D emittance, and 200 MeV/c momentum beam. Figure taken from Ref. [80].

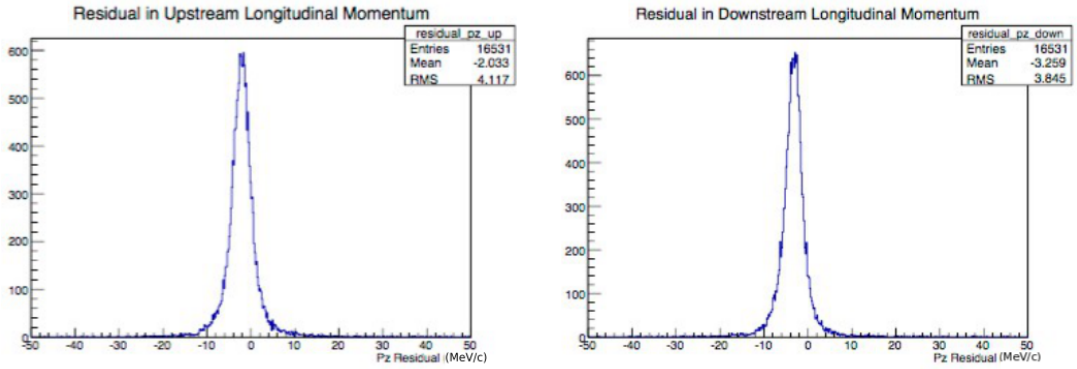

Figure 2.27: The p_z residuals of the upstream (left) and downstream (right) trackers for a 6π mm·rad 4D emittance, and 200 MeV/c momentum beam. Figure taken from Ref. [80].

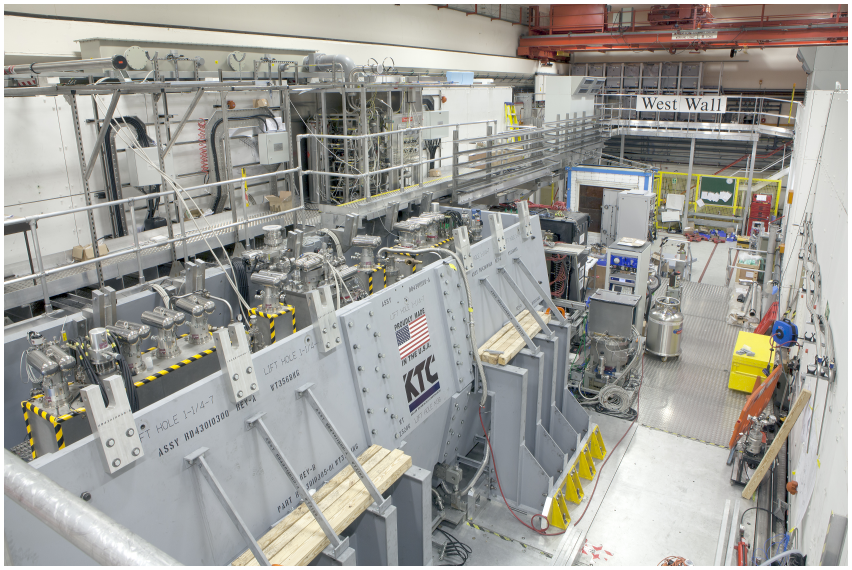

Figure 2.28: Step IV cooling channel with the partial return yoke installed in the MICE hall.

near optimal data taken with this detector can now be analysised which will be the subject under discussion in chapter 6.

2.3.8 Superconducting Magnets

In the MICE cooling channel, superconducting magnets are required in order to achieve the necessary gradients in the focus coils around the absorber and in the spectrometer solenoids surrounding each of the trackers. As discussed in Section 2.2, in order to maximise the ionisation cooling the muon beam should be strongly focused as it passes through the liquid hydrogen absorber hence the requirement for superconducting magnets. Studies have been performed to investigate the size of the magnetic fields both inside and outside the MICE hall [82; 83]. Racks with the electronics for the read out equipment and compressors for the cooling are located in the hall. If the magnet field inside the hall is too large in the position where this equipment is located, it would not be safe to operate the experiment. Similarly the MICE control room is located adjacent to the MICE hall, the extent to which magnet fields from the hall would penetrate the control room was similarly taken into account.

To mitigate the effects of the large magnetic fields being generated in the hall, magnetic shielding in the form of a partial return yoke (figure 2.28) was installed in the MICE hall. Magnetic shielding consists of metallic alloys with a high magnetic permeability, which draw the magnetic field lines into themselves greatly reducing the field beyond the shielding. This shielding lowers the magnetic field in the MICE hall to a level which allows the experiment to be safely operated and the detectors to work correctly.

2.4 MICE Analysis User Software (MAUS)

MAUS is the MICE project's tracking, detector reconstruction and accelerator physics analysis framework [84]. It performs a number of roles, with its core functionality based on the GEANT4 toolkit for modelling physical processes involving particle tracking. The response of detector electronics to particles interacting within the detector volume is also modelled in MAUS. This raw output is built up into higher level objects based on the specifications of each detector. Each detector group is required to provide algorithms to digitise and treat the raw data such that it may be handled by the MICE analysis group. The software is particular to each detector and varies from building spacepoints in the TOFs to performing pattern recognition and track building in the trackers. Further details can be found in Section 2.3.

The objects output from this framework can be used to perform various accelerator physics tasks natively, with the output packaged in a format that can be readily analysed in common software packages such as ROOT [85]. While MAUS is used for offline analysis, it also is the framework for the online running of the MICE experiment. It is the successor to the G4MICE software package [86] that performed a similar function in the early stages of the MICE experiment.

Data is organised into discrete blocks in the MAUS data structure called spills. This structure derives from the way in which MICE is fed by the ISIS proton synchrotron where one dip of the MICE target corresponds to one particle burst in MICE, referred to as a spill. The MAUS Application Programming Interface (API) is highly modular with a workflow that includes:

- input modules, which create instances of the MAUS spill structure,
- map modules, which modify a single spill item. This allows the reconstruction to be parallelised across multiple nodes.
- Reduce modules, which act on a collection of spills creating plots or calculating variables from a run and
- output modules, which store instances of the MAUS data structure.

This structure allows new functionality to be easily incorporated into the framework in self-contained modules.

2.4.1 Configuration Database

The MICE experiment is currently under construction, with new detectors and equipment installed as they become available. In order to keep track of the various geometries and beam line

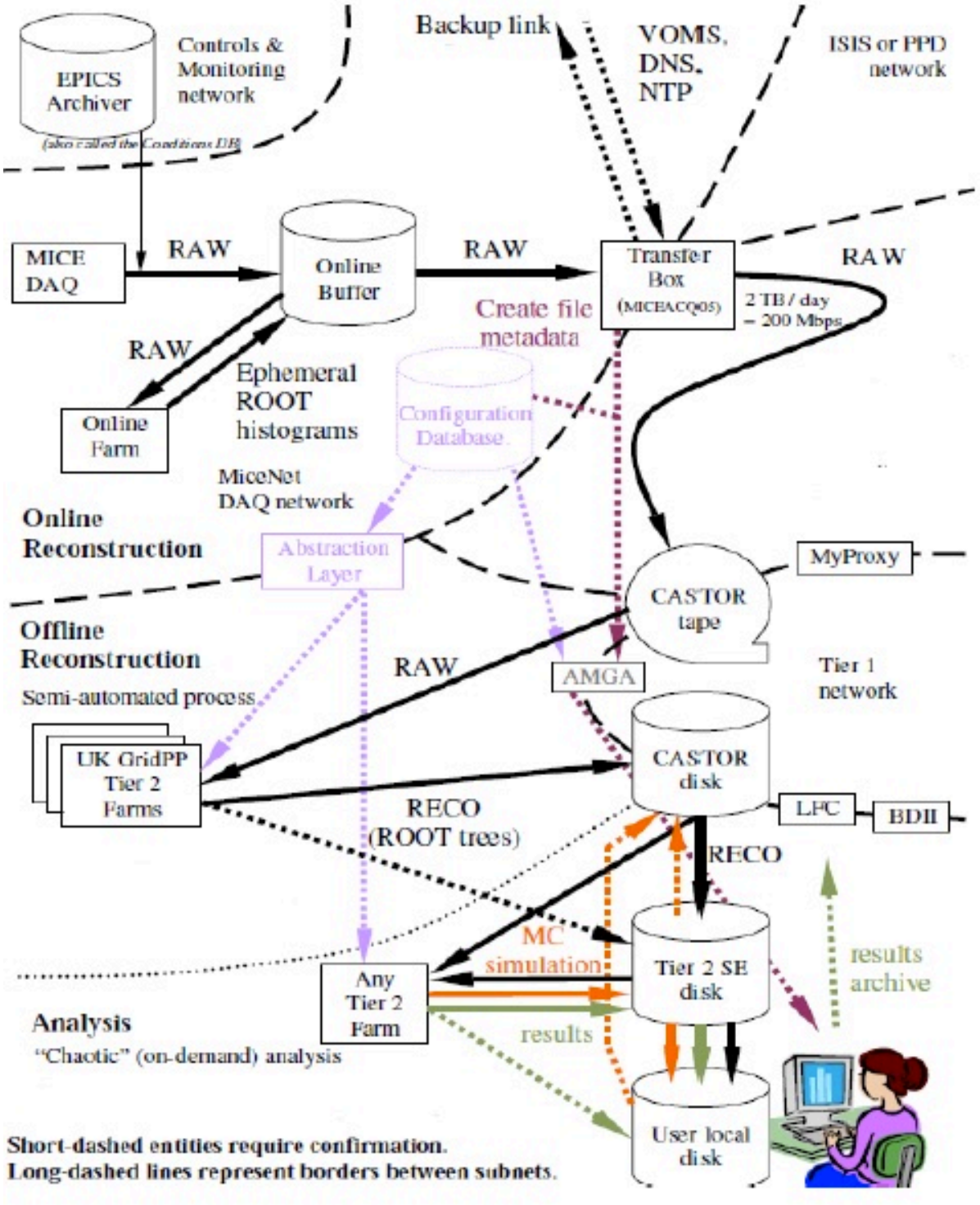

Figure 2.29: An analysis of the data flow of the MICE Experiment [87]. The area we are concerned with here relates to the configuration database and interface only. These are highlighted in purple. This diagram is included to illustrate that the database is integral to data flow in MICE, and that other systems exist to handle non-configuration data. Figure taken from Ref. [69].

settings, the CDB was developed [69; 88]. The CDB was written in mySQL and is a relational database. A relational database holds records as lists of (attribute, value) pairs of inhomogeneous type. The database exists as a web interface and can also be accessed via various Python scripts within MAUS. It currently maintains records on the Geometry, Calibration, Cabling, Set Values, Tagged Set Values and Alarm Handler Limits. A full diagram of the MICE data flow is shown in figure 2.29, illustrating the CDB's place in this flow. It exists as an interface between the online running of the experiment and the offline analysis. Configurations of beam line settings can be loaded at run time from the CDB during online running and are saved to the CDB so the events of the run can be reconstructed offline.

The CDB is described as 'bi-temporal'. Following information being written to the database it may be discovered that a detector was miscalibrated at the time of the run or that a component of the beam line was misaligned for a particular run. The correct information should be entered into the CDB if an anomaly is discovered, however the information that was known at the time should be kept. The correct information allows the data collected to be sensibly analysed and the original information establishes clear documentation of where an anomaly arose. Designing the CDB in this manner has the additional advantage that, as the experiment evolves, the geometry of previous configurations will have a set period of validity. The bi-temporal nature of the CDB reflects this.

2.5 Conclusions

A brief exposition of accelerator physics and its relation to the MICE experiment has been given. Specifically, the concepts of emittance and ionisation cooling have been introduced, which are central to the goals of the MICE experiment that seeks to demonstrate the reduction of the normalised emittance of a muon beam across the range of emittances and momenta likely to be seen by a muon beam at the neutrino factory. Starting from the definition of emittance and multiple Coulomb scattering the ionisation cooling formula has been derived. The MICE experimental setup has been explained with attention given to the Steps relevant to this thesis.

Chapter 3

Emittance measurement in MICE Step I beam line

In order to understand the analysis of any of the MICE data a complete set of Monte Carlo (MC) simulations are required. These simulations should accurately model the MICE beam line including its layout, the optics of the beam line magnets and the tracking and interactions of particles. MC should be available for all of the configurations in which MICE will take data. The tracking and reconstruction software were updated and validated with Step I data. This code had to be maintained and is now used for the generation of Monte Carlo events in MICE.

3.1 Geometry

Geometry files describing the MICE beam line in the various Steps can be downloaded using MAUS from the Configuration Database (CDB), which is described in Section 2.4.1. The CDB contains CAD accurate drawings of the beam line and software tools have been developed to convert these into a format that can be used by MAUS. An example of the Step IV GDML geometry from the CDB is shown in figure 3.1. This ensures that all of the details from the beam line engineers are included directly in the simulations and reconstruction of the experiment run for the offline analysis.

The upstream beam line is modelled in G4beamline, where upstream refers to the beam line from the pion production target to 1 m downstream of D2. The remaining beam line elements and cooling channel are simulated in MAUS. This was a conscious decision on the part of the developers as running end to end simulations would be highly inefficient. G4beamline simulates a muon beam generated by protons incident on a titanium target. Pions are generated in 4π with only a small fraction traveling down the beam pipe. As the beam travels along the MICE beam line, only particles within the momentum bite of the dipole magnets and focused by the

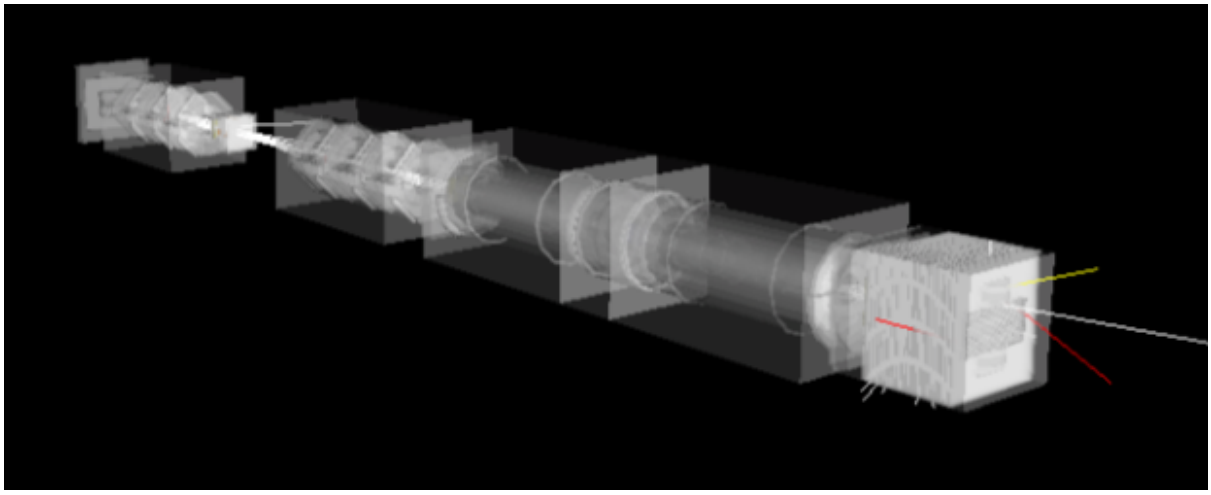

Figure 3.1: Visualiser view of MAUS gdml geometry created from CAD drawings, figure taken from Ref. [87].

quadrupole triplets are transported to the cooling channel. As a consequence, for 10^{15} protons on target only $\sim 10^5$ particles reach the downstream detectors (e.g. TOF1). The computational demands of running such simulations to generate output of statistical significance could not realistically be met with the computing resources available. For this reason, simulations from the target to D2 are produced by G4beamline and the output passed to MAUS. This division of labour allows a complete simulation of the beam line to be achieved on a realistic timescale.

The geometry describing the MICE beam line in G4beamline was original developed by Tom Roberts and Marco Apollonio, based on engineering drawings and surveys of the MICE hall [89]. As both G4beamline and MAUS are built on the GEANT4 software package, they build geometries in a similar manner by adding elements whether they be physical (blocks of lead, scintillator etc.) or fields (electromagnetic) into a world volume. However, unlike the MAUS geometry that converts CAD drawings to geometries, the G4beamline geometry must be built by hand and is referred to as a "deck". Updating this deck and making it compatible with the latest surveys is discussed in Section 3.2.1.

3.2 G4beamline

G4beamline is a software package created by Muons Inc. [90]. It was written in C++ and incorporates the GEANT4 and CLHEP libraries whilst providing a simple Java interface for the user. High statistics simulations of muon beams can be generated including situations involving muons interacting or decaying in matter.

3.2.1 Integration of G4beamline into MAUS

A number of G4beamline decks were in circulation in the MICE collaboration in 2012. These decks described the MICE beam line in various configurations. They were developed independently by MICE collaborators performing a variety of beam line studies. Some described the Step I beam line, others the final cooling demonstration configuration. In each case the beam line layout and optics was hard coded into the deck, providing ample opportunity for human error to arise. Furthermore, as the groups or persons were working on different aspects of the MICE beam line the decks continued to evolve separately, which could lead to separate analyses coming to contradictory conclusions. The solution was to incorporate all the known information about the Step I beam line into one deck, validate this deck with Step I data and then make it publicly available as a third party package in MAUS as the official MICE Step I deck.

To this end, a MAUS map module was written from which G4beamline can be run as a third-party software within MAUS allowing users to access the functionality of G4beamline. A MAUS map modifies a single Spill item [91], in this case generating MC events and appending them to an empty MAUS Spill object. Once the MC data has been generated with the G4beamline map, it is passed through the normal MAUS processing and treated like any other particle whether data or toy MC. The integration of the two software packages has a number of advantages.

Firstly, MAUS is maintained on Launchpad, a tool for multi-developer projects, easing version control and automating merges between various development branches. As G4beamline is now a third-party package of MAUS, it is brought under the same version-control scheme. The G4beamline deck published on Launchpad and validated with MICE Step I data became the official G4beamline deck. This prevents different analysis groups creating different MC samples to seed their MAUS simulations. When an individual makes changes to this deck, the nature and time of the changes are recorded. In the event that any discrepancies arise, the record can be checked and the changes identified.

Secondly, MAUS is installed on the Grid, the worldwide distributed computing service for particle physics [92]. Running G4beamline simulations of MICE requires large computer resources. On the local PPE batch system at Glasgow simulations take of order 48 hours to be completed. The Grid [93; 94] is a distributed computing network consisting of dozens of computing nodes around the world acting in concert. Large scale data processing can be run in parallel across the nodes allowing computationally demanding processes to be carried out quickly. MAUS is installed across all the Grid nodes for which MICE has permissions to run.

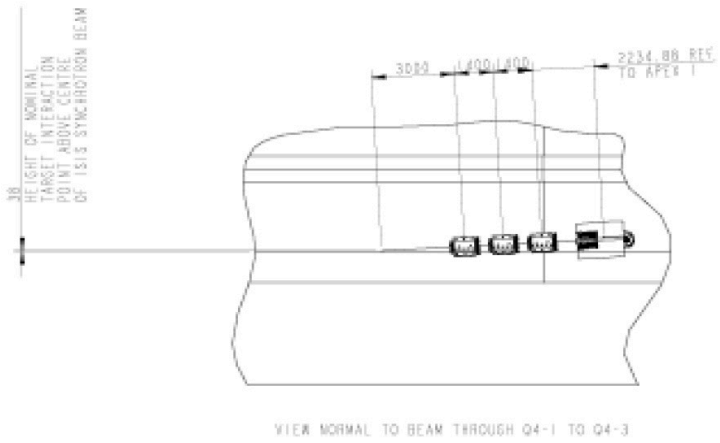

Figure 3.2: View normal to beam through first quadrupole triplet, figure taken from Ref. [89].

As G4beamline is now a third-party package within MAUS, large scale production jobs to build MC libraries with G4beamline can now be carried out on the Grid. As part of MAUS, G4beamline users can access these resources and this allows large scale MC production jobs to be run in a timely manner.

Furthermore, G4beamline can also take advantage of the MAUS tools for accessing the Configuration Database. MAUS users can select a particular MICE run and the map module will retrieve the magnet currents and proton absorber thickness for the run specified from the CDB. This reduces the human error in hard coding such information into the G4beamline configuration files.

3.2.2 Beam Parameters Modelled in G4beamline

To make the simulations compatible with data, the most up-to-date survey information on the Step I beam line was collected, as summarised in table 2.1. This information was used to update the layout of the beam line components and reflected the changed position of several detectors (TOFs and Cherenkov detectors) and more accurate surveys pertaining to the position of the dipole magnets.

Not only were the position of the beam line components in z amended to match these surveys but the vertical positions were also changed. In the original decks, the beam line is assumed to lie entirely within one $x - z$ plane. However consultation with previous surveys between the ISIS synchrotron and the MICE hall [89] show them to be at two different elevations, as can be seen in figure 3.2, with the target level with the ISIS beam line and the DS and downstream beam line at $+42.7\,\text{cm}$. The beam line components rise in y position in increments between the target station and the DS after which point the beam line is in the MICE hall and

all downstream components are at a single elevation. This interplay between the beam line optics and the change in elevation affects the size and dispersion of the downstream beam, which necessarily must be modelled in simulation to give good agreement with MICE data. Therefore, the G4beamline deck which has become the official MICE deck included this additional information.

In addition to changing the layout of the beam line, the composition of some of the beam line components in the simulation was changed to more accurately model the physical MICE beam line. The proton absorber, described in Section 2.3.4, consists of several sheets of borated polyethylene, which can be inserted into the beam line in various configurations. It removes protons in positive MICE muon beams that would otherwise contaminate the downstream sample. In previous versions of the deck, this was defined as blocks of pure polyethylene and in others entirely absent. In the deck incorporated in MAUS the material definitions were updated to reflect the absorbers' known composition [95] and the code developed to allow users to run with or without the absorber.

Earlier iterations of the deck also included a variety of cuts on the particles tracked from the target into the first quadrupole triplet. The number of particles in the beam line is greatest immediately downstream of the target of which only a small number will be transported down to the cooling channel. Therefore, the intention was to cut out particles which were unlikely to be transported and save on the computing time required to complete simulations. However these cuts also changed the downstream beam parameters and complicated the comparison between MC and data. Consequently these cuts were removed in the official deck.

In addition to improving the agreement between MC and data, several tools were developed to aid the process of optimising the beam line optics. Figures showing the horizontal RMS beam size and beta function as a function of position along the MICE beam line are presented in figures 3.3 and 3.4. Similar plots for the vertical RMS beam size and beta function are shown in figures 3.5 and 3.6. The mean beam position in x and y are shown in figures 3.7 and 3.8 respectively. Finally, the mean energy and number of particles in the beam is shown in figures 3.9 and 3.10.

The discontinuities in plots 3.3, 3.4, 3.5 and 3.6 are clearly aligned with the apertures of the beam line magnets Q4 and Q7. Figure 3.9 shows that a substantial fraction of the beam particles are killed at these discontinuities as they are incident on the iron of these magnets. This behaviour is due to the beam not being sufficiently focused by the optical set up and the result is scraping of the beam along the beam line elements. Figure 3.7 shows that the beam is

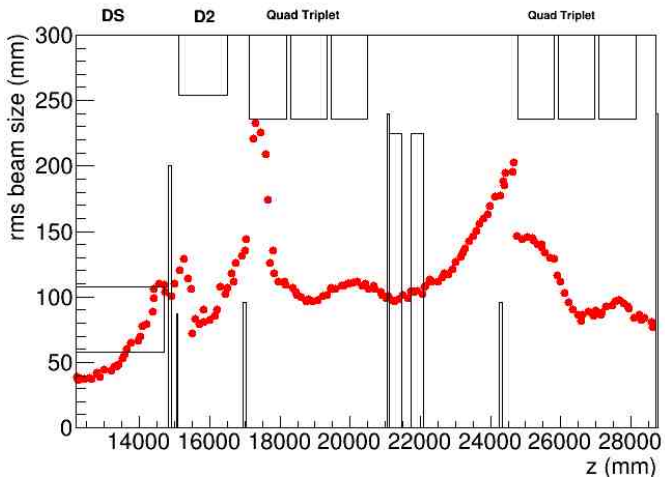

Figure 3.3: Horizontal RMS beam size as a function of position along the MICE beam line, 6π mm· rad, 200 MeV/c μ^+ beam. The boxes in along the beam line represent the various particle identification detectors.

clearly off-centre after passing through D2. This suggests that the beam is being understeered by D2, which could be the cause of scraping at Q4. The energy loss shown in figure 3.10 can be used as a cross-check that components are placed correctly in the G4beamline geometry and that the material behaviour is consistent with expectation.

These tools also make clear which beam line elements are responsible for the beam loss. Efforts are being made to produce beam line settings which result in a matched beam in the upstream spectrometer solenoid. To date, this has involved a study with a simple beam optics software package Trace3D [96]. When these current configurations are ready they can be tested and refined with the aid of these tools. Furthermore by comparing figure 3.4 with figure 3.3, it can be determined whether the scraping is due to dispersion or due to the betatron function of the beam envelope.

3.3 Grid Services

The task of job submission to the Grid is handled by the middleware package Ganga [97]. The Grid connects many disparate computing resources around the globe for the purpose of high energy physics. Ganga has been developed as a way of bridging between different processing systems providing a single command set. The project can be viewed as a homogeneous environment for processing data on heterogeneous resources, as summarised in figure 3.11. The Ganga API allows for the specification, submission, bookkeeping and post-processing of computational tasks on a wide set of distributed resources, with the front end presented in user-friendly python. The functionality exists to run jobs on the local system for debugging and

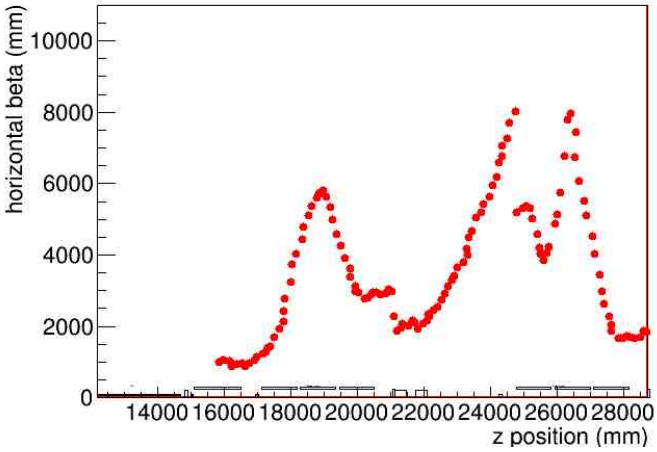

Figure 3.4: Horizontal β function of beam as a function of position along MICE beam line, 6π mm· rad, 200 MeV/c μ^+ beam.

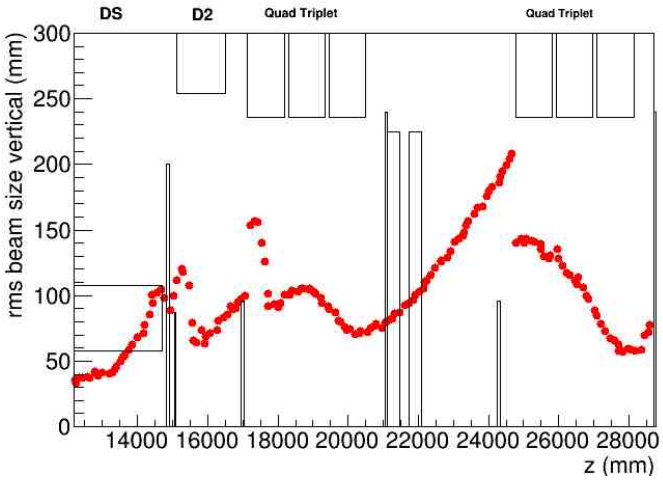

Figure 3.5: Vertical RMS beam size as a function of position along the MICE beam line, 6π mm· rad, 200 MeV/c μ^+ beam. The boxes in along the beam line represent the various particle identification detectors.

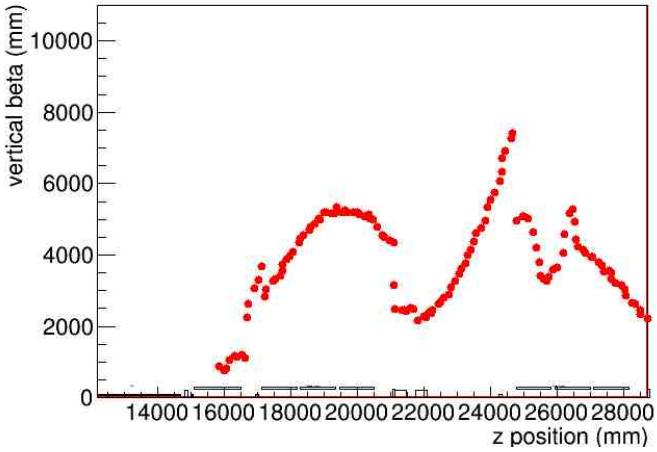

Figure 3.6: Vertical β function of beam as a function of position along MICE beam line, 6π mm· rad, 200 MeV/c μ^+ beam.

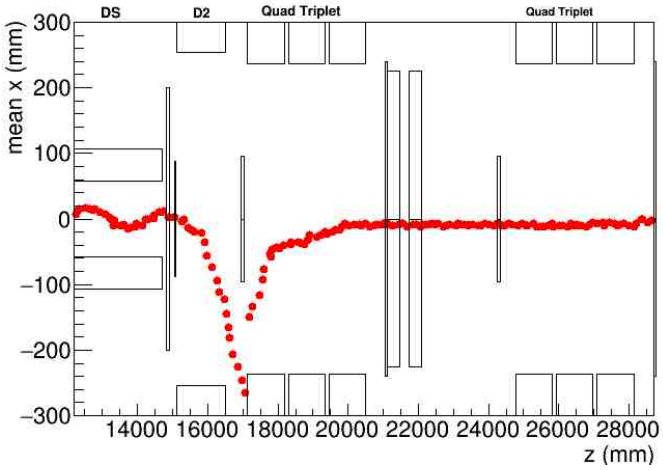

Figure 3.7: Vertical beam position as a function of position along the MICE beam line, 6π mm· rad, 200 MeV/c μ^+ beam. The boxes in along the beam line represent the various particle identification detectors.

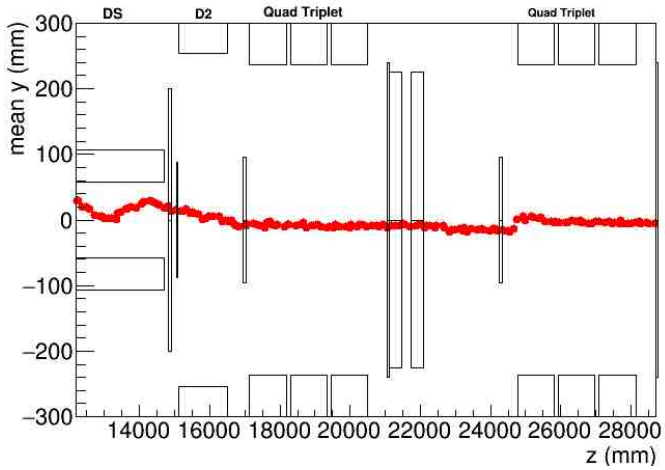

Figure 3.8: Horizontal beam position as a function of beam as a function of position along MICE beam line, 6π mm· rad, 200 MeV/c μ^+ beam. The boxes in along the beam line represent the various particle identification detectors.

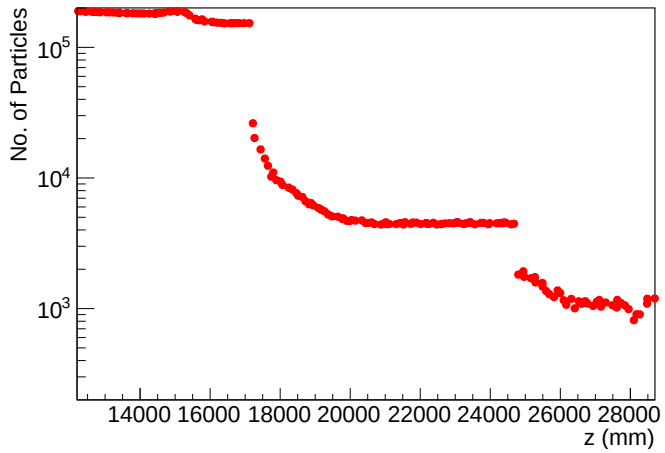

Figure 3.9: Number of particles in beam as a function of position along the MICE beam line, 6π mm· rad, 200 MeV/c μ^+ beam.

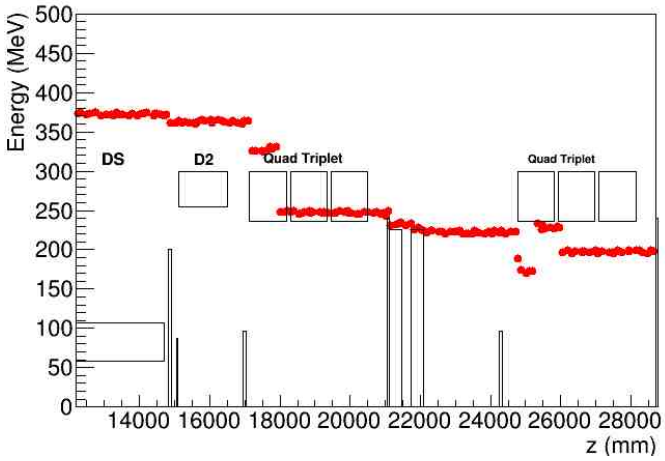

Figure 3.10: Mean energy of particles as a function of beam as a function of position along MICE beam line, 6π mm· rad, 200 MeV/c μ^+ beam. The boxes in along the beam line represent the various particle identification detectors.

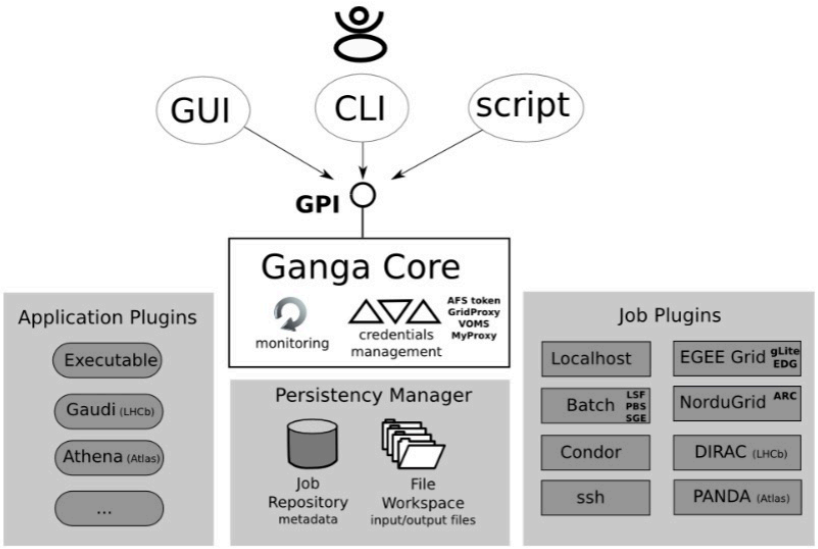

Figure 3.11: The overall architecture of Ganga. The user interacts with the Ganga Public Interface (GPI) via the Graphical User Interface (GUI), the Command-Line Interface in Python (CLIP), or scripts. Plugins are provided for different application types and backends. All jobs are stored in the repository. Figure taken from Ref. [97].

then seamlessly switch to submitting on the wider Grid system for large scale jobs. A number of scripts were prepared, tailored to MAUS' needs on the Grid and to run MAUS jobs with Grid resources. This included the functionality to easily collect output of G4beamline jobs run through MAUS to seed downstream simulations. These resources were made publicly available so any MAUS user could run G4beamline via the Grid.

3.4 G4beamline and MAUS Beam Library

As described in Section 2.4, MAUS uses the output from G4beamline as input. With MAUS installed on the Grid and G4beamline integrated into MAUS as a third party software, large scale MC jobs can be run. A number of jobs were required in order to generate beams with each of the beam line settings for which MICE will take data. The input MC generated in this exercise formed a "beam library". Users can access the files on the Glasgow Grid Storage Element (SE) and use the G4beamline MC to seed their MAUS jobs. This MC was used in a variety of Step I and IV analyses.

The files on the Glasgow SE consist of JSON documents of particles that can be used to seed downstream simulation in MAUS. JSON documents are one of the data storage formats of MAUS. It is an ascii format which maps the spill structure of the MICE data, where the top level is its spill with each spill containing a number of particles and each particle having a number of parameters describing it position, momentum etc. All of these JSON documents have an address associated with them describing where they are stored on the Grid. For every Grid job with MAUS the addresses of the output were collected and stored in a text file. This text file is one item in the beam library, where each item of the beam library lists the locations of all of the SE files associated with one beam line setting and the entire library is located on a MICE web server.

A user performing an analysis would run the MAUS MC script, which will pull the files from the SE at the addresses fed to it by the beam library file. This allows any MAUS user requiring a MC beam to seed their downstream simulations in MAUS to pull a beam from the pre-generated beam library. As previously discussed in Section 3.2, this is essential as the computing and temporal requirements of running end to end simulations are vast. However the upstream beam line is unlikely to change so, by having a sample of seed distributions already generated, numerous downstream simulations can be run without requiring the simulation to start at the pion production target.

3.5 Emittance measurement in MICE Step I beam line

In 2010, data was taken with MICE in its Step I configuration. For this Step I data, a novel technique to measure the emittance of the beam was developed using the TOF detectors [64], as the trackers had not yet been installed in the MICE hall. In a conventional setup, the emittance of a beam would be measured with three beam monitors at different positions. With all of the elements of the covariance matrix in hand, the beam emittance can be calculated. In this novel technique, the spatial coordinates of individual particles are measured at two detectors for which the transfer matrix is known. This technique is possible because the MICE beam is large in spatial extent and low in intensity compared with conventional beams. As part of this analysis, the MICE muon beam was characterised more generally by inspection of its Twiss parameters and beam profile.

The G4beamline simulations by Apollonio et. al. [98] showed circular symmetric profiles for the beam at TOF1. However data showed a clear asymmetry in the xy-profile of the beam at TOF1, as can be seen in figure 3.12. The previous set of G4beamline simulations were based on an unvalidated geometry with the magnet currents tuned for that geometry. At the time of Step I running, the CDB had not yet been fully implemented, hence could not be used to validate the simulated configuration. It is clear that the origin of the asymmetry in the beam line is due to the magnet currents not being correctly optimised (see Section 3.2.2).

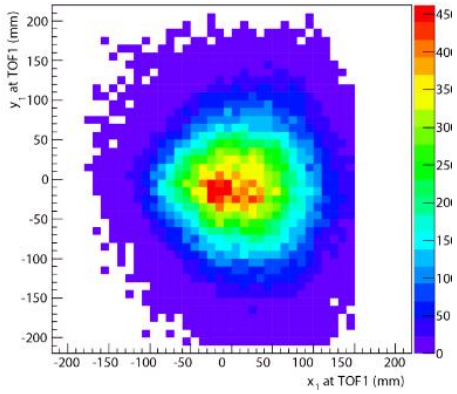

Figure 3.12: Data xy-distribution at TOF1 6π mm· rad, 200 MeV/c μ^+ beam. The left most bar in the TOF detector was uncalibrated during this run which is why this area is unpopulated. (figure taken from Ref. [98])

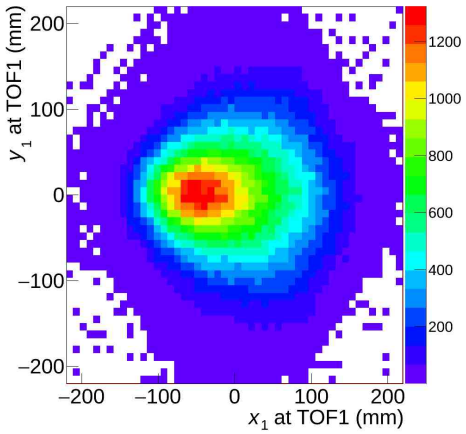

Figure 3.13: Updated G4BL xy-distribution at TOF1 6π mm· rad, 200 MeV/c μ^+ beam.

The geometry configuration used in this analysis incorporated all of the updates discussed in Section 3.2 and the beam line settings were taken directly from the run conditions spreadsheet. The beam line settings used for running MICE were calculated with Decay-TURTLE [99]. This

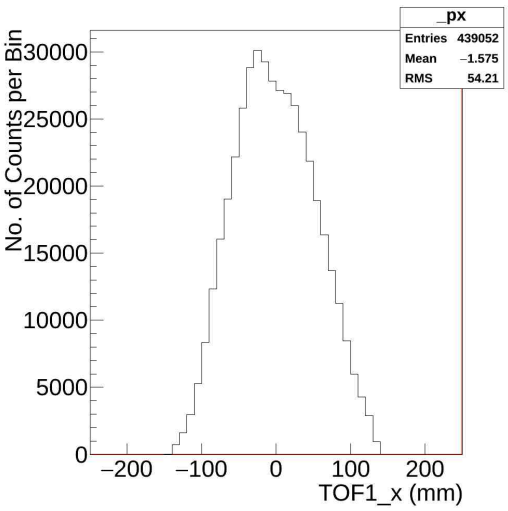

Figure 3.14: Data x-projection at TOF1 6π mm· rad, 200 MeV/c μ^+ beam.

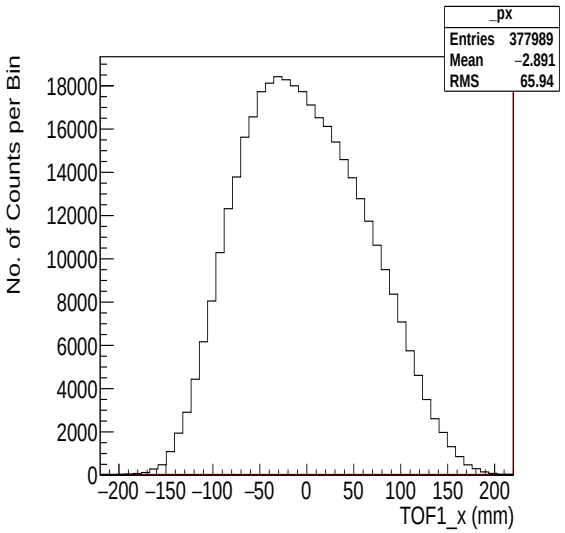

Figure 3.15: G4BL x-projection at TOF1 6π mm· rad, 200 MeV/c μ^+ beam.

beam optics program gives first order estimates of the required currents with further refinement done in G4beamline, further details can be found in Section 2.3.3. A comparison of the beam profiles (figures 3.13 and 3.12) and projections (figures 3.15 & 3.14) for data and MC from the updated simulation show good agreement.

Using this updated deck, G4beamline simulations were run tracking particles from the target to TOF0. From TOF0 to TOF1 the particles were propagated with G4MICE , the predecessor to MAUS which performed a similar function. The output was analysed in ROOT and compared to Step I data. A number of parameters were of interest in this study including the dispersion of the beam η (figure 3.18), the RMS beam size σ (figures 3.19, 3.20), the beta function of the beam β (figures 3.21, 3.22), and the normalised emittance of the beam ϵ_n (figures 3.23, 3.24).

3.5.1 Emittance Measurement Technique

A summary of how the beam parameters were measured will be given following [64]. An initial p_z is hypothesised for each muon between TOF0 and TOF1. From this estimate, the transfer matrices $M_x(p_z)$ and $M_y(p_z)$ are calculated between the time of flight detectors. The TOF detectors give a measurement of the position of hits (x_0, y_0) and (x_1, y_1). With knowledge of the transfer matrices, the trace-space vectors, (x_0, x_0') and (y_0, y_0'), and (x_1, x_1') and (y_1, y_1') can be determined by rearrangement of the transport equation:

$$\begin{pmatrix} x_1 \\ x_1' \end{pmatrix} = M_x \begin{pmatrix} x_0 \\ x_0' \end{pmatrix}, \tag{3.1}$$

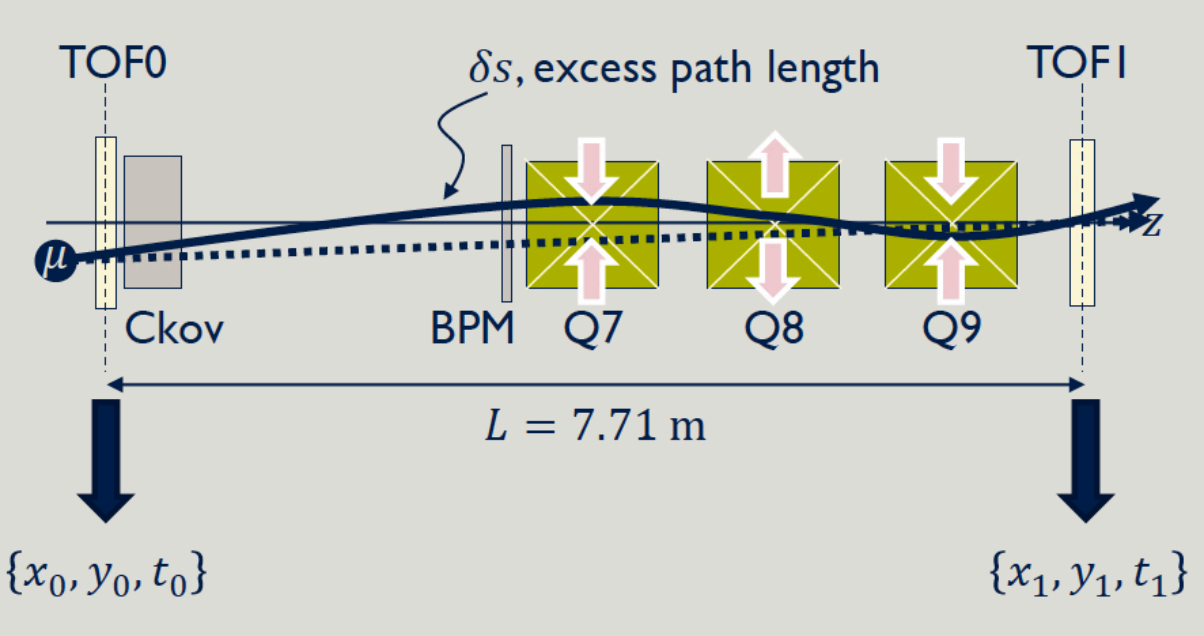

Figure 3.16: The beam parameters are measured by tracking the muons between the two time of flight detectors in the MICE beam line. The technique described in the text predicts the optical behaviour through the quadrupole triplet accounting for the additional path length and multiple scattering off air. Figure taken from Ref. [100].

with

$$M_x = \begin{pmatrix} M_{11}^x & M_{12}^x \\ M_{21}^x & M_{22}^x \end{pmatrix} \tag{3.2}$$

giving

$$\begin{pmatrix} x_0' \\ x_1' \end{pmatrix} = \frac{1}{M_{12}^x} \begin{pmatrix} -M_{11}^x & 1 \\ -1 & M_{22}^x \end{pmatrix} \begin{pmatrix} x_0 \\ x_1 \end{pmatrix}. \tag{3.3}$$

A similar expression can be derived for (y_0', y_1').

$$\begin{pmatrix} y_1 \\ y_1' \end{pmatrix} = M_y \begin{pmatrix} y_0 \\ y_0' \end{pmatrix}, \tag{3.4}$$

with

$$M_y = \begin{pmatrix} M_{11}^y & M_{12}^y \\ M_{21}^y & M_{22}^y \end{pmatrix} \tag{3.5}$$

giving

$$\begin{pmatrix} y_0' \\ y_1' \end{pmatrix} = \frac{1}{M_{12}^y} \begin{pmatrix} -M_{11}^y & 1 \\ -1 & M_{22}^y \end{pmatrix} \begin{pmatrix} y_0 \\ y_1 \end{pmatrix}. \tag{3.6}$$

Muons are then tracked between TOF0 and TOF1 based on the estimated trace-space vectors with a correction added to account for path length, Δs. The algorithm is iterative, proceeding until a stable solution is found for each muon. Additional corrections for energy loss in the air between the detectors are also applied (≈ 1.5 MeV/c).

In order to determine the transfer matrices, the field generated by the final quadrupole triplet must be taken into account. The fields are described by an OPERA [101] field model fitted with two hyperbolic tangent functions. Therefore the expression for x_1' required to determine the horizontal emittance at TOF1 can be expressed as

$$x_1' = A(p_z)x_0 + B(p_z)x_1, \tag{3.7}$$

where

$$\begin{aligned} A_x &= -1/M_{12}^x \\ B_y &= M_{22}^x/M_{12}^x \end{aligned} \tag{3.8}$$

with the coefficients $A(p_z)$ and $B(p_z)$ [102] for a 6π mm· rad, 200 MeV/c beam shown in figure 3.17. The coefficients are momentum dependent and change rapidly below 200 MeV/c. The y_1' variable can be similarly determined. With this in hand, the trace space vectors at both TOF counters, as well as the momentum for each individual muon, can be determined. The path length correction is essential to avoid a systematic underestimation of p_z of around 4 MeV/c. With the trace space vectors and momentum measurement, the covariance matrix, $\Sigma_{x,y}$ can be calculated and from this the optical parameters of the beam can be extracted.

A number of optical parameters characterise the beam, namely:

$$\begin{aligned} \varepsilon_x &= \sqrt{\text{det}\Sigma_x} \\ \beta_x &= \frac{\Sigma_{11}}{\varepsilon_x} \\ \sigma_x &= -\frac{\Sigma_{12}}{\varepsilon_x} \end{aligned} \tag{3.9}$$

which can be similarly defined for y. The parameters σ and β are momentum dependent and given the large spread in momentum in the MICE beam, these parameters are effective parameters which describe the distribution in phase space in the context of MICE. The TOF detectors in the hall, unlike in simulation, have a finite spatial and angular resolution leading to a small increase in the apparent emittance of the beam. Acting in the opposite manner, the

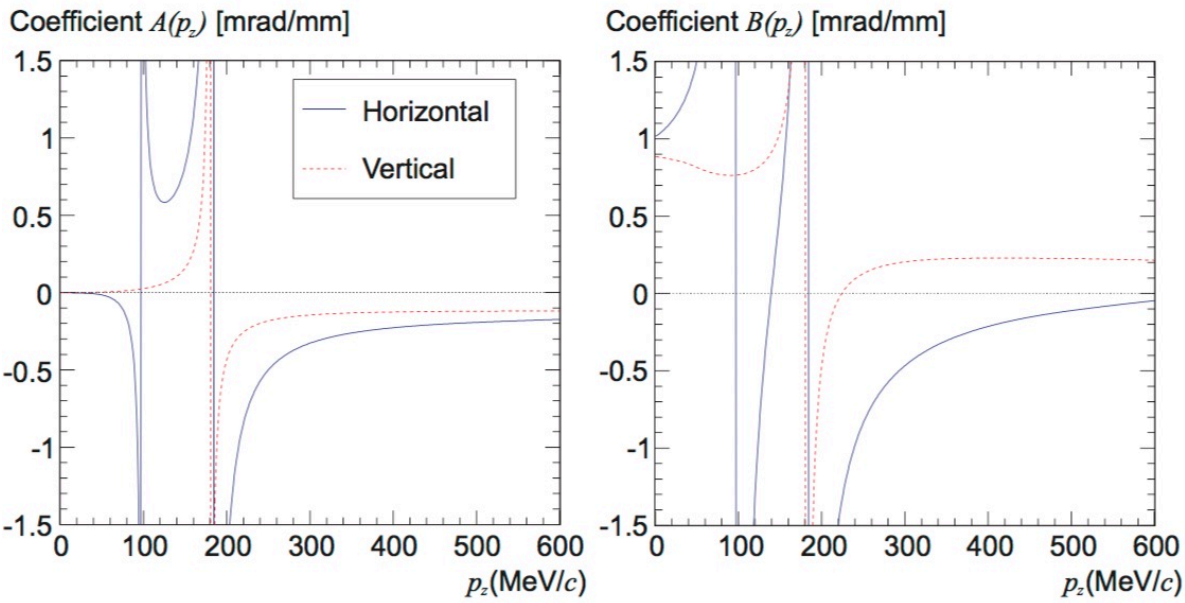

Figure 3.17: The reconstruction coefficients A(p_z) (top) and B(p_z) (bottom) for the 6π mm·rad, 200 MeV/c baseline muon beam. The solid (blue) lines are for x (horizontal); the dashed (red) lines are for y (vertical). Figure taken from Ref. [64].

multiple scattering off air between the two TOF detectors will lead to an underestimate of the emittance. It is therefore necessary to include a small correction in the determination of the covariance matrices to compensate for the effects of resolution and scattering. This is done by means of a resolution matrix which is determined by running the simulation and taking the difference between the reconstructed and truth values for the covariance matrix. This can be stated as:

$$\Sigma_{\text{Corrected}} = \Sigma_{\text{Measured}} - (\Sigma_{\text{Reco-sim}} - \Sigma_{\text{True-sim}}) \tag{3.10}$$

After this correction has been applied, the calculated emittance shows a small reduction in the horizontal plane with the final result shown in figure 3.23. The converse is true for the vertical plane, with the correction increasing the emittance, figure 3.24. This is due to the final quadrupole triplet defocusing in the vertical plane resulting in clipping of the beam through these magnets. Additional corrections to account for the natural dispersion in the MICE beam due to D2 were also included. To extract the intrinsic horizontal emittance of the beam from the measured covariance matrix, the dispersion characterised by η and η' is subtracted [103]:

$$\begin{aligned} \Sigma_{11} &\rightarrow \Sigma_{11} - \eta^2\delta^2 \\ \Sigma_{12} &\rightarrow \Sigma_{12} - \eta\eta'\delta^2 \\ \Sigma_{11} &\rightarrow \Sigma_{11} - \eta'^2\delta^2 \end{aligned} \tag{3.11}$$

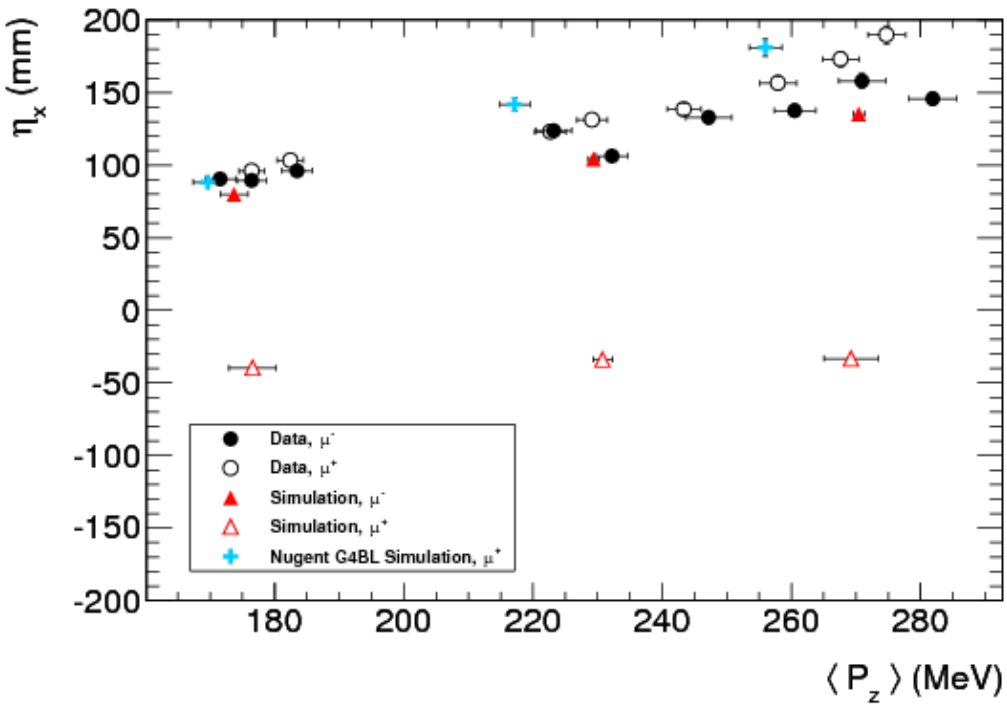

Figure 3.18: Horizontal Beam dispersion 6π mm· rad, 200 MeV/c μ^+ beam.

where $\eta = [x\delta]/[\delta^2]$, $\eta' = [x'\delta]/[\delta^2]$ and $\delta = (p_z - \bar{p}_z)/\bar{p}_z$.

3.5.2 Simulation Validation

While previous iterations of the simulations predicted that the MICE muon beam had a negative dispersion, an unphysical prediction, the new simulations predicted a positive dispersion. Not only is the value positive but it is also in agreement with the data. Whilst the improvement in the predicted value of η is a substantial improvement on previous simulations, the new simulations maintain the accuracy of the old simulations in predicting the other beam parameters in all cases bar one, the case of the beam vertical beta. Figure 3.22 shows the new value is slightly worse, possibly due to the roll around the z-axis not being included in the simulated position of the first dipole magnet. As shown, the predicted value of each of these parameters for all the beams simulated, 6π mm· rad, 140 MeV/c, 6π mm· rad, 200 MeV/c and 6π mm· rad, 240 MeV/c, are in good agreement with the measured values (figures 3.19, 3.20, 3.21, 3.18, 3.23 and 3.24). In each case, the updated simulations are shown in blue with the previous simulation shown in hollow red triangles. This served as a fitting validation of the new simulations demonstrating that they were capable of matching, and in some cases improving, upon the accuracy of the previous batch of simulations.

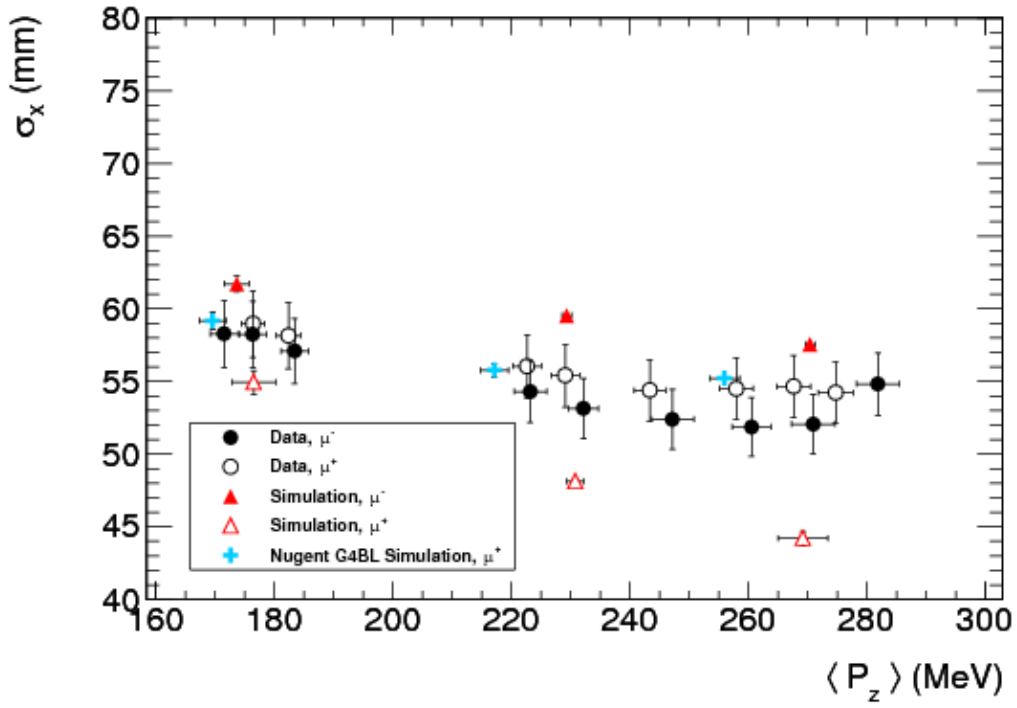

Figure 3.19: Horizontal σ at TOF1 6π mm· rad, 200 MeV/c μ^+ beam.

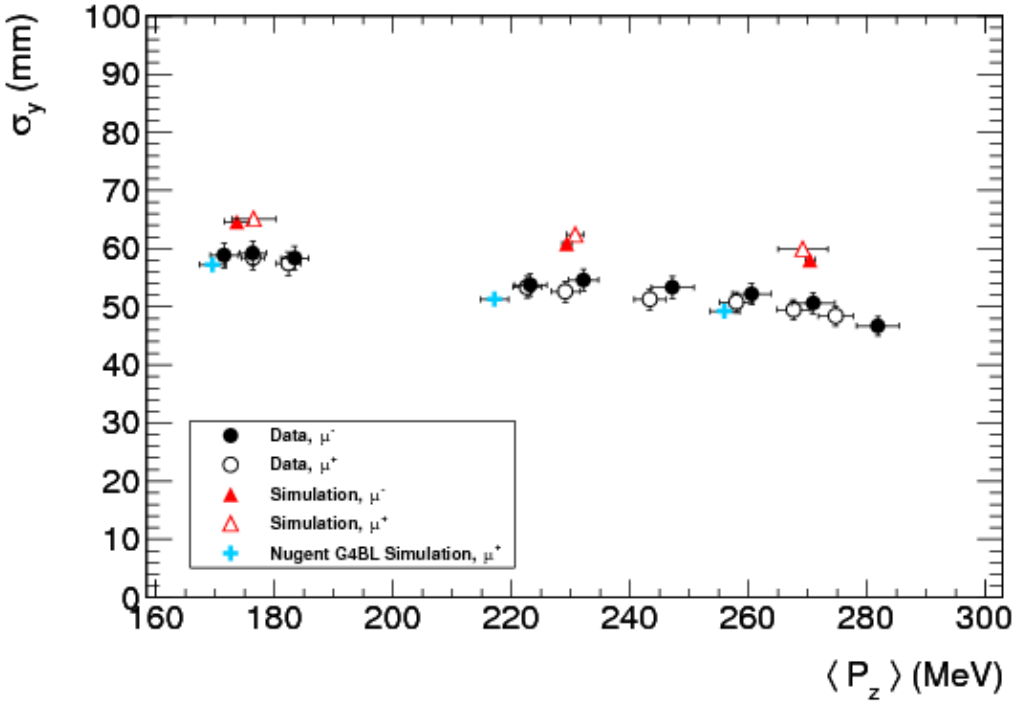

Figure 3.20: Vertical σ at TOF1 6π mm· rad, 200 MeV/c μ^+ beam.

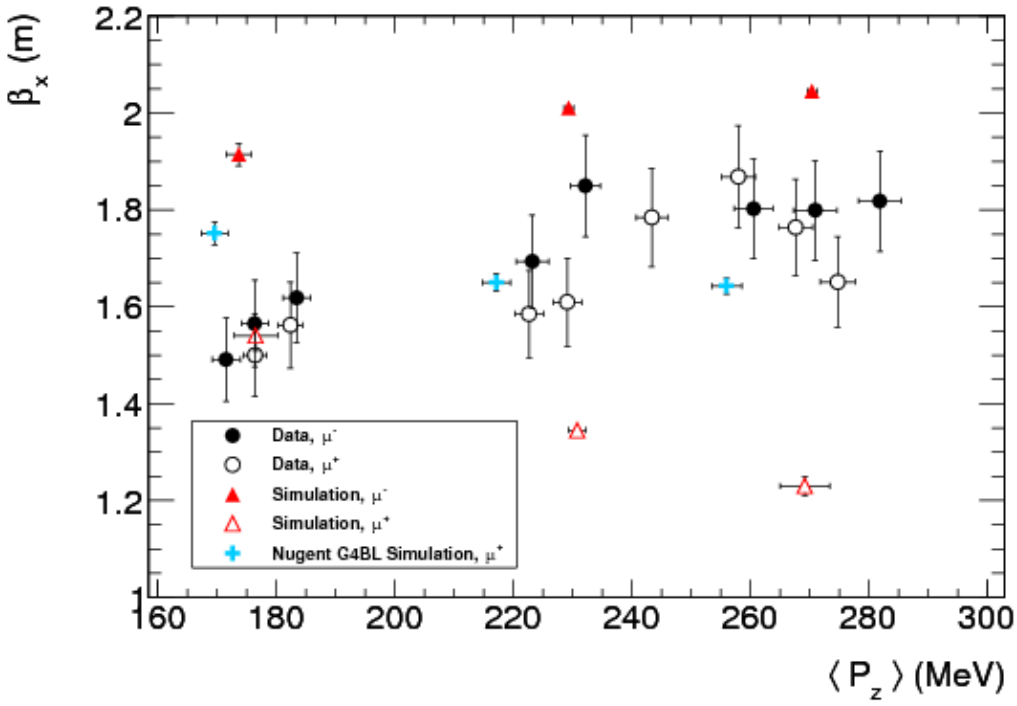

Figure 3.21: Horizontal β at TOF1 6π mm· rad, 200 MeV/c μ^+ beam.

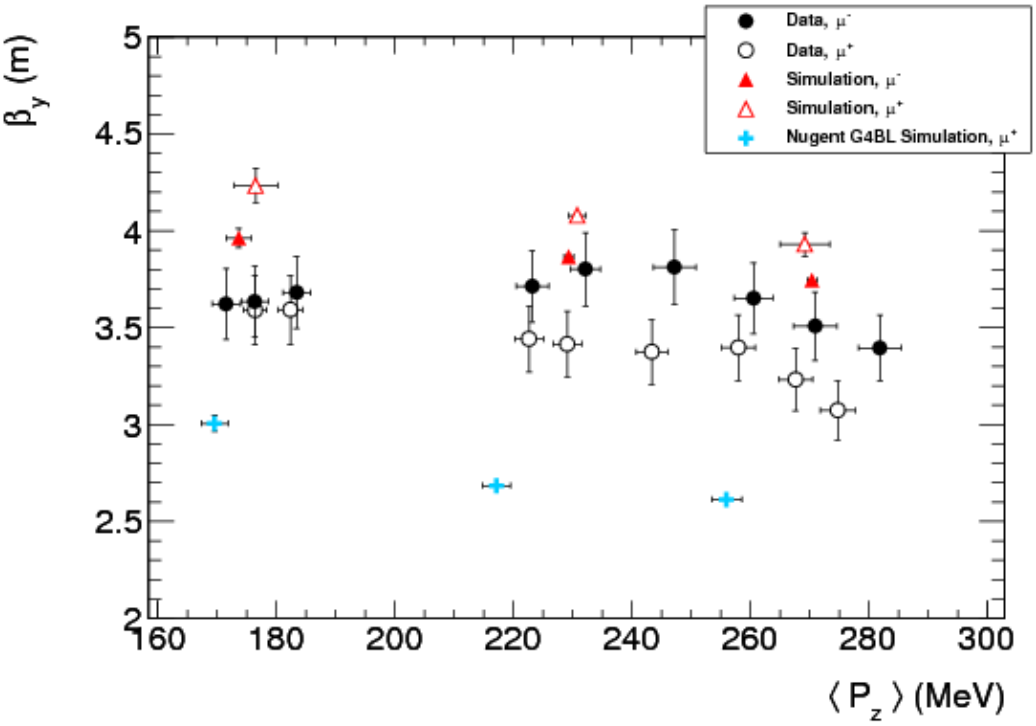

Figure 3.22: Vertical β at TOF1 6π mm· rad, 200 MeV/c μ^+ beam.

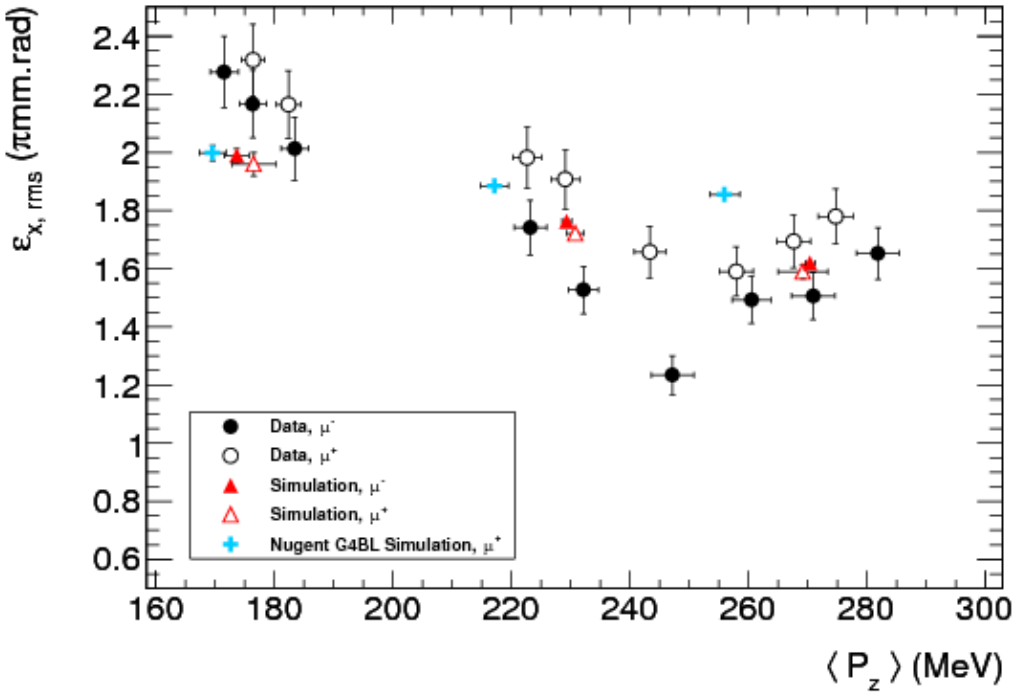

Figure 3.23: Horizontal emittance at TOF1 6π mm· rad, 200 MeV/c μ^+ beam.

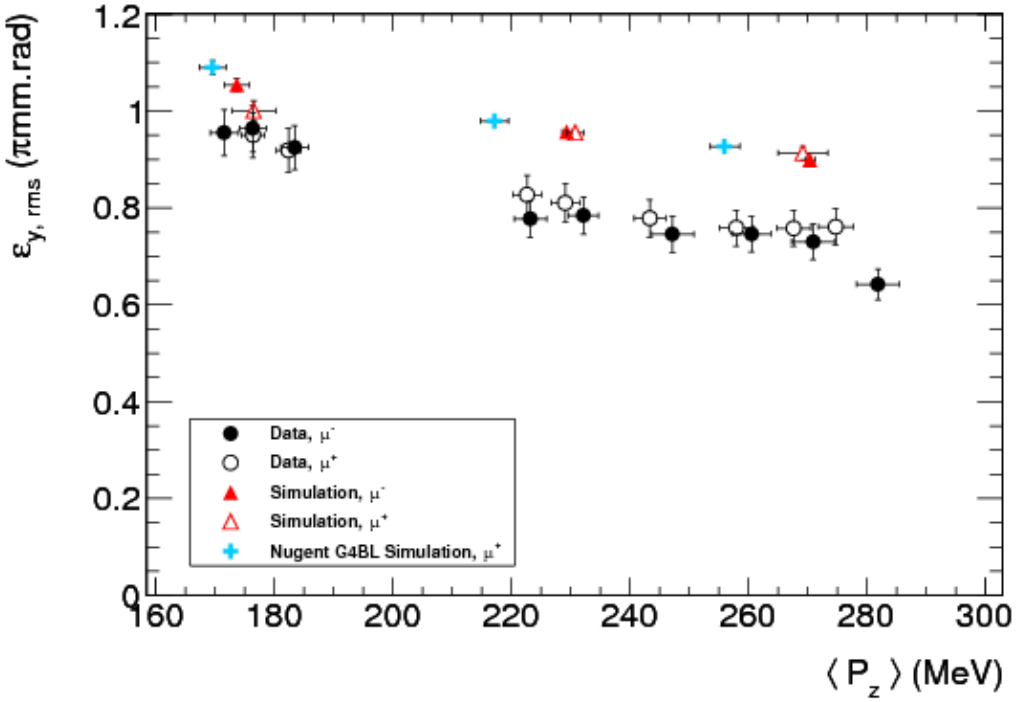

Figure 3.24: Vertical emittance at TOF1 6π mm· rad, 200 MeV/c μ^+ beam.

3.6 Conclusions

With the G4beamline deck validated with Step I data, a beam library has been built. As stated in Section 2.4, responsibility for simulating different sections of the MICE beam line is divided into two separate stages. This is done as the MICE beam line is designed to be highly selective and only particles within a narrow momentum range are selected. To complete all simulations within the times scale of MICE, simulations from the target to 1 m downstream of D2 are performed in G4beamline and from this point onwards is the remit of MAUS. The components upstream of the interface point are unlikely to be moved or modified, so once a set of simulations has been run this can be safely used as a seed for all downstream simulations in MAUS with the validation showing good agreement between the updated simulations and Step I data.

Chapter 4

Measurement of the pion contamination in the MICE beam

The MICE experiment will perform a systematic investigation of ionisation cooling with muon beams of momentum between 140 and 240 MeV/c. The measurement of ionisation cooling in MICE relies on the selection of a pure sample of muons that traverse the experiment. To make this selection, the MICE Muon Beam is designed to deliver a beam of muons with less than $\sim$1% contamination. To make the final muon selection, MICE employs a particle-identification (PID) system upstream and downstream of the cooling cell. The PID system includes time-of-flight hodoscopes, threshold-Cherenkov counters and calorimetry. This chapter describes a measurement of the pion contamination in the MICE Muon Beam using the TOF and KL detectors, which led to a MICE publication [63].

4.1 Introduction

The MICE experiment will demonstrate the principle of ionisation cooling as a technique for reducing the phase-space volume occupied by a muon beam. In the final cooling demonstration three lithium hydride (LiH) absorbers, two radio-frequency (RF) cavities and two Focus Coil solenoid magnets will be used to reduce the transverse emittance of the muon beam by up to 8%, depending on the beam configuration [104]. The goal of MICE is to measure the transverse normalised emittance before and after the cooling channel with an accuracy of 0.1%. Any unidentified contamination in the muon beam from pions and electrons can affect the accuracy of the measurement of the muon-beam emittance. Electrons are identified using the time-of-flight (TOF) system [105] and the Electron–Muon Ranger (EMR) detector [106; 65] after the cooling channel. Pions in the beam are also identified by the TOF system, the two aerogel Cherenkov detectors [107], the KL detector [76] and the EMR. In order to achieve 0.1% accuracy in the emittance measurement, it is essential that the muon sample selected in the beam

has a pion contamination below $\sim$1%.

The particle identification should achieve a pion rejection factor between 10 and 100, so a pion contamination in the beam of $\sim$ 1% should reduce the misidentified pion contamination in the muon sample to less than 0.1%, required to achieve the physics goals. The pion contamination of the MICE Muon Beam was measured in dedicated data-taking runs in order to qualify the muon beam and to ensure that MICE can achieve its stated physics goals [68; 64]. This analysis will be presented in this chapter

For a muon beam entering the cooling channel with a nominal momentum of 200 MeV/c and 4D normalised emittance $\epsilon_N = 5.8\pi$ mm $\cdot$ rad, a 6% cooling effect is expected [66]. Conventional emittance-measurement techniques based on beam-profile monitors cannot achieve the required precision, so MICE has been designed as a single-particle experiment, in which each muon is measured using state-of-the-art particle detectors and the bunched muon-beam is reconstructed offline [64].

The MICE instrumentation includes a PID system that allows a pure muon beam to be selected. In this thesis, however, the pion contamination of the MICE Muon Beam is measured on a statistical basis using data taken before the MICE tracking spectrometers and the EMR were installed. The analysis is accomplished by combining the TOF (Section 2.3.6.2) velocity information with the KL (Section 2.3.6.3) calorimetric information.

4.2 MICE Muon Beam

The required transverse emittance range of the MICE muon beam is $3 \leq \epsilon_N \leq 10\pi$ mm $\cdot$ rad, with mean momenta $140 \leq p_\mu \leq 240$ MeV/c and root-mean-squared (RMS) momentum widths of $\sim$ 20 MeV/c. The diffuser placed at the entrance to the upstream spectrometer solenoid blows up the beam and generates the required range of emittance in the beam. In order to perform the muon-emittance measurement with the required accuracy of 0.1% it is essential to limit the pion and electron contamination of the muon sample to less than 0.1%. This is achieved by designing a muon beam with $\sim$1% contamination and then by using the PID system to further identify electrons and pions passing through.

The design of the MICE Muon Beam is briefly summarised here and is reported in detail in chapter 2. By capturing pions of transverse momentum up to $\sim$70 MeV/c, and increasing their path length by deflecting them onto helical trajectories, the decay solenoid increases the

probability of muon capture between D1 and D2 by an order of magnitude compared to a simple quadrupole channel.

The composition and momentum spectra of the beams delivered to MICE are determined by the interplay between the two bending magnets D1 and D2. In normal ("$\pi \rightarrow \mu$ mode" or "muon") operation, D2 is set to half the momentum of D1, selecting backward-going muons in the pion rest frame and producing an almost pure muon beam. Pions of high momentum that do not decay may be present in the beam and it is this small contamination that is the focus of the measurement presented in this chapter. In the absence of a precise momentum measurement from the spectrometer, single-particle pion identification is not possible, since the particle mass cannot be obtained by combining the momentum with the velocity obtained from either the TOF or Cherenkov detectors. Therefore, the measurement has been performed on a statistical basis using the KL and TOF information. In Step IV, global particle identification is performed using the complete suite of MICE PID detectors to produce log-likelihoods of particle type. Alternatively, by setting $p_{D1} \simeq p_{D2}$, a mixed beam containing pions, muons and electrons is obtained. This "calibration mode" is used to calibrate the particle identification detectors and is used in the analysis to provide "templates" for the particle-identification performance of the KL and TOF detectors to be determined.

The nominal values of the beam momenta, p_μ, are those evaluated at the centre of the central LiH absorber when MICE is in its final cooling demonstration phase, taking into account the energy lost by the particles along the muon beam in the TOF and Cherenkov detectors, the proton absorber (for positive polarity beams), the diffuser and the air along the particle trajectories. For example, a momentum at D2, $p_{D2} = 238\,\text{MeV}/c$, implies a momentum value $p_\mu = 200\,\text{MeV}/c$ at the centre of the central absorber.

Data were taken in December 2011 with MICE in its Step I configuration as described in Section 2.3.1, including the upstream TOF0 and TOF1 detectors, Cherenkov detectors and the downstream TOF2 and KL detectors, which were operated in a temporary position about 2 m downstream of TOF1. The precise distances between TOF0 (TOF1) and TOF1 (TOF2) in this configuration are respectively 770.5 cm and 240.5 cm. The correspondence between beam momentum at various points in the MICE beam for the muon-beam configuration and the different calibration beams used in this analysis is summarised in table 4.1.

Table 4.1: Summary of runs used in this analysis. The muon runs correspond to a nominal setting $(\varepsilon_n, p_\mu) = (6\pi\,\text{mm}\cdot\text{rad}, 200\ \text{MeV}/c)$. Reported momenta are at the entrance of the quoted detectors.

Muon runs				
p_{D2} (MeV/c)	p_{TOF0} (MeV/c)	p_{TOF1} (MeV/c)	p_{TOF2} (MeV/c)	# events (10^3)
238	220	204	190	270
Calibration runs				
p_{D2} (MeV/c)	p_{TOF0} (MeV/c)	p_{TOF1} (MeV/c)	p_{TOF2} (MeV/c)	# events (10^3)
222	217	194	181	195
258	254	231	219	235
280	276	254	242	167
294	290	268	257	354
320	316	295	284	265
362	358	337	326	448

4.3 Method for determining the contamination in the MICE Muon Beam

The purpose of the analysis presented here is to determine the pion contamination of the MICE Muon Beam by using information from the TOF system and the KL detector. Figure 4.1 shows distributions of the time-of-flight of particles between TOF0 and TOF1, with a positive $\pi \to \mu$ beam of nominal momentum 200 MeV/c (figure 4.1a) and with a calibration beam of $p_{D2} \simeq$ 222 MeV/c (figure 4.1b). An electron peak is observed that is well separated from the main muon peak, but the level of the pion contamination under the muon peak cannot be determined from this distribution alone, as the muon and pion distributions overlap. However, for the 222 MeV/c calibration beam, the electron, muon and pion peaks are well separated by their time-of-flight. The muon peak in the $\pi \to \mu$ beam is broader than that of the calibration beam, since the muons selected by D2 originate from pion decays in a range of angles in the backward hemisphere of the pion rest frame [68].

The pion contamination under the muon peak was estimated using the G4beamline simulation package [90] and the MAUS package [108] to simulate the detector response. Figure 4.2a compares distributions of flight time from TOF0 to TOF1 for reconstructed positive-beam data and corresponding Monte Carlo simulations of 6π mm $\cdot$ rad positive muon beams with nominal beam momentum $p_\mu = 200$ MeV/c. The electron contamination is underestimated in the Monte Carlo simulation because the simulation does not transport particles that interact in the material at the edge of the beam acceptance, but charge exchange interactions may produce neutral pions, and these can decay to electrons and positrons in the beam line. Furthermore, the tail of the time-of-flight distribution is also underestimated in the Monte Carlo simulation. Due to

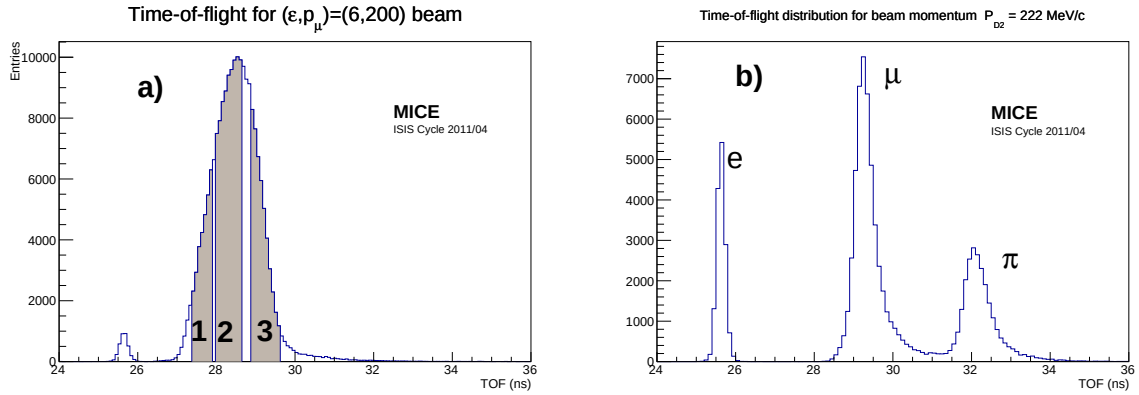

Figure 4.1: (a) Time of flight distributions between TOF0 and TOF1 for a positive muon beam with a nominal momentum of 200 MeV/c (the left peak is due to electrons). The labels 1, 2 and 3 in the muon peak refer to the three time-of-flight intervals, highlighted in grey, used in the analysis. (b) Positive "calibration" beam taken with p_{D2} =222 MeV/c, showing clear electron, muon and pion peaks.

these differences between data and Monte Carlo simulation, this pion contamination analysis is purely based on data, and the Monte Carlo simulation is only used to validate the method.

Figure 4.2b shows the momentum distribution at TOF1 of the electron, pion and muon peaks for the same Monte Carlo simulation, showing that the pion contamination under the muon peak is predominantly due to high momentum pions (with a smaller low momentum component) that are selected by the D2 dipole magnet and are subsequently transported by the beam. Since the muon sample and the higher-momentum pions that contaminate it have similar times of flight, the TOF detectors cannot be used to distinguish them from each other. Therefore, the residual pion contamination in the beam, after the application of time-of-flight requirements suitable for the selection of muons, can only be measured using the spectrum of energy deposited in KL. The pion contamination is a function of the position at which it is measured. According to the G4beamline simulation, the contamination under the muon peak at TOF0 is estimated to be 1.78%, reducing to 0.38% at TOF1 and 0.22% at KL. The contamination under the muon peak is summarised in figure 4.3.

The pion contamination is studied in positive-muon-beam runs with nominal beam momentum 200 MeV/c (p_{D2} = 238 MeV/c) and with a sample corresponding to approximately 270×10^3 triggers. The study is performed as a function of the time-of-flight of the beam particles in three distinct time-of-flight intervals (referred to below as "Points 1, 2 and 3"). The choice of time-of-flight interval is dictated by the availability of calibration data for which the specified interval is populated mainly by muons or mainly by pions. Pairs of calibration runs for which muons and pions present time-of-flight values within the same range (see table 4.2)

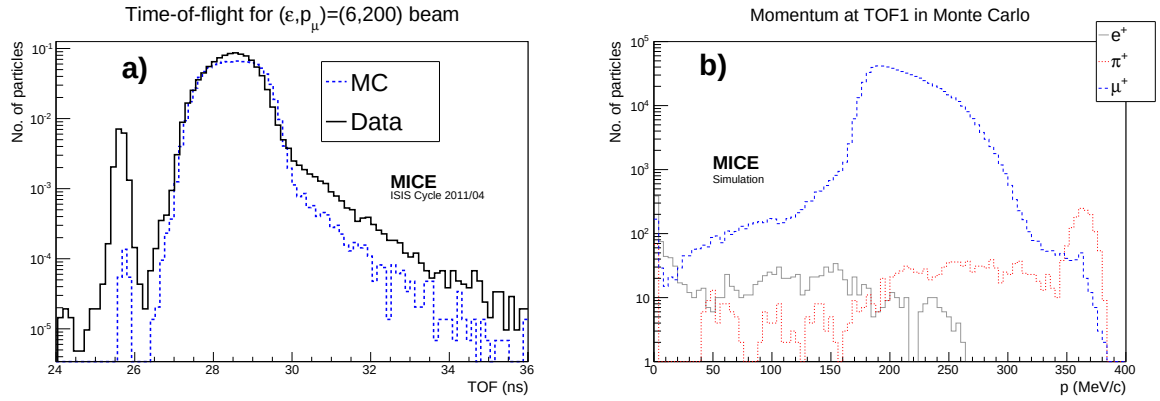

Figure 4.2: (a) Time-of-flight distributions between TOF0 and TOF1 for data and Monte Carlo simulation for a 6π mm $\cdot$ rad positive muon beam with nominal beam momentum $p_\mu = 200$ MeV/c. (b) Momentum distribution for beam particles at TOF1 for a simulated positive 6π mm $\cdot$ rad beam at 200 MeV/c (the time-of-flight between TOF0 and TOF1 is required to satisfy $26.2 <$ TOF < 32 ns).

Table 4.2: Paired beam settings for three time-of-flight intervals ("Points").

	TOF interval, ns	muons from runs with P_{D2} (MeV/c)	pions from runs with P_{D2} (MeV/c)
Point 1	27.4 – 27.9	294	362
Point 2	28.0 – 28.6	258	320
Point 3	28.9 – 29.6	222	280

are defined for each point and are used to benchmark the KL response to muons or to pions of given time-of-flight. In figure 4.1a, the three points are highlighted in grey in the time-of-flight distribution of particles in the MICE Muon Beam.

The widths of the intervals were determined by taking into account the overlap regions between the calibration runs. In each of these time-of-flight intervals the spectra of the KL response can be extracted for muons and pions separately from the calibration runs. These spectra are then used as templates for the response to muons and pions in that time-of-flight interval for the muon runs. As an example, figure 4.4 shows the time-of-flight distributions in two paired beam settings. The interval 28.0–28.6 ns in the TOF0–TOF1 time-of-flight (point 2) is populated mainly by muons for one beam setting and by pions for the other. Similar plots are shown for MC beams in figure 4.5.

Calibration runs have a different number of muons and pions in a given time of flight window, due to their different momentum distributions. This can be taken into account either by making the time of flight windows smaller or by re-weighting the KL response templates by the distribution of muons or pions in time of flight in the calibration samples. The former approach

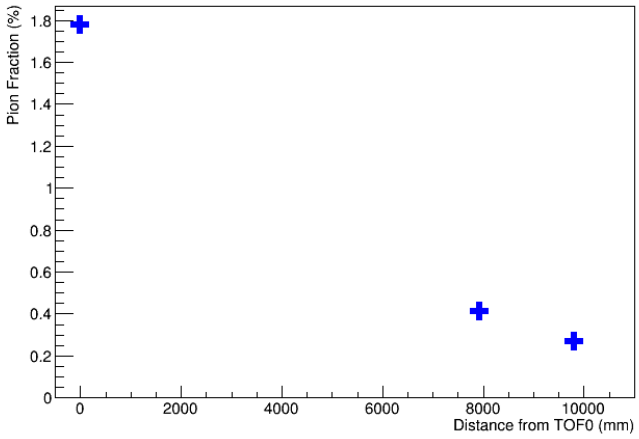

Figure 4.3: Pion contamination in a 6 π mm $\cdot$ rad positive muon beam, at momentum $p_\mu = 200$ MeV/c at different positions along the beam line as deduced from G4beamline and MAUS Monte Carlo simulations. The three points refer to the position of the TOF0, TOF1, and KL positions in the MICE Step I configuration. The z coordinate is in mm in the MICE reference system, with the origin moved to the position of TOF0. The simulation includes a proton absorber of 83 mm. A cut between 26.2 and 32 ns on the time-of-flight between TOF0 and TOF1 is applied.

requires increasing the available statistics and the latter has the feature that the fits to the re-weighted templates do not follow Poissonian errors. While other solutions to the problem exist [109], the beam is split into the time-of-flight ranges defined in table 4.2 into finer intervals, in order to calculate the systematic error due to this effect.

The minimum ionising responses of muons and pions in the KL are similar, but pions can also undergo hadronic interactions, which are visible as a tail in the KL response to pions. The normalised ADC products are summed for all scintillator slabs in the KL that have a signal above a threshold. The KL response to muons and pions in calibration runs and to a particle mix in the $\pi \rightarrow \mu$ beam mode are added together for the three TOF intervals (Points 1, 2 and 3) and shown in figure 4.6. An additional constraint was imposed that only one track was present in both the time-of-flight detectors, associated to only one hit in the KL detector. The distribution for the pions displays a larger tail than that for the muons, due to the presence of hadronic interactions. This feature is used in the following analysis to estimate the contamination on a statistical basis.

The MAUS simulation of the KL response was fine-tuned in order to match features observed in the data. The following features were taken into account:

- Poisson smearing of the photon count produced in the scintillating fibres and the photo-electrons produced at the photocathode of the PMT;

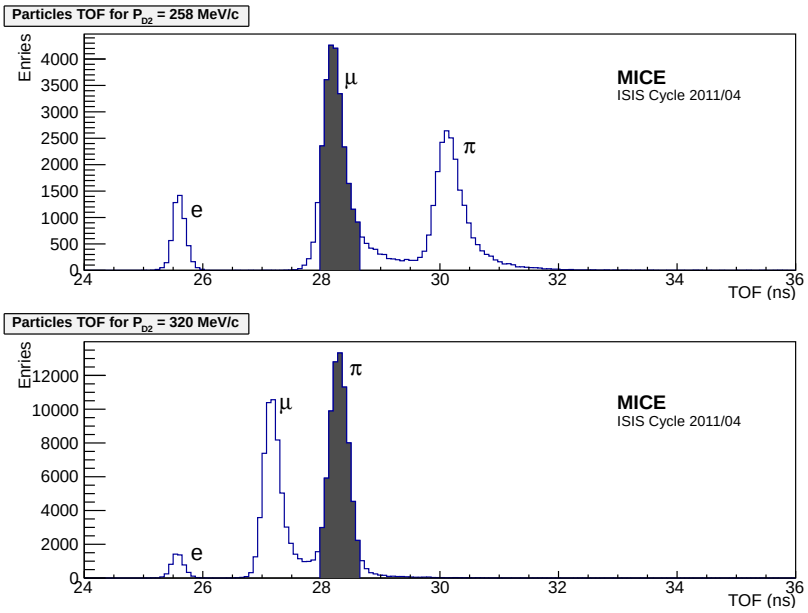

Figure 4.4: Time-of-flight distributions in two paired beam settings. The interval 28.0–28.6 ns (shaded) is populated by muons (pions) in the upper (lower) plot.

- The distribution of photomultiplier gain, assumed to be Gaussian with mean $\sim 2 \times 10^6$ and standard deviation equal to half the gain [110]; and
- The conversion factors from calibrations were carried out by the KL group and implemented and optimised by the author into the KL simulation and digitisation code. These include the following parameters: photoelectrons to ADC counts (250,000 PE/ADC), from MeV to photoelectrons (0.000125 MeV/PE), the two-component scintillating-fibre attenuation lengths (2400 mm and 200 mm), the scintillating-fibre collection efficiency (3.6%), the light-guide collection efficiency (85%) and the photomultiplier-tube quantum efficiency (26%), in order to obtain $\sim$1060 ADC counts for a minimum-ionising peak.

The Monte Carlo simulation of the KL response to muons and pions for the calibration runs and for the simulated $\pi \rightarrow \mu$ beam are shown in figure 4.7. The features of the simulated Monte Carlo KL response to pions and muons follow closely that from the data in figure 4.6.

The fraction of pions and muons in the $\pi \rightarrow \mu$ beam is extracted by exploiting the information contained in the full KL response spectrum for the sums of the three time-of-flight intervals. The method employs the ROOT TFractionFitter [111; 112] to fit the normalised muon and pion templates to the actual KL spectrum in the MICE data. This was carried out for both the extracted MICE data and for the simulated Monte Carlo distributions for the 6π mm $\cdot$ rad, 200 MeV/c $\pi \rightarrow \mu$ beam. The fits for the weighted sum of the three time-of-flight windows

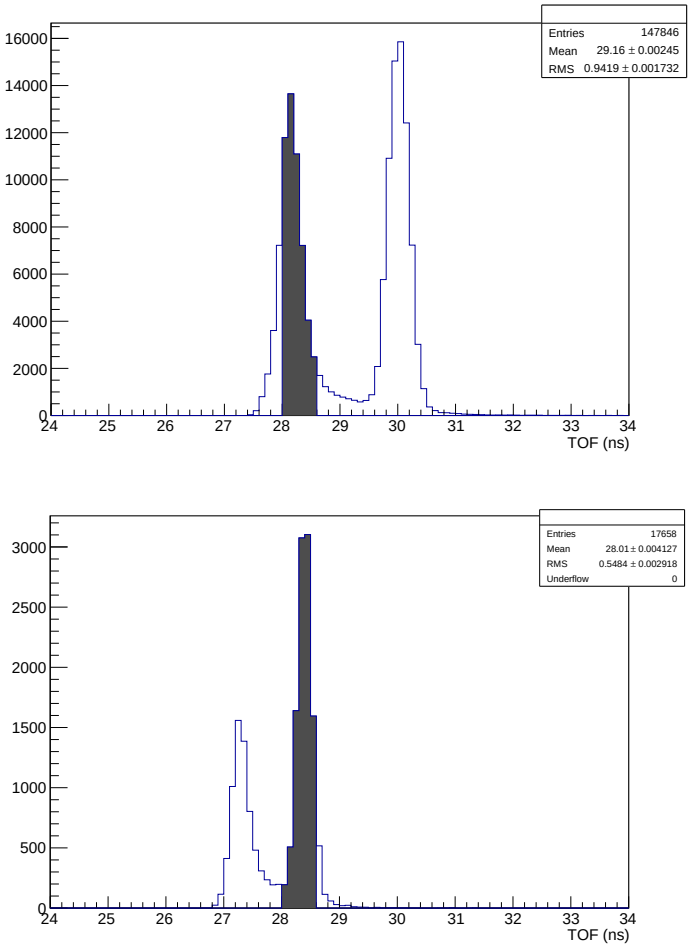

Figure 4.5: Monte Carlo simulation of the time-of-flight distributions of two paired beam settings. The interval 28.0-28.6 ns (shaded) is populated by muons (pions) in the top (bottom) plot.

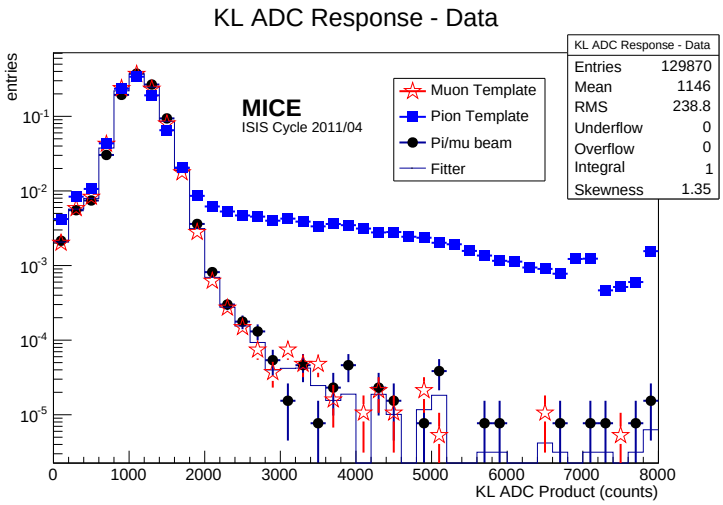

Figure 4.6: Muon template (red stars) and pion template (blue squares) data for the sum of the three TOF data intervals from calibration runs, compared to MICE $\pi \rightarrow \mu$ beam data (black dots). The histogram is the result of a fit of the $\pi \rightarrow \mu$ beam to the fraction of pions and muons based on the two templates. Plots are normalised to unity.

(27.4 ns – 27.9 ns, 28.0 ns – 28.6 ns, 28.9 ns – 29.6 ns) are shown as histograms for the data in figure 4.6 and for the Monte Carlo simulation in figure 4.7. The comparison between MC and data for each point is given in figure 4.8. The fits take into account both data and template statistical uncertainties through a standard likelihood-fit method.

4.4 Results of the pion contamination in the muon beam and systematic errors

The data from the 6π mm $\cdot$ rad, 200 MeV/c muon beam encompassing the three time-of-flight windows includes $N_b = 129870$ beam events. The fractions of muon and pion events predicted by TFractionFitter were allowed to converge without any restrictions. The total fitted number of muon events was $N_\mu = 130173$, which yields $N_\pi = -303 \pm 509$ pion events, compatible with zero. Similarly, for the Monte Carlo simulation, the fitted number of muon events $N_\mu^{MC} = 127772$ was also compatible with the number in the beam $N_b^{MC} = 127695$, which also yielded a number of pions compatible with zero, $N_\pi = -77 \pm 505$. The errors quoted here are the statistical errors only.

The Feldman–Cousins likelihood-ratio ordering-procedure [113] is a unified frequentist method to construct single- and double-sided confidence intervals for parameters of a given model adapted to data. It provides a natural transition between single-sided confidence intervals, used to define upper or lower limits, and double-sided ones. It is particularly useful near the bound-

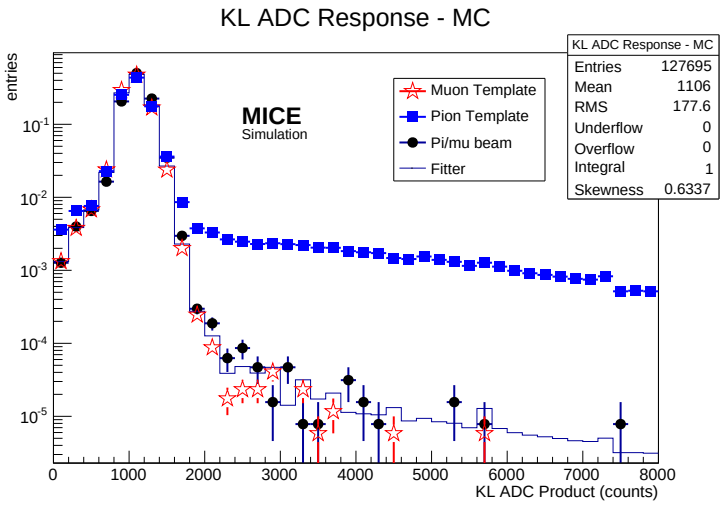

Figure 4.7: Monte Carlo simulation of the muon template (red stars) and pion template (blue squares) for the sum of the three TOF data intervals, compared to the simulated MICE $\pi \rightarrow \mu$ beam data (black dots). The histogram is the result of a fit of the simulated $\pi \rightarrow \mu$ beam to the fraction of pions and muons based on the two templates. Plots are normalised to unity.

aries of physical regions, while providing a true confidence interval. The Feldman–Cousins procedure was used to extract an upper limit of the pion contamination in the $\pi \rightarrow \mu$ beam at the KL detector position $f_\pi < 0.69\%$ at 90% C.L. An upper limit for the Monte Carlo simulation at the KL position $f_\pi^{MC} < 0.86\%$ at 90% C.L. was also derived, to be compared to the "true" pion contamination from the Monte Carlo simulation of $0.22 \pm 0.01\%$. Plots of the Feldman-Cousins curves of the range of true number of pions, given a measured number of pion are summarised in figure 4.9.

The sources of systematic errors considered in this analysis were:

- Finer subdivision of the time-of-flight windows;
- Shift in the calibration of the time-of-flight windows;
- Binning of the KL ADC histograms;
- Effects of muon contamination in the pion templates (pion contamination in the muon template was found to be negligible); and
- Loosening the constraint that there is only one hit in the KL detector ($N_{KL} = 1$) to having one or more hits in KL ($N_{KL} > 0$).

The systematic errors for both data and the Monte Carlo simulation on the pion contamination are given in table 4.3. The systematic error due to the dependence on the time-of-flight

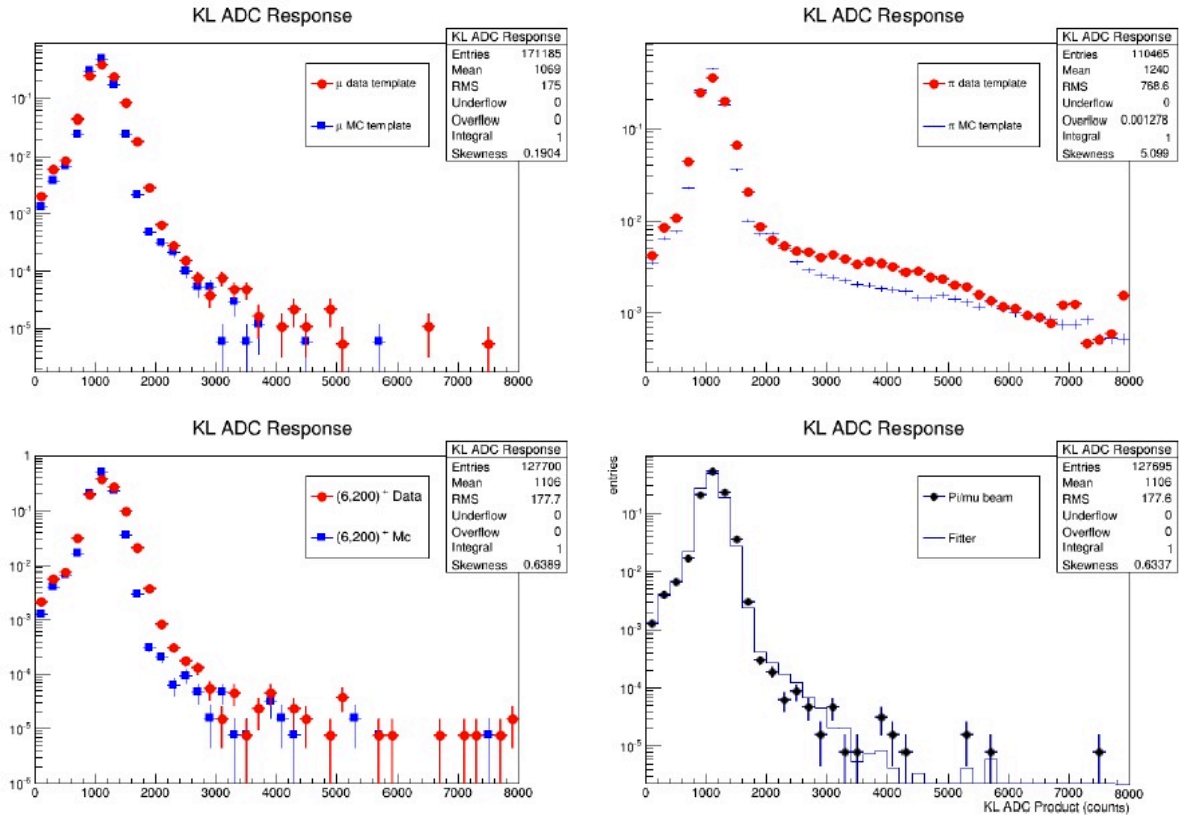

Figure 4.8: KL ADC product distributions for the muon template (top left), pion template (top right) and for the 6 mm rad, 200 MeV/c pion-muon beam (bottom left) for data and Monte Carlo. The bottom right plot shows the fit to the KL ADC product distribution of the Monte Carlo 6 mm·rad, 200 MeV/c pion-muon beam.

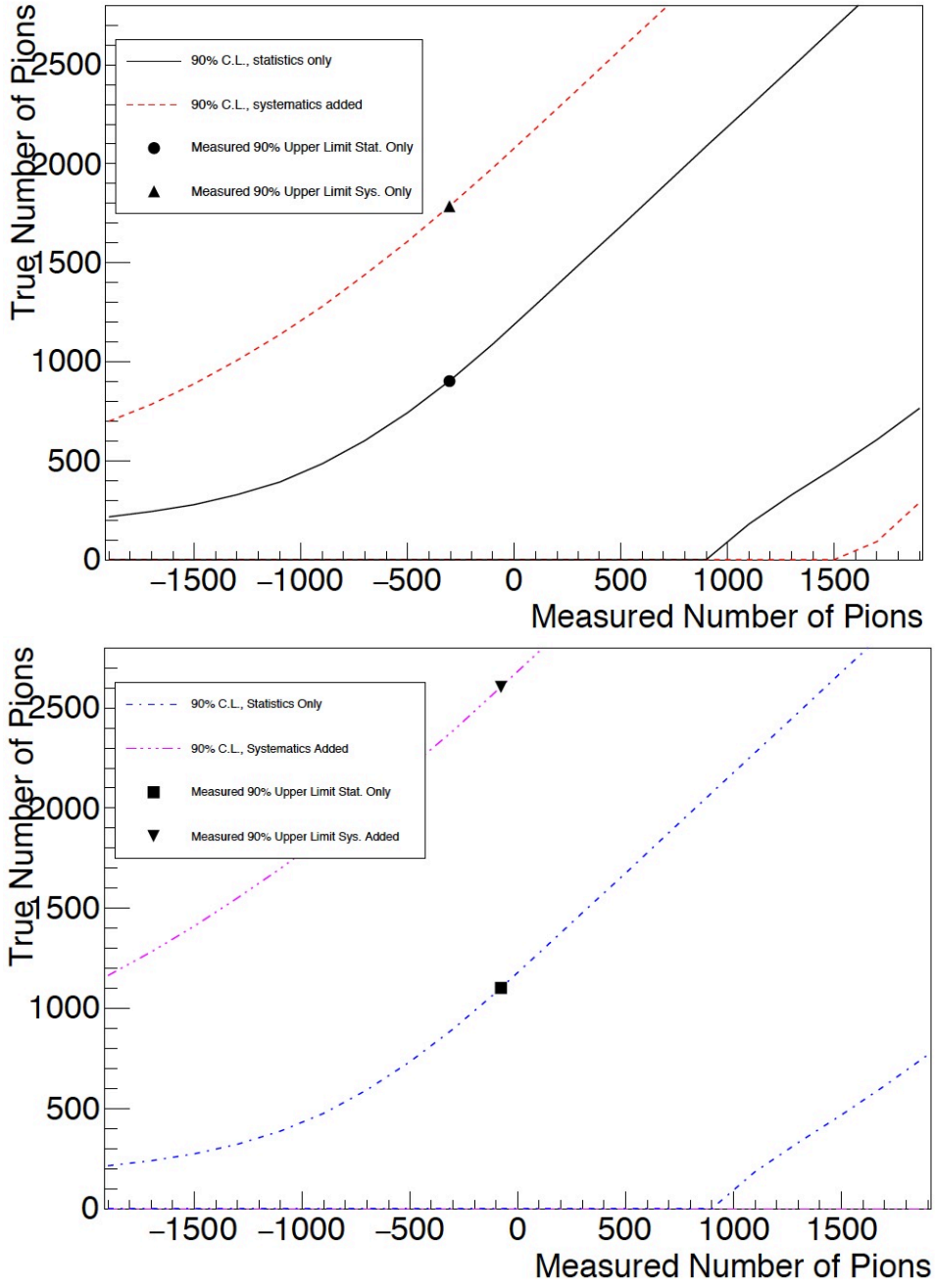

Figure 4.9: Feldman-Cousins statistical 90% confidence levels as a function of the results of the fitted number of pions for the comparison of the data with 129870 events (left) and Monte Carlo with 127772 events (right). The plots show the confidence level bands assuming the statistical error only and assuming a systematic error of 0.34% for the data and 0.45% for the Monte Carlo simulation that is added in quadrature to the statistical error.

distribution was determined by further subdividing the time-of-flight ranges associated with each point. Doubling the number of time-of-flight bins varies the fitted pion contamination by 0.18%. The dependence of the pion-fraction obtained on the time-of-flight calibration is determined by shifting independently the time-of-flight values in the calibration runs by an amount compatible with the electron peak position (± 0.1 ns). This results in a small variation in the pion contamination of 0.04% for data and 0.28% for Monte Carlo. The dependence on the histogram binning of the KL ADC distribution was also assessed by doubling and halving the bin-size to yield a variation in the fitted pion contamination of 0.14% in data and 0.16% in simulation. There is a small bias in the determination of the pion contamination due to the expected muon contamination in the pion template. For example, the nominal value is 25.1% muons in the pion template for point 1, 26.1% muons for point 2 and 26.2% muons for point 3. Setting the muon contamination in the pion template to zero in the Monte Carlo results in a shift in the pion contamination in the $\pi \to \mu$ beam by 0.03%. Loosening the number of KL hits from $N_{KL} = 1$ to $N_{KL} > 0$ results in a change in the fit of 0.25%.

The quadratic sum of the total systematic errors is shown in the bottom row of table 4.3. The total systematic error for the pion contamination is found to be 0.34% in data and 0.45% in Monte Carlo. These systematic errors are used to obtain the following yields: $N_\pi = -303 \pm 509$ (stat)± 442 (syst) for the data and $N_\pi = -77 \pm 505$ (stat)± 575 (syst) for the Monte Carlo. The statistical and systematic errors are added in quadrature and the Feldman–Cousins procedure is repeated to extract new upper limits of the pion contamination in the $\pi \to \mu$ beam at the KL position of $f_\pi < 1.37\%$ at 90% C.L. including systematic errors. An upper limit for the Monte Carlo simulation with systematic errors was also derived: $f_\pi^{MC} < 2.06\%$ at 90% C.L. An analysis using only the TOF and Cherenkov detectors has obtained a comparable limit [114].

Table 4.3: Sources of systematic errors in the evaluation of the pion contamination.

Effect	Assessment method	Absolute Impact on π contamination	
		Data	MC
Time-of-flight distribution	Finer subdivision	0.18%	0.18%
Time-of-flight calibration	Shift calibrations by ± 0.1 ns	0.04%	0.28%
Histogram binning	Double/halve bin sizes	0.14%	0.16%
Bias due to contamination in templates	Create pure templates in MC	0.03%	0.03%
Bias in selection	Cut KL cell hits > 0	0.25%	0.25%
	Total	0.34%	0.45%

4.5 Conclusions

An upper limit to the pion contamination in the MICE Muon Beam at the position of the KL detector has been determined using precision time-of-flight counters in combination with the KL calorimeter. The measurements were carried out in a variety of time-of-flight windows and the analysis yielded a pion contamination compatible with zero. The Monte Carlo expectation for the pion contamination of a $\pi \rightarrow \mu$ beam of 6π mm $\cdot$ rad emittance and 200 MeV/c nominal momentum is $(0.22 \pm 0.01)\%$ at the KL and an upper limit on the pion contamination in the Monte Carlo simulation extracted with this method is $f_{\pi}^{MC} < 2.1\%$ including the systematics errors. The upper limit for the pion contamination of the MICE Muon Beam in its Step I configuration at the KL position was found to be $f_{\pi} < 1.4\%$ at 90% C.L., including systematic errors. This upper limit on the pion contamination in the MICE Muon Beam, combined with the performance of the PID system, meets the experimental requirement.

Chapter 5

Alignment of the MICE trackers

Prior to any scattering or emittance measurement being performed using the MICE trackers the system had to be accurately aligned. A complete survey covering all components of the MICE muon beam, MICE experiment and associated instrumentation was done prior to the Step IV data taking campaign. This information is encoded into the MC generated and to all of the processed data from the experiment ensuring that all pertinent alignment information is included in the simulations and data used in MICE analyses. Working from the final processed data a cross check of the alignment information is detailed in this chapter. The approach adopted was to perform a non-iterative global alignment method, as implemented with the BACH software [115], developed for the AIDA Alignment work package [116]. This software uses an algorithm based on the Millepede method, which is a non-iterative method that minimises a χ^2 function by a single matrix inversion technique [117; 118] and has been adopted by LHC experiments, such as CMS [119] and LHCb [120].

5.1 MICE Apparatus

The MICE Step IV experiment is described in Section 2.3.1 and the MICE tracker is detailed in Section 2.3.7. The alignment data was collected using an empty channel, in which there was no target material in the channel between the two trackers. Pions and electrons are rejected by the particle identification system, with further details given in chapter 2.3.6. The number of triggers taken are summarised in table 5.2 using data taken in the run numbers summarised in table 5.2. The alignment data were taken during the 2015/04 ISIS user cycle from the 23rd of February until the 24th of March 2016. The measurements were carried out without a magnetic field either in the tracker volume or surrounding the absorber.

Only tracks that have digits in TOF1 in both planes, with one muon reconstructed in each event and within the time of flight window, are selected for the analysis. The time of flight win-

Table 5.1: Summary of data taken for alignment study.

Beam line settings (P of beam between TOF1-2 in MeV/c)	Absorber	No. of triggers
244	Empty channel	3.47×10^5

Table 5.2: Data runs used for the alignment study.

Beam line settings (P of beam between TOF1-2 in MeV/c)
244
Zero Absorber
7727 7817 7733 7818 7737 7819 7738 7844 7741 7845 7775 7847 7776 7848 7790 7849 7794 7851 7795 7852 7796 7853 7805 7854 7808 7855 7809 7856 7813 7858 7814 7859 7816 7860

dow, measured between TOF0 and TOF1, was defined between 27.1 to 27.3 ns. The tracks are projected downstream from the upstream tracker volume to the reference plane of the downstream tracker and must be within a 150 mm radius to be selected. Data were taken with the beam operating in "muon mode" (Section 4.2) giving an almost pure muon beam at a mean momentum of 243.6 ± 0.2 MeV/c after selection.

5.2 Millepede Alignment Software Package

The BACH software was adapted to the specific geometry of the two-tracker system of MICE. The first evaluation of the position of the ten tracker planes (five in the upstream tracker and five in the downstream tracker) is provided by mechanical survey measurements. These are required as a starting point for the track-based alignment algorithm. Track residuals are used to perform the Millepede alignment. A residual is the distance between a measured hit point on a tracker plane and the interception point of the corresponding track with the plane. The alignment constants are evaluated from the track residuals by solving a minimisation problem that yields the optimal set of alignment constants given the measured residuals. The residuals can be written as a combination of the track parameters and the misalignment constants. The Millepede algorithm minimises the total χ^2 given by the sum of all the residuals with a single iteration over the data, thereby determining all alignment constants and track parameters at the same time by a single matrix inversion. Figure **??** shows an example of the alignment behaviour.

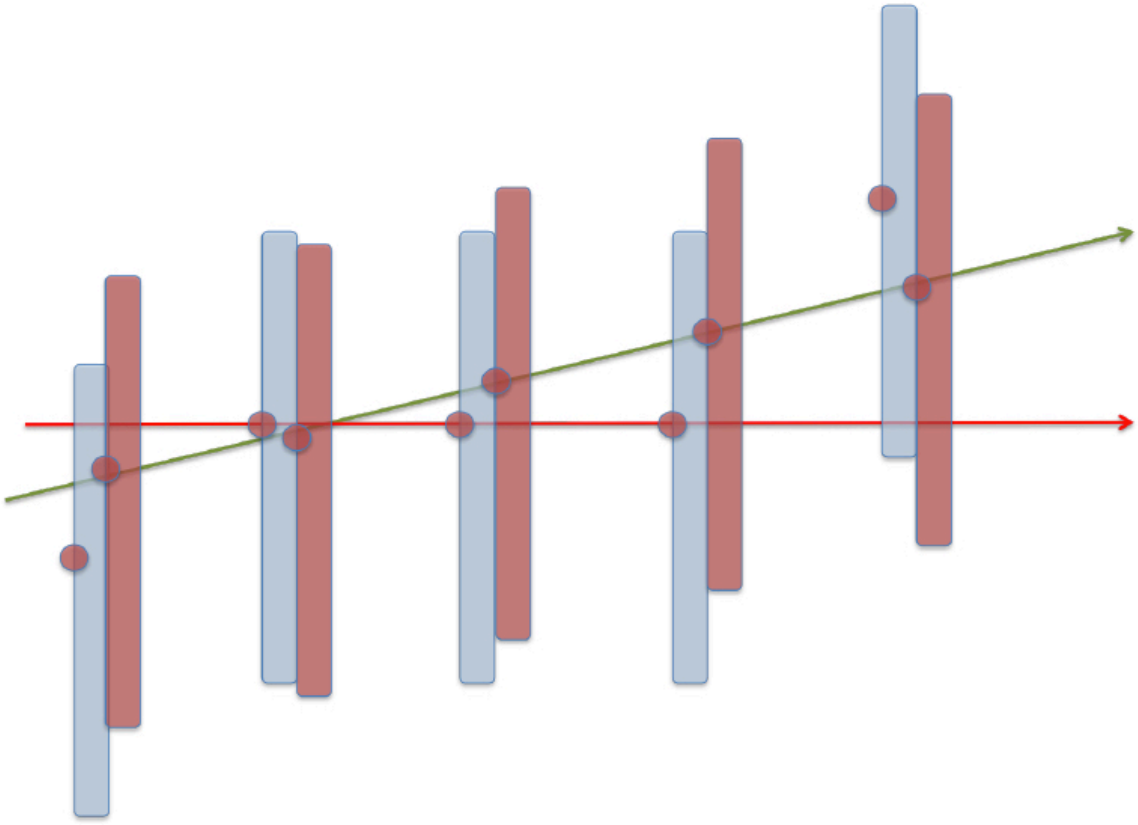

Figure 5.1: This figure illustrates the alignment proceedure employed by Millepede. Each detector plane is allowed to move provided that the global χ^2 is minimised at the end of the procedure. Blue boxes represent the initial alignment, red boxes the alignment result. A track parallel to the z-axis (red line) will be reconstructed as a sloped track (green line) and hence a detector shearing will be introduced. Figure taken from Ref. [116]

In a linear model, the measured quantity $\mathbf{x} = (x, y, z)$ is described as,

$$\mathbf{x} = \left(\mathbf{a}_{ij}^T \mathbf{d}_i\right) + \left(\boldsymbol{\alpha}_{ij}^T \boldsymbol{\delta}_i\right) + \mathbf{r}, \tag{5.1}$$

where $\mathbf{a}$ is a matrix of global derivatives affecting the location of the detector planes, $\mathbf{d}$ is a vector of the alignment parameters, $\boldsymbol{\alpha}$ is a matrix containing the track parameters for each track, $\boldsymbol{\delta}$ is a vector of the input parameters (the local derivatives of each tack), $\mathbf{r}$ is the residual vector, j represents the track-index and i the index of the tracker plane. In the case of a linear track model, for track j at plane i,

$$x_i = a_j \cdot z_i + b_j, \tag{5.2}$$

$$y_i = c_j \cdot z_i + d_j, \tag{5.3}$$

then

$$\boldsymbol{\alpha}_{ij}^T = \begin{pmatrix} 1 & z_{hit} & 0 & 0 & 0 & 0 \\ 0 & 0 & 1 & z_{hit} & 0 & 0 \\ 0 & 0 & 0 & 0 & 0 & z_{hit} \end{pmatrix} \text{ and } \boldsymbol{\delta}_i^T = \begin{pmatrix} b_j & a_j & d_j & c_j & 0 & 1 \end{pmatrix}, \tag{5.4}$$

with z_{hit} the z-position of a hit. The alignment parameters are,

$$\mathbf{d}_i^T = \begin{pmatrix} \Delta x_i & \Delta y_i & \Delta z_i & \Delta\theta_{xi} & \Delta\theta_{yi} & \Delta\theta_{zi} \end{pmatrix}, \tag{5.5}$$

where $(\Delta x_i, \Delta y_i, \Delta z_i)$ are the displacements and $(\Delta\theta_{xi}, \Delta\theta_{yi}, \Delta\theta_{zi})$ are the rotations around the x, y and z axes for plane i. Ignoring second order corrections, a real hit vector $\mathbf{x}_{hit}^{real}$ should be related to the hit vector $\mathbf{x}_{hit}$ by,

$$\mathbf{x}_{hit}^{real} = \begin{pmatrix} 1 & \Delta\theta_z & \Delta\theta_y \\ -\Delta\theta_z & 1 & \Delta\theta_x \\ -\Delta\theta_y & -\Delta\theta_x & 1 \end{pmatrix} \left(\mathbf{x}_{hit} - \begin{pmatrix} \Delta x \\ \Delta y \\ \Delta z \end{pmatrix} \right) \approx \begin{pmatrix} x_{hit} - \Delta x + y_{hit}\Delta\theta_z + z_{hit}\Delta\theta_y \\ y_{hit} - \Delta y - x_{hit}\Delta\theta_z + z_{hit}\Delta\theta_x \\ z_{hit} - \Delta z - x_{hit}\Delta\theta_y - y_{hit}\Delta\theta_x \end{pmatrix}. \tag{5.6}$$

Table 5.3: Misalignment constants after the internal Millepede alignment.

Plane	x position after alignment (mm)	y position after alignment (mm)
USS Plane 1	0	0
USS Plane 2	-0.044 $\pm$0.007	-0.055 $\pm$0.007
USS Plane 3	-0.050 $\pm$0.006	0.069 $\pm$0.006
USS Plane 4	0.025 $\pm$0.002	-0.020 $\pm$0.002
USS Plane 5	0	0
DSS Plane 1	0	0
DSS Plane 2	0.059 $\pm$0.006	0.010 $\pm$0.006
DSS Plane 3	0.069 $\pm$0.013	-0.058 $\pm$0.014
DSS Plane 4	-0.001 $\pm$0.016	0.002 $\pm$0.017
DSS Plane 5	0	0

Therefore, the matrix of global derivatives $\mathbf{a}$ is given by,

$$\mathbf{a}^T\mathbf{d} = \sum\left(\frac{\partial \mathbf{x}_{hit}^{real}}{\partial \mathbf{d}}\mathbf{d}\right) = \begin{pmatrix} -1 & 0 & 0 & 0 & z_{hit} & y_{hit} \\ 0 & -1 & 0 & z_{hit} & 0 & -x_{hit} \\ 0 & 0 & -1 & -y_{hit} & -x_{hit} & 0 \end{pmatrix} \begin{pmatrix} \Delta x \\ \Delta y \\ \Delta z \\ \Delta\theta_x \\ \Delta\theta_y \\ \Delta\theta_z \end{pmatrix}. \tag{5.7}$$

Assuming that the number of tracks used for the alignment is ν, and that the number of planes being aligned is $n = 10$, then the number of local measurements will be $N = n \cdot \nu$. Therefore, the χ^2 is the sum of the squared residuals weighted by their variances σ^2_{ijk},

$$\chi^2 = \sum_{i=0}^{n}\sum_{j=0}^{\nu}\sum_{k}^{x,y,z} \frac{\left(\left[x_{ij} - \left(\mathbf{a}_{ij}^T\mathbf{d}_i\right) - \left(\boldsymbol{\alpha}_{ij}^T\boldsymbol{\delta}_j\right)\right]_k\right)^2}{\sigma^2_{ijk}}. \tag{5.8}$$

The set of track and alignment parameters that minimises the χ^2 function is the one that corresponds to the real alignment. This is written out in a large $N \times N$ matrix with six alignment parameters, $n = 10$ planes to be aligned for ν tracks. Millepede inverts this large matrix to extract the alignment parameters.

Due to the tracks being close to perpendicular to the tracker planes, the alignment procedure is not sensitive to translations in z (Δz), and to rotations around the x and y axes ($\Delta\theta_x$, $\Delta\theta_y$). Therefore, in practice, this is constrained to be zero and there are only three alignment constants for each plane to be aligned, for a total of 30 constants.

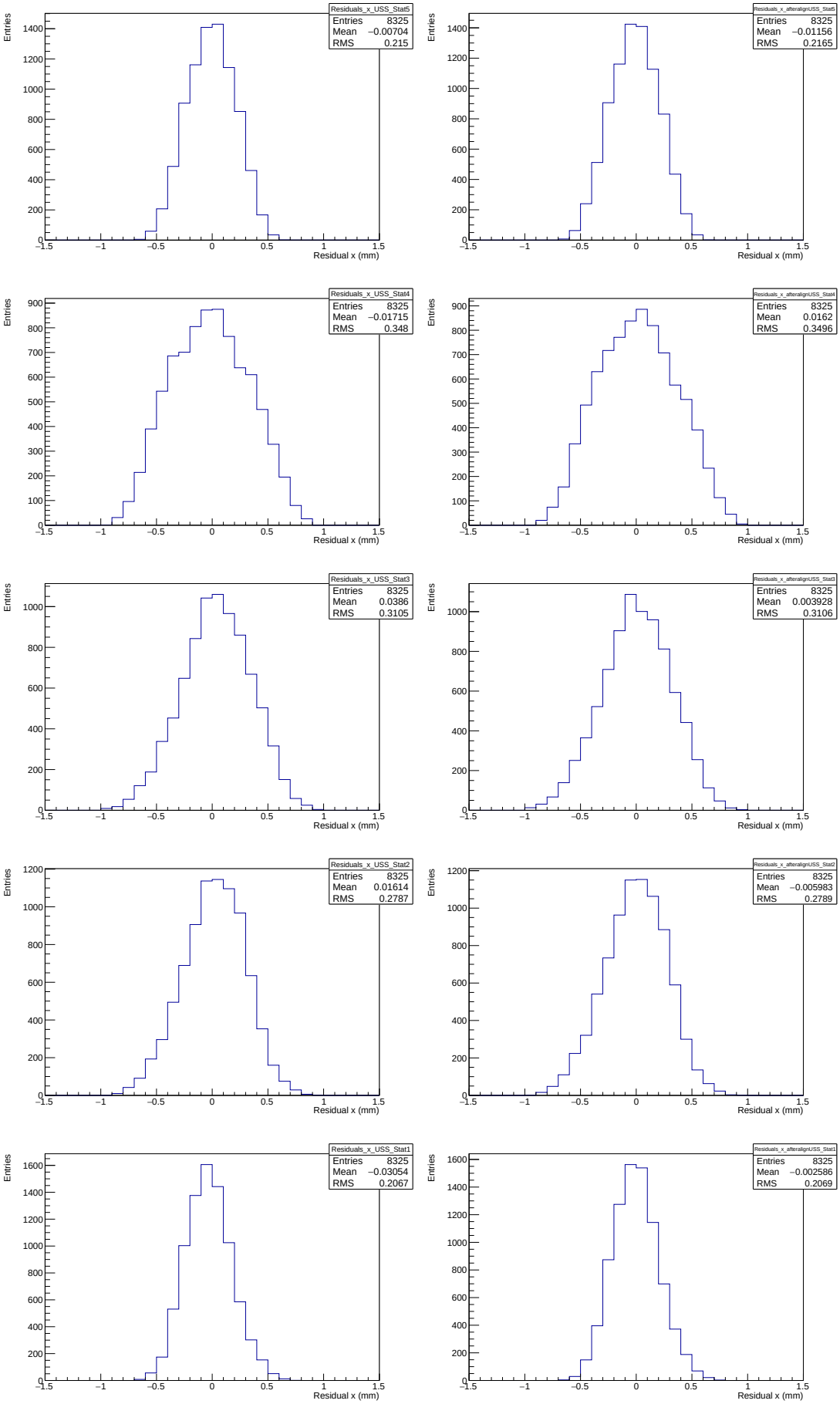

Figure 5.2: x residuals for upstream tracker planes before (left) and after (right) the upstream internal Millepede alignment procedure

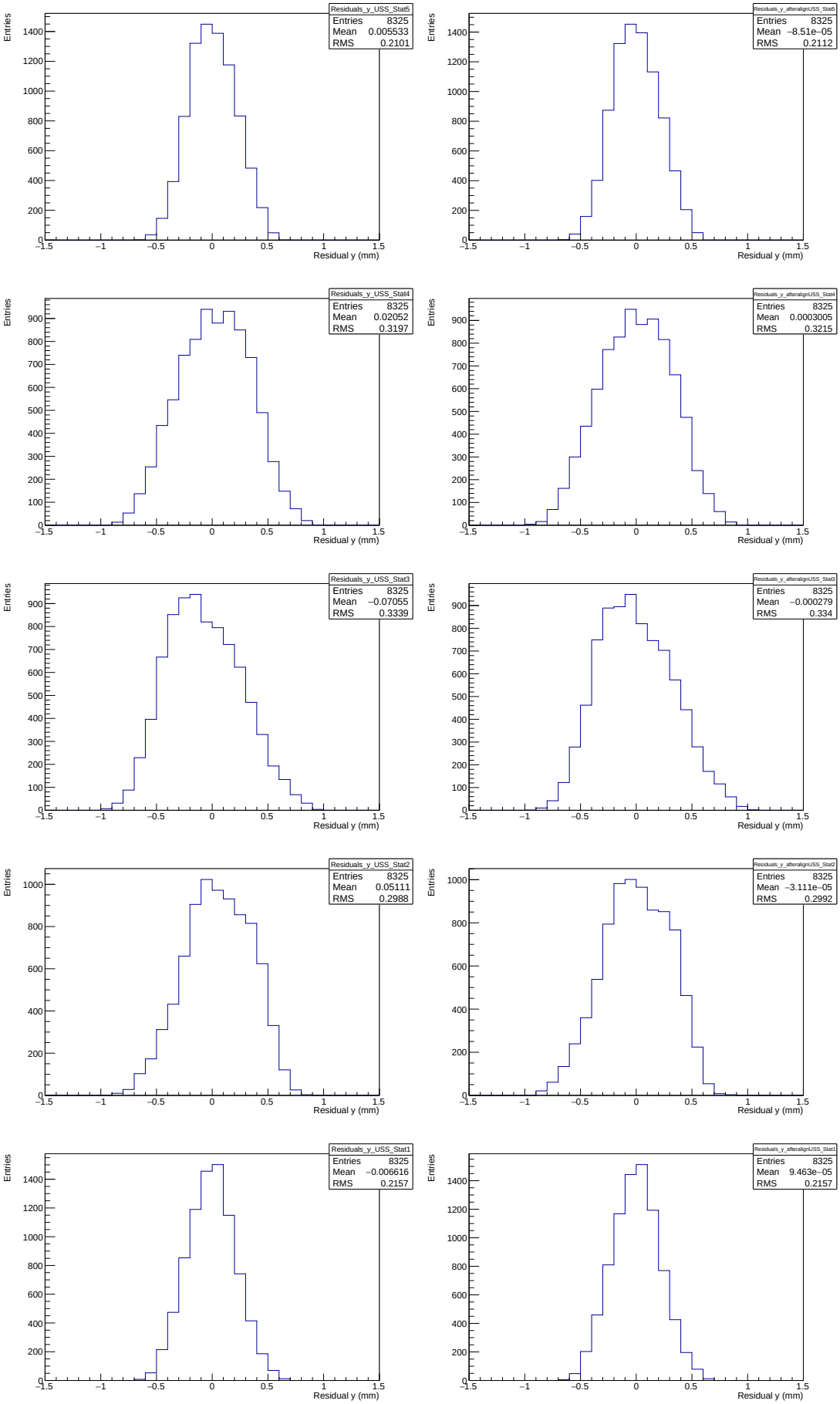

Figure 5.3: y residuals for upstream tracker planes before (left) and after (right) the internal Millepede alignment procedure

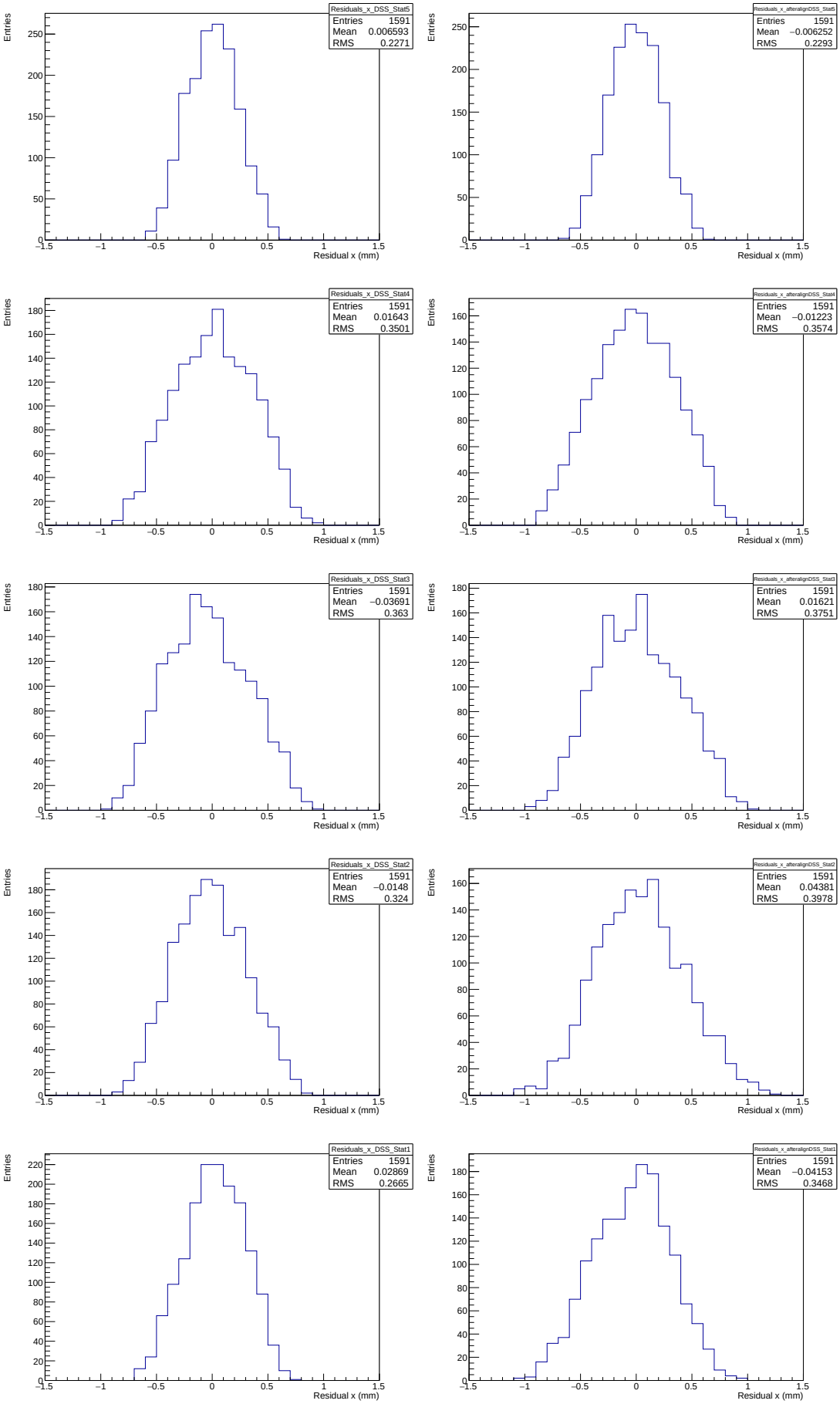

Figure 5.4: x residuals for downstream tracker planes before (left) and after (right) the internal Millepede alignment procedure

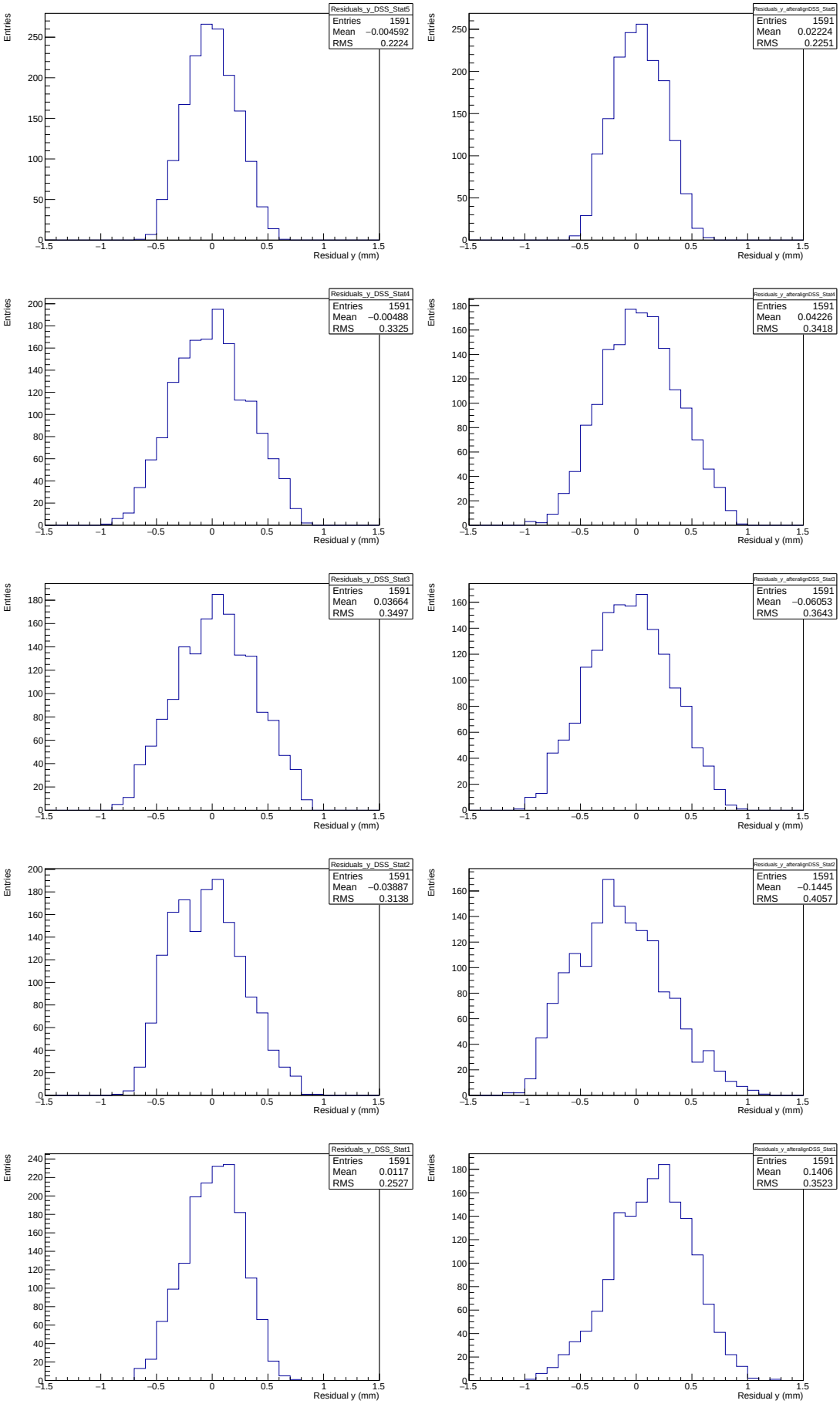

Figure 5.5: y residuals for downstream tracker planes before (left) and after (right) the internal Millepede alignment procedure

Table 5.4: Misalignment constants after the global Millepede alignment.

Plane	x position after alignment (mm)	y position after alignment (mm)	θ_z position after alignment (mrad)
USS Plane 1	-0.093 $\pm$0.028	0.022 $\pm$0.028	-2.30 $\pm$0.54
USS Plane 2	-0.004 $\pm$0.027	-0.066 $\pm$0.028	-2.01 $\pm$0.53
USS Plane 3	-0.009 $\pm$0.027	0.011 $\pm$0.027	-1.75 $\pm$0.50
USS Plane 4	0.055 $\pm$0.026	-0.057 $\pm$0.026	-2.25 $\pm$0.47
USS Plane 5	0.028 $\pm$0.026	-0.024 $\pm$0.026	-2.34 $\pm$0.48
DSS Plane 1	0	0	0
DSS Plane 2	-0.004 $\pm$0.033	0.058 $\pm$0.033	-0.05 $\pm$0.58
DSS Plane 3	0.021 $\pm$0.033	-0.037 $\pm$0.033	0.54 $\pm$0.61
DSS Plane 4	-0.019 $\pm$0.033	0.008 $\pm$0.033	0.47 $\pm$0.62
DSS Plane 5	-0.083 $\pm$0.033	0.040 $\pm$0.033	-0.92 $\pm$0.67

5.3 Internal Tracker Alignment

The BACH software was adapted for the particular geometry of the MICE trackers. The algorithm started from constraints measured by a Coordinate Measurement Machine (CMM) when the tracker was under construction. Planes 1 and 5 of each of the trackers were fixed, and the other three planes were translated with respect to each of the other two planes. A consistent internal alignment for each tracker can then be achieved. The residual distributions achieved for both of the sets of trackers are shown in figures 5.2, 5.4, 5.3 and 5.5. All distributions are centred around zero, showing that a consistent set of alignment constants for each of the tracker planes has been achieved. The alignment constants are shown in table 5.3.

5.4 Tracker to Tracker Alignment

A global track is then fitted to the ten spacepoints in both trackers, five upstream and five downstream. The alignment of the ten tracker stations is performed with the reference plane of the downstream tracker held fixed and all other stations allowed to float. The final alignment including all tracker stations is summarised in table 5.4 with the misalignment angle between the trackers being $\theta_x = 0.032 \pm 0.055$ mrad and $\theta_y = 0.013 \pm 0.069$ mrad. These angles are calculated by fitting a straight line to the final positions reported in table 5.4 and then taking the difference upstream and downstream. In the scattering analysis (see chapter 6) the downstream tracks are rotated by -0.032 mrad in θ_x and 0.013 mrad in θ_y thus removing bias due to misalignment between the trackers.

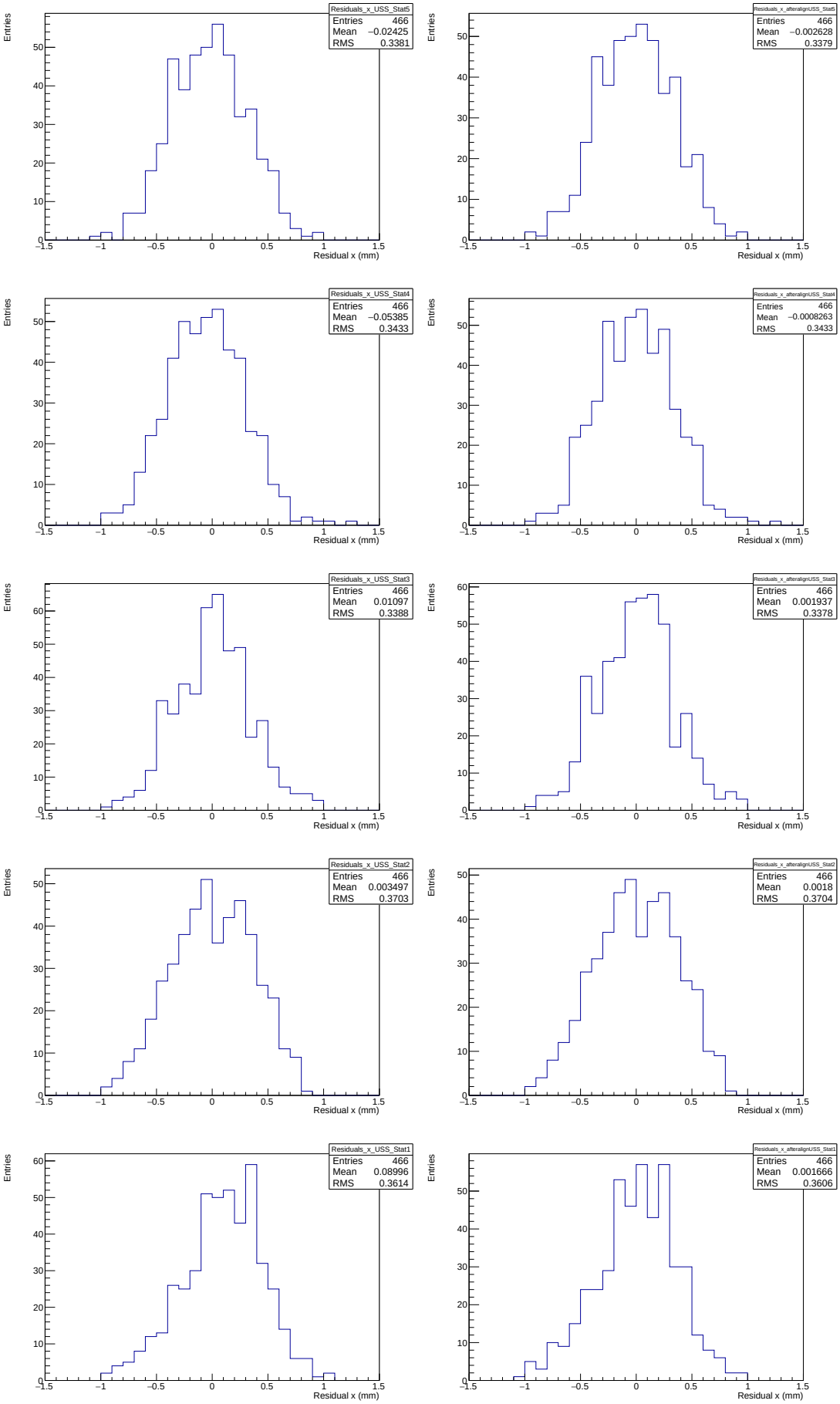

Figure 5.6: x residuals for upstream tracker planes before (left) and after (right) the Millepede alignment procedure

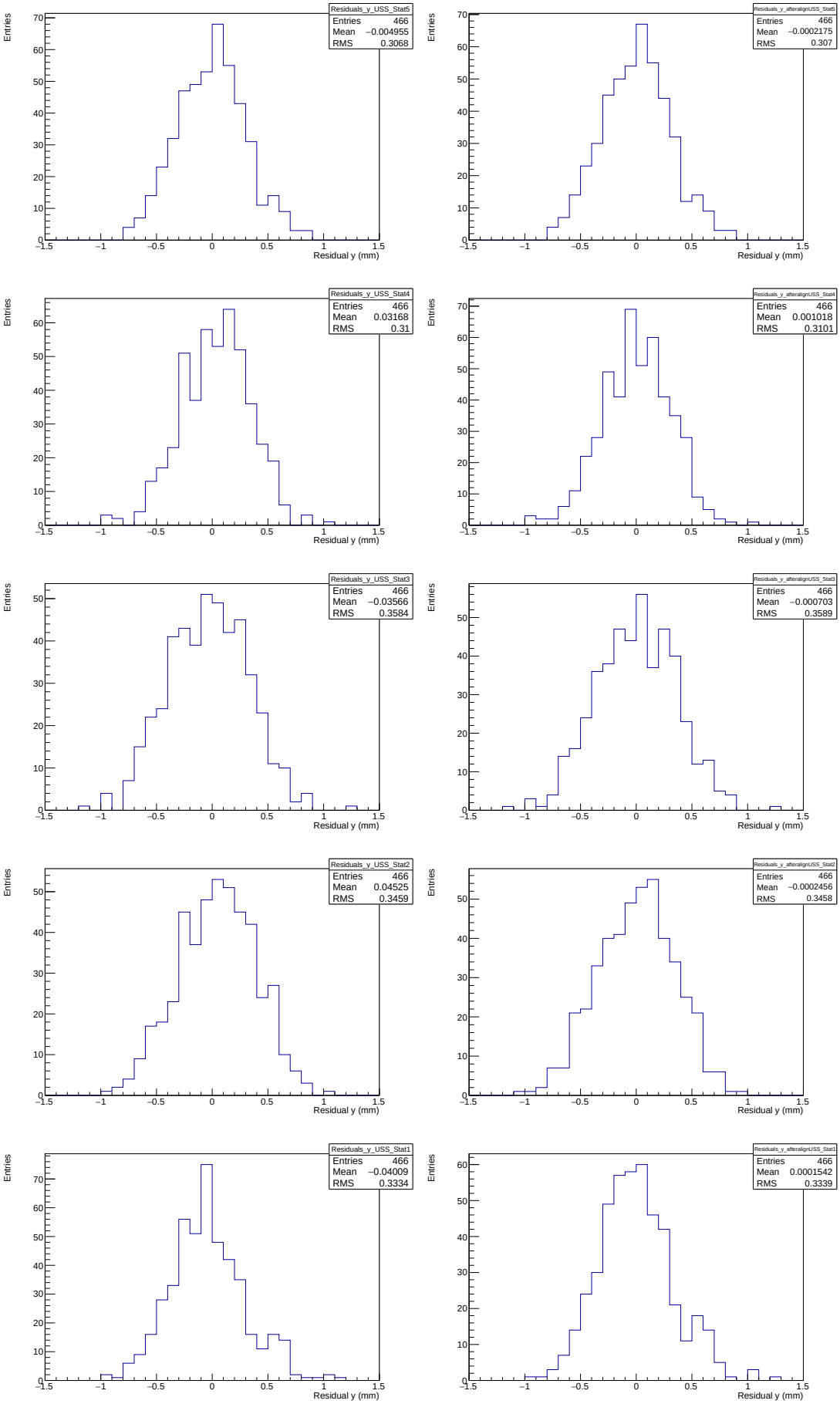

Figure 5.7: y residuals for upstream tracker planes before (left) and after (right) the Millepede alignment procedure

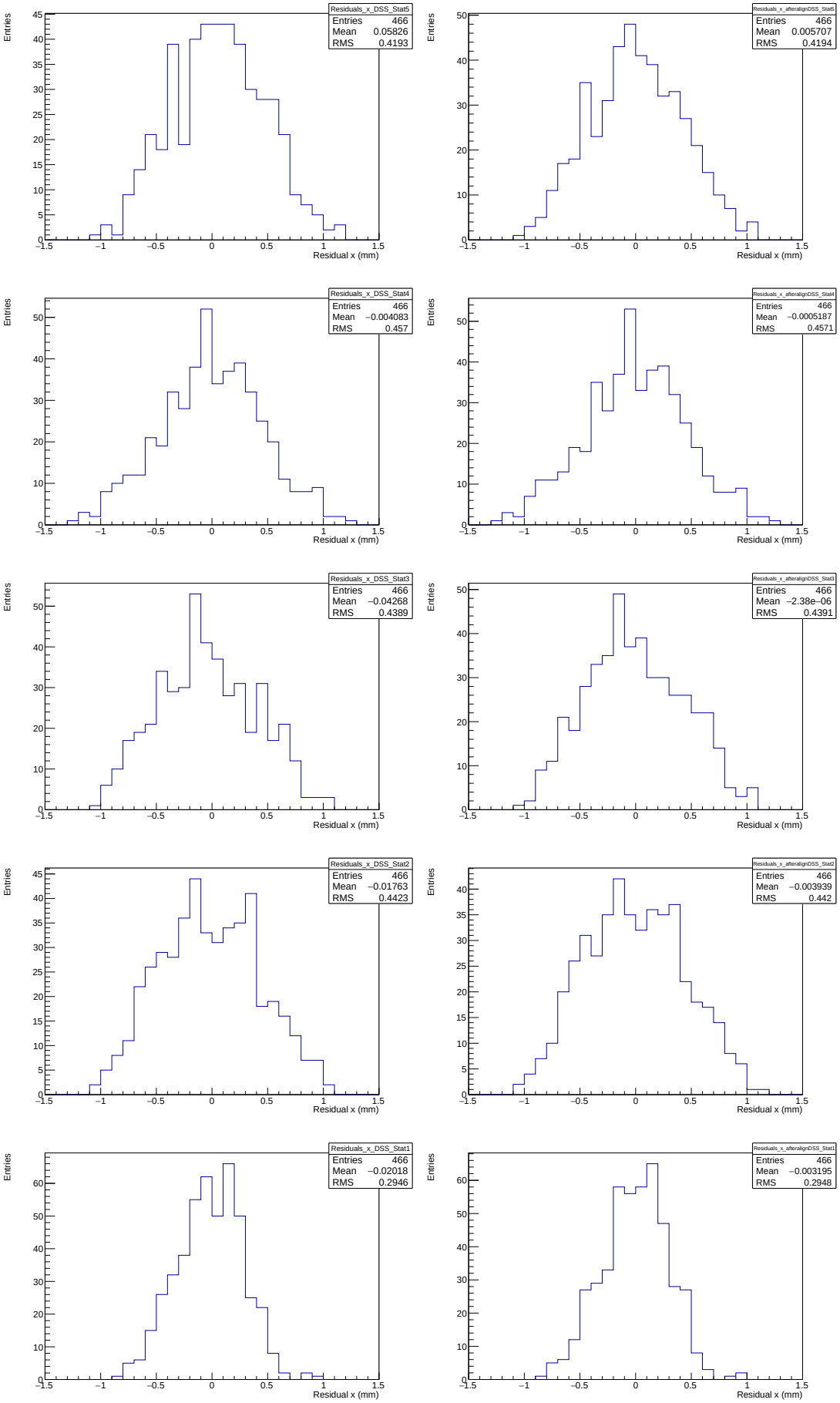

Figure 5.8: x residuals for downstream tracker planes before (left) and after (right) the Millepede alignment procedure

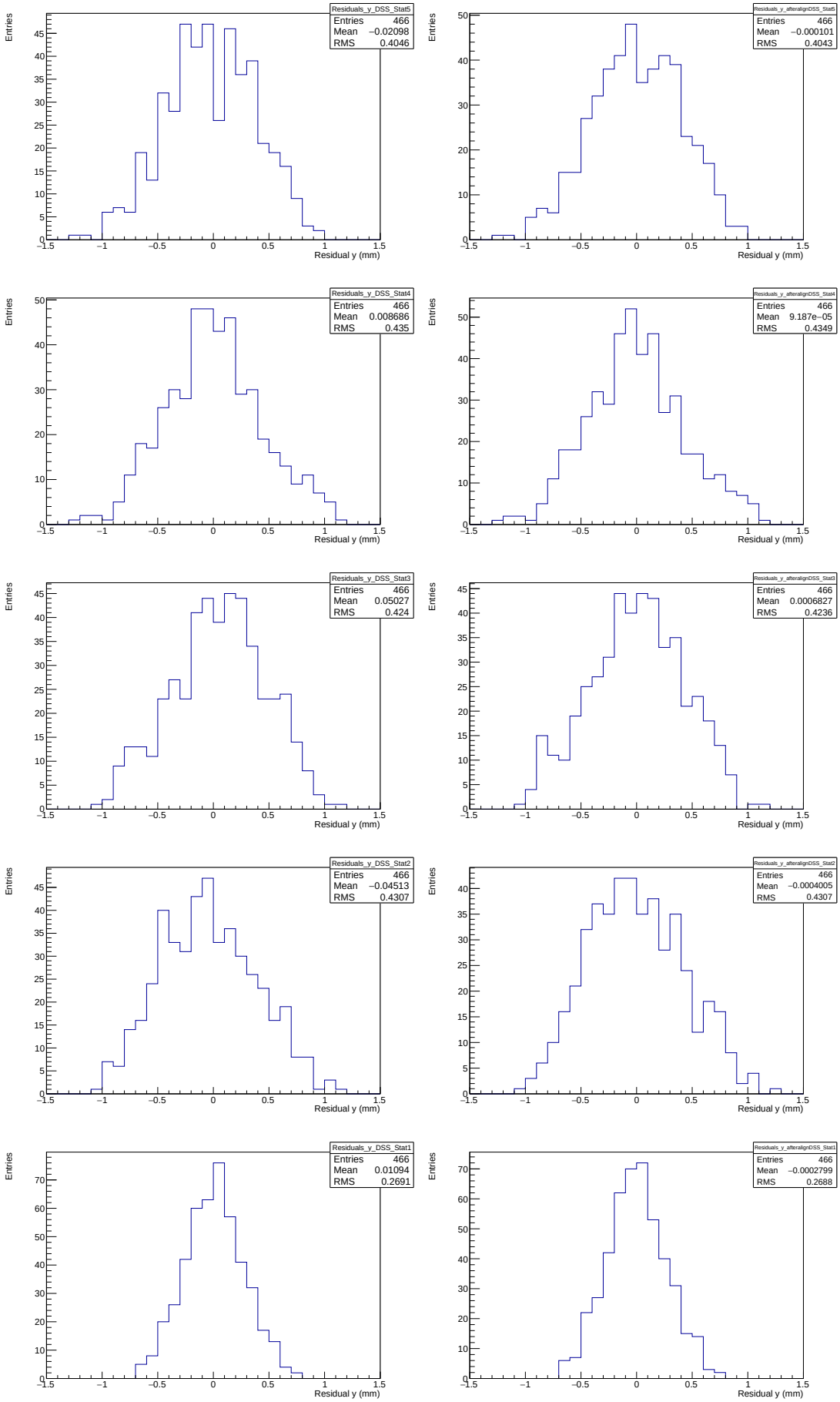

Figure 5.9: y residuals for downstream tracker planes before (left) and after (right) the Millepede alignment procedure

Table 5.5: Mean and RMS of residuals in x for both the up- and downstream tracker planes

	Before Millepede alignment		After Millepede alignment	
Plane	mean (mm)	RMS (mm)	mean (mm)	RMS (mm)
USS Plane 1	0.08996 ± 0.01674	0.3614 ± 0.0118	0.00166 ± 0.01670	0.3606 ± 0.0118
USS Plane 2	0.00350 ± 0.01715	0.3703 ± 0.0121	0.00018 ± 0.01716	0.3704 ± 0.0121
USS Plane 3	0.01097 ± 0.01570	0.3388 ± 0.0111	0.00193 ± 0.01565	0.3378 ± 0.0110
USS Plane 4	-0.05385 ± 0.01590	0.3433 ± 0.0112	-0.00082 ± 0.01590	0.3433 ± 0.0112
USS Plane 5	-0.02425 ± 0.01566	0.3381 ± 0.0110	-0.00262 ± 0.01565	0.3379 ± 0.0110
DSS Plane 1	-0.02018 ± 0.01365	0.2946 ± 0.0096	-0.00319 ± 0.01366	0.2948 ± 0.0096
DSS Plane 2	-0.01763 ± 0.02049	0.4423 ± 0.0144	-0.00393 ± 0.02047	0.4420 ± 0.0144
DSS Plane 3	-0.04268 ± 0.02033	0.4389 ± 0.0438	-0.00000 ± 0.02034	0.4391 ± 0.0143
DSS Plane 4	-0.00408 ± 0.02117	0.4570 ± 0.0149	-0.00051 ± 0.02117	0.4571 ± 0.0149
DSS Plane 5	0.05826 ± 0.01942	0.4193 ± 0.0137	0.00570 ± 0.01943	0.4194 ± 0.0137

Table 5.6: Mean and RMS of residuals in y for both the up- and downstream tracker planes

	Before Millepede alignment		After Millepede alignment	
Plane	mean (mm)	RMS (mm)	mean (mm)	RMS (mm)
USS Plane 1	-0.04009 ± 0.01545	0.3334 ± 0.0109	0.00015 ± 0.01547	0.3339 ± 0.0109
USS Plane 2	0.04525 ± 0.01602	0.3459 ± 0.0113	-0.00024 ± 0.01602	0.3458 ± 0.0113
USS Plane 3	-0.03566 ± 0.01660	0.3584 ± 0.0117	-0.00070 ± 0.01663	0.3589 ± 0.0117
USS Plane 4	0.03168 ± 0.01436	0.3100 ± 0.0101	0.00101 ± 0.01437	0.3101 ± 0.0101
USS Plane 5	-0.00495 ± 0.01421	0.3068 ± 0.0100	-0.00021 ± 0.01422	0.3070 ± 0.0100
DSS Plane 1	0.01094 ± 0.01247	0.2691 ± 0.0088	-0.00027 ± 0.01245	0.2688 ± 0.0088
DSS Plane 2	-0.04513 ± 0.01995	0.4307 ± 0.0141	-0.00040 ± 0.01995	0.4307 ± 0.0141
DSS Plane 3	0.05027 ± 0.01964	0.4240 ± 0.0138	0.00068 ± 0.01963	0.4236 ± 0.0138
DSS Plane 4	0.00868 ± 0.02015	0.4350 ± 0.0142	0.00009 ± 0.02015	0.4349 ± 0.0142
DSS Plane 5	-0.02098 ± 0.01874	0.4046 ± 0.0132	-0.00010 ± 0.01873	0.4043 ± 0.0132

5.5 Conclusions

The Millepede alignment algorithm was used to accurately align the two MICE trackers. This technique is a non-iterative method that minimises a χ^2 function by a single matrix inversion technique which is computationally fast and minimises the associated error. The result of the Millepede alignment shows that the two MICE trackers are well aligned within the current processed data and with the misalignment constants calculated by Millepede any residual bias introduced into any measurement of scattering or emittance made with the MICE trackers can be corrected.

Chapter 6

Multiple Coulomb Scattering in MICE Step IV

A number of different absorber materials can be installed in the focus coil module of the MICE cooling channel. In this thesis the results of the measurement of the scattering of muons in gaseous xenon and lithium hydride are reported. The motivation for the gaseous xenon measurement is to benchmark Multiple Coulomb Scattering (MCS) in a high-Z material, in order to perform further measurements of MCS in the MICE experiment using lower-Z materials, such as lithium hydride (LiH) and liquid hydrogen. From this baseline the same analysis was applied to the lithium hydride data, a material for which it is essential to accurately model the MCS for the demonstration of ionisation cooling required for muon acceleration. The design of the neutrino factory front-end from the International Design Study for a Neutrino Factory (IDS-NF) includes a cooling channel with lithium hydride absorbers [48]. Data were also taken with the absorber removed from the cooling channel. These data are then used to deconvolve detector effects and a comparison with models implemented in GEANT4 and a formula recommended by the PDG [121] was made.

6.1 Introduction

In ionisation cooling [122; 62], a muon beam passes through a cooling channel, which includes low-Z absorbers and accelerating RF cavities, to reduce the emittance of the initial muon beam. Ionisation cooling relies on the balance of energy loss in the absorber, the cooling term, and MCS, the heating term that increases the emittance of the beam.

The PDG recommends an approximate multiple scattering formula [121; 123], which is found to be accurate to approximately 11%:

$$\theta_0 \approx \frac{13.6\,\mathrm{MeV}}{p_\mu \beta_{\mathrm{rel}}} \sqrt{\frac{\Delta z}{X_0}} \left[1 + 0.0038 \ln \left(\frac{\Delta z}{X_0} \right) \right], \tag{6.1}$$

where θ_0 is the rms width of the projected scattering angle distribution, X_0 is the radiation length of the material and Δz is the thickness of the absorber, p_μ is the momentum of the muon and $\beta_{\mathrm{rel}} = p_\mu c / E_\mu$, with E_μ its energy. From this an approximate cooling formula can be derived (ignoring the logarithmic term of equation 6.1),

$$\frac{d\varepsilon_n}{dz} = -\frac{\varepsilon_n}{E_\mu \beta_{\mathrm{rel}}^2} \left\langle \frac{dE_\mu}{dz} \right\rangle + \frac{\beta}{2 m_\mu \beta_{\mathrm{rel}}^3} \frac{(13.6\ \mathrm{MeV})^2}{E_\mu X_0}, \tag{6.2}$$

where ε_n is the normalised transverse (two-dimensional) emittance of the beam, β is the betatron function, and m_μ the energy and mass of the muons [124]. Given that the goal of MICE is to measure the reduction in normalised emittance with 1% precision, which requires an absolute emittance measurement precision of 0.1%, this approximate formula is not sufficient for the needs of MICE. This demands an accurate measurement of MCS for relevant low-Z materials, such as liquid hydrogen and lithium hydride, where simulations are not in good agreement with data. The MUSCAT experiment carried out a measurement of muon scattering in low-Z materials [125] and found significant differences between a number of models and the measured distributions.

The theory of Multiple Coulomb Scattering, developed by Rossi and Greisen [126] and Molière [127] considered the Rutherford scattering with a low angle cut-off

$$\frac{d\langle \theta_0^2 \rangle}{dz} = 16\pi N_A \frac{Z^2}{A} r_e^2 \left(\frac{mc}{p_\mu \beta} \right)^2 \ln \left[196 Z^{-1/3} \left(\frac{Z}{A}^{1/6} \right) \right] \approx \frac{(21.2\mathrm{MeV})^2}{p_\mu^2 \beta^2} \frac{1}{X_0} \tag{6.3}$$

where only interactions with the atomic nucleus are included, with a distribution proportional to Z^2, where Z is the atomic number of the scattering material. Bethe [128] adapted the Molière theory to include atomic electron scattering, which implied a proportionality of $Z(Z+1)$ however this theory still assumed equal weight was given to both nuclear and atomic electron scattering. Early theories of MCS were reviewed by Scott [129]. Further modifications were made to the original theory by Lynch and Dahl to incorporate a path length dependance which resulted in the PDG formulate quoted in expression 6.1. Both the Molière and Bethe theories were compared to MCS data for a variety of absorbers in MUSCAT, and it was found that these theories did not describe low-Z materials adequately. A new theory, covering both energy loss and multiple scattering (ELMS) based on electromagnetic first principles, was developed by Allison and Holmes [130; 131] and shows good agreement with hydrogen data. ELMS

does not rely on the relative constributions from the nuclear and atomic electron cross-sections but instead includes the contributions from all processes that impact the interaction between charged particles, nuclei and electron, namely the Bethe-Bloch energy loss, Cherenkov and longitudinal photons and was based on the Rutherford cross-section. However, this model relies on accurate dielectric constant data for each material, currently only developed for hydrogen, and time-consuming numerical integration.

Instead, most particle physics simulations use GEANT4 [132] to evaluate particle interactions with matter. GEANT4 makes a parameterisation of the scattering distribtution for a finite thickness of the material then proceeds stepwise through the simulated material calculating the contribution for each step. Multiple scattering in GEANT4 does not use a small angle approximation and relies on a full Legendre polynomial expansion, where the default physics list evaluates the Urban cross-section [133; 134] for most particles and the Wentzel single-scattering cross-section for muons. This model works well for high-Z materials but overestimates scattering for low-Z materials. Alternative models which can overcome these shortcomings have been proposed, namely the Cobb-Carlisle model [124; 135] which samples directly from the Wentzel single-scattering cross-section and simulates all collisions with nuclei and electrons. This includes a cut-off for the nuclear cross-section and seperate contributions from the nuclear and atomic electron scattering

$$\frac{d\langle\theta_0^2\rangle}{dz} = 8\pi N_A \frac{Z^2}{A} r_e^2 \left(\frac{mc}{p_\mu \beta}\right) \left[\ln\left[\left(\frac{\theta_2}{\theta_1}^2\right) + 1\right] - 1 + \frac{1}{Z}\left(\ln\left[\left(\frac{\theta_2^e}{\theta_1^e}^2\right) + 1\right] - 1\right)\right] \tag{6.4}$$

Given the various models, MICE will need to measure MCS for low-Z materials, such as liquid hydrogen and lithium hydride, to perform an accurate measurement of ionisation cooling. In order to validate the methods being adopted by MICE to measure MCS, it is also necessary to perform measurements in a higher-Z absorber. The liquid hydrogen absorber to be deployed in MICE is 30 cm thick ($3.4\%X_0$) and the lithium hydride absorber has a thickness of 65 mm ($6.7\%X_0$). Gaseous xenon ($Z = 54$) was chosen to perform a high-Z measurement of MCS, since the vessel available has a thickness of 30 cm, which implies a total absorption length of $2.0\%X_0$ in xenon gas at atmospheric pressure, similar to the absorption length of liquid hydrogen. The expected width of the multiple scattering distribution will be of a similar size to that of liquid hydrogen and should be measurable with the MICE apparatus. In this thesis the scattering of muon data on gaseous xenon and lithium hydride is reported and the analysis strategy to be adopted by MICE for all scattering measurements is developed.

6.2 MICE apparatus and beam conditions

The MICE Step IV apparatus used for the scattering of muons in xenon is shown schematically in figure 6.1. It consists of a xenon absorber on either side of upstream and downstream scintillating fibre trackers. Each tracker contains five planes of scintillating fibres, with an expected position resolution of 661 μm [136] operated in this configuration without a magnetic field. The trackers reconstruct tracks based on a Kalman filter [81]. Pions and electrons are rejected by the particle identification system, with further details given in chapter 2.3.6.

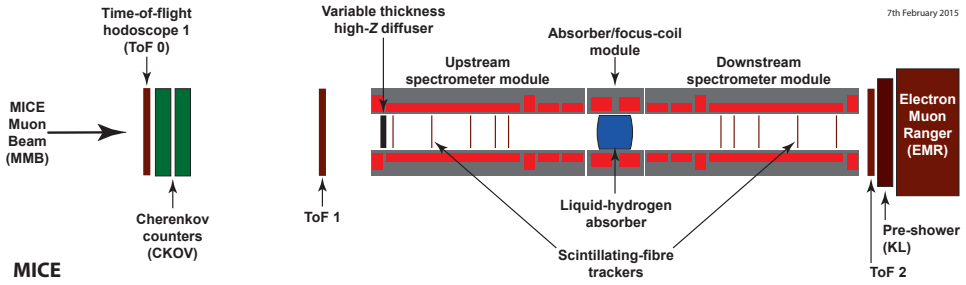

Figure 6.1: Schematic view of the MICE Step IV configuration used to perform the multiple scattering on xenon.

The MICE Muon Beam has been fully characterised [64] and a pion contamination of less than 1.4% at 90% C.L. was measured in chapter 4, and published in [63]. For the two different absorber materials two different beam line modes were used for the data collection. For the gaseous xenon data the MICE beam was operated in "calibration mode" (Section 4.2) where the beam contained a mixture of pions, muons and electrons, and with the muons centred around 210 MeV/c. For the lithium hydride data the beam was operated in "muon mode" (Section 4.2) giving an almost pure muon beam at a variety of momenta [1]. In both cases, for this measurement a beam with a 3π mm· rad emittance beam was selected. For the xenon absorber all data were collected with a beam of 210 MeV/c muons while, for the lithium hydride, data were taken for 167, 206 and 244 MeV/c muons. Further details on the MICE muon beam line are given in chapter 2.3.

The number of triggers for each of the absorber and momentum settings are summarised in table 6.2. The gaseous xenon data were collected between 13$^{\text{th}}$ and 17$^{\text{th}}$ December 2015, while the lithium hydride MCS data taking period was during the 2015/04 ISIS user cycle from the 23rd of February until the 24th of March 2016. The volume between the absorber and the

[1] During the December 2015 running the MICE muon beam line decay solenoid was offline for repairs. It was for this reason that the beam line settings were changed from the nominal "muon" mode to "calibration" mode in order to compensate for the reduced rate in this mode.

Table 6.1: Summary of data taken for MCS study.

Beam line settings (P of beam between TOF1-2 in MeV/c)	Absorber	No. of triggers
210	Gaseous xenon (30 cm)	2.76×10^5
	Empty absorber vessel	2.08×10^5
244	Lithium hydride (65 mm)	1.58×10^6
	Empty channel	3.47×10^5
206	Lithium hydride (65 mm)	2.14×10^6
	Empty channel	3.65×10^5
167	Lithium hydride (65 mm)	2.12×10^6
	Empty channel	6.72×10^5

two trackers was filled with helium to minimise multiple scattering not due to the absorber. The measurements were carried out without a magnetic field either in the tracker volume or surrounding the absorber. For the "empty" absorber volume runs in December, the absorber vessel was filled with helium, a requirement to prevent a pressure failure of the absorber vessel windows. During the 2015/04 data taking period, the channel was entirely empty when the lithium hydride was removed. Momentum measurements were carried out using the time-of-flight difference between TOF1 and TOF2.

Only tracks that have hits in TOF1 in both planes, with one muon reconstructed in each event and within the time of flight window, are selected for the analysis. The time of flight window, measured between TOF0 and TOF1, for the xenon analysis was 27.0 to 28.4 ns and the lithium hydride runs it was 28.7 to 28.9 ns for the 167 MeV/c run, 27.7 to 27.9 ns for the 206 MeV/c run and 27.1 to 27.3 ns for the 244 MeV/c run. Tracks are projected downstream from the upstream tracker volume to the reference plane of the downstream tracker and must be within a 150 mm radius from the centre of the reference plane to be selected. The complete selection for the xenon analysis is shown in table 6.3 and for the lithium hydride analysis is summarised in table 6.4. A distribution of the time-of-flight between TOF0 and TOF1 for particles selected in the xenon runs, shows distinct peaks for electrons, muons and pions (figure 6.2, left). The momentum of the particles is measured using the time-of-flight difference t_{12} between TOF1 and TOF2, making assumptions about the particle mass m:

$$p = \frac{m}{\sqrt{\frac{t_{12}^2 c^2}{L^2} - 1}}, \tag{6.5}$$

with $L = 822.2\,\text{cm}$, the distance between TOF1 and TOF2, and c the speed of light. In figure 6.2, right, the momentum of particles with a TOF01 greater than 26 ns is shown. Particles with a TOF01 time-of-flight less than 29 ns are assumed to be muons and above 29 ns are assumed to be pions. A TOF01 cut between 27 ns and 28.4 ns selects a beam of muons with high purity

Table 6.2: Data runs used for MCS study.

Beam line settings (P of beam between TOF1-2 in MeV/c)							
210	167	206	244	210	167	206	244
Helium	Zero Absorber			Xenon	Lithium Hydride		
7578 7586	7666 7675	7469 7652	7516 7517	7551 7553	7764 7826	7726 7807	7727 7817
7587 7588	7676 7680	7672 7673	7674 7682	7554 7556	7766 7827	7729 7834	7733 7818
7589 7590	7683 7684	7681 7695	7685 7691	7557 7558	7767 7831	7735 7835	7737 7819
7591	7690 7692	7696	7693 7694	7559 7560	7768 7832	7736 7836	7738 7844
				7562 7563	7777 7833	7740 7837	7741 7845
				7564 7566	7782 7861	7754 7838	7775 7847
				7568 7569	7783 7863	7770 7841	7776 7848
				7570 7571	7785 7864	7771 7842	7790 7849
				7572 7573	7786 7865	7772 7843	7794 7851
				7575 7576	7787 7866	7773 7778	7795 7852
				7577 7579	7799 7800	7784 7788	7796 7853
				7580 7580	7806 7822	7789 7797	7805 7854
				7581 7583	7823 7824	7798 7804	7808 7855
					7825		7809 7856
							7813 7858
							7814 7859
							7816 7860

Table 6.3: Summary of xenon data taken for MCS study.

Cut	No. of events after cut
	210 MeV/c (27 - 28.4 ns)
TOF1 hit	7515150
TOF cut	5267625
1 track	305539
track proj. cut	21611

($> 99.9\%$).

6.3 Multiple Coulomb Scattering Analysis

After aligning the two trackers (see chapter 5), the momentum vector of the muon at the final plane of the upstream tracker ($\mathbf{p}_u$) and the momentum vector of the muon after the absorber at the first plane of the downstream tracker ($\mathbf{p}_d$) are measured. Two sets of projected angles are defined, the scattering angle projected onto the y-z plane, which is called θ_x, and the scattering angle projected onto the x-z plane, which is called θ_y (figure 6.6). Both of these angles are signed, and are defined as follows:

Table 6.4: Summary of lithium hydride data taken for MCS study.

Cut	No. of events after cut		
	167 MeV/c (28.7 - 28.9 ns)	206 MeV/c (27.7 - 27.9 ns)	244 MeV/c (27.1 - 27.3 ns)
TOF1 hit	1282488	1223560	1239827
TOF cut	1206510	746025	1119000
1 track	68108	40056	58469
track proj. cut	6150	4894	8337

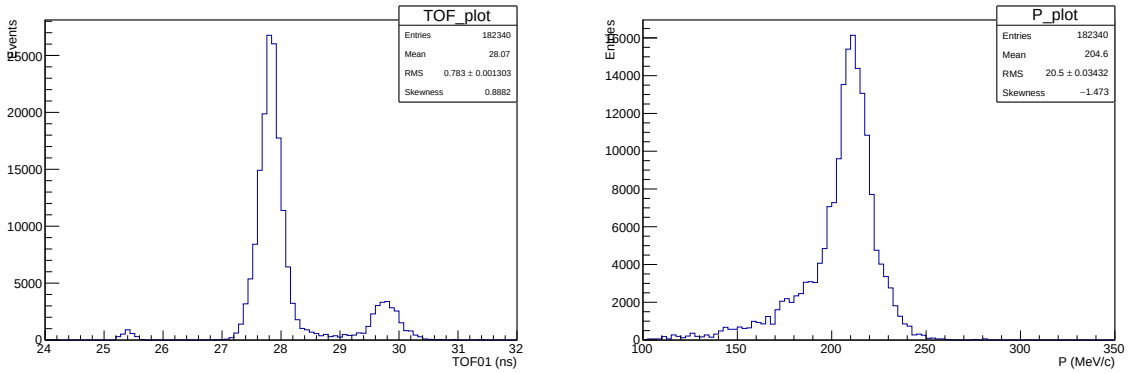

Figure 6.2: Time-of-flight between TOF0 and TOF1 for particles in the 210 MeV/c muon beam for the xenon scattering run (left). Momentum determined for particles with TOF01 greater than 26 ns, assuming a muon hypothesis below 29 ns and a pion hypothesis above 29 ns.

$$\theta_x = \tan^{-1}\left(\frac{p_{yu}}{p_{zu}}\right) - \tan^{-1}\left(\frac{p_{yd}}{p_{zd}}\right), \tag{6.6}$$

$$\theta_y = \tan^{-1}\left(\frac{p_{xu}}{p_{zu}}\right) - \tan^{-1}\left(\frac{p_{xd}}{p_{zd}}\right), \tag{6.7}$$

where p_{xu}, p_{yu}, p_{zu} are the projections of the upstream momentum vector on the x, y, z axes and p_{xd}, p_{yd}, p_{zd} are the projections of the downstream momentum vector on the x, y, z axes. A schematic of the measured angle is shown in figure 6.6. The final result quoted for each beam is the one standard deviation width of the Gaussian fit to the central distribution, between -40 mrad and 40 mrad, of the projected scattering angle distribution. A three-dimensional scattering angle (figure 6.5), which is always positive, is also defined and is given by the definition:

$$\theta = \cos^{-1}\left(\frac{\mathbf{p}_u \cdot \mathbf{p}_d}{|\mathbf{p}_u|\,|\mathbf{p}_d|}\right). \tag{6.8}$$

In the small angle approximation, $\langle\theta^2\rangle \approx \sigma^2_{\theta_x} + \sigma^2_{\theta_y}$.

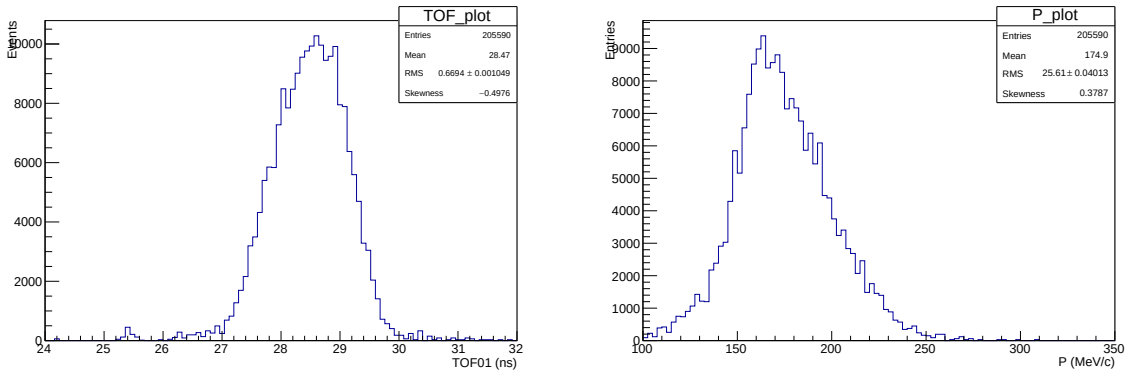

Figure 6.3: Time-of-flight between TOF0 and TOF1 for particles in the muon beam for the lithium hydride (167 MeV/c) scattering run before selection (left). Momentum determined for particles with TOF01 greater than 26 ns, assuming a muon hypothesis.

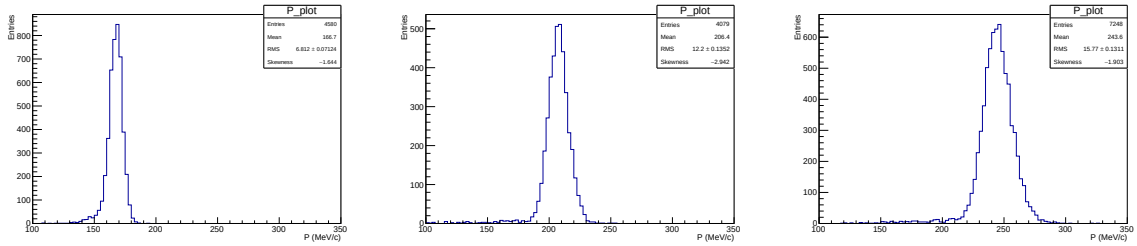

Figure 6.4: Momentum for selected muons determined using TOF12 time-of-flight for 167 (left), 206 (middle) and 244 (right) MeV/c runs. Momentum determined for particles with TOF01 assuming a muon hypothesis.

6.3.1 Deconvolution of Scattering Data

The true scattering distributions must be unfolded from the measured raw scattering distributions. This is to remove the effects introduced by scattering due to other elements in the MICE detector, taking into account the tracker resolution. The unfolding step employs Gold's deconvolution algorithm, to extract the true scattering due to the absorber material as was described in [137]. This technique is employed in nuclear γ-ray spectroscopy and image restoration. This method had the advantage over other methods in that it did not rely on MC or scattering models and was a purely data driven technique making use of all of the data collected. The scattering distribution that is measured by MICE can be stated as:

$$x'(\theta) = \int_{-\infty}^{t} x(\Theta)h(\theta - \Theta)d\Theta + n(\theta) = x(\theta) * h(\theta) + n(\theta), \tag{6.9}$$

where $x'(\theta)$ is the scattering distribution measured with the absorber in the channel including scattering contributions from interstitial material in the channel and the resolution of the tracker. $h(\theta)$ is the scattering distribution measured with the absorber removed but still including the interstitial material and the tracker resolution. $x(\theta)$ is the scattering distribution

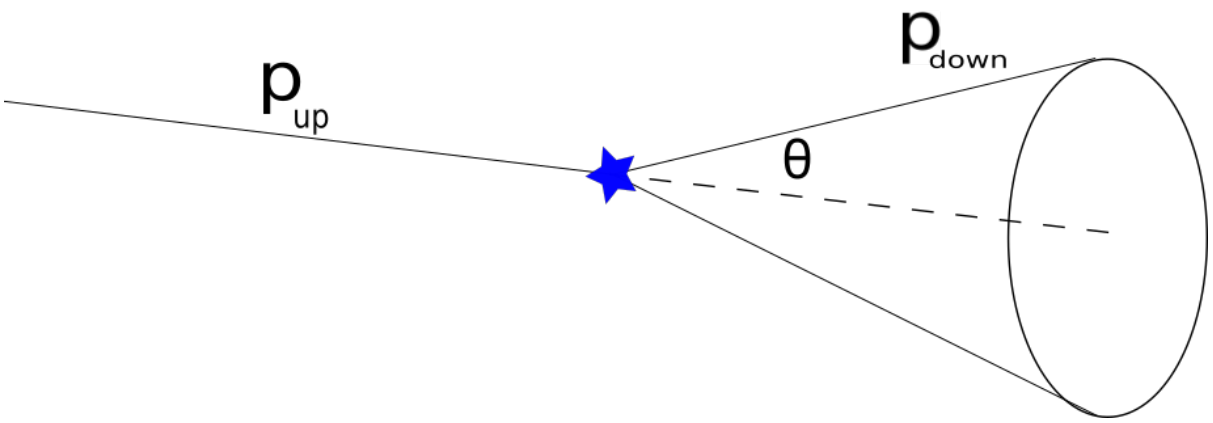

Figure 6.5: The 3D scattering angle is shown as θ for a muon scattering at the point highlighted by the star which can be any point in the target absorber. The p_{up} and p_{down} are the momentum vectors of the muon up- and downstream of the absorber.

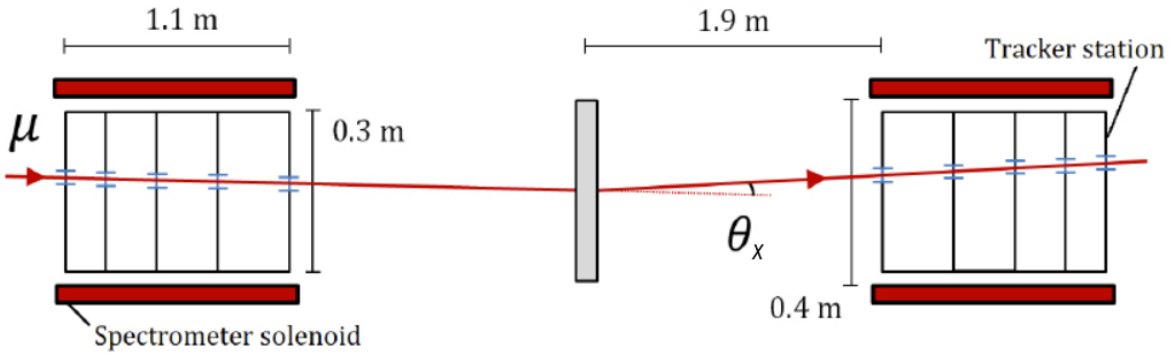

Figure 6.6: The projected scattering angle measurements using straight muon tracks (no magnetic field) in Step IV. Figure taken from Ref. [124].

due only to the absorber material without the interstitial material in the channel and without the tracker resolution. $n(\theta)$ is additive noise and the $*$ denotes the convolution operator. For discrete systems, this statement can be expressed as:

$$x'(i) = \sum_{k=0}^{i} x(k)h(i-k) + n(i) = x(i) * h(i) + n(i), \tag{6.10}$$

an expression which represents a general system of linear equations that can be written in matrix form as:

$$x' = Hx + n \tag{6.11}$$

where the matrix H has dimension $N \times M$, the vectors x' and n have N elements and the vector x has M elements, while $N \geq M$. To find a least squares solution of the system of linear equations given in 6.11

$$||Hx - x'||^2 \tag{6.12}$$

must be minimised. Several methods have been developed that regularise the output and prevent large fluctuations entering the solution. One such method is the Gold algorithm. Starting from the expression:

$$x' = H'x \tag{6.13}$$

where $H' = H^{\boldsymbol{T}} H H^{\boldsymbol{T}}$ and $H^{\boldsymbol{T}}$ is a Toeplitz matrix[2]. x' is known from data, and the method iterates over:

$$x_i^{(k+1)} = \frac{x'_i}{\sum_{m=0}^{N-1} H'_{im} x_m^{(k)}} x_i(K) \tag{6.14}$$

where

$$\begin{aligned} i &= 0, 1, ..., N-1, \\ k &= 1, 2, 3, ..., L, \\ x^0 &= [1, 1..., 1]^T \end{aligned} \tag{6.15}$$

and where L is the number of iterations. The method also incorporates a boosted deconvolution technique whereby for each iteration if the repetition number, R, is greater than r which

[2]A Toeplitz matrix is an $n \times n$ matrix $T_n = [t_{k,j}; k, j = 0, 1, ..., n-1]$ where $t_{k,j} = t_{k-j}$ [138]

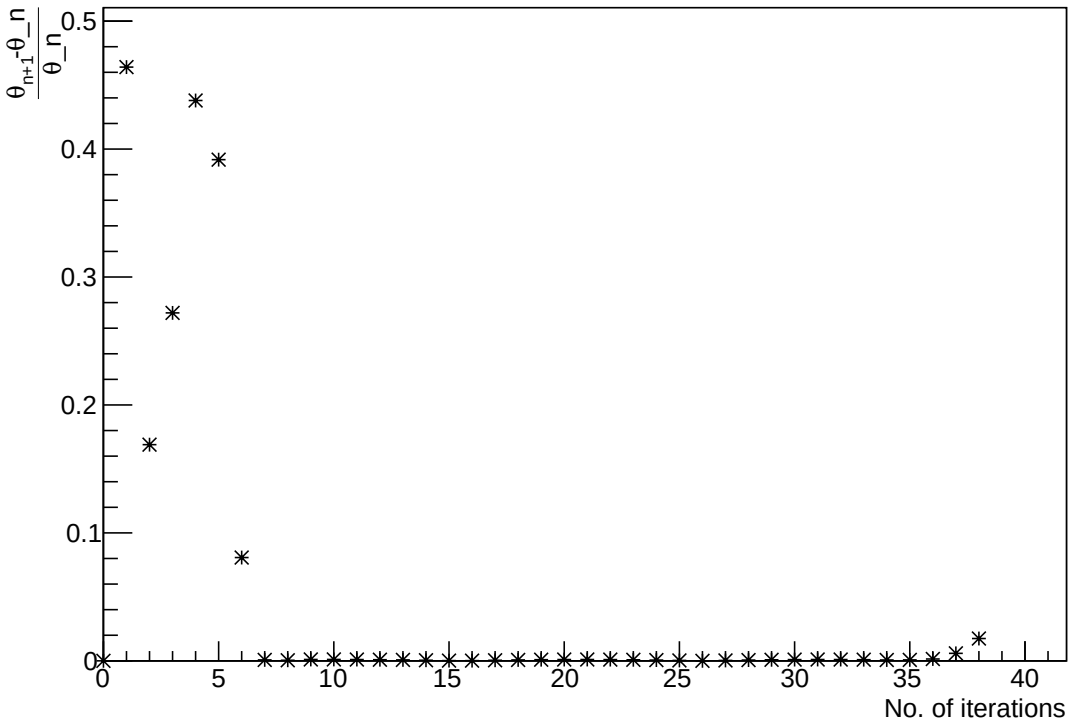

Figure 6.7: The convergence plot for the 204 MeV/c θ_x scattering deconvolution distribution. After less than ten iterations the algorithm converges to a stable solution as the relative change in the width of the scattering distribution from iteration to iteration goes to zero.

is initially defined to be one then

$$x^{(0)}(i) = [x^{(L)}(i)]^p \tag{6.16}$$

where p is the boosting coefficient and r now becomes $r = r + 1$ whereafter the deconvolution continues. In this particular case $r = 0$. This method is encapsulated in a ROOT class TSpectrum [137] and was used to treat the data as an unfolding step. Data were taken both with and without the absorber in the channel as summarised in table 6.2. The ROOT class accepts histograms as input and the scattering distributions for the two cases, with and without absorber, were used as input with the output being the final measured scattering distribution. The algorithim typically converged to a solution after ~ 10 iterations with an example convergence plot shown in figure 6.7.

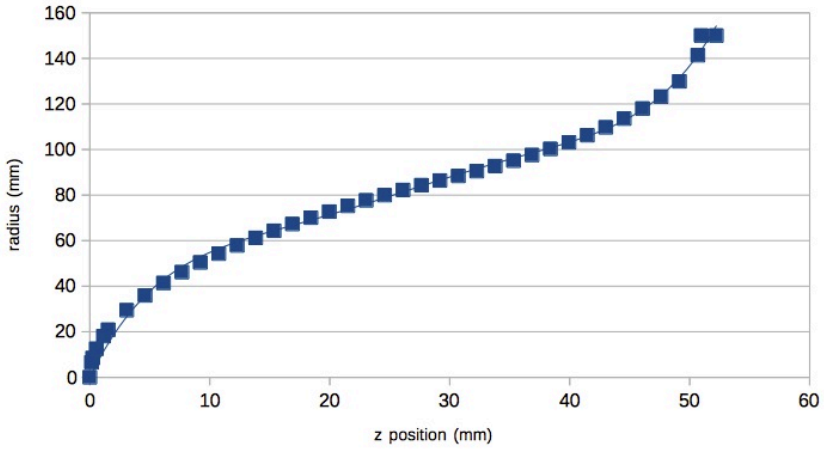

Figure 6.8: The surface of the xenon vessel is described by this polynomial. The data points represent the position of tessellated solids in the simulation and the curve is described by equation 6.17.

6.3.2 Correction for path length in the absorber

The geometry of the up- and downstream face of the xenon absorber vessel (figure 6.8) can be described by the polynomial:

$$r = 5.009^{-6}x^5 - 0.0007x^4 + 0.034x^3 - 0.815x^2 + 10.867x. \tag{6.17}$$

where r is the radius and the x is the transverse position along the absorber surface. This curve is rotated through 360° by GEANT when constructing the geometry in simulation. Tracks at different positions within the beam will intersect the surface at different z positions and traverse different distances in the absorber. To account for this in the scattering distributions the path length in the absorber was calculated for each track and the projected scattering angle weighted to the fraction of a radiation length seen by each track. The path length in the absorber was calculated by extrapolating the tracks measured in the spectrometer solenoids to the surface of the absorber. The point where the straight tracks intersect the surface of the absorber was calculated numerically. Both of the functions describing the straight tracks and the surface of the absorber were incremented in 1 mm steps and the radius determined at each step. When the radius determined by the parametric description of the straight track in 3D is smaller than the radius of the surface the stepping is stopped. With all three coordinates for the intersection point up- and downstream, the vector between the two points can be calculated and the distance determined. One full radiation length in gaseous xenon is 15470 mm with all measured angles weighted to the fraction of this radiation length traversed by the track.

The surface of the lithium hydride was by contrast much simpler in that it was flat and so all tracks enter and exit the absorber material at the same z position. As in the xenon case

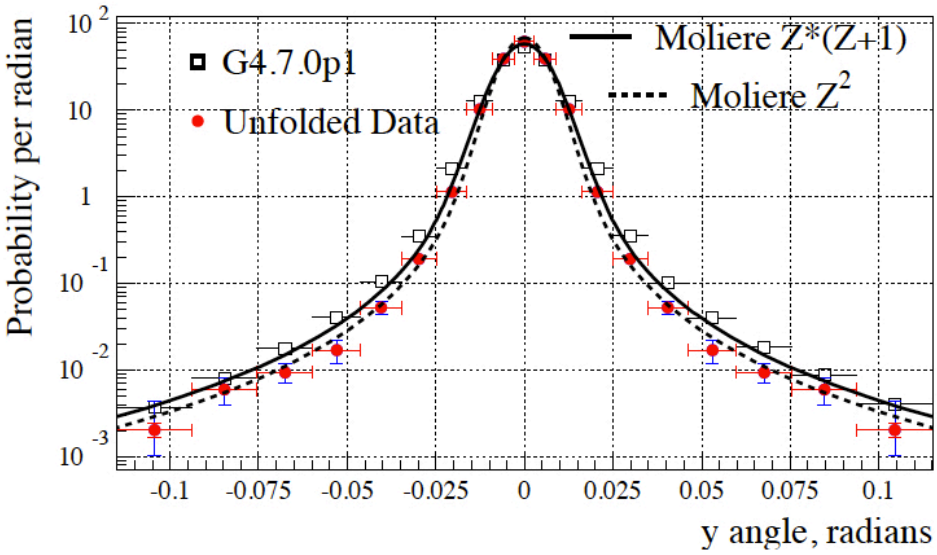

Figure 6.9: The deconvolved θ_y scattering distribution reported by MuScat for the lithium hydride target.

tracks are projected to the absorber surface and the distance through the absorber calculated. The fraction of a radiation length in the absorber was then used to normalise these plots with a single radiation length in lithium hydride being 971 mm.

6.3.3 MuScat

The MuScat experiment collected scattering data in a variety of target materials in April and May 2003. The experiment was located at the TRIUMP labaratory in Canada with the primary goal being the measurment of the scattering distributions of muons for the purposes of modelling both multiple coulomb scattering and ionisation cooling. The experiment ran off the M11 beam line and measurements of the scattering muon tracks were made with a scintillating fibre tracker and the TINA calorimeter with further details given in [125].

Of interest here is the lithium hydride data that MuScat collected during this run. The muons had a momentum of 172 MeV/c and were highly collomated by the MuScat apparatus. The MuScat results are shown in figure 6.9 which can be compared to the scattering distribution reported in this thesis for 167 MeV/c muons shown in figure 6.16. MuScat shows their data superimposed on a variety of different scattering models some of which are reported here, such as the GEANT4 and Moliere models.

6.4 Analysis of xenon scattering data

The purpose of the analysis presented here is to determine multiple scattering distributions of 210 MeV/c muons impinging on a gaseous xenon target, consisting of 2.0% of a radiation length. The analysis follows the procedure outlined in Section 6.3 for the definitions of the scattering angles and the deconvolution treatment described in Section 6.3.1. The raw data yields projected scattering angle distributions are shown in figure 6.10, and the three-dimensional scattering angle squared distribution of muons interacting with the gaseous xenon absorber in MICE is shown in figure 6.11. The deconvolved distributions are shown in figures 6.12 and 6.13.

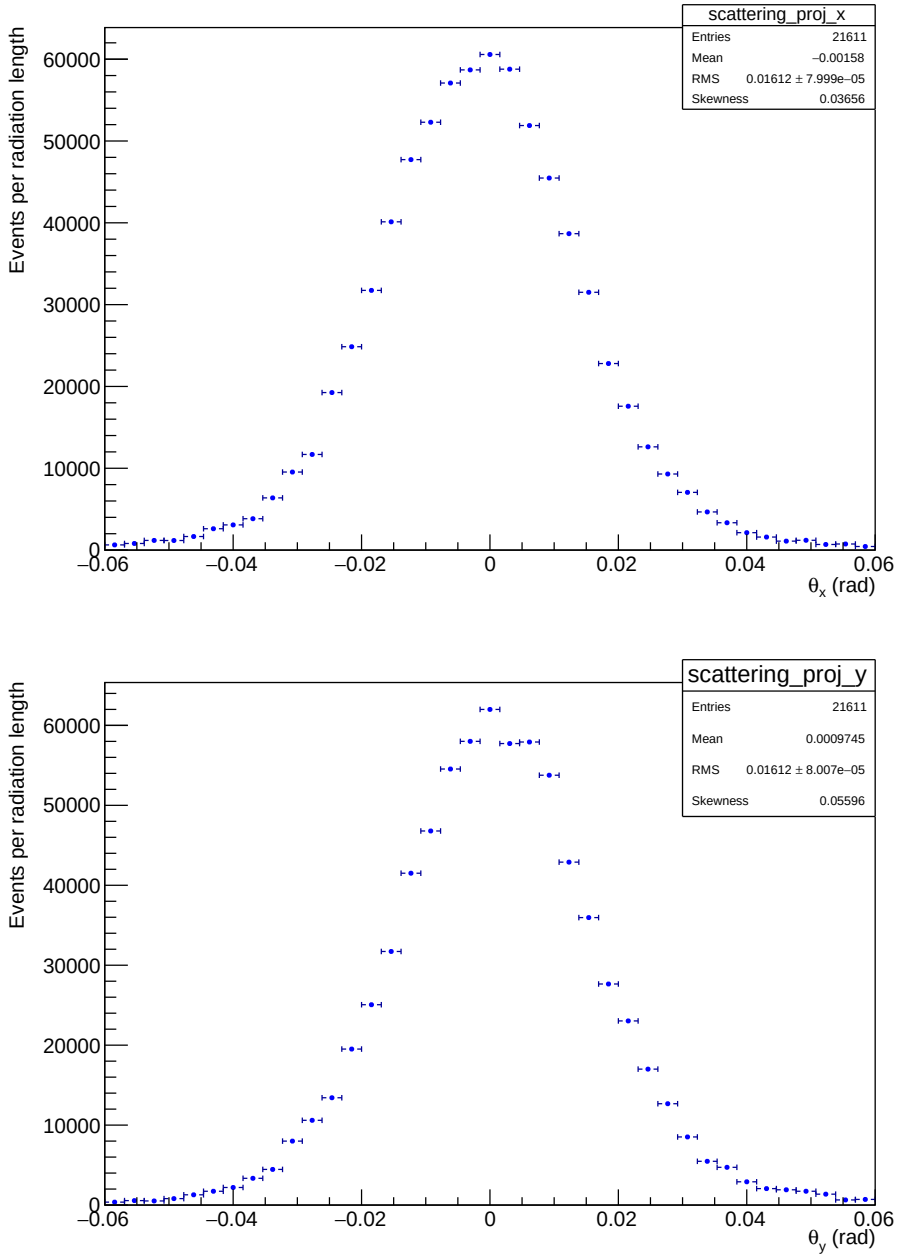

Figure 6.10: Projected θ_x (top) and θ_y (bottom) scattering angular distributions of muons on gaseous xenon, measured by the MICE experiment.

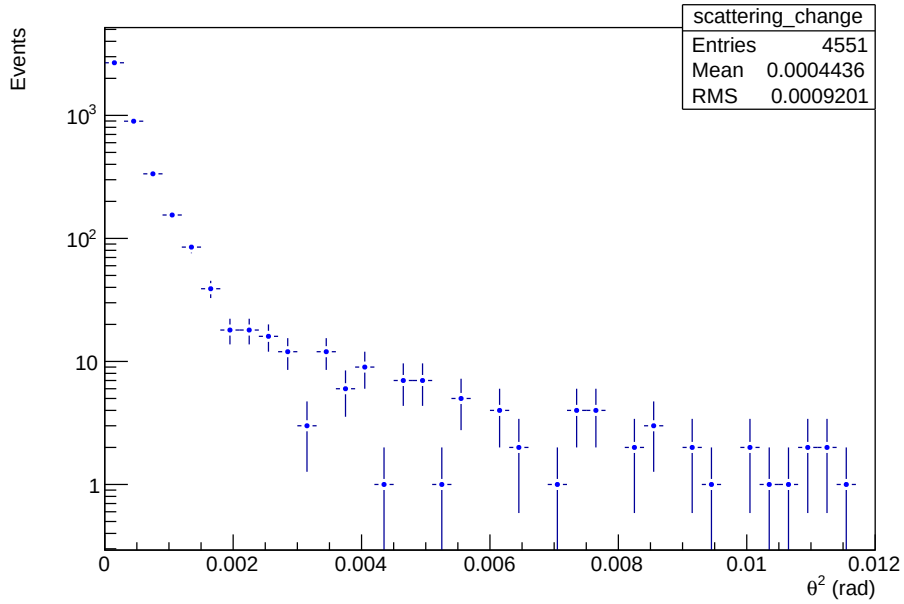

Figure 6.11: Three-dimensional scattering angular squared distributions (θ^2) of muons on gaseous xenon, measured by the MICE experiment.

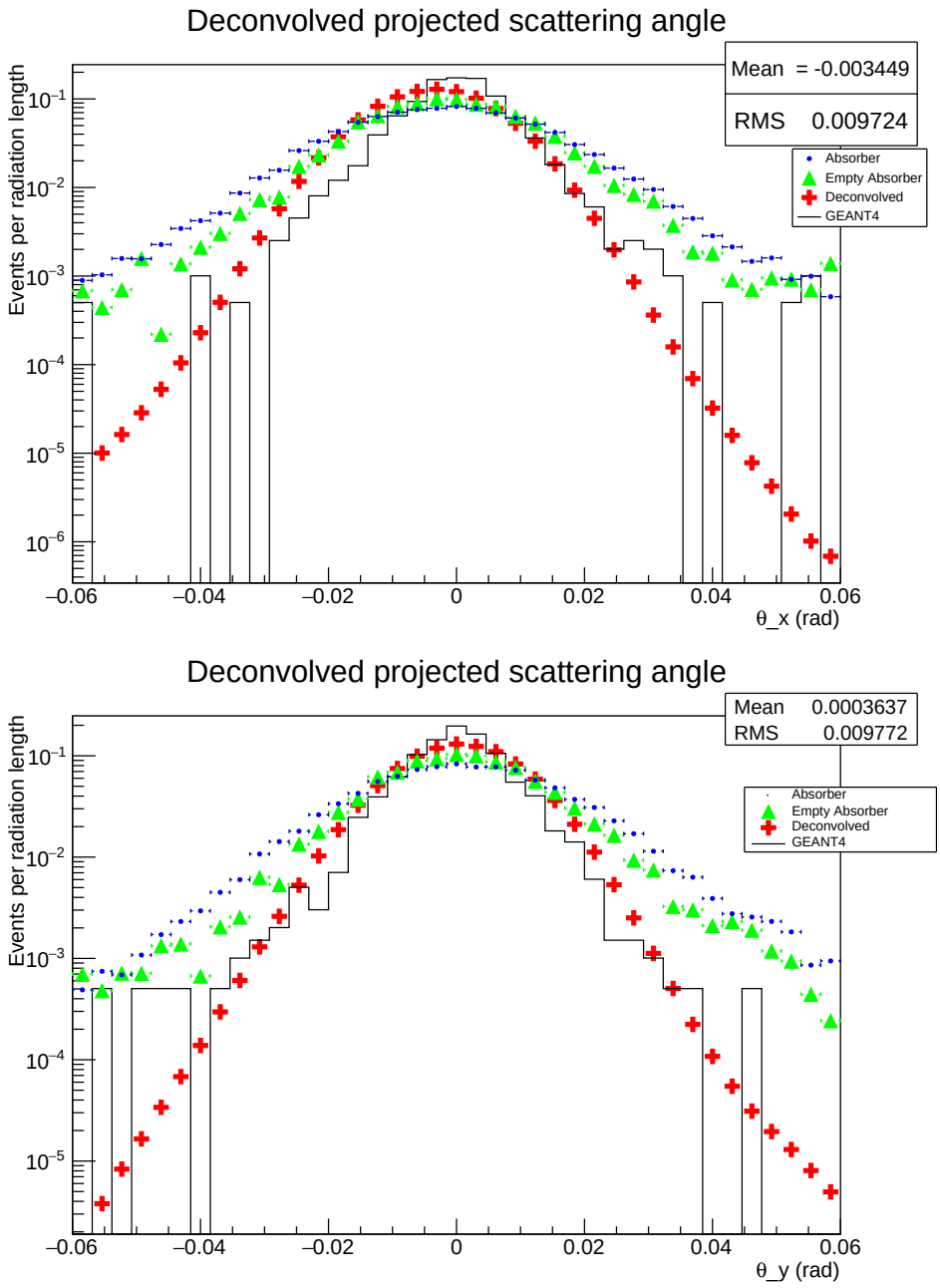

Figure 6.12: The scattering distributions after the Gold deconvolution of the helium channel data from the xenon absorber data for θ_x (top) and θ_y (bottom).

Table 6.5: The data and PDG simulated predictions for the one standard deviation width of the Gaussian fitted to the scattering distribution for the xenon data. The errors are statistical only.

Type		Width of Gaussian for angular distribution (mrads)
		Xe
Raw Data	θ_x	15.24 ± 0.02
	θ_y	15.28 ± 0.02
Particle Data Group	θ_{proj}	10.10
Geant4	θ_x	7.38 ± 0.15
	θ_y	7.43 ± 0.15
Deconvolved Data	θ_x	9.67 ± 0.01
	θ_y	9.67 ± 0.01
	$\langle\theta\rangle$	9.67 ± 0.01

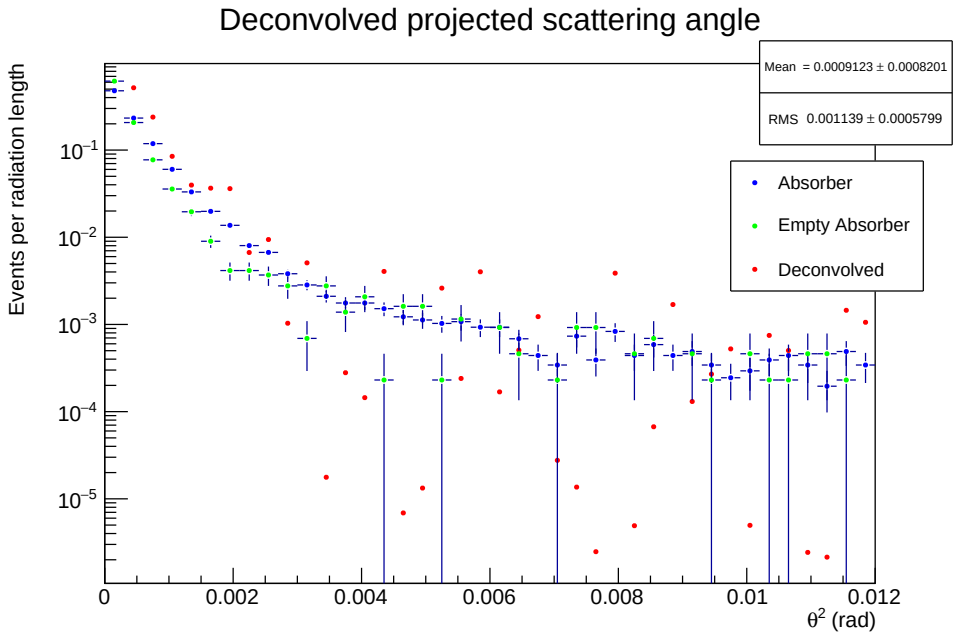

Figure 6.13: Deconvolved three-dimensional scattering angle squared distributions (θ^2) of muons on gaseous xenon, measured by the MICE experiment.

6.5 Analysis of lithium hydride scattering data

The measurement of the MCS in lithium hydride was carried out in the same manner as the measurement for gaseous xenon introduced in Section 6.3. The raw scattering distributions were treated with the same deconvolution procedure. The raw scattering distributions are shown in figures 6.14, 6.18 and 6.22. The plots with the Gold deconvolution in figures 6.16, 6.20 and 6.24. The MCS in lithium hydride was measured at several momentum as summarised in table 6.2. Inspection of equation 6.1 shows that the MCS has a dependence on the momentum of the particle therefore the scattering was measured across the momentum range at which MICE

will measure ionisation cooling to fully characterise the MCS contribution to the cooling performance of the channel. Data were also taken at 167 MeV/c to compare with the measurement performance by MuScat. The width of the Gaussian fitted to the scattering distribution with the momentum of the muon beam is shown in figure 6.26.

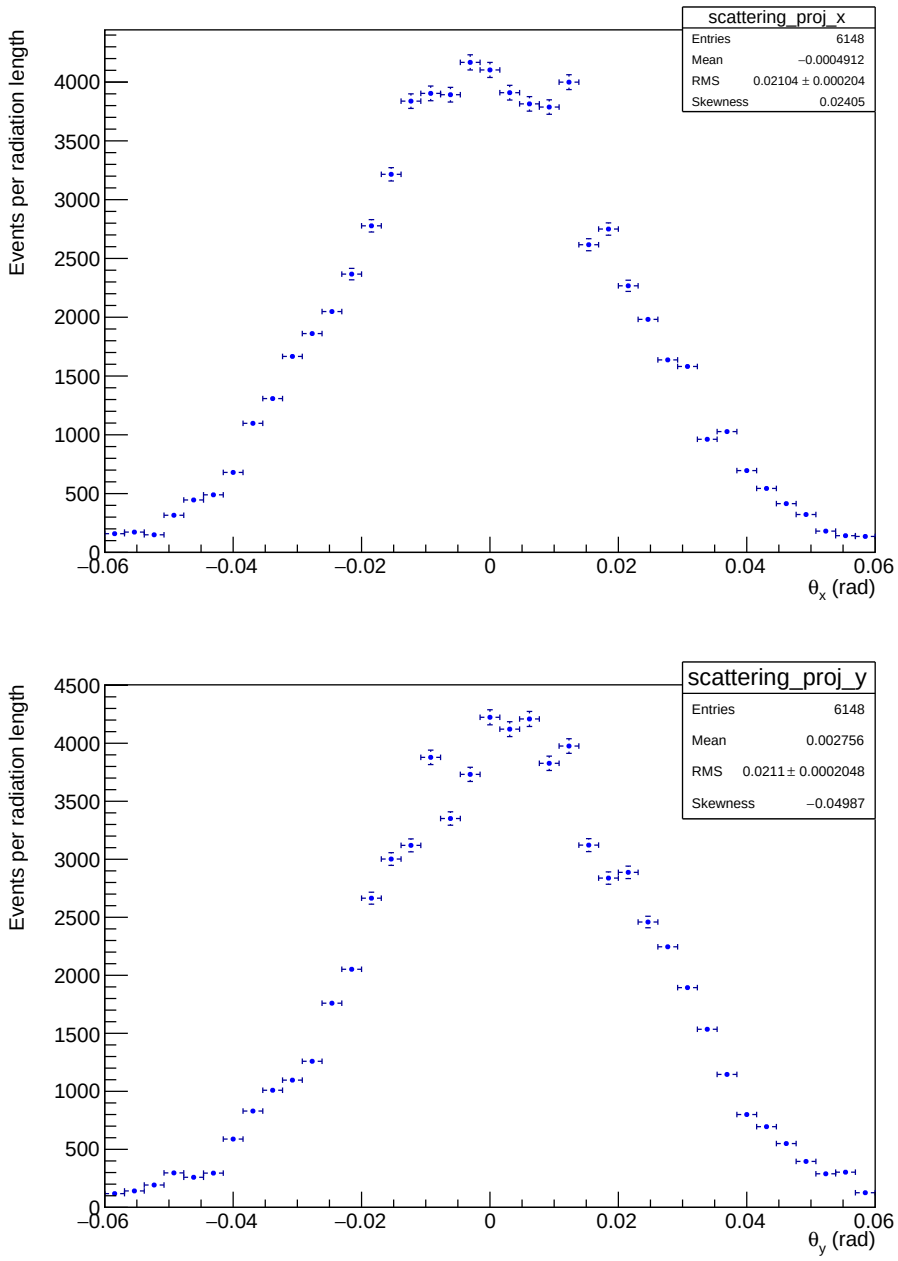

Figure 6.14: Projected θ_x (top) and θ_y (bottom) scattering angular distributions of 167 MeV/c muons on lithium hydride, measured by the MICE experiment.

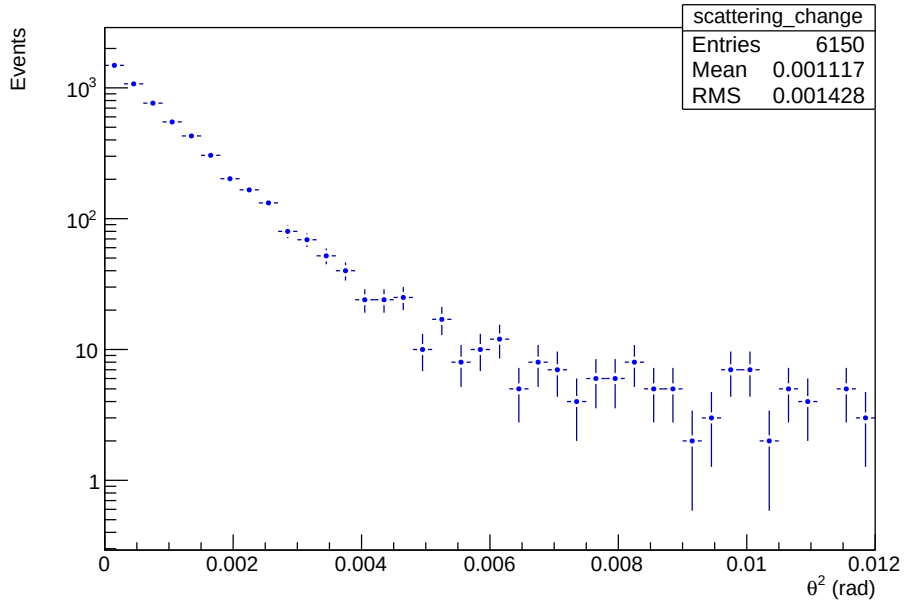

Figure 6.15: Three-dimensional scattering angle squared distributions (θ^2) of 167 MeV/c muons on lithium hydride, measured by the MICE experiment.

6.6 Systematic Errors and Multiple Scattering Results

Statistical errors are based on the number of events in the distribution. The systematic errors are determined by performing the complete analysis under different assumptions. Any difference in the width of the projected scattering distribution under each new assumption is treated as a systematic error.

- TOF selection: The time of flight window selected is shifted by 0.1 ns and the analysis is repeated.
- Projected tracks radius cut: As described in Section 6.3 tracks in the upstream tracker are projected to the downstream tracker reference plane, the plane closest to the absorber, and must be within 150 mm radius from the centre at this plane. The distance from the reference plane downstream to the centre of the downstream tracker is $\sim$ 550 mm and the angular acceptance of the trackers is 50 mrad, therefore tracks within the outer $\sim$ 15 mm of this radius may include fringe effects. The radius is reduced by 15 mm and the analysis is repeated to account for this.
- Alignment: The upstream and downstream trackers are shifted in space by the resolution of the alignment constants determined, and the analysis is repeated.
- Number of bins: The number of bins is halved and the analysis is repeated.

Table 6.6: Summary of systematic errors for xenon data.

Systematic error	% change in Gaussian width fitted to scattering distribution	
	x	y
TOF window	0.31	0.10
Radius proj. tracks	0.21	0.31
Millepede alignment	0.10	0.00
Half no. of bins	0.52	0.21
Total	0.64	0.39

Table 6.7: Summary of systematic errors for lithium hydride 167 MeV/c data.

Systematic error	% change in Gaussian wdith fitted to scattering distribution	
	x	y
TOF window	4.28	4.39
Radius proj. tracks	2.33	1.48
Millepede alignment	0.05	0.22
Half no. of bins	1.30	1.76
Total	5.04	4.96

The total systematic error is the quadratic sum of all the systematic errors. The θ_x and θ_y projections agree with each other, showing that the deconvolution technique removes any inherent biases associated with the measurement system. The final extracted width of the Gaussian fitted to the projected scattering distribution are tabulated in table 6.11. The result is compared to the prediction from GEANT4 where a selection identical to that used for the data was applied to the MC.

The widths of Gaussian fits of the projected distributions are compared to that of the expected widths from the Particle Data Group formula in equation 6.1 for xenon ($Z = 54$), with $2.0\%X_0$ absorber thickness for muons with average momentum of 210 MeV/c in table 6.11 and for lithium hydride with muons at the three momentum points (167, 206 & 244 MeV/c).

Table 6.8: Summary of systematic errors for lithium hydride 206 MeV/c data.

Systematic error	% change in Gaussian width fitted to scattering distribution	
	x	y
TOF window	4.43	1.22
Radius proj. tracks	0.63	0.57
Millepede alignment	0.07	0.00
Half no. of bins	0.07	0.29
Total	4.48	1.90

Table 6.9: Summary of systematic errors for lithium hydride 244 MeV/c data.

Systematic error	% change in Gaussian width fitted to scattering distribution	
	x	y
TOF window	2.37	3.89
Radius proj. tracks	1.06	0.91
Millepede alignment	0.16	0.00
Half no. of bins	0.08	0.41
Total	2.60	4.02

Table 6.10: The data and PDG simulated predictions for the width of the Gaussian fitted to the projected scattering distribution for the xenon data. The errors are statistical and systematic.

Type		Width of Gaussian fitted to angular distribution (mrads)
		Xe
Raw Data	θ_x	15.24 ± 0.02
	θ_y	15.28 ± 0.02
Particle Data Group	θ_{proj}	10.10
Geant4	θ_x	7.38 ± 0.15
	θ_y	7.43 ± 0.15
Deconvolved Data	θ_x	$9.67 \pm 0.01 \pm 0.06$
	θ_y	$9.67 \pm 0.01 \pm 0.04$
	$\langle\theta\rangle$	$9.67 \pm 0.01 \pm 0.07$

Table 6.11: The data and PDG simulated predictions for the width of the Gaussian fitted to the projected scattering distribution for the lithium hydride data. The errors are statistical and systematic.

Type		Width of Gaussian fitted to angular distribution (mrads)		
		LiH (167 MeV/c)	LiH (206 MeV/c)	LiH (244 MeV/c)
Raw Data	θ_x	21.44 ± 0.10	16.93 ± 0.06	14.63 ± 0.04
	θ_y	21.47 ± 0.10	16.91 ± 0.06	14.53 ± 0.04
Particle Data Group	θ_{proj}	24.71	18.81	15.36
Geant4	θ_x	17.51 ± 0.19	14.33 ± 0.35	11.80 ± 0.08
	θ_y	17.56 ± 0.20	14.35 ± 0.35	11.88 ± 0.08
Deconvolved Data	θ_x	$18.44 \pm 0.09 \pm 0.93$	$14.21 \pm 0.05 \pm 0.64$	$12.25 \pm 0.03 \pm 0.32$
	θ_y	$18.23 \pm 0.09 \pm 0.90$	$13.97 \pm 0.05 \pm 0.27$	$12.07 \pm 0.03 \pm 0.49$
	$\langle\theta\rangle$	$18.34 \pm 0.06 \pm 1.29$	$14.09 \pm 0.04 \pm 0.70$	$12.16 \pm 0.02 \pm 0.60$

6.7 Conclusions

The multiple scattering distributions of 210 MeV/c muons impinging on gaseous xenon with 2.0% of a radiation length and for muons with average momenta of 167 MeV/c, 206 MeV/c and 244 MeV/c traversing a LiH absorber of 6.7% of a radiation length using the MICE apparatus have been extracted in this chapter. The developed techniques to perform measurements of projected scattering angles and the three-dimensional scattering angle have been described and were applied to both the xenon and the lithium hydride data. The detector effects were deconvolved with the empty absorber data, in order to extract the best measurement of the true scattering distributions. These distributions have been compared to the GEANT4 expectation and the expectation from an approximate formula recommended by the PDG. For the xenon data good agreement is observed between the approximate PDG formula and the data and for the lithium hydride the PDG formula is shown to over estimate the width of the projected scattering distributions while GEANT4 is consistent within the errors.

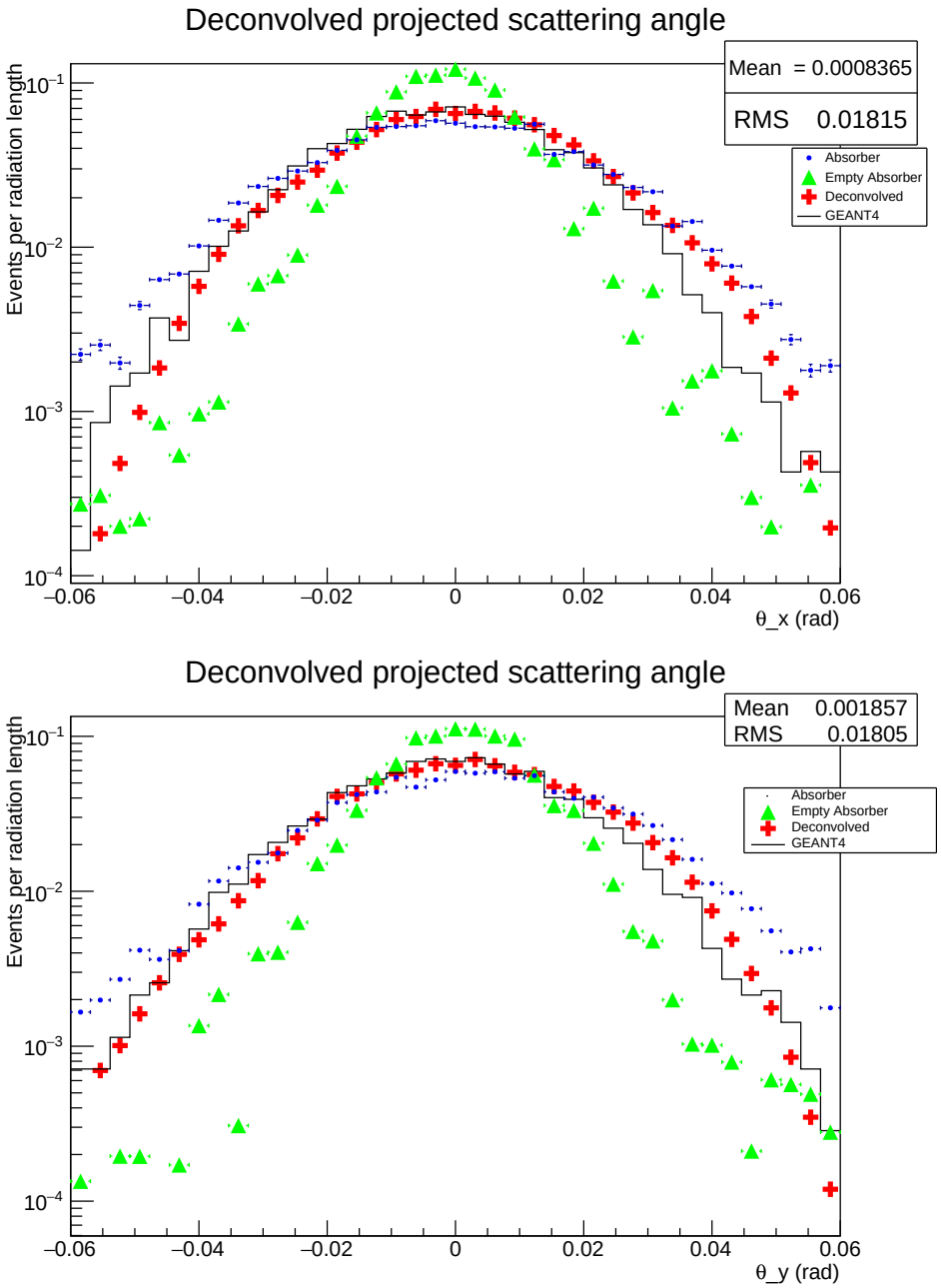

Figure 6.16: The scattering distributions after the Gold deconvolution of the empty channel data from the absorber data for θ_x (top) and θ_y (bottom) for 167 MeV/c muons on lithium hydride.

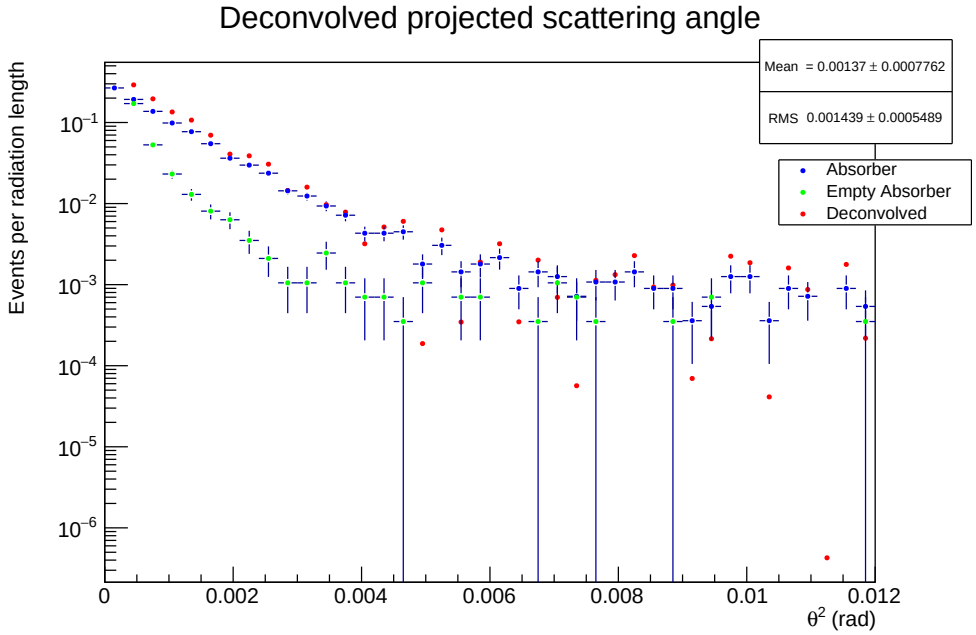

Figure 6.17: Deconvolved three-dimensional scattering angle squared distributions (θ^2) of 167 MeV/c muons on lithium hydride, measured by the MICE experiment.

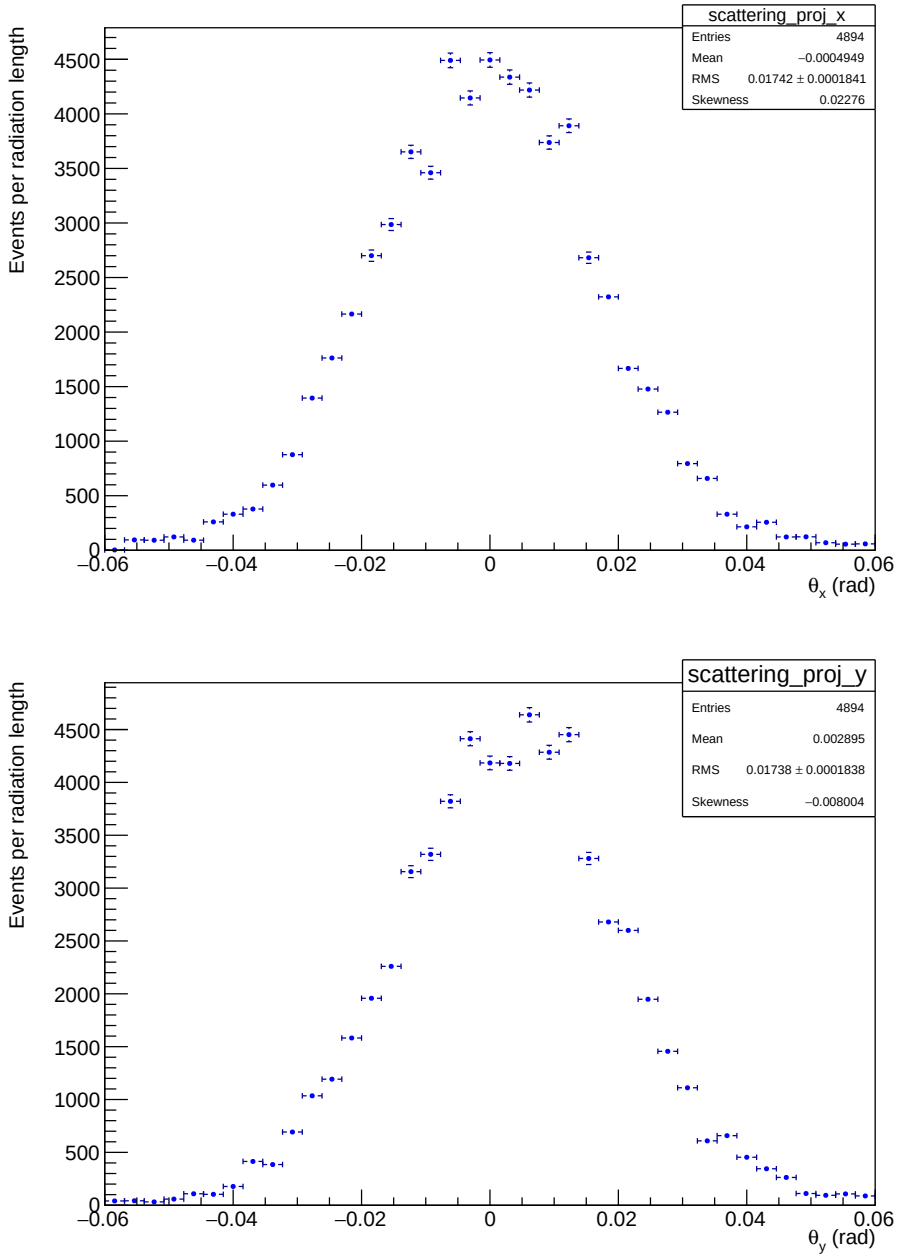

Figure 6.18: Projected θ_x (top) and θ_y (bottom) scattering angular distributions of 206 MeV/c muons on lithium hydride, measured by the MICE experiment.

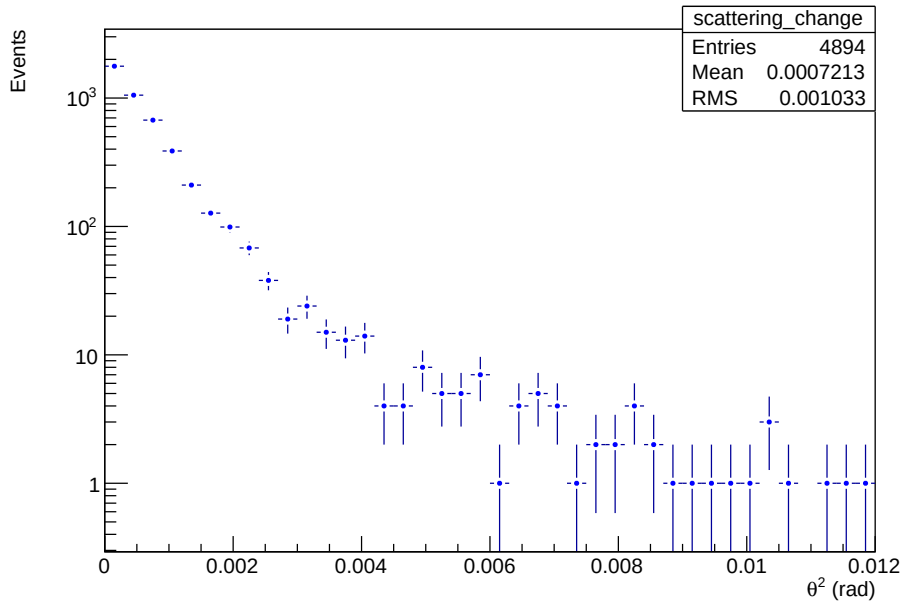

Figure 6.19: Three-dimensional scattering angle squared distributions (θ^2) of 206 MeV/c muons on lithium hydride, measured by the MICE experiment.

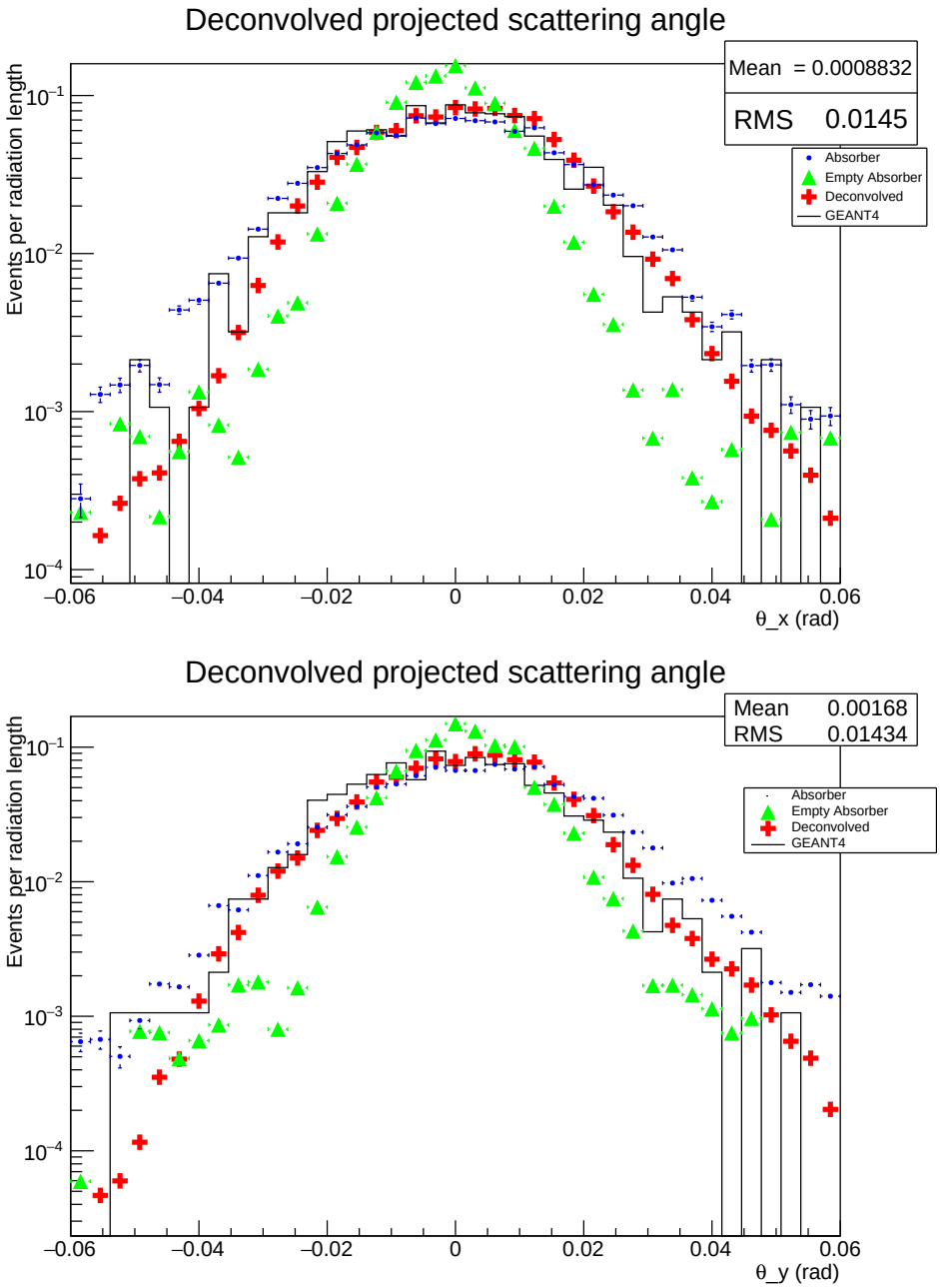

Figure 6.20: The scattering distributions after the Gold deconvolution of the empty channel data from the absorber data for θ_x (top) and θ_y (bottom) for 206 MeV/c muons on lithium hydride.

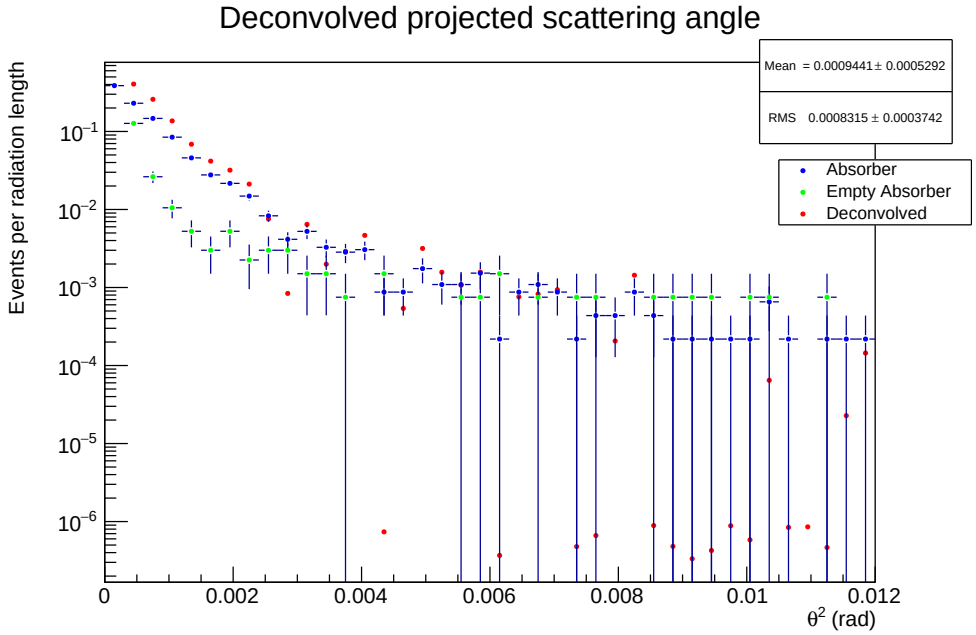

Figure 6.21: Deconvolved three-dimensional scattering angle squared distributions (θ^2) of 206 MeV/c muons on lithium hydride, measured by the MICE experiment.

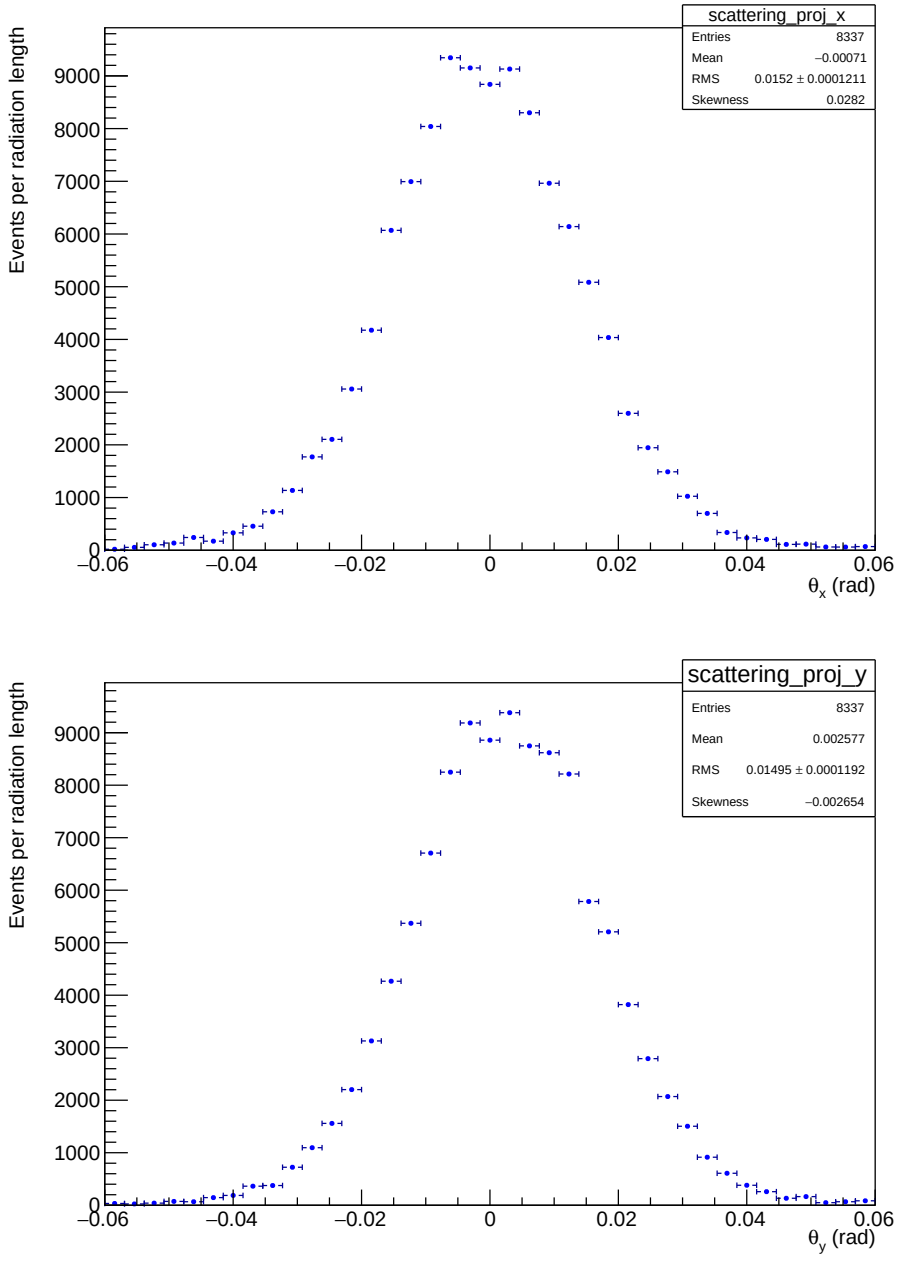

Figure 6.22: Projected θ_x (top) and θ_y (bottom) scattering angular distributions of 244 MeV/c muons on lithium hydride, measured by the MICE experiment.

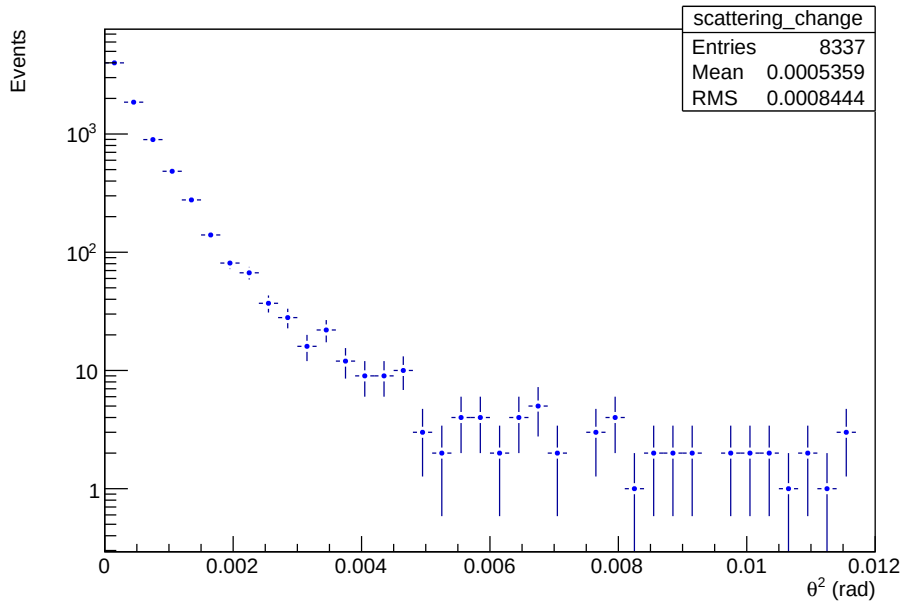

Figure 6.23: three-dimensional scattering angle squared distributions (θ^2) of 244 MeV/c muons on lithium hydride, measured by the MICE experiment.

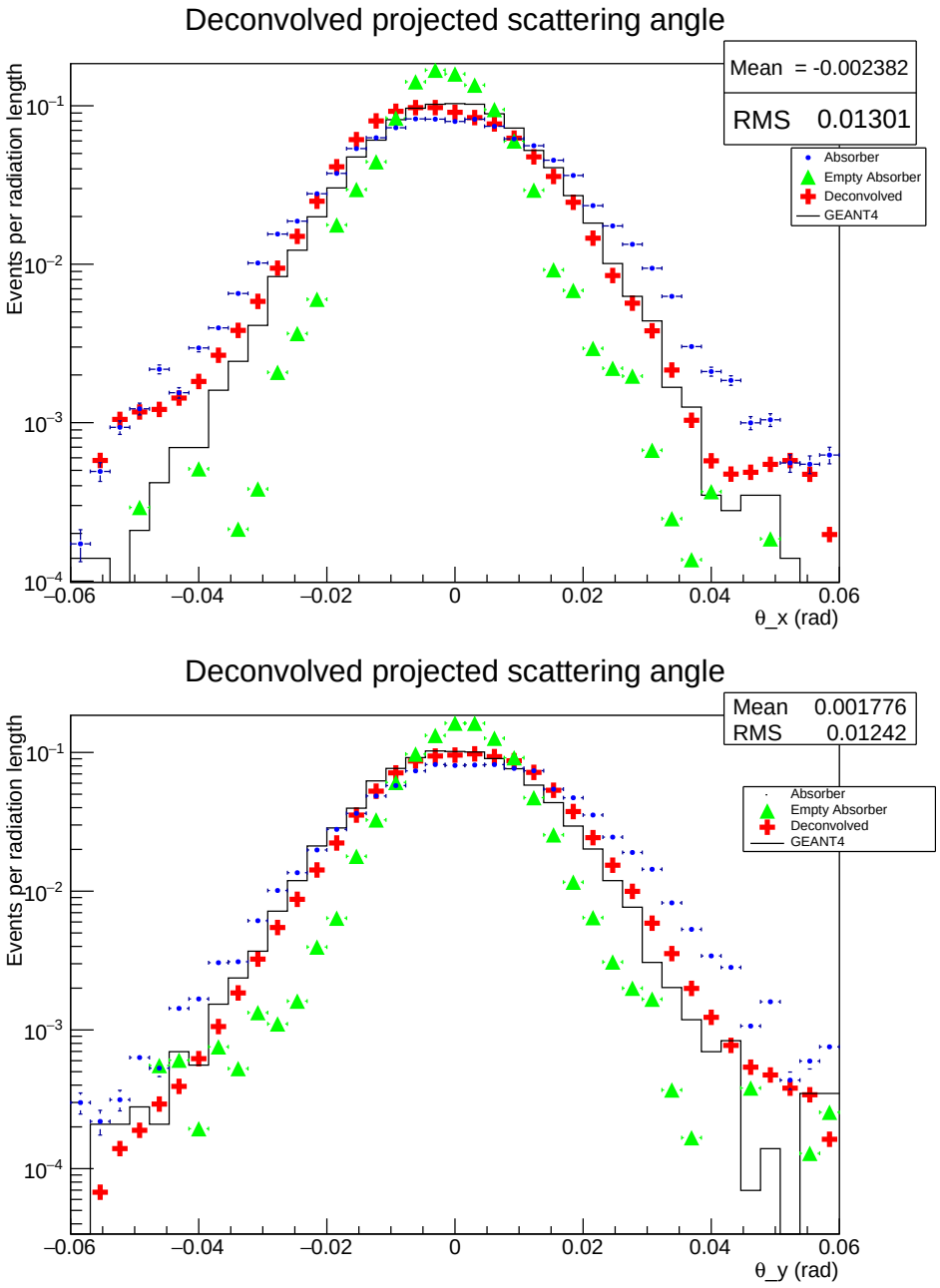

Figure 6.24: The scattering distributions after the Gold deconvolution of the empty channel data from the absorber data for θ_x (top) and θ_y (bottom) for 244 MeV/c muons on lithium hydride.

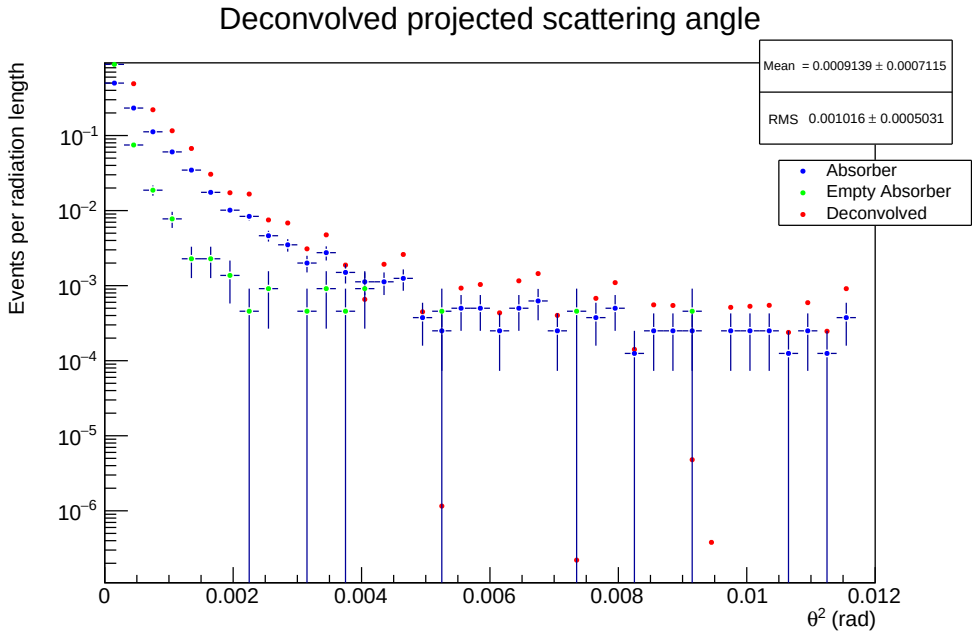

Figure 6.25: Deconvolved three-dimensional scattering angle squared distributions (θ^2) of 244 MeV/c muons on lithium hydride, measured by the MICE experiment.

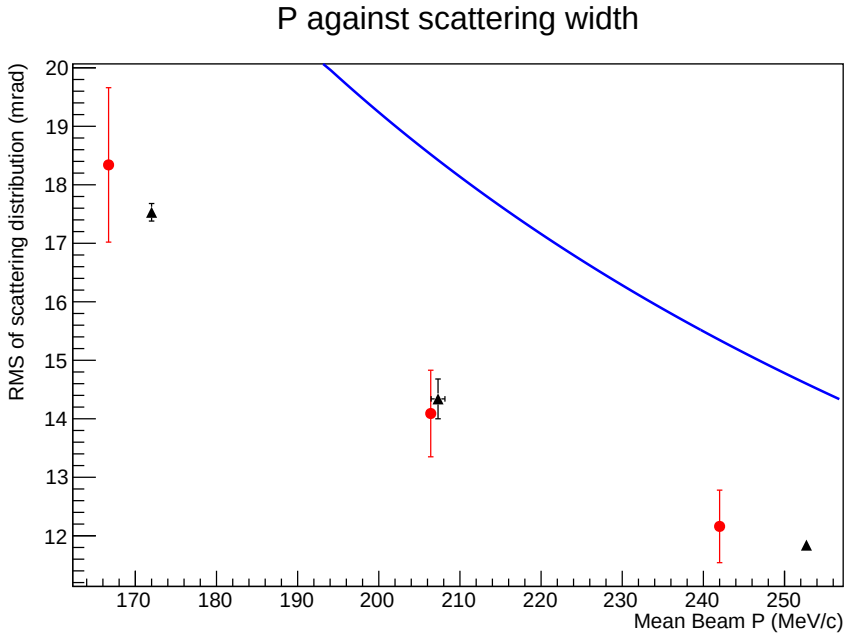

Figure 6.26: The width of the scattering distributions for lithium hydride plotted as a function of the average beam momentum. The red circles are the measured deconvolved data, the black triangles are the GEANT4 prediction and the blue line shows the PDG formula prediction.

Chapter 7

Conclusions

Neutrino oscillations are the first observed phenomena beyond the SM and, as such, offer a unique probe of nature. While all of the oscillation parameters have now been measured, it is desirable to measure these parameters to the precision achieved in the quark sector. If such precision can be achieved this would allow a statement to be made about the value of δ_{CP} in the lepton sector. Given the constraints on δ_{CP} in the quark sector, the CP violation phase in the lepton sector may be the only way to explain the observed baryon asymmetry in the universe. To this end, designs have been developed for the "ultimate precision" machine, the neutrino factory. This facility will be capable of providing beams of neutrinos from 10^{21} muon decays per year, measuring the CP violating phase to 5° accuracy. The near detector station and the muon storage beam setup will also allow the neutrino cross-sections to be measured with unprecedented accuracy. This can provide invaluable information for other future accelerator neutrino experiments. The MICE experiment will demonstrate a novel cooling technique which will form a crucial part of the neutrino factory design.

Simulations for the MICE experiment rely chiefly on two software packages, MAUS and G4beamline. The large scale simulations from the pion production target through the upstream beam line are performed with G4beamline and the various downstream configuration specific simulations are done in MAUS, using the G4beamline seed particles. To ensure consistency, G4beamline is now included in MAUS as a third party package, with the setup amended to reflect the latest survey measurements of the MICE hall. The studies described in chapter 3 validate these simulations showing the agreement between the new simulations and data over a number of beam parameters. With these updated simulations, new large scale jobs were run on the Grid with the newly installed software providing simulations for a variety of analyses within MICE.

In 2011, data were taken with MICE in its Step I configuration, which was used to determine the pion contamination in the MICE muon beam. Timing information from the TOF detectors was used to select calibration samples of pions and muons in the MICE muon beam. The signature of each of these samples in the KL detector was then weighted against the response with the muon beam used for the emittance reduction experiment and the analysis yielded a pion contamination compatible with zero. The Monte Carlo expectation for the pion contamination of a $\pi \rightarrow \mu$ beam of 6π mm $\cdot$ rad emittance and 206 MeV/c nominal momentum is $(0.22 \pm 0.01)\%$ at the KL and an upper limit on the pion contamination in the Monte Carlo simulation extracted with this method is $f_{\pi}^{MC} < 2.1\%$ including the systematics errors. The upper limit for the pion contamination of the MICE Muon Beam in its Step I configuration at the KL position was found to be $f_{\pi} < 1.4\%$ at 90% C.L., including systematic errors. This upper limit on the pion contamination in the MICE Muon Beam, combined with the performance of the PID system, meets the experimental requirement.

Critical to the success of the neutrino factory will be effective cooling of the muon beam before injection into the front end. The cooling performance will be determined by the material physics parameters of the absorber material in the cooling channel, namely lithium hydride. To that end, the multiple scattering in lithium hydride, which will act as the absorber in the beam, has been measured as part of Step IV, using the two MICE scintillating fibre trackers. These were first aligned using empty channel data taken in March 2016 with the Millepede alignment software package, which is a non-iterative method that minimises a χ^2 function by a single matrix inversion technique.

After correcting for biases due to any misalignment, the multiple scattering was measured first in xenon, to benchmark subsequent measurements, and then in lithium hydride. The final result shows that for high-Z materials, the PDG scattering formula and GEANT4 are accurate, however for the low-Z materials such as lithium hydride the PDG formula overestimates the width of the projected scattering distributions while GEANT4 is consistent within errors. These multiple scattering results in lithium hydride are essential to be able to extract the final cooling performance in the MICE ionisation cooling demonstration and for the final design of a neutrino factory.

Bibliography

[1] W. Pauli, "Dear radioactive ladies and gentlemen," *Phys. Today* **31N9** (1978) 27.

[2] F. A. Scott, "Energy Spectrum of the Beta-Rays of Radium E," *Phys. Rev.* **48** (1935) 391–395.

[3] C. L. Cowan, Jr., F. Reines, F. B. Harrison, H. W. Kruse, and A. D. McGuire, "Detection of the free neutrino: A confirmation," *Science* **124** (July, 1956) 103–104.

[4] A. D. Sakharov, "Violation of CP invariance, C asymmetry, and baryon asymmetry of the universe," *Pisma Zh. Eksp. Teor. Fiz.* **5** (1967) 32–35. [Usp. Fiz. Nauk161,61(1991)].

[5] **Particle Data Group** Collaboration, K. Nakamura *et al.*, "Review of particle physics," *J. Phys.* **G37** (2010) 075021.

[6] A. G. Cohen, S. L. Glashow, and Z. Ligeti, "Disentangling Neutrino Oscillations," *Phys. Lett.* **B678** (2009) 191–196, arXiv:0810.4602 [hep-ph].

[7] S. M. Bilenky and B. Pontecorvo, "Lepton Mixing and Neutrino Oscillations," *Phys.Rept.* **41** (1978) 225–261.

[8] S. Goswami, A. Bandyopadhyay, and S. Choubey, "Global analysis of neutrino oscillation," *Nucl. Phys. Proc. Suppl.* **143** (2005) 121–128, arXiv:hep-ph/0409224 [hep-ph].

[9] **Super-Kamiokande Collaboration** Collaboration, Y. Fukuda *et al.*, "Evidence for oscillation of atmospheric neutrinos," *Phys.Rev.Lett.* **81** (1998) 1562–1567, arXiv:hep-ex/9807003 [hep-ex].

[10] L. Wolfenstein, "Neutrino Oscillations in Matter," *Phys. Rev.* **D17** (1978) 2369–2374.

[11] S. P. Mikheev and A. Yu. Smirnov, "Resonance Amplification of Oscillations in Matter and Spectroscopy of Solar Neutrinos," *Sov. J. Nucl. Phys.* **42** (1985) 913–917. [Yad. Fiz.42,1441(1985)].

[12] K. Nakamura and S. T. Petcov, "Neutrino Mass, Mixing and Oscillations." http://pdg.lbl.gov/2013/reviews/rpp2013-rev-neutrino-mixing.pdf, 2013.

[13] A. de Gouvea, "On determining the neutrino mass hierarchy." http://theory.fnal.gov/seminars/slides/2006/AGouvea.pdf, 2006.

[14] E. D. Church, K. Eitel, G. B. Mills, and M. Steidl, "Statistical analysis of different muon-anti-neutrino → electron-anti-neutrino searches," *Phys. Rev.* **D66** (2002) 013001, arXiv:hep-ex/0203023 [hep-ex].

[15] **MiniBooNE** Collaboration, A. A. Aguilar-Arevalo *et al.*, "Improved Search for $\bar{\nu}_\mu \to \bar{\nu}_e$ Oscillations in the MiniBooNE Experiment," *Phys. Rev. Lett.* **110** (2013) 161801, arXiv:1207.4809 [hep-ex].

[16] P. Huber, M. Mezzetto, and T. Schwetz, "On the impact of systematical uncertainties for the CP violation measurement in superbeam experiments," *JHEP* **03** (2008) 021, arXiv:0711.2950 [hep-ph].

[17] **nuSTORM** Collaboration, P. Kyberd *et al.*, "nuSTORM - Neutrinos from STORed Muons: Letter of Intent to the Fermilab Physics Advisory Committee," arXiv:1206.0294 [hep-ex].

[18] J. A. Formaggio and G. P. Zeller, "From eV to EeV: Neutrino Cross Sections Across Energy Scales," *Rev. Mod. Phys.* **84** (2012) 1307, arXiv:1305.7513 [hep-ex].

[19] D. Casper, "The Nuance neutrino physics simulation, and the future," *Nucl. Phys. Proc. Suppl.* **112** (2002) 161–170, arXiv:hep-ph/0208030 [hep-ph]. [,161(2002)].

[20] *Fundamental Physics at the Intensity Frontier*. 2012. arXiv:1205.2671 [hep-ex]. http://inspirehep.net/record/1114323/files/arXiv:1205.2671.pdf.

[21] O. Palamara, "Recent results and perspectives in neutrino oscillation physics," *AIP Conf.Proc.* **1560** (2013) 155–162.

[22] **T2K** Collaboration, K. Abe *et al.*, "Measurement of the Inclusive Electron Neutrino Charged Current Cross Section on Carbon with the T2K Near Detector," *Phys. Rev. Lett.* **113** no. 24, (2014) 241803, arXiv:1407.7389 [hep-ex].

[23] **MINERvA** Collaboration, J. Wolcott *et al.*, "Measurement of electron neutrino quasielastic and quasielasticlike scattering on hydrocarbon at $\langle E_\nu \rangle$ = 3.6 GeV," *Phys. Rev. Lett.* **116** no. 8, (2016) 081802, arXiv:1509.05729 [hep-ex].

[24] **MINERvA** Collaboration, J. Wolcott, "Electron Neutrino Charged-Current Quasielastic Scattering in the MINERvA Experiment," in *10th International Workshop on Neutrino-Nucleus Interactions in the Few GeV Region (NuInt15) Osaka, Japan, November 16-21, 2015*. 2015. arXiv:1512.09312 [hep-ex]. http://inspirehep.net/record/1411824/files/arXiv:1512.09312.pdf.

[25] **Daya Bay** Collaboration, F. P. An *et al.*, "A side-by-side comparison of Daya Bay antineutrino detectors," *Nucl. Instrum. Meth.* **A685** (2012) 78–97, arXiv:1202.6181 [physics.ins-det].

[26] Y. Ding, Z. Zhang, J. Liu, Z. Wang, P. Zhou, and Y. Zhao, "A new gadolinium-loaded liquid scintillator for reactor neutrino detection," *Nuclear Instruments and Methods in Physics Research Section A: Accelerators, Spectrometers, Detectors and Associated Equipment* **584** no. 1, (2008) 238 – 243. http://www.sciencedirect.com/science/article/pii/S016890020702092X.

[27] **Daya Bay** Collaboration, D. M. Webber, "An Improved Measurement of Electron Antineutrino Disappearance at Daya Bay," arXiv:1211.1609 [hep-ex]. [Nucl. Phys. Proc. Suppl.233,96(2012)].

[28] **JUNO** Collaboration, Z. Djurcic *et al.*, "JUNO Conceptual Design Report," arXiv:1508.07166 [physics.ins-det].

[29] **KamLAND** Collaboration, S. Abe *et al.*, "Precision Measurement of Neutrino Oscillation Parameters with KamLAND," *Phys. Rev. Lett.* **100** (2008) 221803, arXiv:0801.4589 [hep-ex].

[30] **Super-Kamiokande** Collaboration, Y. Ashie *et al.*, "A Measurement of atmospheric neutrino oscillation parameters by Super-Kamiokande I," *Phys. Rev.* **D71** (2005) 112005, arXiv:hep-ex/0501064 [hep-ex].

[31] B. Cleveland, T. Daily, J. Davis, Raymond, J. R. Distel, K. Lande, *et al.*, "Measurement of the solar electron neutrino flux with the Homestake chlorine detector," *Astrophys.J.* **496** (1998) 505–526.

[32] T. Gaisser and F. Halzen, "IceCube," *Ann. Rev. Nucl. Part. Sci.* **64** (2014) 101–123.

[33] D. Abdurashitov *et al.*, "Results from SAGE," *Phys. Lett.* **B328** (1994) 234–248.

[34] **GALLEX** Collaboration, W. Hampel *et al.*, "GALLEX solar neutrino observations: Results for GALLEX IV," *Phys. Lett.* **B447** (1999) 127–133.

[35] **Borexino** Collaboration, G. Alimonti *et al.*, "The Borexino detector at the Laboratori Nazionali del Gran Sasso," *Nucl. Instrum. Meth.* **A600** (2009) 568–593, arXiv:0806.2400 [physics.ins-det].

[36] **SNO Collaboration** Collaboration, J. Farine, "Measurement of the rate of $\nu_e + d \to p + p + e^-$ interactions produced by B-8 solar neutrinos at the Sudbury Neutrino Observatory," *Phys. Atom. Nucl.* **65** (2002) 2147–2155.

[37] **SNO** Collaboration, J. Boger *et al.*, "The Sudbury neutrino observatory," *Nucl. Instrum. Meth.* **A449** (2000) 172–207, arXiv:nucl-ex/9910016 [nucl-ex].

[38] R. Ospanov, *A measurement of muon neutrino disappearance with the MINOS detectors and NuMI beam*. PhD thesis, Texas U., 2008. http://lss.fnal.gov/cgi-bin/find_paper.pl?thesis-2008-04.

[39] **MINOS** Collaboration, L. H. Whitehead, "Neutrino Oscillations with MINOS and MINOS+," *Nucl. Phys. B* (2016) , arXiv:1601.05233 [hep-ex].

[40] **MINOS** Collaboration, P. Adamson *et al.*, "Electron neutrino and antineutrino appearance in the full MINOS data sample," *Phys. Rev. Lett.* **110** no. 17, (2013) 171801, arXiv:1301.4581 [hep-ex].

[41] **MINOS** Collaboration, P. Adamson *et al.*, "An improved measurement of muon antineutrino disappearance in MINOS," *Phys. Rev. Lett.* **108** (2012) 191801, arXiv:1202.2772 [hep-ex].

[42] **T2K** Collaboration, K. Abe *et al.*, "Observation of Electron Neutrino Appearance in a Muon Neutrino Beam," *Phys. Rev. Lett.* **112** (2014) 061802, arXiv:1311.4750 [hep-ex].

[43] **NOvA** Collaboration, P. Adamson *et al.*, "First measurement of electron neutrino appearance in NOvA," *Phys. Rev. Lett.* **116** no. 15, (2016) 151806, arXiv:1601.05022 [hep-ex].

[44] P. Vahle, "New Results from NOνA." http://neutrino2016.iopconfs.org/IOP/media/uploaded/EVIOP/event_948/11.30_-_has_to_be_PDF.pdf, 2016.

[45] **DUNE** Collaboration, R. Acciarri *et al.*, "Long-Baseline Neutrino Facility (LBNF) and Deep Underground Neutrino Experiment (DUNE)," arXiv:1601.05471 [physics.ins-det].

[46] K. Abe *et al.*, "Letter of Intent: The Hyper-Kamiokande Experiment Detector Design and Physics Potential," arXiv:1109.3262 [hep-ex].

[47] P. Coloma, P. Huber, J. Kopp, and W. Winter, "Systematic uncertainties in long-baseline neutrino oscillations for large θ_{13}," *Phys. Rev.* **D87** no. 3, (2013) 033004, arXiv:1209.5973 [hep-ph].

[48] **IDS-NF** Collaboration, S. Choubey *et al.*, "International Design Study for the Neutrino Factory, Interim Design Report," arXiv:1112.2853 [hep-ex].

[49] J. Burguet-Castell, D. Casper, E. Couce, J. J. Gomez-Cadenas, and P. Hernandez, "Optimal beta-beam at the CERN-SPS," *Nucl. Phys.* **B725** (2005) 306–326, arXiv:hep-ph/0503021 [hep-ph].

[50] J.-E. Campagne, M. Maltoni, M. Mezzetto, and T. Schwetz, "Physics potential of the CERN-MEMPHYS neutrino oscillation project," *JHEP* **04** (2007) 003, arXiv:hep-ph/0603172 [hep-ph].

[51] **LAGUNA** Collaboration, D. Angus *et al.*, "The LAGUNA design study towards giant liquid based underground detectors for neutrino physics and astrophysics and proton decay searches," in *European strategy for future neutrino physics. Proceedings, Workshop, Geneva, Switzerland, October 1-3, 2009*, pp. 226–229. 2010. arXiv:1001.0077 [physics.ins-det]. https://inspirehep.net/record/841615/files/arXiv:1001.0077.pdf.

[52] **LBNE** Collaboration, T. Akiri *et al.*, "The 2010 Interim Report of the Long-Baseline Neutrino Experiment Collaboration Physics Working Groups," arXiv:1110.6249 [hep-ex].

[53] P. Huber, M. Lindner, T. Schwetz, and W. Winter, "First hint for CP violation in neutrino oscillations from upcoming superbeam and reactor experiments," *JHEP* **11** (2009) 044, arXiv:0907.1896 [hep-ph].

[54] C. T. Rogers, D. Stratakis, G. Prior, S. Gilardoni, D. Neuffer, P. Snopok, A. Alekou, and J. Pasternak, "Muon front end for the neutrino factory," *Phys. Rev. ST Accel. Beams* **16** (2013) 040104.

[55] J. S. Berg *et al.*, "A Cost-effective design for a neutrino factory," *Phys. Rev. ST Accel. Beams* **9** (2006) 011001, arXiv:physics/0511092 [physics].

[56] **CMS** Collaboration, S. Chatrchyan *et al.*, "Observation of a new boson with mass near 125 GeV in pp collisions at $\sqrt{s}$ = 7 and 8 TeV," *JHEP* **06** (2013) 081, arXiv:1303.4571 [hep-ex].

[57] S. Geer, "Neutrino beams from muon storage rings: Characteristics and physics potential," *Phys. Rev.* **D57** (1998) 6989–6997, arXiv:hep-ph/9712290 [hep-ph].

[58] H. Wiedemann, *Particle Accelerator Physics*. Graduate Texts in Physics. Springer, Berlin, Germany, 2015. http://www.springer.com/us/book/9783319183169?wt_mc=ThirdParty.SpringerLink.3.EPR653.About_eBook.

[59] C. Rogers, *Beam dynamics in an ionisation cooling channel*. PhD thesis, Imperial Coll., London, 2007. http://lss.fnal.gov/cgi-bin/find_paper.pl?thesis-2008-100.

[60] **Particle Data Group** Collaboration, C. Amsler *et al.*, "Review of Particle Physics," *Phys. Lett.* **B667** (2008) 1–1340.

[61] A. N. Skrinsky, "Intersecting storage rings at Novosibirsk," *AIP Conf. Proc.* **352** (1996) 6.

[62] D. Neuffer, "Principles and Applications of Muon Cooling," *Part. Accel.* **14** (1983) 75.

[63] **MICE** Collaboration, M. Bogomilov *et al.*, "Pion Contamination in the MICE Muon Beam," *JINST* **11** no. 03, (2016) P03001, arXiv:1511.00556 [physics.ins-det].

[64] **The MICE Collaboration** Collaboration, D. Adams *et al.*, "Characterisation of the muon beams for the Muon Ionisation Cooling Experiment," *Eur. Phys. J.* **C73** (2013) 2582, arXiv:1306.1509 [physics.acc-ph].

[65] **MICE** Collaboration, D. Adams *et al.*, "Electron-Muon Ranger: performance in the MICE Muon Beam," *JINST* **10** no. 12, (2015) P12012, arXiv:1510.08306 [physics.ins-det].

[66] V. Blackmore, C. Hunt, J. B. Lagrange, J. Pasternak, C. Rogers, C. Snopok, and H. Witte, "The MICE Ionisation Cooling Demonstration: Technical Note." http:

//mice.iit.edu/micenotes/public/pdf/MICE0452/MICE0452.pdf, 2014.

[67] C. Booth, P. Hodgson, P. J. Smith, and J. Tarrant, "MICE Target Hardware," *Conf. Proc.* **C100523** (2010) 3488–3490.

[68] **MICE Colaboration** Collaboration, M. Bogomilov *et al.*, "The MICE Muon Beam on ISIS and the beam-line instrumentation of the Muon Ionization Cooling Experiment," *JINST* **7** (2012) P05009, arXiv:1203.4089 [physics.acc-ph].

[69] D. A. J. Forrest, *The Muon Ionization Cooling Experiment*. PhD thesis, University of Glasgow, 2011.

[70] M. Bogomilov, O. M. Bonesini, M. Hansen, Y. Karadzhov, D. Orestano, and L. Tortora, "Measurement of the pion contamination in the MICE beam." http://mice.iit.edu/micenotes/public/pdf/MICE0416/MICE0416.pdf, 2013.

[71] K. L. Brown, F. Rothacker, D. C. Carey, and F. C. Iselin, "Transport: A Computer Program for Designing Charged Particle Beam Transport Systems,".

[72] D. C. Carey, K. L. Brown, and F. C. Iselin, "Decay TURTLE (Trace Unlimited Rays Through Lumped Elements): A Computer Program for Simulating Charged Particle Beam Transport Systems, Including Decay Calculations,".

[73] J. Pasternak, "Private communication," 2014.

[74] L. Cremaldi, D. Sanders, D. Summers, M. Drews, D. Kaplan, D. Rajaram, and M. Winter, "Progress on Cherenkov Reconstruction in MICE Note 473." "http://mice.iit.edu/micenotes/public/pdf/MICE0473/MICE0473.pdf", 2015.

[75] M. Bonesini, "The TOF1 local shielding." http://mice.iit.edu/micenotes/public/pdf/MICE0455/MICE0455.pdfbertoni, 2015.

[76] R. Bertoni, M. Bogomilov, M. Bonesini, A. de Bari, G. Cecchet, Y. Karadzhov, F. T. L. Orestano, D. Pastore, and R. Tsenov, "Analysis of PID detectors (TOF and KL) performances in the MICE 2010 run." http://mice.iit.edu/mnp/MICE0337.pdf, 2011.

[77] R. Bertoni, M. Bonesini, A. de Bari, and G. Cecchet, "The Refurbishing of MICE TOF0 and TOF1 detectors." "{http://mice.iit.edu/mnp/MICE0363.pdf}", 2012.

[78] D. A. Sanders, "MICE Particle Identification Systems," arXiv:0910.1332 [physics.ins-det]. [Conf. Proc.C090504,1696(2009)].

[79] R. Asfandiyarov *et al.*, "The design and construction of the MICE Electron-Muon Ranger," arXiv:1607.04955 [physics.ins-det].

[80] A. Dobbs, C. Hunt, K. Long, E. Santos, and C. Heidt, "The Reconstruction Software for the MICE Scintillating Fibre Trackers." http://mice.iit.edu/micenotes/public/pdf/MICE0451/MICE0451.pdf, 2014.

[81] R. Fruhwirth, "Application of Kalman filtering to track and vertex fitting," *Nucl. Instrum. Meth.* **A262** (1987) 444–450.

[82] H. Witte, "Presentation at MICE Collaboration Meeting (CM35): Return Yoke." http://indico.cern.ch/conferenceOtherViews.py?view=, 2013.

[83] P. Smith, "Presentation at MICE Collaboration Meeting (CM34): Stray Magnetic Field Modelling." http://indico.cern.ch/conferenceOtherViews.py?view=, 2013.

[84] C. Tunnell and C. Rogers, "MAUS: MICE Analysis User Software," *Conf. Proc.* **C110904** (2011) 850–852.

[85] I. Antcheva *et al.*, "ROOT: A C++ framework for petabyte data storage, statistical analysis and visualization," *Comput. Phys. Commun.* **182** (2011) 1384–1385.

[86] M. Ellis, "MICE Software Design and Physics Performance,". [Conf. Proc.C0710083,763(2007)].

[87] R. Bayes, "Presentation at mice collaboration meeting (CM41): Geometry Status," 2015. https://indico.cern.ch/event/360388/contributions/1773929/attachments/717963/985526/GeometryStatus.pdf.

[88] D. Forrest, "The MICE Configuration Database System." http://hep04.phys.iit.edu/cooldemo/micenotes/public/pdf/MICE0327/MICE0327.pdf, 2011.

[89] C. Colin, M. Hills, A. Mariani, J. Giles, and A. Austin, "Survey of MICE Beamline." http://mice.iit.edu/micenotes/public/pdf/MICE0216/MICE0216.pdf, 2008.

[90] T. Roberts *et al.*, "G4beamline, A "Swiss Army Knife" for Geant4, optimized for simulating beamlines." http://www.muonsinc.com/muons3/G4beamline, 2013.

[91] "MAUS Software Userguide." http://micewww.pp.rl.ac.uk/maus/MAUS_latest_version/maus_user_guide/node4.html#SECTION00460000000000000000, 2014.

[92] D. Britton *et al.*, "GridPP: the UK grid for particle physics," *Phil. Trans. R. Soc. A* **367** (2009) 2447–24.

[93] **GridPP Collaboration** Collaboration, P. Faulkner *et al.*, "GridPP: Development of the UK computing Grid for particle physics," *J.Phys.* **G32** (2006) N1–N20.

[94] D. Forrest and F. Soler, "A new application for the Grid: muon ionization cooling for a Neutrino Factory," *Phil. Trans. Roy. Soc. Lond.* **A368** (2010) 4103–4113.

[95] "Quadrant borated Polyethylenes." http://micewww.pp.rl.ac.uk/projects/operations/wiki/BeamlineDocsBoratedPE, 2014.

[96] L. A. A. C. Group, "Trace3d." http://laacg.lanl.gov/laacg/services/download_trace.phtml, 2014.

[97] F. Brochu, U. Egede, J. Elmsheuser, K. Harrison, R. W. L. Jones, H. C. Lee, D. Liko, A. Maier, J. T. Moscicki, A. Muraru, G. N. Patrick, K. Pajchel, W. Reece, B. H. Samset, M. W. Slater, A. Soroko, C. L. Tan, and D. C. Vanderster, "Ganga: a tool for computational-task management and easy access to grid resources,". http://arxiv.org/abs/0902.2685.

[98] M. Apollonio and M. Rayner, "Optimization of the MICE Muon Beam Line," *Conf. Proc.* **C100523** (2010) 3461–3463.

[99] AccelSoft Inc, "PBO Lab DECAY-TURTLE Application Module." http://www.ghga.com/accelsoft/decay.html, 2002.

[100] V. Blackmore, "Presentation at mice collaboration meeting (CM34): A tour of the step i emittance paper," 2012. https://indico.cern.ch/event/208246/contributions/409959/attachments/321101/447949/Blackmore_MICECM34.pdf.

[101] "Vector Fields Simulation Software.". http://www.cobham.com.

[102] M. A. Rayner, *The development of a novel technique for characterizing the MICE muon beam and demonstrating its suitability for a muon cooling measurement*. PhD thesis, Oxford U., 2011. http://lss.fnal.gov/archive/other/thesis/rayner-m.pdf.

[103] L. Merminga, P. L. Morton, J. Seeman, and W. L. Spence, "Transverse phase space in the presence of dispersion," *Conf. Proc.* **C910506** (1991) 461–463.

[104] **MICE** Collaboration, P. Hanlet, "Progress Towards the Completion of the MICE Demonstration of Sustainable Ionization Cooling," *PoS* **NUFACT2014** (2015) 066.

[105] **Mice** Collaboration, R. Bertoni *et al.*, "The design and commissioning of the MICE upstream time-of-flight system," *Nucl. Instrum. Meth.* **A615** (2010) 14–26, arXiv:1001.4426 [physics.ins-det].

[106] D. Lietti *et al.*, "The prototype of the MICE Electron-Muon Ranger: Design, construction and test," *Nucl.Instrum.Meth.* **A604** (2009) 314–318.

[107] L. Cremaldi, D. A. Sanders, P. Sonnek, D. J. Summers, and J. Reidy, Jr, "A Cherenkov Radiation Detector with High Density Aerogels," *IEEE Trans. Nucl. Sci.* **56** (2009) 1475–1478, arXiv:0905.3411 [physics.ins-det].

[108] "MAUS homepage." http://micewww.pp.rl.ac.uk/projects/maus, 2014.

[109] L. M. Caminada, *Study of the Inclusive Beauty Production at CMS and Construction and Commissioning of the CMS Pixel Barrel Detector*. PhD thesis, Zurich, ETH.

[110] *The Telecommunications and Data Acquisition Progress Report*. **42-68**. H. H. Tan, "A statistical model of the photomultiplier gain process with applications to optical pulse detection". jpl.nasa.gov/progress_report//68H.PDF.

[111] R. Brun and F. Rademakers, "ROOT - An Object Oriented Data Analysis Framework," *Nucl. Instrum. Meth.* **389** (1997) 81–86.

[112] R. Barlow and C. Beeston, "Fitting using finite Monte Carlo samples," *Comp. Phys. Commun.* **77** (1993) 219–22.

[113] G. J. Feldman and R. D. Cousins, "A Unified approach to the classical statistical analysis of small signals," *Phys. Rev.* **D57** (1998) 3873–3889, arXiv:physics/9711021 [physics.data-an].

[114] L. Cremaldi, D. Sanders, D. Drews, D. Kaplan, and M. Winter, "Progress on Cherenkov Reconstruction in MICE," 2015.

[115] "BACH Alignment Package." http://aidasoft.web.cern.ch/Bach.

[116] S. Borghi, C. Hombach, and C. Parkes, "AIDA Alignment package user guide," *AIDA-NOTE-2014-001* (Apr, 2014) . https://cds.cern.ch/record/1701341.

[117] V. Blobel and C. Kleinwort, "A New method for the high precision alignment of track detectors," in *Advanced statistical techniques in particle physics. Proceedings, Conference, Durham, UK, March 18-22, 2002*, pp. URL–STR(9). 2002. arXiv:0807.5067 [hep-ex]. http://www.ippp.dur.ac.uk/Workshops/02/statistics/proceedings//blobel1.pdf.

[118] V. Blobel, "Software alignment for tracking detectors," *Nucl. Instrum. Meth.* **A566** (2006) 5–13.

[119] **CMS** Collaboration, S. Chatrchyan *et al.*, "Alignment of the CMS tracker with LHC and cosmic ray data," *JINST* **9** (2014) P06009, arXiv:1403.2286 [physics.ins-det].

[120] S. Viret, C. Parkes, and M. Gersabeck, "Alignment procedure of the LHCb Vertex Detector," *Nucl. Instrum. Meth.* **A596** (2008) 157–163, arXiv:0807.5067 [physics.ins-det].

[121] **Particle Data Group** Collaboration, K. A. Olive *et al.*, "Review of Particle Physics," *Chin. Phys.* **C38** (2014) 090001.

[122] D. Neuffer, "Principles and Applications of Muon Cooling," *Proceedings, 12th International Conference on High-Energy Accelerators, HEACC 1983* **C830811** (1983) 481.

[123] G. R. Lynch and O. I. Dahl, "Approximations to multiple Coulomb scattering," *Nucl. Instrum. Meth.* **B58** (1991) 6–10.

[124] T. Carlisle, "Step IV of the Muon Ionization Cooling Experiment (MICE) and the multiple scattering of muons," *DPhil thesis, University of Oxford* (2013) .

[125] D. Attwood *et al.*, "The scattering of muons in low Z materials," *Nucl. Instrum. Meth.* **B251** (2006) 41–55, arXiv:hep-ex/0512005 [hep-ex].

[126] B. Rossi and K. Greisen, "Cosmic-ray theory," *Rev. Mod. Phys.* **13** (1941) 240–309.

[127] G. Moliere, "Theory of the scattering of fast charged particles. 2. Repeated and multiple scattering," *Z. Naturforsch.* **A3** (1948) 78–97.

[128] H. A. Bethe, "Moliere's theory of multiple scattering," *Phys. Rev.* **89** (1953) 1256–1266.

[129] W. T. Scott, "The theory of small-angle multiple scattering of fast charged particles," *Rev. Mod. Phys.* **35** (1963) 231–313.

[130] W. W. M. Allison, "Calculations of energy loss and multiple scattering (ELMS) in molecular hydrogen," *J. Phys.* **G29** (2003) 1701–1703.

[131] S. Holmes, "The Physics of Muon Cooling for a Neutrino Factory," *DPhil thesis, University of Oxford* (2006) .

[132] **GEANT4** Collaboration, S. Agostinelli *et al.*, "GEANT4: A Simulation toolkit," *Nucl. Instrum. Meth.* **A506** (2003) 250–303.

[133] L. Urban, "A model for multiple scattering in Geant4,". CERN-OPEN-2006-077.

[134] V. N. Ivanchenko, O. Kadri, M. Maire, and L. Urban, "Geant4 models for simulation of multiple scattering," *J. Phys. Conf. Ser.* **219** (2010) 032045.

[135] T. Carlisle, J. Cobb, and D. Neuffer, "Multiple Scattering Measurements in the MICE Experiment," *Conf. Proc.* **C1205201** (2012) 1419–1421.

[136] M. Ellis *et al.*, "The Design, construction and performance of the MICE scintillating fibre trackers," *Nucl. Instrum. Meth.* **A659** (2011) 136–153, `arXiv:1005.3491 [physics.ins-det]`.

[137] M. Morhac, J. Kliman, V. Matousek, M. Veselsky, and I. Turzo, "Efficient one- and two-dimensional gold deconvolution and its application to γ-ray spectra decomposition," *Nucl. Instr. and Meth. A* **401** no. 2-3, (1997) 385–408.

[138] R. M. Gray, "Toeplitz and circulant matrices: A review," *Foundations and Trends in Communications and Information Theory* **2** no. 3, (2006) 155–239. `http://dx.doi.org/10.1561/0100000006`.